Numerical Evaluation of Forces on Piled Bridge Foundations in Laterally Spreading Soil

WA-RD 874.1

Pedro Arduino
Christopher R. McGann
Alborz Ghofrani

April 2017

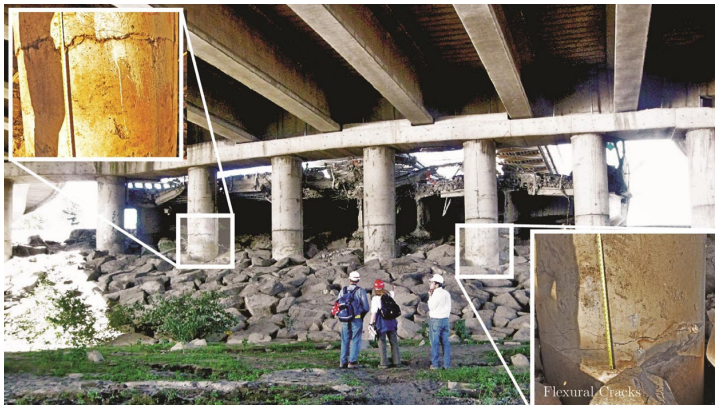

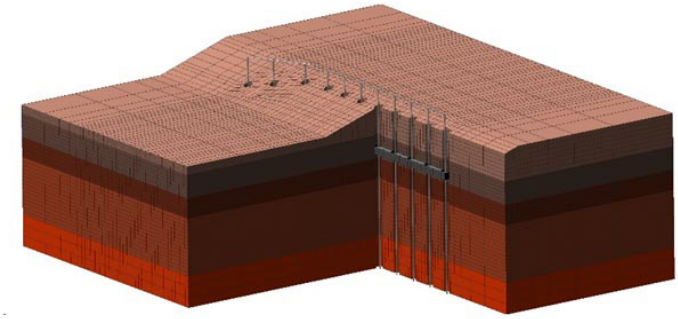

Washington State Department of Transportation
Office of Research & Library Services

WSDOT Research Report

17-10-0407

Research Report
Research Project WA-RD 874.1

Numerical Evaluation of Forces on Piled Bridge Foundations in Laterally Spreading Soil

Final Report to
Washington State Department of Transportation (WSDOT)

by

Pedro Arduino

Christopher R. McGann

Alborz Ghofrani

University of Washington

Department of Civil and Environmental Engineering

2017

TECHNICAL REPORT DOCUMENTATION PAGE

1. Report No. WA-RD 874.1	2. Government Accession No.	3. Recipient's Catalog No.
4. Title and Subtitle Numerical Evaluation of Forces on Piled Bridge Foundations in Laterally Spreading Soil		**5. Report Date** April 2017 **6. Performing Organization Code**
7. Author(s) Pedro Arduino, Christopher McGann, Alborz Ghofrani		**8. Performing Organization Report No.**
9. Performing Organization Name and Address Washington State Transportation Center (TRAC) University of Washington, Box 354802 University District Building, 1107 NE 45th Street, Suite 535 Seattle, Washington 98105-4631		**10. Work Unit No.** **11. Contract or Grant No.** **Agreement T4118 Task 86**
12. Sponsoring Agency Name and Address Washington State Department of Transportation, Research Office Transportation Building, MS 47372 Olympia, Washington 98504-7372 Project Manager: Lu Saechao, 360-705-7260		**13. Type of Report and Period Covered** Final Research Report **14. Sponsoring Agency Code**

15. Supplementary Notes

Conducted in cooperation with the U.S. Department of Transportation, Federal Highway Administration.

16. Abstract

The response of piled bridge foundations to liquefaction-induced lateral soil deformation is an important design consideration in seismically active regions. Recent research and case history data suggest that three-dimensional deformation of the approach embankment can significantly influence the loads placed on the embedded foundations during a flow failure or lateral spreading event. For example, the 2010 Maule earthquake in Chile caused widespread lateral spreading in the soil surrounding the Mataquito River bridge, however, only insignificant structural damage was observed in the bridge itself. The discrepancy between the amount of soil deformation and structural damage suggests that design procedures for this load case that do not make adequate consideration for 3D soil deformation mechanisms may lead to overly conservative and expensive design solutions. In contrast, observed lateral spreading and damage near the Llacolén bridge was more relevant and resulted in the collapse of one of the approach sections. The Llacolén bridge approaches show lesser 3D effects on both sides of the bridge and therefore larger loads on the structural components. In this work, finite element models of the Mataquito River and Llacolén bridges are created using the OpenSees computational framework to investigate possible reduction in foundation loads during lateral spreading implied by the observed structural damage at the sites. These models include beam on nonlinear Winkler foundation models, dynamic effective stress models of the bridge-foundation-soil system in plane strain, and 3D models of the bridge abutments, approach embankments, and surrounding soils. This numerical work seeks to frame load reduction mechanisms in the context of a simplified analysis procedure for the lateral spreading load case. The results of the numerical models for the Mataquito and Llacolén bridges, along with a preliminary parameter study conducted using an independent set of 3D finite element models, indicate that consideration for the 3D geometry of the bridge site and structure may result in tangible reductions in foundation bending demands and abutment displacements compared to those returned by a plane strain description of the problem or simplified analysis using 1D models. This analysis procedure is modified to better consider the findings of this work and it is recommended to use in the design of bridge foundations subjected to lateral spreading. Finally, an approach is proposed to estimate the reductions in abutment displacement and associated foundation bending demands for a given site geometry. The latter is based on results from a preliminary parametric study and would require further development and validation to use in practice.

17. Key Words	18. Distribution Statement
Lateral spreading, Deep Foundations, Drilled Shafts, Soil Liquefaction, Lateral Loads, Liquefaction-Induced Lateral Displacements	No restrictions. This document is available through the National Technical Information Service, Springfield, VA 22161.

19. Security Classif. (of this report)	20. Security Classif. (of this page)	21. No. of Pages	
None	None		

DISCLAIMER

The contents of this report reflect the views of the authors, who are responsible for the facts and the accuracy of the data presented herein. The contents do not necessarily reflect the official views or policies of the Washington State Transportation Commission, Department of Transportation, or the Federal Highway Administration. This report does not constitute a standard, specification, or regulation.

EXECUTIVE SUMMARY

Numerical Evaluation of Forces on Piled Bridge Foundations in Laterally Spreading Soil

Pedro Arduino, Christopher R. McGann and Alborz Ghofrani

The response of piled bridge foundations to liquefaction-induced lateral soil deformation is an important design consideration in seismically active regions. Recent research and case history data suggest that three-dimensional deformation of the approach embankment can significantly influence the loads placed on the embedded foundations during a flow failure or lateral spreading event. For example, the 2010 Maule earthquake in Chile caused widespread lateral spreading in the soil surrounding the Mataquito river bridge, however, only insignificant structural damage was observed in the bridge itself. The discrepancy between the amount of soil deformation and structural damage suggests that design procedures for this load case that do not make adequate consideration for 3D soil deformation mechanisms may lead to overly conservative and expensive design solutions. In contrast, observed lateral spreading and damage near the Llacolén bridge was more relevant and resulted in the collapse of one of the approach sections. The Llacolén bridge approaches show lesser 3D effects on both sides of the bridge and therefore larger loads on the structural components.

In this work finite element models of the Mataquito river and Llacolén bridges are created using the OpenSees computational framework to investigate possible reduction in foundation loads during lateral spreading implied by the observed structural damage at the sites. These models include beam on nonlinear Winkler foundation models, dynamic effective stress models of the bridge-foundation-soil system in plane strain, and 3D models of the bridge abutments, approach embankments, and surrounding soils. This numerical work seeks to frame load reduction mechanisms in the context of a simplified analysis procedure for the lateral spreading load case.

The results of the numerical models for the Mataquito and Llacolén bridges, along with a preliminary parameter study conducted using an independent set of 3D finite element models, indicate that consideration for the 3D geometry of the bridge site and structure may result in tangible reductions in foundation bending demands and abutment displacements compared to those returned by a plane strain description of the problem or simplified analysis using 1D models. This reduction increases as the depth of the liquefiable layer and the effective width of the approach embankment

are decreased. An existing simplified analysis procedure is modified to better consider the findings of this work and it is recommended to use in the design of bridge foundations subjected to lateral spreading. Finally, an approach is proposed to estimate the reductions in abutment displacement and associated foundation bending demands for a given site geometry. The latter is based on results from a preliminary parametric study and would require further development and validation to use in practice.

TABLE OF CONTENTS

LIST OF FIGURES

LIST OF TABLES

Chapter 1

BACKGROUND AND INTRODUCTION

Seismic design of bridge foundations is a significant aspect to the general design process for bridges in certain parts of the world. For river-spanning bridges, a critical part of the seismic design effort is an assessment of the effects of liquefaction-induced flow failure or lateral spreading on the bridge foundations. Current design procedures for this load case generally prescribe simplified analytical methods based on a two-dimensional description of the site geometry. The assumption of plane strain for this type of analysis is a practical approach that will typically lead to conservative foundation designs. Due to the uncertainty involved in the lateral spreading problem, such conservatism is generally desired, however, for the case of an approach embankment built with finite lateral extents, it is hypothesized that the use of design procedures based on plane strain assumptions may result in overly conservative and expensive design solutions.

Numerous bridges affected by lateral spreading during past earthquakes have displayed three-dimensional soil deformation effects that cannot be captured in a two-dimensional analysis. In many of these cases, it is apparent that the bridge and its foundations have altered the near-field deformation pattern of the laterally spreading soil, and it is likely that the resistance provided by the bridge leads to reductions in foundation demands as compared to those predicted under the assumption of plane strain. The pile pinning analysis procedure (Martin et al., 2002; Ashford et al., 2011), offers a simplified method to account for the lateral resistance provided by bridge foundations during lateral spreading; including 3D effects in a simplified manner. However, this approach has not been validated against recorded case histories and does not offer a way to directly evaluate when significant resistance can be expected and when it cannot.

The objective of this research is to identify and quantify the mechanisms implied by the case history record that may result in potential reductions in the bridge foundation demands developed during lateral spreading through consideration for the three-dimensional geometry of the bridge site. This work involves a review of relevant case histories and recent work, with a focus on numerical modeling strategies, and the development of numerical models that capture the kinematic loading conditions and 3D effects of the problem. The results obtained from the numerical modeling effort are

used to validate and inform the existing pile pinning analysis approach. In addition, a preliminary procedure to assess the expected amount of lateral pinning resistance for a given combination of bridge foundation, soil profile, and approach embankment is presented.

1.1 Representative Case Histories

During liquefaction-induced lateral spreading, a bridge approach embankment, and any native crustal soil above the liquefied zone, will tend to deform towards the river, imposing lateral loads on the bridge foundations in their path. In some cases, due to the combination of the lateral stiffness of the foundation and the limited transverse extents of the embankment there is a tendency for the embankment soil to slump down and flow around the bridge foundation instead of flowing directly into it. This type of 3D embankment deformation has been documented during reconnaissance efforts following multiple earthquakes for which liquefaction-induced lateral spreading was observed along river banks. Several typical cases are discussed in the following sections to provide context and motivation for this research.

1.1.1 Bandai Bridge, 1964 Niigata Earthquake

The Bandai Bridge, finished in 1929, is located in the central part of Niigata City, Japan, spanning the Shinano River. Liquefaction-induced lateral spreading during the M7.5 June 16, 1964 Niigata earthquake caused dramatic bank convergence in the area of the bridge. The Bandai Bridge is an arched reinforced concrete bridge with abutments founded on piles and piers founded on pneumatic caissons (Katayama et al., 1966). The bridge was damaged during the lateral spreading of the river bank, however, the damage was not catastrophic. The abutments settled and rotated with attendant cracking, and the piers settled unevenly. Regardless of the damage sustained, evidence of three-dimensional embankment deformation and foundation pinning effects was observed at this site.

Aerial photographs taken before and after the earthquake were used to measure permanent ground displacements (Hamada and O'Rourke, 1992). These photographs visually demonstrate the restraining effect of the piled bridge abutments on the lateral flow of soil. The ground displacement vectors determined from the photogrammetric analyses, Figure 1.1, support the visual evidence, indicating that river bank displacements near the bridge foundations are lesser than those further away, and that displacements behind the abutments have components parallel to the river bank. The presence of longitudinal cracking near the southern abutment also suggests that the embankment soils spread parallel to the river bank in this area. Further evidence of three-dimensional effects in

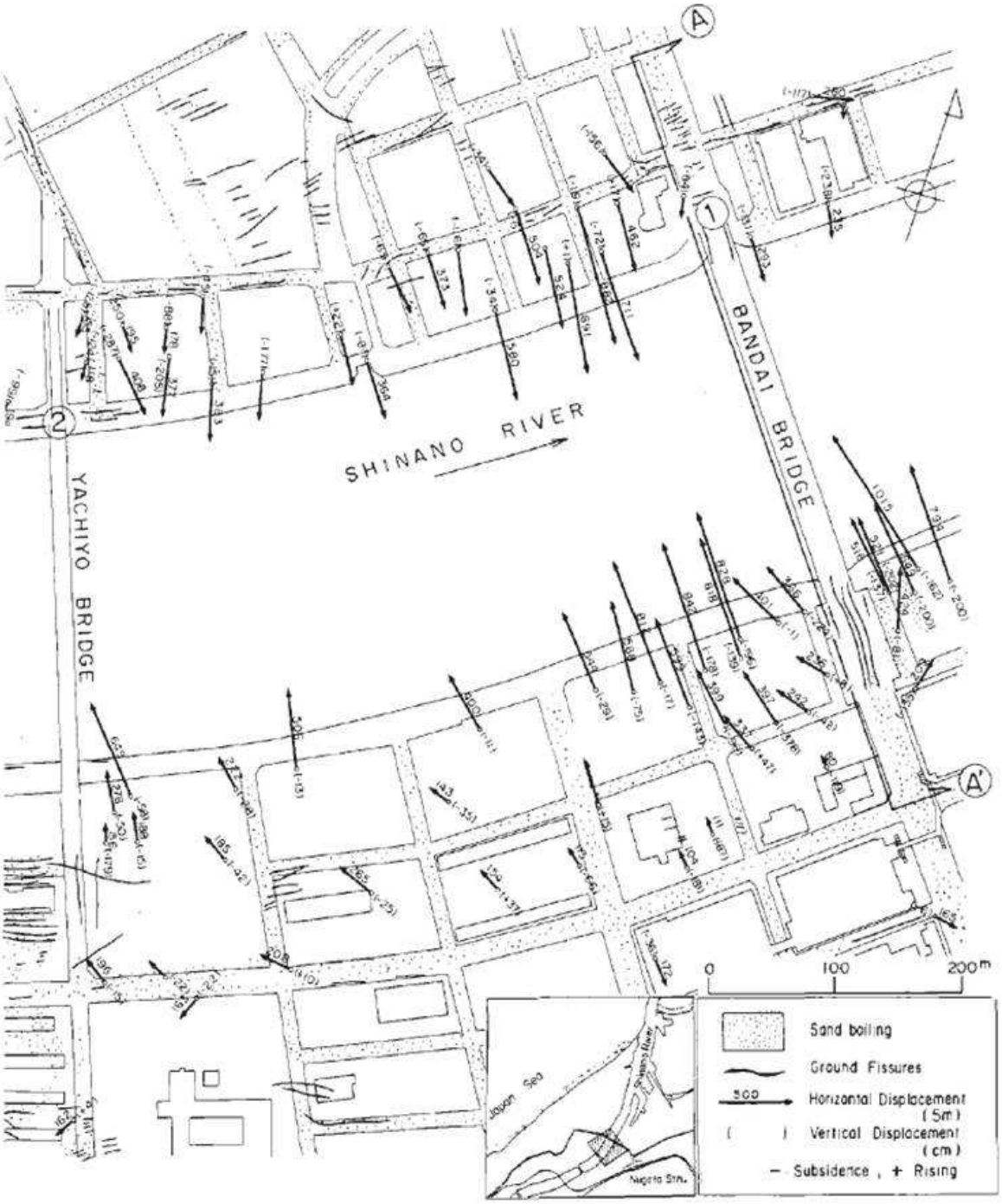

Figure 1.1: Permanent ground displacement vectors in vicinity of Bandai Bridge (Hamada and O'Rourke, 1992).

Figure 1.2: Northern approach to Landing Road Bridge two days after the Edgecumbe event. Ejected sand is visible on the ground surface (Berrill and Yasuda, 2002).

the embankment deformation is given by Katayama et al. (1966), who report the settlement and swelling-out of the road surface in the vicinity of each abutment.

1.1.2 Landing Road Bridge, 1987 Edgecumbe Earthquake

The Landing Road Bridge, constructed in 1962, spans the Whakatane River in the Bay of Plenty Region of New Zealand. The abutments of the Landing Road Bridge are supported by groups of eight raked piles, and the northern-most spans extend over a wide floodplain on the bank of the river as shown in Figure 1.2. Extensive liquefaction-induced lateral spreading of the northern river bank occurred near the bridge during the M6.3 March 2, 1987 Edgecumbe earthquake (Pender and Robertson, 1987). Minor rotation of the northern abutment was observed ($\sim 0.5°$), with cracking in the piles taking place near the connection to the pile cap on the river side (Berrill et al., 2001).

Observed cracks due to lateral spreading in the northern floodplain were parallel to the river bank except in the immediate vicinity of the bridge where they met the bridge axis at approximately 45° (Berrill et al., 2001). Settlement took place in the northern approach embankment, with cracks in the roadway observed extending back a distance of approximately 200 m. The general deformation pattern observed at the bridge demonstrates the resistance to ground displacements provided by the bridge foundations and a corresponding three-dimensional aspect to the embankment deformation.

Figure 1.3: Settlement and longitudinal cracking of southern approach embankment at Rio Estrella Highway Bridge (Youd, 1993).

1.1.3 Rio Estrella Highway Bridge, 1991 Costa Rica Earthquake

Liquefaction-induced lateral spreading occurred near several river-spanning bridges due to the M7.5 April 22, 1991 earthquake in Limon Province, Costa Rica (Franke, 2011). Among these, the highway bridge over the Rio Estrella demonstrates the behavior of interest in this work. After the strong shaking, there was evidence of widespread liquefaction and lateral spreading with displacements as large as 1 to 3 m near the southern bridge abutment, which consists of a concrete wall supported on two groups of twenty piles (Priestley et al., 1991; Franke, 2011).

Very little permanent displacement or rotation of the south abutment was observed. Despite this lack of permanent abutment displacement, the southern bridge span became unseated and collapsed into the river. The approach embankment for the southern abutment failed due to the lateral spreading, settling approximately 2 m and spreading perpendicularly to the longitudinal direction of the bridge with large cracks occurring parallel to the bridge axis as shown in Figure 1.3.

1.1.4 Mataquito River Bridge, 2010 Maule Earthquake

The Mataquito River Bridge, constructed in 2006, spans the Mataquito River between Quivolgo and Iloca, Chile. Liquefaction-induced lateral spreading occurred on both banks of the river due to the M_w8.8 February 27, 2010 offshore Maule earthquake. The bridge has seat-type abutments founded on 4×2 drilled shaft groups, and the interior piers are supported by 3×1 groups of shafts. Lateral soil displacements of up to 2.5 m occurred near the northeast abutment, involving the approach embankment and a 100 m floodplain sloping gently toward the river. Similar lateral spreading effects were observed on the opposite bank, however, the corresponding embankment soils were not

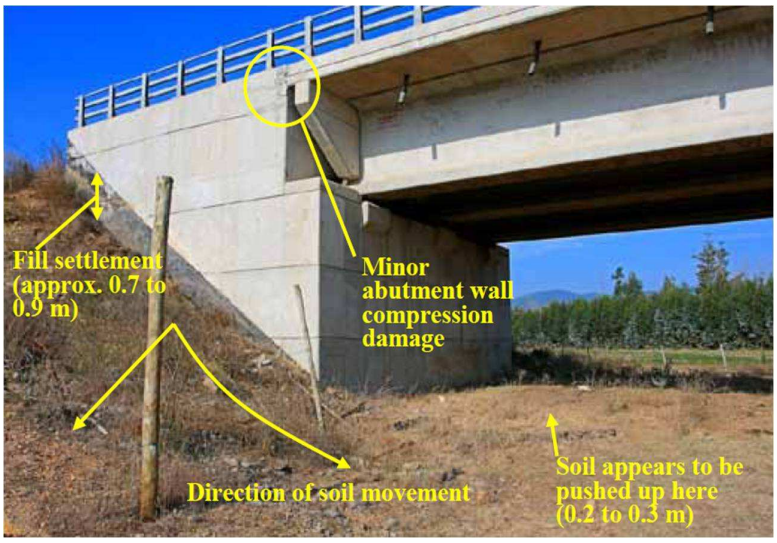

Figure 1.4: Settlement and lateral spreading deformation of northeast approach embankment to Mataquito River Bridge (FHWA, 2011).

involved (FHWA, 2011).

The bridge foundations reportedly did not experience significant permanent lateral deformations, and all bridge spans remained intact and functional. The northeast approach embankment settled approximately 0.7 to 1 m relative to the bridge deck, Figure 1.4. Longitudinal roadway cracks suggest that there was a component of embankment deformation perpendicular to the bridge axis of approximately 0.6 m (GEER, 2010a), indicating that some of the soil moved around the abutment rather than directly into it. This 3D effect may have reduced the forces applied to the foundations, contributing to the minimal damage and deformation observed in the bridge.

1.1.5 Llacolén Bridge, 2010 Maule Earthquake

The 2160 m long Llacolén bridge spans the Bío Bío river between the cities Concepción and San Pedro de la Paz. The superstructure, consisting of four traffic lanes and pedestrian sidewalks, is supported by column bents with inverted-T cap beams, which in turn carry the loads from simply-seated, prestressed I-girders forming the deck of the bridge.

During the Maule earthquake, the eastern bank of the Bío Bío river experienced an extensive amount of lateral spreading due to liquefaction. The northeastern approach of the Llacoln bridge was reported to experience about 25 cm of lateral displacement towards the river and 40 cm of settlement. As a result, the approach span of the bridge was unseated while the westbound entrance came very close to collapse, Figure 1.5. Other than the collapse of the northeastern span, the remaining parts of the bridge remained operable.

Figure 1.5: Lateral spreading and span collapse of northeast approach embankment to Llacolén Bridge (FHWA, 2011).

1.1.6 Various Bridges, 2010 Darfield and 2011 Christchurch Earthquakes

The M7.1 September 4, 2010 Darfield and M6.3 February 22, 2011 Christchurch earthquakes in New Zealand caused liquefaction to occur over much of the city of Christchurch. Liquefaction-induced lateral spreading affected several bridges spanning the Avon and Heathcote rivers, with most of the associated damage concentrated on the abutments, approaches, and piers rather than the superstructure (Wotherspoon et al., 2011). Three-dimensional deformation of approach embankments during lateral spreading was observed at multiple sites for bridges spanning the Avon River.

The South Brighton Bridge, constructed in 1980, has an approximately 70 m span with seat-type abutments and a single central pier (GEER, 2010b). The abutments and pier are supported on raked prestressed concrete piles. Liquefaction-induced lateral spreading occurred on both banks of the river due to the Darfield earthquake, causing significant cracking in the approach embankments. These cracks were perpendicular to the river bank near the abutments, becoming parallel to the river in the surrounding ground. Similar damage occurred during the Christchurch earthquake, increasing the permanent deformation (Wotherspoon et al., 2011). Figure 1.6(a) shows the observed longitudinal surface cracks in the western approach to the bridge, and Figure 1.6(b) shows and aerial view of the bridge site with visible lateral spreading surface cracks along the river banks.

The ANZAC Drive Bridge, built in 2000, is a newer three span bridge supported by two 2-column bents and concrete abutments with wing-walls, all founded on piles (GEER, 2011). Minor liquefaction and lateral spreading occurred due to the Darfield event with no attendant damage (Wotherspoon et al., 2011). Severe liquefaction and significant lateral spreading occurred on both river banks near the bridge due to the Christchurch earthquake, with more pronounced evidence on the southern

(a) (b)

Figure 1.6: South Brighton Bridge after the Christchurch event. (a) Longitudinal lateral spreading cracks in western approach embankment (Cowan, 2011). (b) Aerial photo with visible lateral spreading cracks on river banks (LINZ, 2011).

(a) (b)

Figure 1.7: ANZAC Drive Bridge after the Christchurch event. (a) Aerial photo (LINZ, 2011). (b) Lateral spreading cracks in southern approach (GEER, 2011).

bank, as shown in Figure 1.7(a). Lateral spreading cracks parallel to the bridge axis were observed on both sides of the southern approach embankment (GEER, 2011), as shown in Figure 1.7(b). Both abutments experienced permanent rotations due to the lateral spreading and the restraint provided by the superstructure.

The Avondale Road Bridge, built in 1962, is a three span bridge supported by two 3-column bents and seat-type abutments with wing-walls, all founded on piles (GEER, 2011). Limited liquefaction was observed due to the Darfield earthquake, with no associated damage to the bridge, however, liquefaction-induced lateral spreading occurred due to the Christchurch earthquake. During the latter event, lateral spreading occurred on both river banks, causing permanent rotations in the

Figure 1.8: Avondale Road Bridge after the Christchurch event. Lateral spreading cracks are visible near the southern approach and along the river bank (LINZ, 2011).

abutments. At the southern abutment, lateral spreading cracks were observed extending from the sides of the abutment, perpendicular to the river bank near the abutment and rotating to a parallel configuration over about 15 m distance (Wotherspoon et al., 2011). Figure 1.8 shows an aerial view of the visible lateral spreading surface cracks at the Avondale Road Bridge site.

1.2 Scope of Work

The research discussed in this document is supported by a review of previous work relevant to the problem and an evaluation of case histories with potential for use in the investigation. From this analysis two case study bridges are chosen for further in-depth analysis. These two bridges are the Mataquito river bridge and the Llacoén bridge. Aside from this preliminary effort, the majority of the research is numerical in nature. All of the numerical work is performed using the OpenSees finite element analysis platform, an open-source computational framework maintained by the Pacific Earthquake Engineering Research (PEER) Center. As part of this effort several numerical tools are implemented or modified within the OpenSees framework.

Three types of numerical analysis are considered for the two chosen case study bridges with varying levels of complexity. These models and their general purposes are summarized as follows:

- Dynamic effective stress plane strain finite element models are developed for the full Mataquito bridge site. These models are used to analyze the site response for a ground motion similar to that which occurred at the Mataquito bridge, and to assess the liquefaction and lateral spreading susceptibility and response of the site.

- Simplified beam on nonlinear Winkler foundation models and associated limit equilibrium

slope stability models are developed for the Mataquito and Llacolén bridges to analyze the bridge abutments and foundations using the pile pinning analysis approach proposed by Caltrans (2011). These models are used to assess the viability of this analysis approach in relation to the observed behavior at each site and through comparison with the other modeling approaches.

- 3D finite element models of the bridge abutment and foundation, approach embankment, and the underlying soils are created for the Mataquito and Llacolén bridges to simulate the effects of lateral spreading on the embedded foundations. These models consider the inherent three-dimensionally of each site that cannot be directly considered in the other modeling approaches, and are used to identify mechanisms leading to reductions in lateral foundation loads from those estimated using simplified descriptions of the problem.

The general and specific development related to these models, along with a discussion of their respective results, are discussed in Chapters 5 through 7 for the Mataquito bridge and Chapters 8 and 9 for the Llacolén bridge. In addition to the numerical models developed for the two case study sites, a third set of 3D FE models is created and analyzed in order to quantify the effects of various geometric site parameters on the reduction in foundation demands as compared to a two-dimensional description of the problem. The development and assessment of these parameter study models are discussed in Chapter 10. A summary of the recommendations for design of deep foundations under lateral spreading kinematic loads and the reduction model for characterization of the geometric effects are presented in an accompanying document.

1.3 Summary

Loads imposed on embedded structures during liquefaction-induced lateral ground deformation are an important consideration in the lateral design of deep foundations for bridges in seismically active regions. A brief review of several case histories documenting bridge performance in past earthquakes demonstrates that the presence of foundation elements influences the deformation of the soil during lateral spreading. In each of the referenced case histories, there is an observed tendency for the approach fill to slump vertically and for the soil to deform perpendicularly to the bridge axis, likely due to the lateral resistance provided by the bridge foundations and superstructure.

An analysis which assumes 2D conditions, i.e., all embankment and native crustal soil behind a bridge abutment will transmit load directly into the foundation during lateral spreading or flow failure, may be over-conservative. A simplified analysis procedure for estimating lateral spreading forces which makes consideration for the effects observed in the case histories, or provides guidance

on when 2D or 3D assumptions are most applicable, would be a valuable tool for bridge design. The research discussed in this document attempts to provide guidance on such a procedure.

Chapter 2

REVIEW OF PILED BRIDGE FOUNDATION ANALYSIS

A significant amount of research has been dedicated to investigating the response of bridge foundations and general deep foundations in liquefied and laterally spreading soil. These investigations have employed different combinations of numerical modeling, experimental testing, and case history evaluation to reach various conclusions. A review of the recent relevant literature follows. For general reference, the following works provide a fairly comprehensive discussion of the issues related to the seismic analysis of bridge foundations and piles (Ledezma and Bray, 2010, 2008; Martin, 2004; Aviram et al., 2008b; Ashford et al., 2011; Finn, 2005; Cubrinovski and Ishihara, 2007; Berrill and Yasuda, 2002)

2.1 Experimental Analysis

The behavior of piled bridge abutments, as well as isolated piles or pile groups, during lateral spreading and other lateral load cases has been studied via numerous experiments. These experiments include centrifuge tests (e.g., Armstrong et al., 2008; Gonzalez Lagos et al., 2007; Tobita et al., 2006; Bhattacharya et al., 2005; Brandenberg et al., 2005; Boulanger et al., 2003; Kondoh and Tamura, 2003; Abdoun and Dobry, 2002), full-size or scaled shake table tests (e.g., Suzuki et al., 2006; Dungca et al., 2006; Cubrinovski et al., 2006; Tokimatsu et al., 2005), and full-scale field tests (e.g., Lemitzer et al., 2010, 2009; Bozorgzadeh et al., 2008; Stewart et al., 2007; Rollins et al., 2005; Wallace et al., 2001; Mokwa and Duncan, 2000; Romstad et al., 1995).

These experiments have provided insights into such phenomena as pile pinning effects during lateral spreading (Armstrong et al., 2008; Gonzalez Lagos et al., 2007), pile buckling in liquefied soil (Bhattacharya et al., 2005), the lateral behavior of pile caps, bridge abutments, and backfill soil (Lemitzer et al., 2009; Bozorgzadeh et al., 2008; Mokwa and Duncan, 2000; Romstad et al., 1995), induced earth pressures on bridge abutments during lateral spreading (Kondoh and Tamura, 2003), the interaction of piles and laterally spreading crustal layers (Knappett et al., 2010; Brandenberg et al., 2007a), and the general response of piles and pile groups to liquefaction and lateral spreading.

2.2 Numerical Analysis

Numerical analysis techniques have become the most viable method of analysis for design purposes, and extensive numerical analyses have been conducted in order to validate and refine existing approaches. As confidence has increased, it has become common for researchers to use numerical analysis to gain further insight on the behavior of deep foundations in liquefied and laterally spreading soil. The majority of the numerical analyses present in the literature can be separated into three broad groups; (1) those that exclusively use a beam on nonlinear Winkler foundation (BNWF) approach to represent soil-foundation interaction, (2) those that model the soil-foundation system in 2D with a plane strain soil continuum, and (3) those that model the full three-dimensionality of the problem. There are obviously hybrid approaches which fit in between these broad categories, however, they serve as useful separators for a survey of the literature.

2.2.1 Beam on Nonlinear Winkler Foundation Models

The use of a BNWF model to represent the interaction between deep foundations and the surrounding soil is prevalent. In this approach, the deep foundation is modeled as a beam-column and the soil is modeled using a series of discrete nonlinear force density-displacement springs. These springs are used to represent both lateral (normal to the pile) and vertical (parallel to the pile) soil response, and are typically derived from experimental testing. In the generally accepted nomenclature for this approach, *p-y* springs (e.g., Reese and Van Impe, 2001; API, 2007) refer to lateral soil-pile interaction, *t-z* springs (e.g., Seed and Reese, 1957; Kraft et al., 1981; Reese et al., 2006) to frictional side resistance, and *Q-z* springs (e.g., Meyerhof, 1976; Vijayvergiya, 1977) to pile end bearing.

BNWF analyses of piles and pile groups have been compared and validated against experimental data or case histories in numerous studies using both pseudo-static pushover approaches (e.g., Boulanger et al., 2003; Tokimatsu et al., 2005; Brandenberg et al., 2007b; Takahashi et al., 2006a; Ashford and Juirnarongrit, 2006; Khalili-Tehrani et al., 2007) and dynamic analysis (e.g., Miwa et al., 2006; Boulanger et al., 2003). In general, good agreement has been observed between the analytical and experimental results for different configurations and loading types, though thoughtful definition of the included nonlinear springs is often required. These types of correlations have increased the viability of the BNWF analysis approach, leading to its ubiquity in current practice.

BNWF methods have been used to model soil-structure interaction in both 2D and 3D, and have been applied to single piles, pile groups, and complete bridge foundations. The BNWF approach has been incorporated into models investigating thermal loads on bridges (e.g., Faraji et al., 2001), models examining the effects of live load distribution on integral abutment bridges (Dicleli and

Erhan, 2005), and in pseudo-static pushover analyses of piles and piled bridge abutments (Silva and Manzari, 2008; Dicleli, 2005). Force-displacement curves representing the lateral response of pile caps and abutments with native and backfill soil have also been investigated (e.g., Dicleli, 2005; Dicleli and Erhan, 2005; Shamsabadi et al., 2007, 2005; Mokwa and Duncan, 2000).

Other work which has employed a BNWF approach includes an examination of the stiffness of piles subject to dynamic shaking in liquefiable soils (Arduino et al., 2006), an analysis of a base-isolated curved bridge using dynamic nonlinear 3D finite element analysis (Ates and Constantinou, 2011), an evaluation of the effects of various bridge abutment modeling decisions on the global seismic response of bridges (Aviram et al., 2008a), and investigations into pile stability and bending-buckling interaction in liquefiable soils (Dash et al., 2010; Knappett and Madabhushi, 2006).

Proposed simplified analysis and design procedures have been developed based on BNWF representations of soil-foundation interaction. Ashour and Ardalan (2011) proposed an analytical method for piles subject to lateral spreading which considers strain wedge effects and accounts for the differing responses of the crust, liquefied soil, and non-liquefied soil. Bradley et al. (2011) proposed a probabilistic framework for pseudo-static analysis of piles in liquefied and laterally spreading soils. Valsamis et al. (2011) proposed a simplified design procedure for single piles in liquefaction-induced lateral spreading based on a parametric analysis. Design charts for the maximum bending moment and displacement of the pile are presented. Brandenberg et al. (2011) developed demand fragility curves for bridges in liquefied and laterally spreading ground using nonlinear equivalent static analysis with inputs sampled using Monte Carlo simulation. Franke (2011) analyzed case history results within the context of performance-based evaluation of bridge foundations.

Cubrinovski and Ishihara (2004) proposed a simplified analysis procedure for piles subject to lateral spreading based on a closed-form solution to the beam on elastic foundation equation. Linear properties were assumed for the soil and pile for this solution, however, simplified models for nonlinear behavior can be incorporated using an equivalent linear approach. Cubrinovski and Ishihara (2006) extended this method to consider pile groups. Meera et al. (2007) and Chang et al. (2008) presented similar finite difference solutions to the beam on Winkler foundation problem for use in the analysis of piles subject to lateral spreading.

2.2.2 Two-Dimensional Finite Element and Finite Difference Models

Plane strain analysis of bridge-foundation-soil systems is an approach which offers refinements over the BNWF approach (e.g., effective stress analysis) at a lower computational cost than fully three-dimensional analysis. Plane strain finite element analysis (FEA) has been used to model pile groups

subject to lateral spreading (Chang et al., 2006), to investigate the relationship between ground motion intensity measures and pile response (Bradley et al., 2009), to model bridge abutments subject to lateral loads and seismic shaking (Shamsabadi et al., 2010; Ooi et al., 2010; Hara et al., 2004), and to model the seismic response of bridge-foundation-soil systems using an effective stress approach (Shin et al., 2008; Bradley et al., 2010).

Despite the applications listed above, plane strain analysis is the least common analytical approach in the literature, likely due to the associated difficulty in modeling deep foundations appropriately. The assumption of plane strain is perfectly applicable to the soil domain in most conditions, and bridge foundations without piles can be modeled effectively (e.g., Shamsabadi et al., 2010). However, plane strain is not applicable to deep foundation bodies, which have inherently small out-of-plane dimensions and interact with the soil in a fundamentally three-dimensional manner.

Several approaches have been used to overcome the non-applicability of deep foundations to plane strain conditions. The most effective and common approach is to use *p-y* curves, which are based on 3D soil-pile interaction, to connect piles modeled as beam-column elements to the adjacent solid elements representing the soil domain (e.g., Shin et al., 2008; Chang et al., 2006). Hara et al. (2004) modeled a pile group using several columns of solid elements, assuming the row of piles to act as a plane strain wall. Ooi et al. (2010), Bradley et al. (2009), and Bradley et al. (2010) used a similar assumption with a pile row acting as a wall in plane strain, but modeled the piles as beam-column elements.

Neither of these approaches are perfect. For example, the assumptions involved with the plane strain wall approach are not applicable to all pile spacings and cannot account for a single pile. When using the *p-y* curve approach, it is important to address the effects of representing the soil using both solid elements and soil-pile interaction springs. It is often assumed that the solid elements represent the far-field soil response while the *p-y* curves represent the near-field response. Modifications to the stiffness of the soil-pile interaction curves such that the combined lateral response of the spring and solid elements approximates a target *p-y* response is another alternative (Armstrong, 2010).

2.2.3 Three-Dimensional Finite Element and Finite Difference Models

Three-dimensional analysis possesses the greatest potential for accurately capturing the full behavior of soil-foundation systems, though it also presents the greatest computational expense. As computing power has increased, the relative cost of 3D numerical analysis has become less prohibitive, and the use of this technique has become more common in both research and practice.

Much of the early work in 3D numerical analysis of deep foundations was conducted by Desai

and his colleagues (e.g., Desai and Appel, 1976; Faruque and Desai, 1982; Muqtadir and Desai, 1986). Other examples of relatively early work in this field include Brown et al. (1989) and Brown and Shie (1990, 1991). These early studies showed that 3D analysis is a viable approach for single and grouped deep foundations, able to incorporate nonlinear constitutive behavior, geometric nonlinearity, interface friction, sloping ground, and other influential factors.

The research program discussed in this document primarily involves the use of 3D FEA as a numerical modeling tool. In order to gain a better understanding of the 3D modeling process, as related to the particular problem under consideration, the literature summary for this topic is presented in greater detail. Each aspect of the full 3D model is separately discussed to provide a more comprehensive survey of the different approaches which have been previously undertaken. These aspects include soil constitutive behavior, the use of mixed elements for fluid-solid coupling, treatments for deep foundations and the soil-foundation interface, and boundary and loading conditions.

2.2.3.1 Soil Constitutive Modeling

Soil constitutive modeling approaches in 3D analyses of soil-foundation systems have ranged from relatively simple Von Mises, Drucker-Prager, and Mohr-Coulomb plasticity models (e.g., Yang and Jeremic, 2002, 2003, 2005; Khalili-Tehrani et al., 2007; Ooi et al., 2010) to more sophisticated alternatives as computing power has increased. An extension of the Duncan and Chang (1970) hyperbolic constitutive model with a yield cap and consideration for soil dilatancy effects was used by Shamsabadi et al. (2010). Multi-surface plasticity models (Prevost, 1977, 1985; Elgamal et al., 2003) have been used to represent the constitutive behavior of both cohesive and cohesionless soils in total and effective stress analyses, respectively (e.g., Elgamal et al., 2006, 2008).

Other approaches are found in the work of Cubrinovski et al. (2008) and Uzuoka et al. (2008), who used a critical state constitutive model for cohesionless soil (Cubrinovski and Ishihara, 1998a,b) in effective stress analyses, Cheng and Jeremic (2009), who used a soil constitutive model based on the work of Manzari and Dafalias (1997) and Dafalias and Manzari (2004), and Takahashi et al. (2006b, 2010) who used a plasticity model with a subloading surface and rotational hardening after Hashiguchi and Chen (1998).

2.2.3.2 Coupled Fluid-Solid Elements

Effective stress analysis requires a method to account for the interaction between the pore fluid and soil skeleton in saturated or partially saturated soil. Various approaches derived from the work of Biot (1941, 1956, 1962) have been developed to accomplish this goal in a numerical setting, each

adding fluid degrees-of-freedom to the system according to different assumptions. Three primary approaches are discussed by Zienkiewicz and Shiomi (1984). These approaches are the **u**-*p*-**U** element formulation, which uses the full system of equations developed for the saturated problem, the **u**-**U** formulation, a simplification of the **u**-*p*-**U** approach which assumes incompressibility for each medium, and the **u**-*p* approach, which simplifies the system by assuming that fluid acceleration can be neglected.

Each of these primary finite element formulations is represented in the literature related to 3D effective stress analyses of soil-foundation systems. Cubrinovski et al. (2008) and Uzuoka et al. (2008) used the **u**-**U** and **u**-*p* element formulations, respectively, in their 3D simulations of shake table tests. Cheng and Jeremic (2009) used the **u**-*p*-**U** element formulation in their numerical simulations of a single pile in liquefiable soil.

2.2.3.3 Deep Foundation Elements and Treatment of Soil-Foundation Interface

Deep foundations have typically been incorporated into 3D FEA using either solid elements (e.g., Yang and Jeremic, 2002, 2003, 2005) or beam-column elements (e.g., Petek, 2006; Cheng and Jeremic, 2009; Elgamal et al., 2008). For solid element approaches, linear elastic foundation constitutive behavior is the predominant choice, though elastoplastic behavior has been considered in some cases. An example of the latter is presented by Khalili-Tehrani et al. (2007), who used a combination of truss and solid elements to represent the elastoplastic response of reinforced concrete piles.

When using solid elements for deep foundations, it is prevalent in the literature to simulate the interface between the foundation and surrounding soil by equating some or all of the displacement degrees-of-freedom at the soil-foundation interface (e.g., Cubrinovski et al., 2008; Uzuoka et al., 2008), or by simulating a frictional interface via a thin layer of solid elements (e.g., Yang and Jeremic, 2002, 2003, 2005) or interface elements with frictional constitutive behavior (e.g., Ooi et al., 2010; Khalili-Tehrani et al., 2007).

The use of beam-column elements to model piles is beneficial, as it simplifies post-processing interpretation of pile shear and moment values, however, it also necessitates special treatment of the soil-pile interface due to the incompatibility of the pile and soil element types. Another advantage of this approach lies in the relative ease with which to consider elastoplastic pile constitutive behavior via fiber section models (e.g., Cheng and Jeremic, 2009; Jeremic et al., 2009; Elgamal et al., 2008).

Interface approaches for models with beam-column pile elements have typically involved rigid no-slip node-to-node contact links (e.g., Elgamal et al., 2008; Jeremic et al., 2009), though other treatments have been used. Cheng and Jeremic (2009) used a combination of rigid links and imper-

meable solid elements to ensure compatibility for both the solid and fluid degrees-of-freedom at the soil-foundation interface. Petek (2006) introduced a 3D beam-solid contact element which creates a frictional stick-slip interface between the beam-column and solid elements, allowing for more realistic soil-foundation interaction. This beam-solid contact element was used to examine numerical *p-y* curves in the 3D FEA of McGann et al. (2010, 2011).

2.2.3.4 Boundary and Loading Conditions

Proper boundary conditions must be devised to ensure the success of a 3D analysis of a soil-foundation system. Boundary conditions for foundation elements typically replace structural components which are not critical to the model, and vary depending upon the particular support conditions assumed at the connection between the critical and non-critical components. Rigid-type connections are commonly represented using rotational fixity, while more flexible connections may be more appropriately modeled with rotational freedom. Translational degrees-of-freedom for foundation elements may also require restriction depending upon the geometry of the model.

Boundary conditions for the soil continuum require somewhat greater care to ensure appropriate results. At a minimum, the boundaries must be fixed such that all rigid body displacement modes are restricted. In static or pseudo-static analyses, the main concern is related to diminishing the effects of the boundary on the portions of the model which are of primary interest. Boundary effects can be controlled for an analysis of a soil-foundation system by extending the limits of the soil continuum away from the location of the foundation elements. The optimal extents are those which minimize the boundary effects while maximizing computational efficiency. A brief study demonstrating boundary effects in analysis of laterally loaded piles is given by McGann (2009).

Minimization of boundary effects is also critical in dynamic analysis, however, devising proper boundary conditions is more difficult than in static or pseudo-static cases. The particular method used for this purpose depends upon the objective of the numerical model. For example, Cubrinovski et al. (2008) and Uzuoka et al. (2008) compared numerical results to shake table tests, therefore, the geometry and boundaries in the model mirrored those in the experiment. All lateral boundaries were fixed against out-of-plane translation to be consistent with the rigid container used in the shake table tests, and input excitations were applied at the fixed base of the model. Specification of boundary and loading conditions in this manner is common for simulations of experimental analysis.

When creating a numerical model for a site in the field, the assumption of rigid boundaries is typically no longer valid. Several strategies have been developed to include the effect of semi-infinite subsurface extents in a numerical model of finite size. The use of periodic boundary conditions, in

which the lateral extents of the model share translational degrees-of-freedom, is one such approach which attempts to appropriately account for the free-field response of the soil domain. Elgamal et al. (2008) used this approach in their model of a complete bridge-foundation-soil system.

Lysmer and Kuhlemeyer (1969) introduced a technique to capture a transmitting boundary through the use of viscous dashpots. By defining the viscous response of the dashpots based on the density and shear wave velocity of the material beyond the boundary, this approach appropriately captures the dissipation of wave energy in the numerical model. When defining transmitting boundaries using the Lysmer and Kuhlemeyer (1969) method, accelerations are not directly applied to the model. Instead, a force is applied using the technique developed by Joyner and Chen (1975). This applied force is proportional to the input velocity and the constitutive properties of the material beyond the boundary. This approach is commonly used in numerical analysis for geotechnical problems to account for the compliance between the soil domain of the model and the semi-infinite media outside of the considered domain. For example, Elgamal et al. (2008) represented an underlying elastic half-space in this manner via dashpots in the three Cartesian directions at each node on the base of their 3D FE model of a full bridge-foundation-soil system.

Another technique which can be used in geotechnical simulations to properly account for the differences in wave behavior inside the finite soil domain represented by the model and the wave behavior in the semi-infinite soil medium is the domain reduction method (Bielak et al., 2003; Yoshimura et al., 2003). The domain reduction method (DRM) consists of two phases. The initial phase involves a background geological model which includes both the source of the earthquake and the region of interest. This background model is used to compute the free-field displacement wavefield demands on the boundary of the smaller region of interest. The second phase involves only the reduced region of interest. In this phase, effective seismic forces are applied at the boundary of the local region. These effective forces are derived from the boundary displacement demand obtained in the initial phase. Jeremic et al. (2009) applied a vertically propagating wave field to their model using the DRM, utilizing equivalent linear site response analysis for the initial analysis phase.

Representation of the initial state of stress is of paramount importance in geotechnical simulations. The soil response (i.e., stress, strain) greatly depends on these initial conditions. Several approaches can be used to create an appropriate initial state. The typical method is to apply gravitational body forces to the elements in the numerical model prior to any further analysis steps. Jeremic et al. (2009) and Cheng and Jeremic (2009) took this a step further, using a staged modeling procedure in which gravitational stresses were first developed in a base soil mesh. After this stage, the soil elements were removed and replaced by foundation elements and gravitational stresses

were developed for the new configuration.

2.2.4 Other Numerical and Analytical Approaches

Investigations into the response of bridge foundations to lateral loads have not always taken a form which fits conveniently into one of the three categories discussed previously. The primary exception to the former categorization is analyses based on slope stability approaches. Such analytical methods have been used to examine pile pinning effects (Boulanger et al., 2006), to assess the nonlinear force-displacement behavior of bridge abutments (Shamsabadi et al., 2007, 2005), to examine displacements of bridge abutments (Basha and Babu, 2009), and to estimate lateral spreading forces on bridge piles (Zha, 2006). Other examples of alternative analytical approaches include the work of Sextos and Taskari (2008), who proposed a multi-platform analysis approach for the analysis of bridge-foundation-soil systems in seismic conditions, and the work of Kotsoglou and Pantazopoulou (2009), who analyzed a bridge-foundation-soil system as an equivalent single degree-of-freedom system.

2.3 Summary

A brief overview of the extensive amount of research related to the effects of liquefaction-induced lateral ground deformation on bridge foundations has been presented. This work has been conducted via experimental and numerical analysis, and significant progress has been made in improving the general understanding of this complex problem. Numerical analyses for this problem have most often used BNWF assumptions, though continuum analyses in two- and three-dimensions have also been explored. Simplified approaches are prevalent because they are efficient and effective, however, it is recognized that certain simplifying assumptions can lead to overconservative solutions.

Chapter 3

REVIEW OF DESIGN PROCEDURES FOR BRIDGE FOUNDATIONS SUBJECT TO LIQUEFACTION-INDUCED LATERAL SPREADING

In a typical bridge analysis or design procedure, the individual component systems are analyzed individually to determine appropriate demands for various load cases. The results of the component analyses are then synthesized into a global bridge analysis to assess the suitability of the entire structure. A balance between engineering rigor and economic efficiency is sought, and the treatment of foundation behavior in the component and global analysis phases is generally simplified. The analytical approaches adopted in practice typically assume the applicability of 1D or 2D descriptions, or incorporate 3D effects in a simplified manner. Fully 3D analysis may be conducted for sites with high levels of importance or certain types of topography, however, widespread use of 3D analysis in practice is limited.

Two example design approaches for bridge foundations subject to liquefaction-induced lateral spreading are discussed in the following sections: the California Department of Transportation (Caltrans) procedure and the Washington State Department of Transportation (WSDOT) procedure. Each design procedure is based off of the applicable American Association of State Highway and Transportation Officials bridge design specifications (AASHTO, 2010a,b), and each approach considers many of the same analysis components, but the two procedures lead to different results due to key differences in the assumptions made.

3.1 Summary of Caltrans Design Guidelines for Lateral Spreading

The current bridge foundation design guidelines for liquefaction-induced lateral spreading used by the California Department of Transportation are contained in an internal policy proposal (Caltrans, 2011). These guidelines are based off of the NCHRP (2002) design recommendations which effectively separate the design problem into two distinct cases: (1) an unrestrained ground displacement case, and (2) a restrained ground displacement case. The unrestrained ground displacement case assumes that the foundation is subject to a broad failure mass and will not provide significant resistance to lateral soil movement. The restrained ground displacement case assumes the failure mass has a limited width and that the foundation provides resistance to soil deformation during lateral spreading. The design processes for the restrained and unrestrained ground displacement cases, per

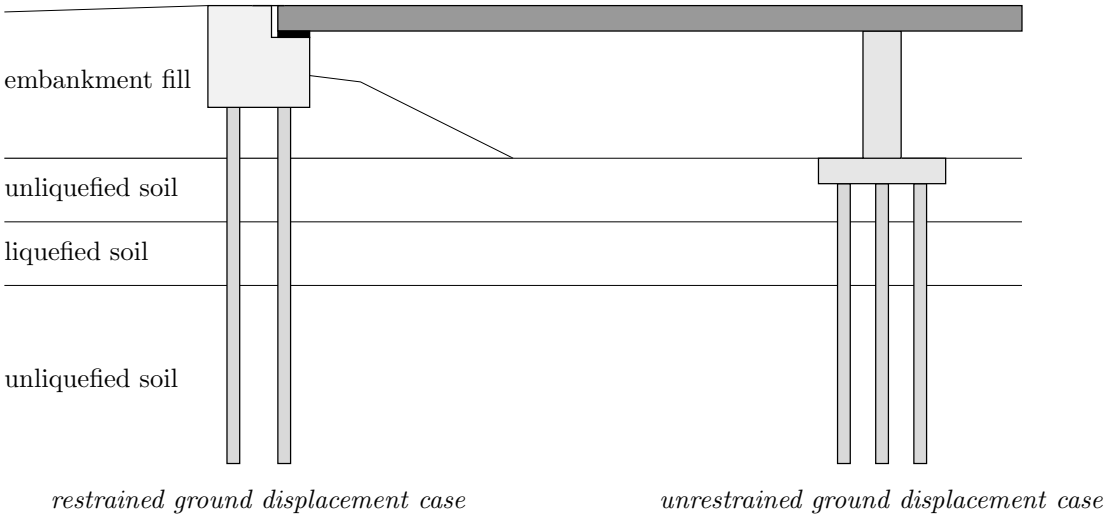

Figure 3.1: Prototype examples for restrained and unrestrained ground displacement cases.

Caltrans (2011), are described in the following discussion.

3.1.1 Restrained Ground Displacement Case

The restrained design case applies to foundations which are assumed to provide partial restraint to soil flow during lateral spreading. The prototype for this case is an approach embankment acting on a pile-supported abutment, see Figure 3.1. Due to the limited width of the embankment, it is assumed that the lateral stiffness of the abutment foundation will provide resistance to soil movement. The procedure recommended for this design case is based on the pile pinning analysis concept (Martin et al., 2002) as refined and expanded upon by later works (Zha, 2004; Boulanger et al., 2006; Ashford et al., 2011). In the pile pinning approach, a beam on nonlinear Winkler foundation (BNWF) model of the foundation is combined with a limit equilibrium slope stability analysis of the embankment to determine the force-displacement state at which the resistance of the foundation is compatible with the deformation of the lateral spreading mass. The method consists of 7 basic steps:

1. **Assess Liquefaction Potential**

   The liquefaction potential of the site soils is characterized for a peak ground acceleration (PGA) corresponding to a 5% in 50 years hazard. This is typically accomplished using a simplified approach (e.g., Youd et al., 2001). Per AASHTO (2010b), the assumption of reduced strength due to pore pressure build-up or full liquefaction is required for soils with a factor of safety against liquefaction less than 1.2.

2. **Estimate Residual Strength of Liquefied Soils**

There are two options which can be used to account for the residual strength of the p-y curves representing liquefied layers in the BNWF model of the soil-foundation system. No explicit preference of method is stated in Caltrans (2011).

(a) The p-multiplier (m_p) approach (e.g., Brandenberg et al., 2007b) may be used to obtain scaled p-y curves for liquefied soils based on a sand-type backbone curve.

(b) The residual strength of the liquefied soil may be estimated using an empirically-based method (e.g., Wang, 2003), and used as the ultimate resistance in the definition of p-y curves for liquefied soils based on a clay-type backbone curve.

3. **Develop Foundation Model**

The numerical BNWF model used to analyze the foundation requires definitions for the equivalent beam representing the foundation, the p-y curves for soil-pile interaction, and a force-displacement curve to capture abutment-embankment interaction. The commercial software LPILE is typically used for this purpose.

(a) ***Definition of equivalent beam:*** The equivalent beam used to model the foundation (piles and cap/abutment) may be defined assuming linear elastic or nonlinear elastoplastic behavior. In both cases, the spatial arrangement of the piles is largely ignored and the equivalent beam is developed in a simplified manner. For linear elastic behavior, the equivalent beam model is obtained by multiplying the bending stiffness, EI, of a single pile by the number of piles in the group. For nonlinear behavior, the moment-curvature response of a single pile is scaled by the number of piles in the group.

The pile cap/abutment is incorporated into the equivalent beam using a large linear elastic bending stiffness which approximates its rigidity relative to the piles. The rotational stiffness of the pile group is modeled using a rotational restraint located at the connection of the piles to the cap/abutment. This restraint is assigned a stiffness equivalent to the estimated rotational stiffness of the pile group after Mokwa and Duncan (2003).

(b) ***Definition of p-y curves for piles:*** The p-y curves used for soil-pile interaction are based on the work of Matlock (1970) for soft clay, Reese and Welch (1975) for stiff clay, and Reese et al. (1974) for sand. The base p-y curves determined for the site using these methods are modified to account for pile group effects and the effects of liquefaction.

- Group effects are considered using a composite group efficiency factor computed as the average of the reduction factors for each row in the pile group as recommended

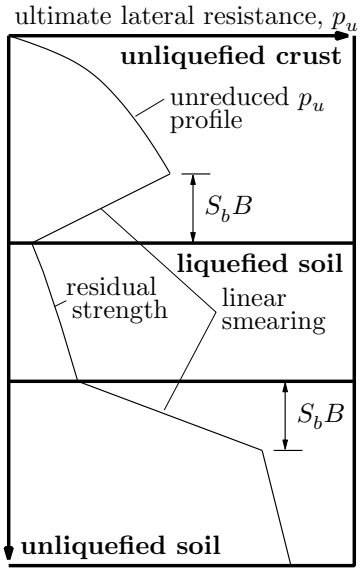

$$S_b = \begin{cases} 2, & B < 1 \text{ ft} \\ 2 - (B-1)/2, & 1 \text{ ft} \leq B \leq 3 \text{ ft} \\ 1, & B > 3 \text{ ft} \end{cases}$$

where B is the pile diameter (units of ft)

Figure 3.2: Smeared profile of ultimate lateral resistance to account for presence of liquefied layer on strength of surrounding soil (after Caltrans, 2011).

by Mokwa and Duncan (2001).

- The *p-y* curves of liquefied soils are defined as discussed in step 2. The influence of the weaker layer of liquefied soil on the surrounding material is accounted for using a linearly smeared ultimate lateral resistance profile as shown in Figure 3.2.

(c) ***Definition of cap/abutment-soil interaction curve:*** A tri-linear force-displacement curve describing the interaction of the cap/abutment with the surrounding soil is defined using the maximum passive load of the soil on the foundation, F_{ult}, and the displacement, Δ_{max}, required to mobilize this force. This curve is shown in Figure 3.3. Two failure cases are considered to determine F_{ult}, with the lesser force controlling the design. The two cases are as follows:

- A log-spiral passive wedge acting on the cap/abutment combined with the lateral resistance provided by the portions of the piles extending through the crust (i.e., soil above the liquefied layer).
- A Rankine passive wedge acting on foundation elements above the liquefied layer assuming that the cap/abutment, crust soil beneath the cap/abutment, and piles within the crust all act as a composite block.

The displacement, Δ_{max}, corresponding to the ultimate passive force is taken as the sum of 5% of the cap/abutment height with an adjustment factor which accounts for the effects of the depth of the liquefied material and the transverse thickness of the cap/abutment after Brandenberg et al. (2007a).

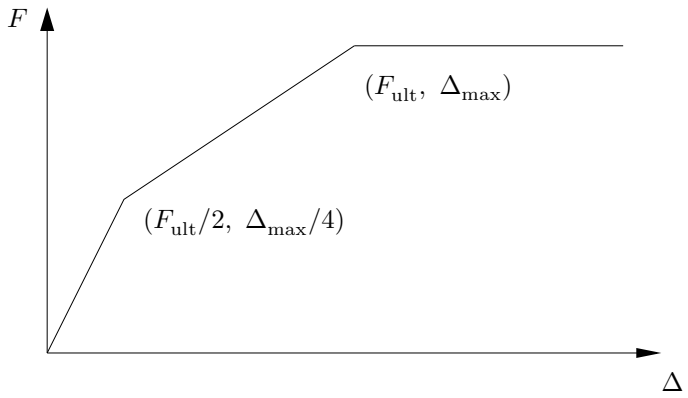

Figure 3.3: Tri-linear force-displacement curve for pile cap/abutment-soil interaction in foundation model (after Caltrans, 2011).

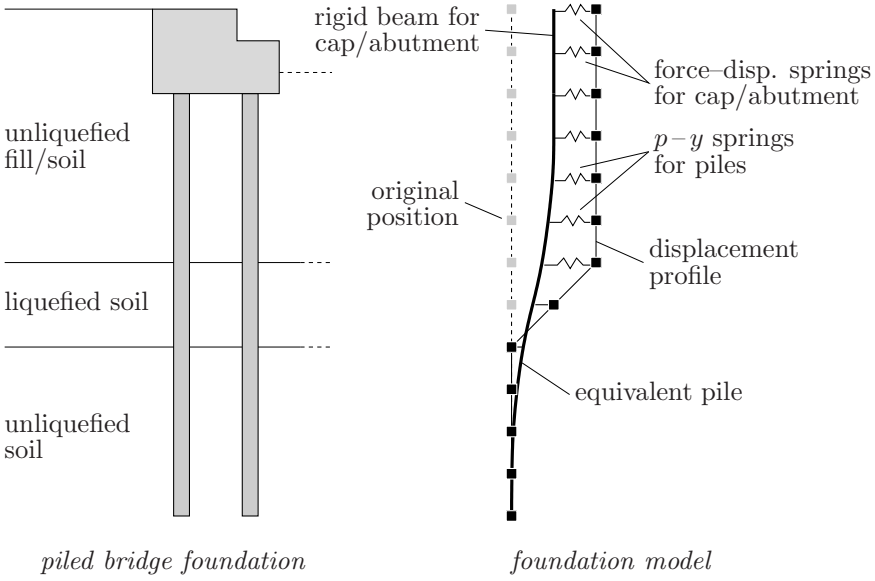

Figure 3.4: Transition from physical bridge foundation to foundation model showing the applied displacement profile for lateral spreading pushover analysis.

4. **Displacement Analysis of Foundation Model**

   Once the foundation model has been completed, a series of pushover analyses are conducted in which increasing crustal displacements are considered. Displacements are applied to the soil end of the *p*-*y* springs using the displacement profile shown in Figure 3.4 to simulate the effects of lateral spreading. For a series of increasing surface displacements, the pile cap displacement and a running average of the shear force at the center of the liquefied layer are recorded to obtain a lateral spreading pushover curve for the foundation.

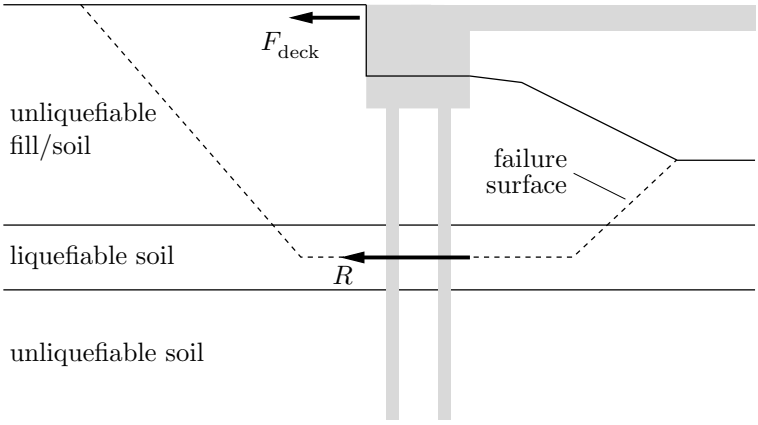

Figure 3.5: Schematic of slope stability analysis considering a deck resisting force, F_{deck}, and foundation resisting force, R.

The running average shear force for each displacement increment is computed as the sum of the current and all previous shear force values divided by the number of terms in the sum. This running average is made in an attempt to account for the discrepancy between the pushover analysis of this design step, in which the shear force increases with increasing ground displacement, and the slope deformation analyses of the next step, in which only constant foundation resisting forces are considered.

5. **Slope Stability and Deformation Analysis of Approach Embankment**

   A pseudo-static slope stability model is used to determine foundation resisting forces, R, at the center of the liquefied layer for a series of horizontal accelerations, k_h, applied in the model as a constant inertial force

   $$F_h = k_h W \tag{3.1}$$

   where W is the weight of the failure mass. For each considered acceleration value, the resisting force for which the slope factor of safety reaches 1.0 is recorded.

   In these analyses, the restraining forces are applied on the lower edge of the failure surface, and the failure surface is constrained to the center of the liquefied layer, as depicted in Figure 3.5. It is also recommended that the failure surface be limited to extending ≤ 4 times the height of the embankment away from the bridge abutment. If it is assumed that the bridge deck will provide longitudinal resistance to abutment movement, a deck resisting force, F_{deck}, is computed based on the full passive resistance of the soil acting on the deck and applied during the slope stability analysis.

   Newmark rigid sliding block analysis is used to compute the slope displacements corresponding

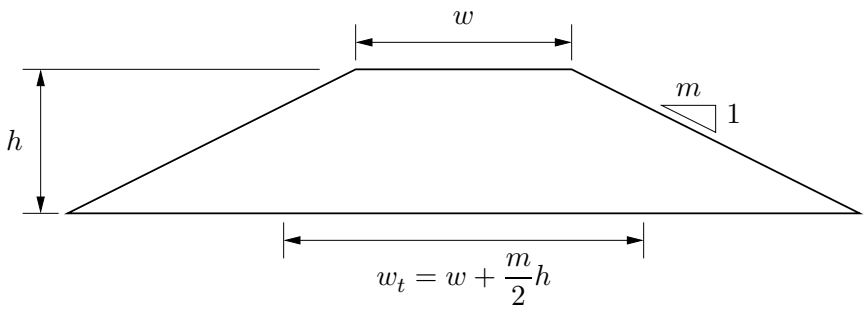

Figure 3.6: Tributary width of embankment, w_t (after Boulanger et al., 2006).

to the k_h coefficients used to determine resisting forces in the slope stability analyses. Typically, a simplified procedure (e.g., Bray and Travasarou, 2007) is used in lieu of site-specific sliding block analysis.

6. **Determine Force-Displacement Compatibility**

   The results of the pushover and slope stability/deformation analyses are used to determine a compatible force-displacement state which considers the restraining effects of the bridge foundation on the deformation of the soil-foundation system during lateral spreading. This is accomplished by plotting the slope force-displacement curve determined from the slope stability/deformation analyses (step 5) with the foundation running average shear force-displacement curve determined in the pushover analyses (step 4) in the manner shown in Figure 3.7.

   The running average forces are used for the foundation force-displacement curve to account for the differences in how the resisting force is handled in the two curves (constant in the slope deformation curve, non-constant in the pushover curve). Because the resisting forces obtained in the slope stability phase represent a force per unit thickness of soil, the lateral spreading pushover curve must be scaled by an appropriate width. For this purpose, the finite transverse thickness of an approach embankment is considered in the scaling factor, as the pushover curve forces are divided by the tributary width of the embankment determined as shown in Figure 3.6.

7. **Assess Foundation Performance**

   The final performance evaluation for the foundation is conducted using a lateral spreading pushover analysis which considers the combined effects of kinematic and inertial loads. A kinematic loading is applied using the displacement profile shown in Figure 3.4 with an applied

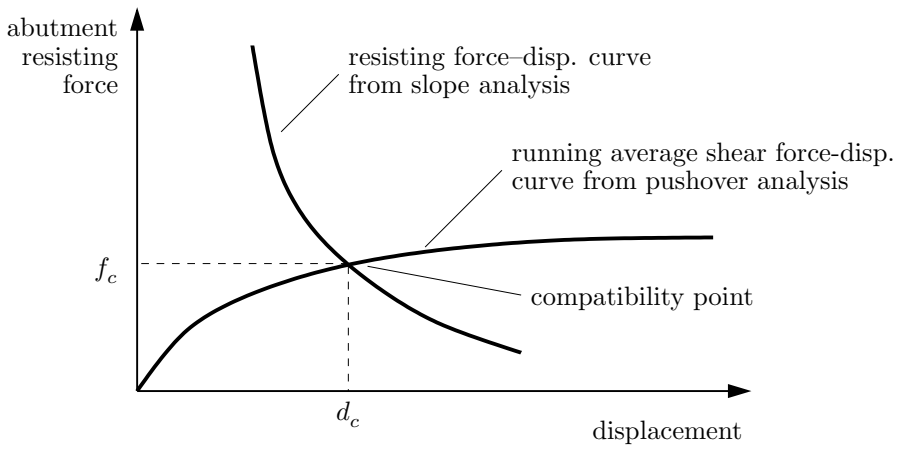

Figure 3.7: Determination of compatible force-displacement state.

surface displacement set as the compatible displacement, d_c, determined in step 6. Consideration for inertial effects is made during this analysis by applying 50% of the inertial loads from any associated superstructure or pile caps, as it is unlikely that lateral spreading occurs during peak shaking.

The inertial effects of superstructure elements for typical bridge bents are considered using an applied moment and shear force pair, which are determined based on the design of the bridge columns. There are two possibilities:

(a) In most cases, the bridge columns are designed to yield and develop plastic hinges prior to the onset of yield in the foundation elements. For this type of design, the inertial moment is set at 1.2 times the plastic moment capacity of the column. For columns which have a pinned connection at the top and a fixed connection at the bottom (free-fixed configuration), the inertial shear force is determined by dividing this inertial moment by the height of the bridge column. For columns with a fixed-fixed configuration, the inertial shear force is set as the inertial moment divided by one-half the column height.

(b) If the column is not expected to yield for the design event, then the inertial shear force is estimated as the product of the tributary mass carried by the bridge column with the spectral acceleration corresponding to the first mode of the column. The inertial moment is set as the product of the inertial shear force with the column height for a free-fixed configuration, or one-half of the same product for a fixed-fixed configuration.

For seat-type abutment foundations, the superstructure is supported by bearings which

can freely rotate, and the only means of transferring inertial shear from the superstructure is through a backwall, typically designed as a weak fuse with limited capacity to transfer load. For these reasons, it is assumed that no inertial loads are transferred from the superstructure for seat-type abutments. To account for the inertial effects of relatively massive foundation bodies, such as a pile cap, an inertial force is computed as

$$f_{\text{cap}} = 0.65 m_{\text{cap}} a_{\text{no liq}} \tag{3.2}$$

where $a_{\text{no liq}}$ is the design PGA without consideration for liquefaction, m_{cap} is the pile cap mass, and the 0.65 factor is used to represent a reduction in PGA due to the onset of liquefaction.

The combined kinematic-inertial pushover analysis is used to determine if the foundation has sufficient capacity under an assumed peak demand case. This analysis is used to evaluate the resulting shear force and bending moment demands for the deep foundations and to assess whether the displacement at the pile cap/abutment is acceptable for the overall bridge structure.

3.1.2 Unrestrained Ground Displacement Case

The unrestrained design case applies to foundations that are assumed to be unable to significantly restrain the flow of soil associated with lateral spreading. An example case is an interior bridge bent foundation embedded in a site with broad transverse continuity as shown in Figure 3.1. In this case, the lateral stiffness of the foundation is insignificant relative to the loads applied by the lateral soil flow. For design purposes, it is assumed that soil movement will be unaffected by the presence of the foundation, though evidence from previous earthquakes shows that this is not true at the local level.

The design process for the unrestrained ground displacement case begins in the same manner as the restrained ground displacement case, with the assessment of liquefaction potential (step 1), estimation of residual strength for liquefied soils (step 2), and the definition of a foundation model (step 3) corresponding exactly. After the completion of these steps, the remaining steps for the unrestrained case differ from those previously discussed.

Estimation of the design ground displacement for the unrestrained case is initiated by evaluating the slope stability factor of safety (FS) assuming the absence of the foundation. If FS $\leq$ 1.05, a flow-type failure is assumed. Typically, an assumption of 5 ft of displacement is made, as this is considered sufficient to mobilize the full passive force of the crust on the foundation, and it is stated

in Caltrans (2011) that as long as the passive force is mobilized, the remaining analysis is insensitive to the specific displacement value. For cases where FS > 1.05, the crustal displacement is estimated using one of two simplified techniques. When the slope has a predictable failure surface, a Newmark sliding block-based approach (e.g., Bray and Travasarou, 2007) is used with an input acceleration set equal to the design PGA. For gentle slopes, where there is greater uncertainty in the failure surface, crustal displacements are estimated using the strain potential procedure of Faris et al. (2006).

The foundation is evaluated using a lateral spreading pushover analysis, with an applied displacement profile as shown in Figure 3.4. The imposed surface displacement in this analysis is set equal to that required to mobilize the full passive soil resistance for the FS ≤ 1.05 case, or to the estimated crustal displacement for the FS > 1.05 case. Inertial loads from the bridge superstructure (if any) are included in this analysis in the manner described in step 7 for the restrained ground deformation case. The bending moment, shear force, and displacement demands computed using the pushover analysis are compared to the allowable foundation performance criteria.

3.2 Washington State Department of Transportation Design Procedure

The Washington State Department of Transportation design guidelines for bridge foundations subject to liquefaction-induced lateral ground deformation are contained in the WSDOT geotechnical design manual, WSDOT (2011b), and WSDOT bridge design manual, WSDOT (2011a). For most scenarios, several alternative analysis procedures are made available, allowing the designer to choose the method most applicable to the particular site, foundation, and structure.

Overall, the WSDOT design procedure for liquefaction-induced lateral ground deformation is similar to the unrestrained ground displacement case presented in Caltrans (2011). The restrained ground displacement case addressed in the Caltrans guidelines, in which a compatible force-displacement state is sought for situations in which there is a limited transverse soil domain, is not explicitly included in the WSDOT procedure. Structural pinning effects are addressed, however, they are not handled using the pile pinning analysis procedure discussed in the previous section.

The WSDOT design procedure for liquefaction-induced lateral ground deformation is summarized in the following discussion. There are two potential outcomes in this procedure: (1) design for a flow-type failure, or (2) design for a lateral spreading type failure. The particular outcome is determined in a four-step procedure using limit equilibrium slope stability analysis. The separate procedures for the two design outcomes are discussed following a summary of the first four steps in the design process.

1. **Assess Liquefaction Potential**

Susceptibility to liquefaction is assessed for the PGA corresponding to the site-specific hazard (typically 7% in 75 years). Liquefaction potential may be assessed using a simplified approach (e.g., Youd et al., 2001; Cetin et al., 2004; Moss et al., 2006; Boulanger et al., 2006; Idriss and Boulanger, 2008), or the performance-based approach of Kramer and Mayfield (2007). For sites which are not well characterized by the simplified methods, nonlinear effective stress site response analysis or laboratory cyclic simple shear or cyclic triaxial shear testing may be used.

2. **Estimate Residual Strength of Liquefied Soils**

Residual undrained shear strength parameters for liquefied soils are obtained from empirically-based relationships (e.g., Idriss and Boulanger, 2007; Olson and Stark, 2002; Wang, 2003). Residual strength conditions are assumed for all soils for which $FS_{liq} < 1.2$, or which are determined to be liquefiable for the return period of interest using the method of Kramer and Mayfield (2007). If a more refined characterization of residual strength is needed, cyclic triaxial shear or cyclic simple shear tests may be used instead of the empirical relationships. The p-multiplier (m_p) approach (e.g., Brandenberg et al., 2007b) may also be used to obtained scaled p-y curves if a BNWF approach is used in the foundation analysis.

3. **Develop Foundation Model**

A numerical model of the soil-foundation system is the primary means of analysis for the effects of liquefaction-induced lateral ground deformation. There are two software options available for use, DFSAP, based on strain wedge theory, and LPILE, based on BNWF analysis using p-y curves.

(a) ***DFSAP Analysis Option:*** The DFSAP program uses strain wedge theory (e.g., Ashour et al., 1998, 2002) for lateral and axial analysis of single and grouped piles or drilled shafts. This software is particularly attractive for drilled shaft foundations for which the length is small relative to the diameter, as such foundations are outside of the scope of most p-y curve-based analysis methods.

The built-in liquefaction option in DFSAP is not used to account for liquefied soils in the analysis. Instead, the soil properties for liquefied soils are modified using a reduced friction angle

$$\phi_{\text{reduced}} = \arctan\left(\frac{S_r}{\sigma'_{vo}}\right) \tag{3.3}$$

where S_r is the estimated residual strength for the liquefied soil and σ'_{vo} is the effective overburden stress at the depth of the liquefied soil layer. The initial stiffness is reduced

in a similar, unspecified, manner, and the soil unit weight is not adjusted for liquefied conditions.

Group efficiency effects are handled internally by the DFSAP program. The passive resistance of footings and pile caps below ground can also be accounted for internally by the DFSAP program, though this resistance should be neglected for areas prone to lateral spreading.

(b) ***LPILE Analysis Option:*** The LPILE program analyzes the laterally loaded deep foundation using a BNWF approach in which the soil is represented using *p*-*y* curves developed for various soil types (Matlock, 1970; Reese et al., 1974; Reese and Welch, 1975). This software is most applicable to relatively long and slender foundations.

When using LPILE, pile group efficiency effects are accounted for using *p*-multipliers as recommended in AASHTO (2010b). The effects of liquefaction on the *p*-*y* curves representing liquefied soil are considered using one of two approaches: (1) curves are scaled using the *p*-multiplier (m_p) approach (e.g., Brandenberg et al., 2007b), or (2) curves are computed using reduced soil properties based on the residual strength of the liquefied soil as is done when using DFSAP.

4. **Determine Potential for Lateral Soil Movement**

The potential for liquefaction-induced lateral soil movement is initially assessed using limit equilibrium slope stability analysis. The analysis is decoupled from all seismic inertial forces, the resistance from any foundation elements in the slope is ignored, and liquefied soils are assigned residual strength values. If the limit equilibrium FS $\leq$ 1.0, it is assumed that a flow-type failure will occur. If FS $>$ 1.0, it is assumed that flow failure is unlikely, and the effects of lateral spreading on the foundation are assessed instead.

3.2.1 Analysis for Flow-Type Failure: FS $\leq$ 1.0

The deformations associated with liquefaction-induced flow failure are typically too large to be acceptable for bridge foundation design if it is assumed that all of the deformation is transferred to the foundation. Due to the involved design assumptions, stabilization of the slope via structural pinning or ground improvement is typically required for the flow-type failure case. In some situations, the lateral capacities of the foundation and soil are such that the liquefied soil and any overlying crust will flow around the foundation, imparting only minimal deformations to the structure. The potential for this flow-around type of behavior is assessed by evaluating the full passive pressure of the soil acting on the foundation.

The lateral force which must be resisted by a foundation providing structural pinning for slope stabilization is estimated by computing the stabilizing force necessary to achieve a target slope stability FS of approximately 1.1. Seismic inertial forces are neglected unless the primary design earthquake is a long duration subduction zone event, in which case an inertial force is considered as

$$f_{\text{inertia}} = 0.25 a_g m \tag{3.4}$$

where a_g is the peak ground acceleration and m is the unstable soil mass.

The force required to bring FS $\geq$ 1.1 may exceed the force which the soil can apply to the foundation. To prevent this situation, it is recommended to check the stabilizing force against a limiting force determined from the full passive pressure of the unstable soil acting on the foundation using one of two approximations:

1. The passive pressure may be multiplied by the gross surface area of the foundation (i.e., width $\times$ height) over which it acts.
2. The normal component of the passive pressure acting on incremental segments along the foundation circumference may be multiplied by the individual lengths of the segments and the interface friction angle. If done in this way, it is recommended that the limiting force be multiplied by a factor of 1.1 to be approximately consistent with how the slope failure force is calculated.

The design load case is determined through a comparison of the estimated stabilizing (from limit equilibrium analysis) and limiting (from passive pressure) forces. The way in which these forces are applied and the manner in which their effects are compared is dependent on certain aspects of the soil profile. If it is determined that the design load case for flow-type failure is not structurally or economically feasible, then stabilizing ground improvement techniques must be explored.

1. For relatively shallow liquefiable layers, the stabilizing force should be applied as a uniform distributed load acting from the bottom of the liquefiable layer to the top of the foundation, as shown in Figure 3.8(a). The passive force should be applied as a linearly-increasing distributed load (passive wedge) acting from the bottom of the liquefiable layer to the top of the foundation, as shown in Figure 3.8(b). The load case which produces the smallest stress in the foundation controls the design.
2. For conditions where the flow failure surface does not extend to the bottom of a deep and/or thick liquefiable layer, multiple failure surfaces for which FS $\leq$ 1.0 are considered. The corresponding stabilizing forces are applied as uniformly distributed loads extending from each

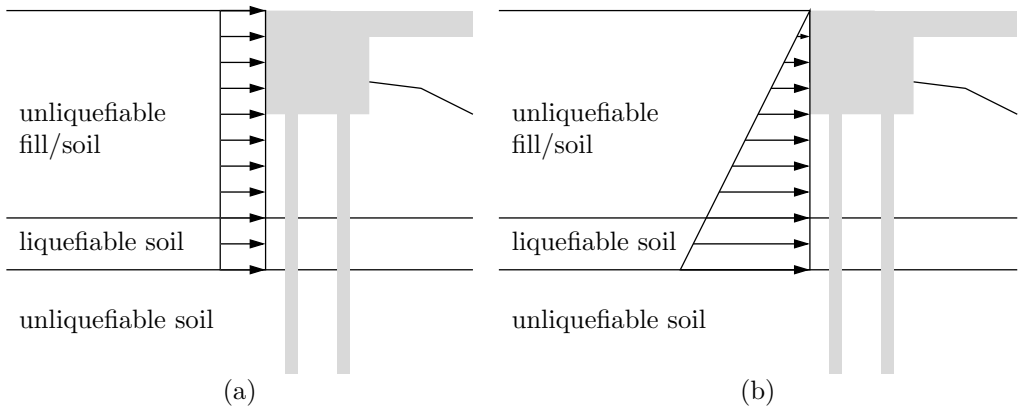

Figure 3.8: Load distributions for shallow liquefied layer in flow-type failure case. (a) Uniform for stabilizing force. (b) Linearly-increasing for passive force.

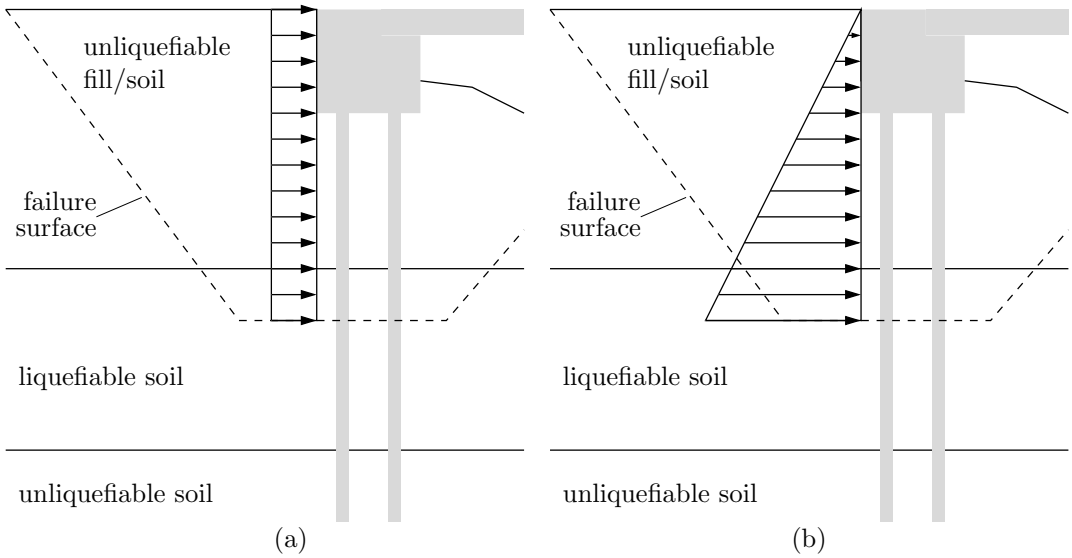

Figure 3.9: Load distributions for flow-type failure case where failure surface does not extend to the bottom of the liquefied layer. (a) Uniform for stabilizing force. (b) Linearly-increasing for passive force.

failure surface to the top of the foundation. These are compared to the limiting passive force, applied as a wedge distribution from the failure surface to the top of the foundation. An example of each distribution is shown in Figure 3.9 for a single failure surface. For the smaller of the two forces determined at each failure surface, the moment and shear at the estimated point of fixity of the foundation are computed. The lateral load distributions which result in the largest bending moment and shear force demands are used as design load cases.

3.2.2 Lateral Spreading Analysis: $FS > 1.0$

The effects of lateral spreading on embedded foundations are assessed using a pushover analysis in which an estimated free-field displacement profile is applied to the free end of the soil-foundation interaction curves used in the soil-foundation model.

A lateral spreading deformation analysis is used to estimate potential ground deformation. This is accomplished using an empirically-derived relationship (e.g., Youd et al., 2002; Kramer, 2008), a Newmark sliding block analysis (e.g., Bray and Travasarou, 2007), or dynamic nonlinear effective stress numerical analysis. The estimated lateral deformation is treated as the free-field displacement of the ground surface in subsequent analyses.

The displacement profile used in the pushover analysis represents the free-field distribution of lateral spreading deformation with depth, and is dependent on the estimated free-field surface deformation. Three methods are available for defining a displacement profile:

1. An empirically-based shear strain profile approach (e.g., Zhang et al., 2004; Idriss and Boulanger, 2008).

2. A set of dynamic nonlinear effective stress analyses using several input motions.

3. Assuming a simplified profile which has a constant displacement in a unliquefied crust and a linearly varying displacement across the liquefied layer as shown in Figure 3.4.

The ultimate lateral resistance and stiffness of the soil-foundation interaction curves representing liquefied soil are reduced to account for residual strength using the methods discussed in step 2. The resistance and stiffness of the unliquefied soil are based on the site soil properties as determined from field exploration and laboratory testing. Group effects are neglected for curves in fully liquefied soil after Rollins et al. (2005). The passive pressure and side friction generated on the pile cap must also be considered in the analysis.

As with the flow failure case, lateral forces are checked against a limiting case corresponding to the passive force of the unstable soil acting on the foundation. If the force applied to the foundation in the pushover analysis exceeds the passive capacity of the soil, it is assumed that the crustal soil will fail during lateral spreading, flowing around or piling-up behind the foundation, and the passive force is used for design. This force is applied as a passive wedge which extends from the ground surface to the lesser of the following depths:

1. The bottom of the liquefied layer.

2. The depth of the failure surface at its intersection with the foundation.

3. The assumed limiting depth for lateral spreading of 50 ft.

For the design load case, the induced loads are checked against the available resistance of the foundation and general bridge system, and the estimated displacements are checked against tolerable values. Mitigation of foundation subsoils may be required if the predicted forces or deformations are large enough to be structurally or economically infeasible.

3.3 Summary

The California Department of Transportation and Washington State Department of Transportation design procedures for bridge foundations subject to liquefaction-induced lateral spreading were presented. Each approach primarily involves the use of simplified analysis methods to determine the design demands for pile and drilled shaft foundations, however, there are differences in how these simplified methods are applied and in how the three-dimensional geometry of the site is incorporated into each procedure.

The Caltrans approach makes an initial distinction between restrained and unrestrained ground displacement based on a qualitative assessment of the geometry of the soil surrounding the foundations. For the restrained ground displacement case, it is assumed that the existence of the foundation will limit the demands that the soil can impose on the bridge structure during lateral spreading. Three-dimensional effects are considered and a compatible force-displacement state is determined and used for the design of the bridge foundations. The unrestrained ground displacement case assumes that the soil displacement will be largely unaffected by the presence of the foundations and the structure is typically designed to withstand the full passive force of the crust.

The WSDOT procedure is similar to the unrestrained ground displacement case from the Caltrans procedure in that the bridge structure is to be designed to withstand the soil displacement, and corresponding lateral forces, that would occur in the absence of the embedded foundations. No direct consideration for 3D effects is made in this procedure, leading to potentially overconservative design solutions for cases which would be considered restrained ground displacement under the Caltrans approach.

Chapter 4

IDENTIFICATION AND SELECTION OF REPRESENTATIVE CASE STUDIES FROM CHILE

The geologic and seismic similarity between Chile and western Washington provides a unique opportunity to learn from the performance of bridges subject to liquefaction-induced lateral spreading. Reconnaissance efforts following the M_w8.8 February 27, 2010 offshore Maule earthquake identified multiple bridge sites subject to liquefaction and lateral spreading. These bridges are listed in Table 4.1, with a brief summary of reported performance. At most of the considered sites, there was a tendency for the crustal soil and approach fill to flow around embedded foundations, inducing only minor damage or lateral movement in the abutments and piers. These effects are manifested as settlement and longitudinal cracking in the approaches and a difference in the flow pattern of near-field and far-field soils.

To aid in an assessment of how the three-dimensional deformation of approach embankments and crustal soil may affect the lateral loads imposed on bridge foundations during lateral spreading, and how the imposed demands may differ from those estimated using current simplified design procedures, several Chilean bridge sites are evaluated for use as case studies. A survey of the information for the bridge sites identified in Table 4.1 indicates that the available structural data consists primarily of construction drawings, and the available geotechnical data consists primarily of standard penetration test (SPT) resistance data. This available data is summarized in Table 4.2. In several cases, the GEER (2010a) reconnaissance team performed site-specific investigations, including light detection and ranging (LIDAR) scans, dynamic cone penetration tests (DCPT), and spectral analysis of surface wave (SASW) evaluations.

4.1 Evaluation of Case Study Sites

Potential case study sites are evaluated with consideration for: (1) the sufficiency of the available data for characterizing the site soil profile and bridge foundations, (2) the presence of 3D deformation effects in the crustal soil and/or approach fill, and (3) the similarity of the bridge site to conditions typical in Washington state. The relative merits of each bridge listed in Tables 4.1 and 4.2 are evaluated using these criteria and summarized in the following discussion. The primary case study sites for the investigation of the effects of 3D soil deformation on the lateral loads imposed on bridge

Table 4.1: Summary of Chilean bridge sites affected by liquefaction-induced lateral spreading with target behavior at approaches (FHWA, 2011; GEER, 2010a).

Site Name	Reported Performance
Puente Mataquito (built 2006)	< 0.02 m lateral movement with minor crushing at NE abutment, 0.7–1.0 m settlement of approach fill at NE abutment, movement of approach fill perpendicular to bridge axis at NE abutment, no movement at SW abutment
Puente Llacolén (built 2000)	no lateral movement or significant damage at SW abutment, 0.25–0.3 m lateral movement of support pier at NE approach, approach span became unseated
Puente Juan Pablo II (built 1973)	significant displacement/rotation and shear failure of NE approach bent, vertical settlement of piers along length of bridge, minor damage to SW approach
Puente Raqui I (built 1992)	no lateral movement or significant damage at SE abutment, movement of approach fill perpendicular to bridge axis at SE abutment, twisting and 0.075–0.1 m lateral movement at NW abutment, 1 m settlement of approach fill at each abutment
Puente Raqui II (built 1992)	no lateral movement with minor damage at abutments, approach fill settlement < 1.5 m, movement of approach fills perpendicular to bridge axis, interior piers tilted laterally with span collapse
Puente Tubul (built 1992)	0.15 m lateral movement at N abutment with interior pier collapse, > 0.1 m lateral movement at S abutment with interior span collapse, 1.0–1.5 m settlement of approach fill at each abutment
Puente La Mochita (built 2004)	no lateral movement or significant damage at either abutment, 0.3–0.8 m settlement of approach fill at each abutment, movement of approach fills perpendicular to bridge axis

foundations during liquefaction-induced lateral spreading are selected and several candidates for future study are identified.

4.1.1 Puente Mataquito

Among the considered Chilean bridge sites, the Mataquito River Bridge (Puente Mataquito) is the most attractive site for use as a case study of three-dimensional lateral spreading effects. Clear evidence of liquefaction-induced lateral spreading was observed at this site, including the type of three-dimensional approach embankment deformation which is of interest in this research, Figures 4.1 and 4.2, and the available structural and geotechnical data is sufficient to create numerical models that are representative of site conditions. Puente Mataquito is a recently constructed bridge founded on grouped drilled shafts, a commonly-used foundation type in Washington state bridges, and the abutments reported performed well during the lateral spreading event.

Table 4.2: Summary of available structural, geotechnical, and miscellaneous data for considered Chilean bridge sites.

Site Name	Available Data
Puente Mataquito	original construction drawings, boring logs from original construction, geotechnical, hydraulic, and structural reports, SASW data
Puente Llacolén	original construction drawings, post-earthquake repair construction drawings, boring logs from post-earthquake repairs, LIDAR, DCPT, and SASW data near NE approach
Puente Juan Pablo II	post-earthquake repair construction drawings, boring logs from post-earthquake repairs, post-earthquake surveying data, LIDAR, DCPT, and SASW data near NE approach
Puente Raqui I	original construction drawings, no geotechnical data
Puente Raqui II	original construction drawings, post-earthquake repair construction drawings, boring logs from post-earthquake repair work
Puente Tubul	original construction drawings, geotechnical report from post-earthquake repairs,
Puente La Mochita	original construction drawings, boring logs from original construction, post-earthquake repair construction drawings, LIDAR scans

Figure 4.1: Lateral spreading on northern river bank at Puente Mataquito as seen from ground surface (GEER, 2010a).

Figure 4.2: Longitudinal crack in northern approach to Puente Mataquito (GEER, 2010a).

4.1.2 Puente Llacolén

The northeast approach to Puente Llacolén was significantly affected by lateral spreading, however, the layout of this approach is not representative of the typical conditions where three-dimensional ground deformation effects have been observed during liquefaction-induced ground failure. As shown in Figure 4.3, the portion of the bridge affected by the lateral ground deformation involves a series of elevated approach spans supported by piers. The abutment and any associated approach fill are located well away from the river and the zone of ground failure. The available geotechnical data for the northeast approach site is limited, but is likely sufficient to characterize the soil conditions in a simplified manner. This site may be useful as a representative case where three-dimensional effects are not applicable. The southwest approach to Puente Llacolén is more representative of the idealized conditions for this study, with a small approach fill and an abutment which performed well during lateral spreading of the surrounding ground, however, there is no available geotechnical information for this side of the bridge and only limited observational data.

4.1.3 Puente Juan Pablo II

As with Puente Llacolén, the layout of Puente Juan Pablo II is such that three-dimensional ground deformation effects do not appear to have been an important factor during the liquefaction-induced

Figure 4.3: Portion of northeast approach to Puente Llacolén affected by liquefaction-induced ground deformation (FHWA, 2011).

lateral spreading which occurred near the northeast approach. In this area, the bridge approach consists primarily of elevated approach spans supported by piers. There is sufficient information for a geotechnical and structural characterization of the site, so Puente Juan Pablo II may be informative as a case study representing conditions where three-dimensional effects do not apply.

4.1.4 Puente Raqui I

Observations at Puente Raqui I suggest that liquefaction-induced lateral spreading occurred, triggering the target 3D deformation pattern in the approach fill at both ends of the bridge (Figure 4.4), however, there is no available geotechnical data with which to characterize the soil profile at this site. In addition, the available structural information is limited, and suggests that grouped timber piles were used as foundations for the abutments and piers. This combination of limited structural information and non-existent geotechnical data indicates that Puente Raqui I is not a strong candidate for further study.

4.1.5 Puente Raqui II

During lateral spreading at both ends of Puente Raqui II, the approach fill settled and deformed perpendicularly to the bridge axis, inducing little or no lateral movement in the abutments, though

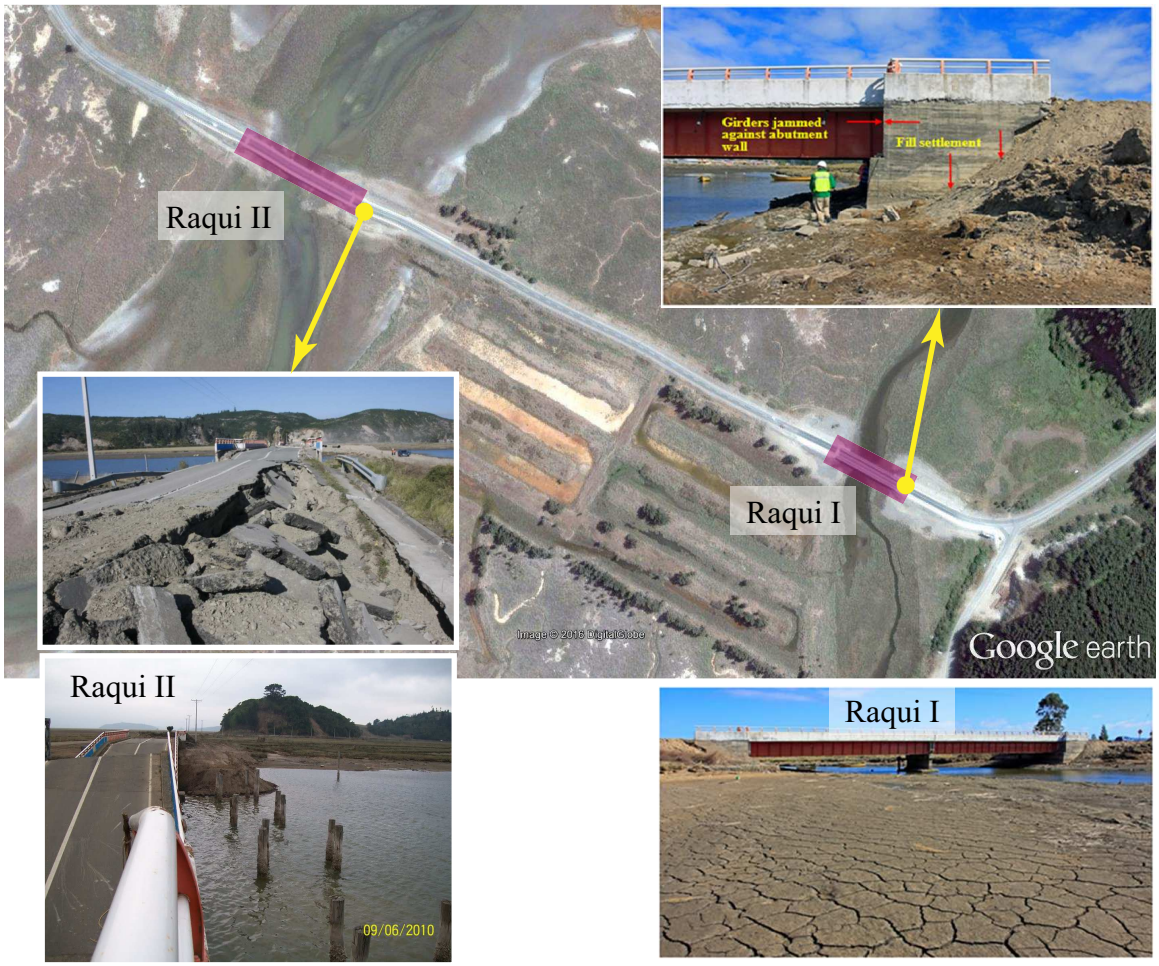

Figure 4.4: Location of the Puente Raqui I and Raqui II.

the lateral movement of some interior piers caused the collapse of the bridge spans as shown in Figure 4.4. Due to post-earthquake reconstruction efforts, there is ample geotechnical data available for the bridge site, however, structural information for the original bridge is limited. Figure 4.5 shows a SPT blow count profile along the axis of the bridge. As with Raqui I, it appears that the abutments and piers for Puente Raqui II were supported on grouped timber piles of unknown number and configuration. Since timber piles are not often used in new bridges, Puente Raqui II is not a preferred case, however, this bridge may be useful as a case study site if no other sites prove to be more promising.

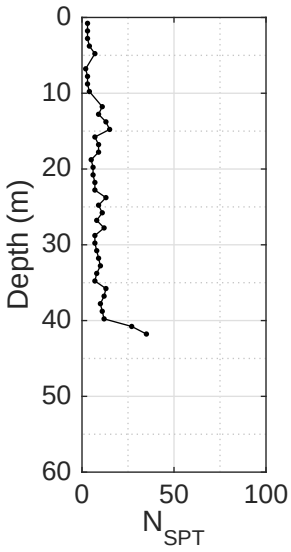

Figure 4.5: A typical SPT blow count profile along the axis of Puente Raqui II.

4.1.6 Puente Tubul

The performance of Puente Tubul during the earthquake and subsequent liquefaction-induced phenomena was somewhat worse than that observed for Puente Raqui II, though the overall behavior was similar between the two sites (Figure 4.6). There is a wealth of available geotechnical data for Puente Tubul, but there is only limited available structural data, though it is likely sufficient for a simplified characterization of the site. Figure 4.7 shows the SPT blow count profiles along the axis of the bridge. As with Puente Raqui II, it appears that the original bridge at this site was supported on grouped timber piles, therefore, this bridge is not a strong candidate for future study.

4.1.7 Puente La Mochita

The Puente La Mochita site meets the specified criteria for selection as a case study, but there are some problematic aspects to this site which reduce its viability for this purpose. As shown in Figure 4.8, the bridge runs parallel to Rio Bío-Bío, spanning a small inlet on the eastern bank. This geometry, combined with the deformation observations made by the FHWA (2011) and GEER (2010a) reconnaissance teams, suggest that the ground deformation mechanism at this site is outside of the scope of the research. Due to this uncertainty in the driving mechanism, Puente La Mochita is not strong selection for use as a case study.

Figure 4.6: Location of the Puente Tubul.

4.2 Overview of Selected Case Study Site: Puente Mataquito

Based on the evaluation of the case studies discussed above, Puente Mataquito and Puente Llacolén are chosen for further analysis. Puente Mataquito is chosen as a first candidate due to the 3D nature of its approach embankments. Puente Mataquito is a 320 m long two-lane highway bridge over the Mataquito river on the coastal route between Iloca and Quivolgo in the Maule region of Chile. Figure 4.9 provides a view of the bridge from the southern river bank near the approach embankment. Puente Mataquito is located near the city of Constitución, as shown in Figure 4.10, about 100 km NW of the 2010 Maule earthquake epicenter at the approximate coordinates: 35.052°W, 72.163°S. The bridge is supported by precast prestressed concrete I-girders over eight 40 m long interior spans.

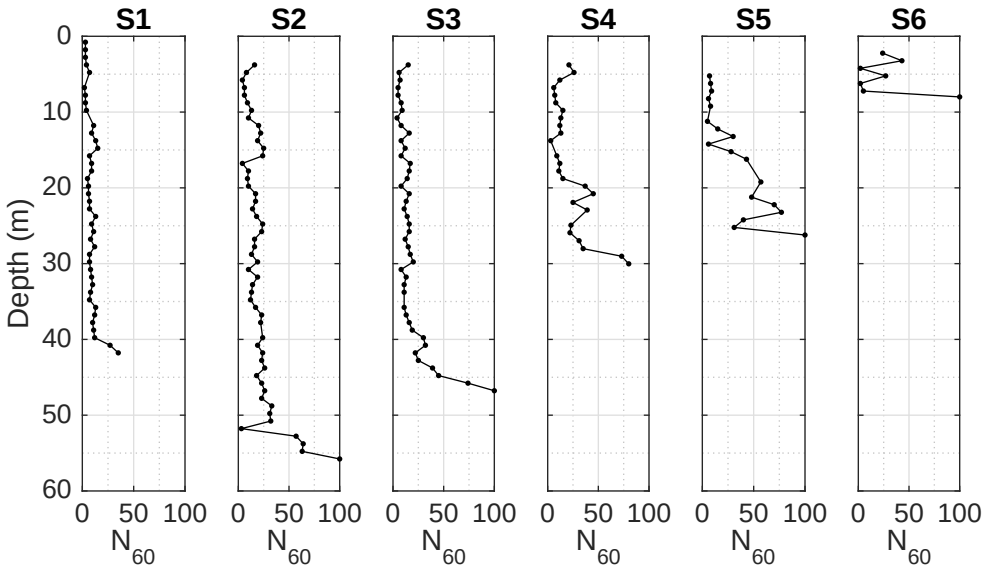

Figure 4.7: SPT blow count profiles along the axis of Puente Tubul. Refer to Figure 4.6 for the location of SPT profiles.

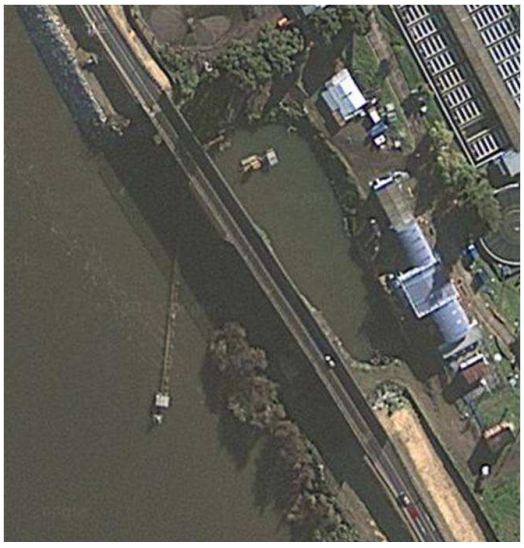

Figure 4.8: Aerial view of Puente La Mochita and surrounding site.

Figure 4.9: Puente Mataquito looking northeast from the southwest approach. Photo retrieved January 14 2013, `www.panoramio.com/photo/8172577`.

There are two seat-type reinforced concrete abutments with wingwalls, founded on 4×2 groups of 1.5 m diameter reinforced concrete drilled shafts. The seven interior piers consist of 3×1 groups of the same 1.5 m diameter shafts, capped at the connection to the bridge girders in the manner visible in Figures 4.9 and 4.11.

Figure 4.10: Location of Puente Mataquito relative to Maule earthquake epicenter and several Chilean cities. Map retrieved January 15 2013, `maps.google.com`.

Figure 4.11: Surface manifestation of lateral spreading at Puente Mataquito. (a) Southwest approach (GEER, 2010a). (b) Northeast approach (MAE, 2010).

Extensive liquefaction and lateral spreading occurred on both river banks at the Puente Mataquito site due to the Maule earthquake. On the northern bank, the observed surface manifestation of lateral spreading extended approximately 270 m from the river's edge, involving a large portion of the surrounding fields. The estimated lateral spreading deformation on the ground surface was about 1.8 m over the approximately 65 m distance from the NE abutment wall to the river's edge (see Figure 4.1). The NE approach embankment settled about 0.7–1.0 m relative to the bridge deck and expanded about 0.6 m away from the road centerline. Reconnaissance teams noted the presence of lateral spreading at the southwest approach, however, there is little available discussion beyond a brief statement that the scope of the spreading appeared to be constrained due to topographic effects (FHWA, 2011; GEER, 2010a; MAE, 2010). Figure 4.11 provides close-up images of the surface manifestation of the lateral spreading at each approach. No ground motion information was recorded for this site, however, the quantity and quality of the available information offsets this omission from the data set. Due to this lack of information on the specific ground motion experienced at the site, an alternative ground motion record is used during dynamic simulations (see Section 6.1.5 for more information).

Though liquefiable soils were identified in the geotechnical report (Petrus, 2006), there is no evidence that lateral spreading was explicitly considered during the design process. The design scour conditions at the site are particularly extreme, and it appears that scour was the controlling lateral load case for the foundations. Regardless of the particular load case that drove the design, and despite the evidence of liquefaction and lateral spreading near each approach, the overall performance of the bridge was favorable. Bridge operation was not affected beyond the easily repairable settlement

and roadway cracking in the northeast approach embankment (FHWA, 2011; GEER, 2010a).

Only minor structural damage was reported, with some typical instances shown in Figure 4.12, however, based on photographs of the bridge, it seems that the movement of the abutment was underreported. Per Figure 4.13, which is taken from the construction drawings for Puente Mataquito, a 20 cm expansion gap is included at the connection of the bridge deck with the abutments. This gap is visible in Figure 4.9, which was taken prior to the Maule earthquake. As shown in Figure 4.12(a), the expansion gap has closed, placing the abutment and deck in direct contact. This observation suggests that the abutment potentially moved $\geq$ 20 cm towards the river, rather than the reported value of $\leq$ 2 cm.

Figure 4.12: Minor structural damage caused by lateral spreading (GEER, 2010a). (a) Crushing of NE abutment. (b) Shearing of bridge girder above interior piers.

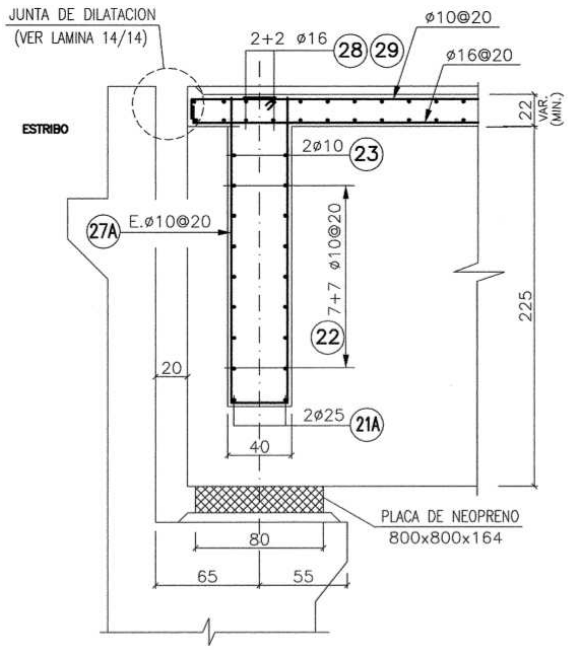

Figure 4.13: Construction detail for abutment to deck connection (courtesy Ministerio de Obras Públicas, Chile).

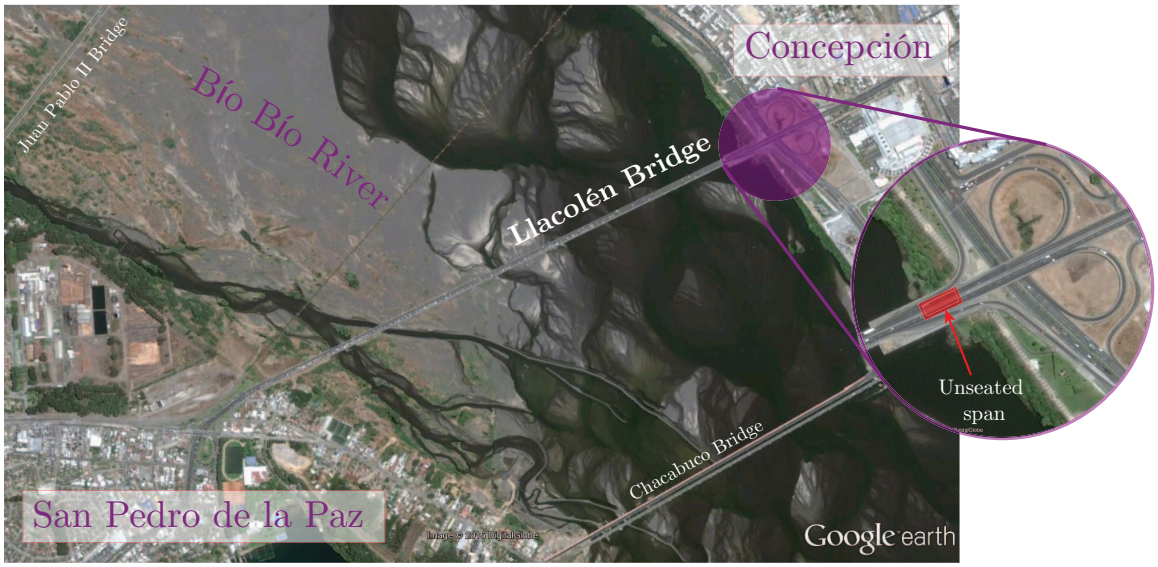

Figure 4.14: Location of the Llacolén bridge site. (Latitude: 36°50′4.00″S, Longitude: 73°4′45.07″W) - Photo taken from Google Earth on 5/2/2016

4.3 Overview of Selected Case Study Site: Llacolén Bridge

In contrast to the previous case Llacolén bridge is chosen as the second candidate for further analyses because of the three dimensional geometry of its northeast approach bent and 2D nature of the approach embankments. The crustal soil at the bridge site extend to a relatively distant location and therefore the lateral ground movement is less restrained by the foundation. Figure 4.14 shows an aerial view of the bridge location. This 2160^{m} long bridge crosses over the Bío-Bío river connecting the cities of Concepción and San Pedro de la Paz. Construction of the Llacolén bridge finished in 2000 and it carries two traffic lanes on each side as well as a sidewalk.

During the 2010 Maule earthquake, the Bío-Bío river eastern bank experienced extensive amount of lateral spreading. The TIRT team reported about 25 cm of lateral displacement in the area close to the northeast approach of the Llacolén bridge. Although the approach span of the bridge was unseated as a result of lateral displacement, unlike many of other bridges crossing the Bío-Bío river in the same region, this bridge did not suffer much damage resulting in other parts of the bridge to remain operable. The bridge consists of 49 spans, not considering the entrance and exit ramps. Bridge bents, typically consisting of six 1.35^{m} diameter columns, carry the loads of the superstructure. The piers are founded on 1.5^{m} diameter reinforced concrete drilled shafts which are tied together at the top by a 1.75^{m} $\times$ 2.5^{m} rectangular cap beam (Figure 4.15a). This beam

also provides the connection between the columns and the piles. Piles are mostly more than 20.0^{m} deep and they extend into a very stiff and dense layer with SPT blow counts of more than 100. Series of precast, pre-stressed reinforced concrete I-girders which are simply seated on column bents with inverted-T cap beams form the bridge deck. Figure 4.15b shows a schematic of the bridge pier transverse cross section. As shown in this figure, two seismic bars located between each pair of adjacent girders are supposed to provide integrity to the bridge during seismic loading. A 10^{cm} expansion joint was designed between the deck slab and the bent on each side. Figure 4.16 depicts a cross-sectional view of the bridge deck and the girders at interior spans. The 21^{cm} thick deck is covered with a 5^{cm} asphalt pavement for the traffic lanes. A 3.5^{m} wide pedestrian sidewalk located on the southern side of the bridge deck indicates a non-uniform live load distribution on the deck which is transmitted to the foundations.

Shown in the magnified section of Figure 4.14, the northeast approach of the bridge consists of geometrically complicated entrances and exits. Having all these structures with different stiffnesses converging in one location results in complex loading conditions on the approach pier foundation. This may be one of the reasons why the approach span collapsed, however, evidence of lateral spreading at the site strengthens the slope failure hypothesis.

During the earthquake, the northeast approach span of the bridge collapsed. Views from north and south of the collapsed span as well as the west-bound entrance - which also nearly unseated - are shown in Figure 4.17. Site investigators observed many flexural cracks on the riverside of the columns which were subject to lateral spreading. These cracks were specifically seen on the pier columns holding the unseated span. These columns are located at the river shoreline and are embedded in the rip-rap. Flexural cracks were seen at the level of rip-rap as well as at the construction joints. A close-up view of these cracks is shown in Figure 4.17. Although unbalanced stiffness of different structures (Entrance and exit ramps) meeting at the approach span could be a major cause of failure, a liquefaction-induced lateral spreading or slope failure is the most probable cause.

Evidences of liquefaction such as sand boils, liquefaction-induced settlement and several lateral spreading cracks were seen on site after the earthquake. These evidences were wide-spread along the northern bank of the Bío-Bío river. Liquefaction of the subterranean soil caused exhaustive damage to nearby bridges. As shown in Figure 4.18, the ground surrounding the approach bent settled up to 40^{cm}. Ground cracks were seen at the bridge site and many sand boils -important indicator of liquefaction - were also seen at the site. The pavement was detached from the approach columns and the resulting gaps were sized from 8^{cm} to 23^{cm}. The variation in amount of separation indicates

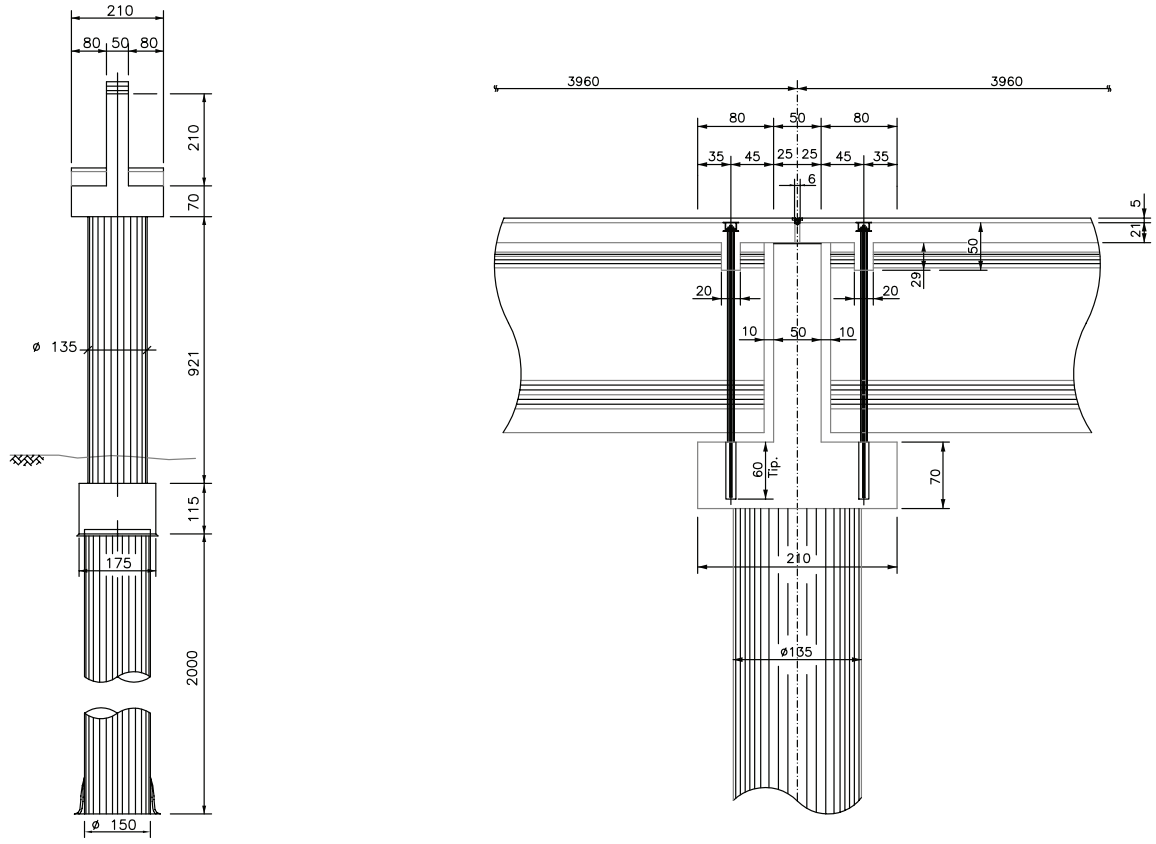

(a) (b)

Figure 4.15: Schematic of (a) bridge approach pier. (b) deck to pier connection. (courtesy Ministerio de Obras Públicas, Chile)

either that the direction of the lateral spreading was not perpendicular to the axis of the bridge pier or that a rotational component exists in the response of the bridge to lateral spreading. The latter deduction seems more reasonable and, as will be presented in the following sections, the 3D FE model results confirm this observation to be due to the inherent 3D effects of the bridge geometry.

Figure 4.19 shows a LIDAR scan of the two northern-most in-river bridge piers. In this figure locations of the fallen span and the approach pier are marked. The scan shows an obvious outward tilting of the bent columns located in the river immediately next to the unseated span. Parts magnified in the image show the relative displacement of the column head to its visible base. As is symbolically shown on the side of the image, direction of the relative displacements are opposite

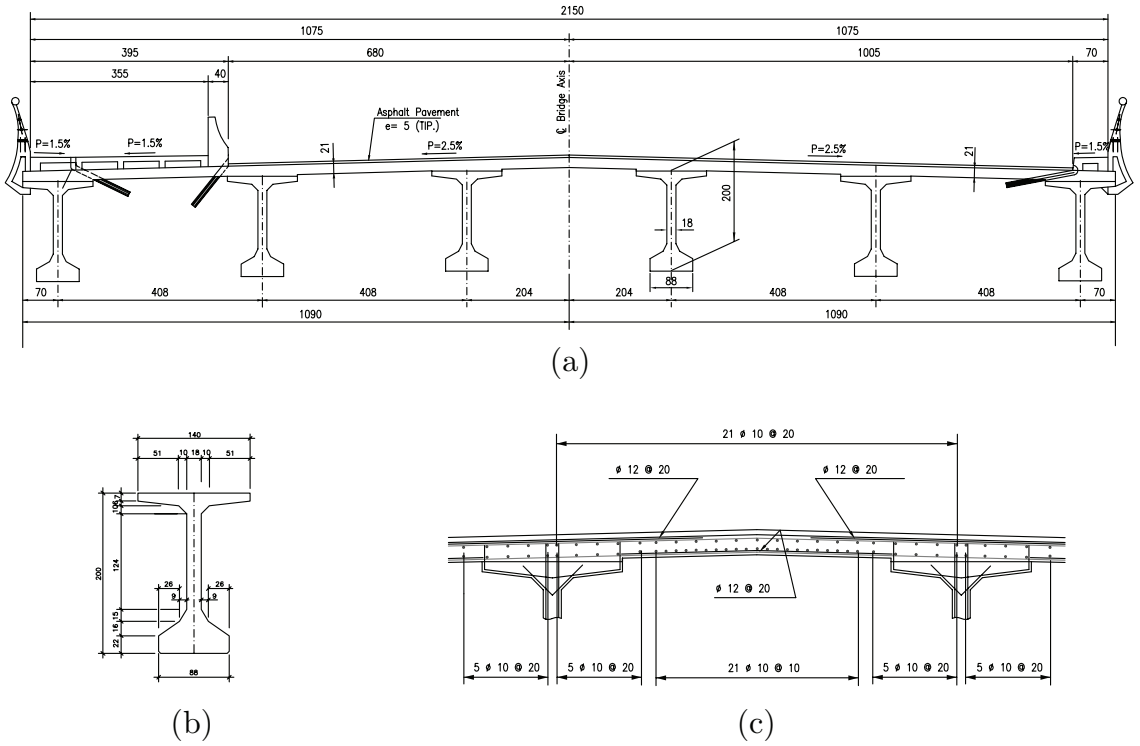

Figure 4.16: Schematic of (a) the bridge superstructure at interior spans. (b) Deck girder beam. (c) Reinforcement arrangement of the deck slab. (courtesy Ministerio de Obras Públicas, Chile)

for the approach pier and the in-river pier. This indicates that the imposed displacements on the subterranean parts of the pier due to lateral spreading was higher for the approach pier than the in-river pier. Another significant conclusion from this observation is that the existence of the bridge deck and the resistance it provides to the whole system is of paramount importance for the analysis.

Based on the observations from post-event explorations and also the information given in the LIDAR scan shown in Figure 4.19, a hypothetical failure mechanism is proposed which explains many aspects of the observations. Figure 4.20 shows details of the proposed failure mechanism. In Figure 4.20a the conditions of the pier and its foundation is shown before the loose sand layer liquefied. During the ground shaking and liquefaction of the loose sand layer, the upper dry crust was displaced towards the river. As a result, large passive forces were exerted on the approach pier foundation. This resulted in movement of the superstructure and closure of the expansion gaps. Any further movement at the top of the columns was impeded because of the resistance provided by the bridge deck. However, the lower parts were still pushed by the dry crust, resulting in a

View From North

View From South

Fallen Span

Westbound Entrance

River-Side View

Figure 4.17: Structural damage caused by lateral spreading. Different views of the fallen span, the almost unseated west-bound entrance and a view from the riverside of the approach pier.

Ground Cracks at the River Bank

Sand Boils

Settlement at Entrance Piers

Separation of the Pavement

Ground Cracks Extending to the Street

Figure 4.18: Manifestations of liquefaction and lateral spreading at the Llacolén bridge site

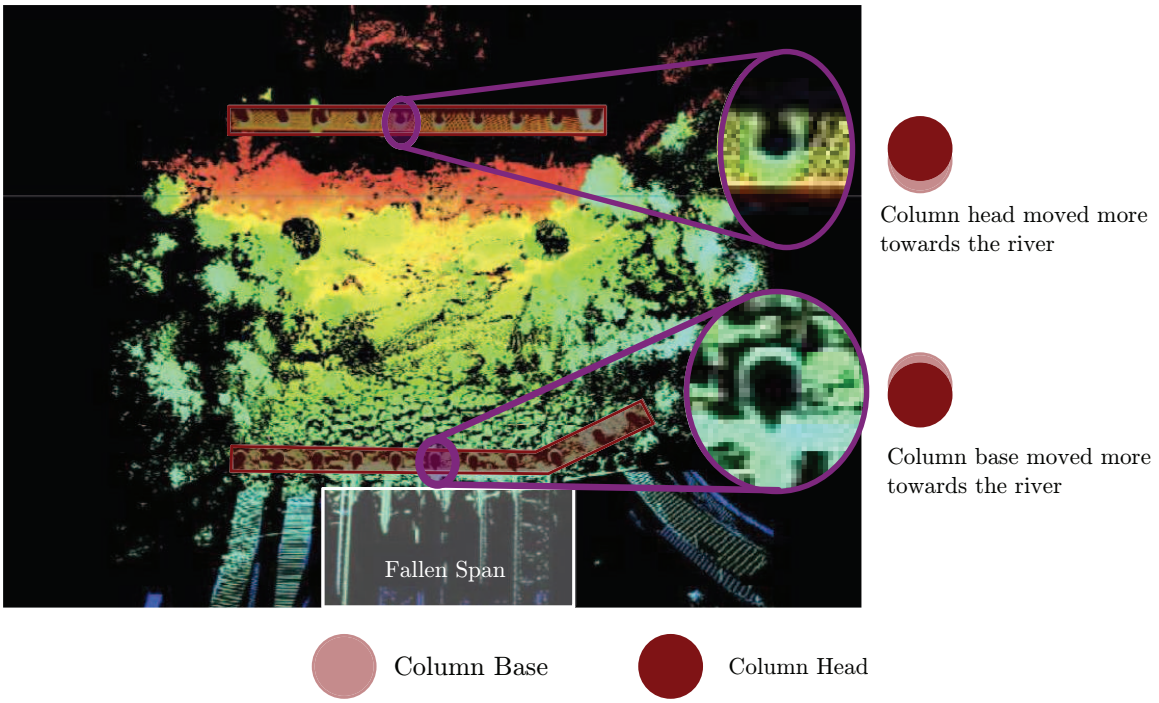

Figure 4.19: LIDAR scan of the Llacolén bridge site. Relative movement of the pier columns to their observable base (The bridge deck is digitally removed)

negative relative displacement between the head and the base of the column. On the other hand, the interior span foundations were not subject to extensive lateral spreading and less lateral movement was induced in the foundation while the superstructure was pushed by the adjacent span, creating a positive relative displacement between the column head and base. This hypothesis explains the observed opposite direction of relative movement between the columns' heads and their visible base in the approach pier and the in-river pier. Collapse of the approach span is also justified if the amount of the lateral movement at the top of approach pier was higher than the length provided for the deck to be seated on the pier. The observed flexural cracks on the river-side of the pier columns at the approach pier can be easily explained by the curvature of the resulting lateral displacements in the pier columns.

4.4 Summary

To gain a better understanding of the ways in which three-dimensional soil deformation affects the lateral loads imposed on piled bridge foundations during lateral spreading, two case study bridge

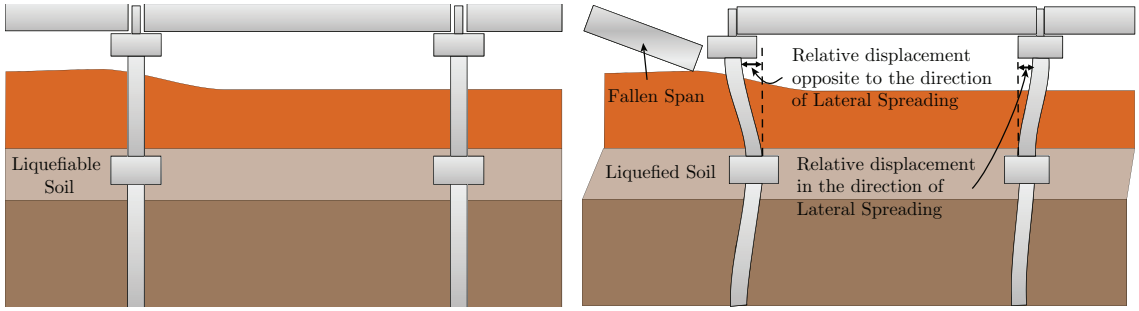

(a) Before (b) After

Figure 4.20: Hypothetical failure mechanism at Llacolén bridge

sites were selected for further analysis. The recent M_w8.8 Maule earthquake off the coast of Chile caused multiple observed cases of lateral spreading at bridge approaches, many of which displayed the target 3D behavior. After a review of the site observations and data available for a series of bridge sites, Puente Mataquito and Lalacolén bridge were selected as the case studies for this research. The bridge sites that are most promising for future studies of this nature are also identified.

Chapter 5

GENERAL MODEL DEVELOPMENT: PUENTE MATAQUITO

Site observations following the M_w8.8 February 27, 2010 offshore Maule earthquake identified widespread lateral spreading at the site of Puente Mataquito, however, the structural damage to the bridge was insignificant in comparison. Numerical models are developed to identify the mechanisms for the reduction in lateral foundation loads implied by the minimal structural damage at this site. These models include beam on nonlinear Winkler foundation (BNWF) models used to test and compare simplified analysis procedures, dynamic effective stress models of the bridge-foundation-soil system in plane strain used to analyze the liquefaction susceptibility and response of the bridge system, and 3D models of the southern bridge abutment, approach embankment, and surrounding soil used to analyze the local effects of lateral spreading on the abutment and foundations and to identify three-dimensional mechanisms that may lead to reductions in estimated lateral loads. Since these models all represent the same structure and site, there are certain shared aspects that appear in all of the models. The development of these general model features is discussed in the following sections. Specific development details for the different modeling approaches are discussed in subsequent chapters dedicated to each aspect of the modeling effort.

5.1 Development of Idealized Soil Profile

The soil profile used for numerical models of the Puente Mataquito site is based on the subsurface explorations (sondajes) made at the site and the soil characterization profile reported by (Petrus, 2006). Initially, only three subsurface explorations were made (Sondajes 1-3), with one near each abutment and one near the center of the bridge. At a later date, three deeper explorations (Sondajes 1a-3a) were made adjacent to each of the originals. Figure 5.1 shows the locations of the six subsurface explorations relative to the bridge abutments and piers. The corresponding SPT resistance profiles are shown in Figure 5.2.

Boring logs for the subsurface explorations reveal a predominantly cohesionless soil profile. Small clay lenses or veins are present, the lower blow counts at depth for Sondajes 2a being one example. For the purposes of the numerical work, minor variations in the soil profile are ignored and all materials are assumed to be cohesionless. The groundwater table is assumed to be at a constant

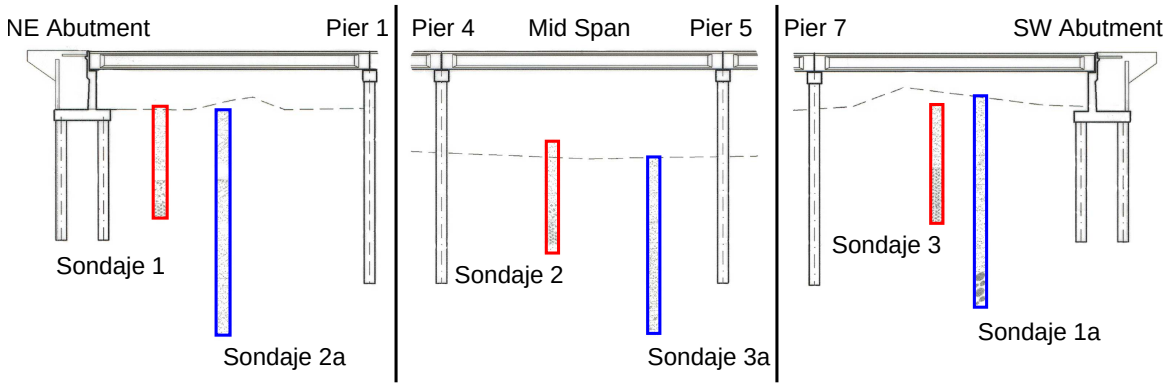

Figure 5.1: Locations of subsurface explorations relative to Puente Mataquito foundations (after Ministerio de Obras Públicas, Chile).

elevation of −0.251 m based on average findings during the site characterization, and all of the soil below the groundwater table is assumed to be saturated.

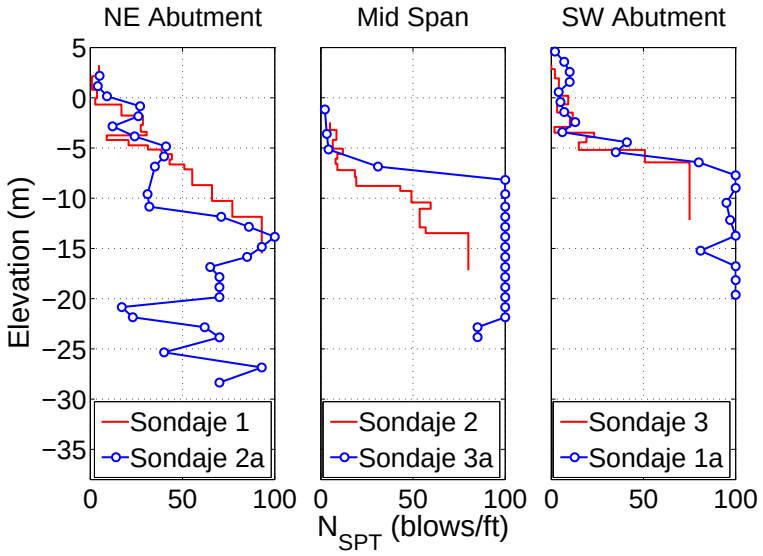

Figure 5.2: SPT resistance profiles for subsurface explorations at Puente Mataquito after Petrus (2006).

The geotechnical report for the project (Petrus, 2006) roughly divides the site into three layers, an upper loose sand layer, a middle layer of denser sand, and an underlying dense gravel layer. The spatial layout of the assumed soil profile is shown in Figure 5.3 with relevant model properties

summarized in Table 5.1. For each layer, a weighted average SPT resistance value is computed from the data presented in Figure 5.2. Representative friction angles, ϕ, for each layer are estimated from these average SPT values using a combination of the correlations proposed by Meyerhof (1956) and Peck et al. (1974). Small strain shear and bulk moduli, $G_{\max}$ and $K_{\max}$, are estimated by correlating the assumed friction angle values to relative densities using the relation proposed in FHWA (1978). Void ratios, e, and phase transformation angles, ϕ_{pt}, are assumed based on the estimated relative densities.

Table 5.1: Model properties for soil layers in idealized soil profile.

Soil Type	ρ (Mg/m^3)	ρ_{sat} (Mg/m^3)	ϕ (°)	G_{max} (MPa)	K_{max} (MPa)	e	ϕ_{pt} (°)
loose sand	1.7	2.16	31	60	175	0.85	29
dense sand	1.7	2.11	36	90	230	0.77	27
gravel	1.7	2.08	42	130	250	0.55	32
fill	1.8	–	42	130	250	0.55	32

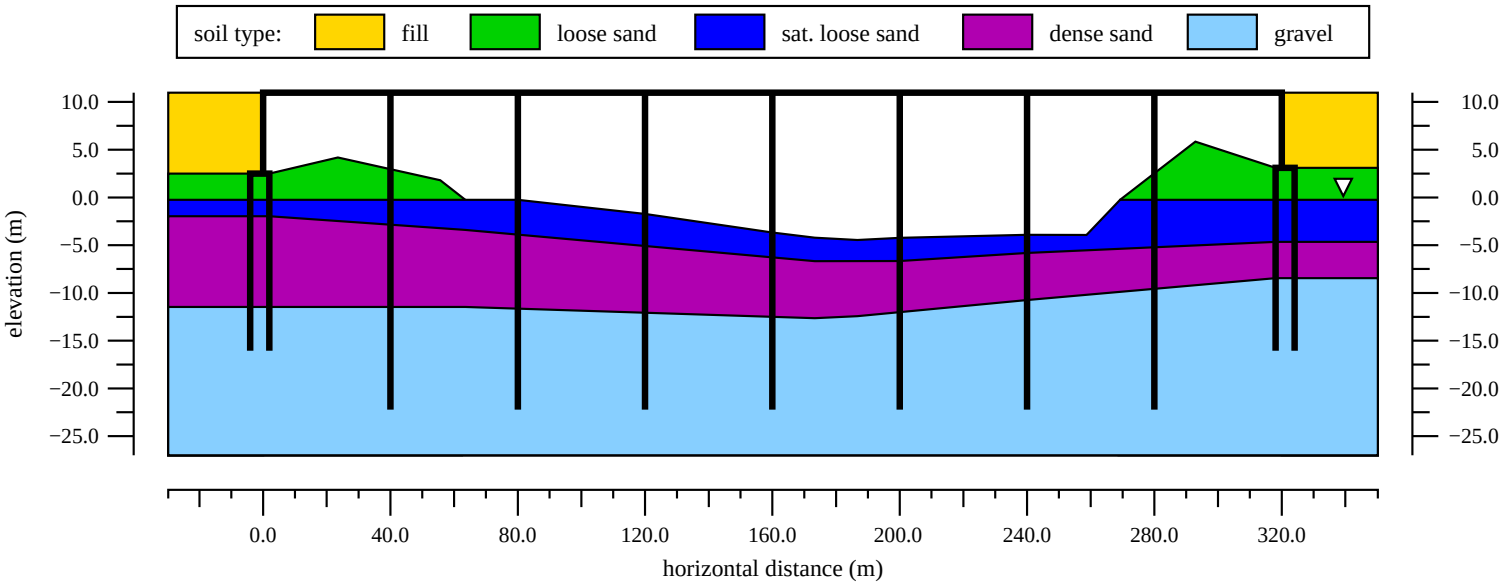

Figure 5.3: Elevation view of bridge and idealized soil profile (vertical scale increased). Horizontal datum is at the northeast bridge abutment.

The properties of the embankment fill are unspecified in the available documentation. The fill is assigned the properties of the gravel layer with a slightly larger mass density to reflect a compacted state. Specific information on the geometry of the approach embankments is similarly unavailable, therefore, a 3H:2V side slope is assumed based on the Chilean Ministry of Public Works (MOP, 2002) recommendations for typical bridge approach embankments. The northeast and southwest approach embankments are assumed to have identical geometries.

5.1.1 Assessment of Liquefaction Potential

The liquefaction susceptibility of the soil at the Puente Mataquito site is assessed using the sand liquefaction triggering relationship of Youd et al. (2001). Assuming a peak ground acceleration (PGA) of 0.4 g based on the recorded PGA in downtown Concepción (Boroschek et al., 2010), a fines content in the range of 5% to 15%, an average reduction coefficient of 0.9, a magnitude scaling factor of 0.75, and a total-to-effective vertical stress ratio of 2, Ledezma (2012) estimated that sands with a normalized SPT value below 28 blows/ft are likely to liquefy in an event similar to the Maule earthquake.

For the SPT blowcount and idealized soil profiles shown in Figures 5.2 and 5.3, this blow count limit indicates that the loose sand layer is highly susceptible to liquefaction and the boundaries of this layer represent the likely scope of liquefaction at the site. The underlying dense sand and gravel layers are much less likely to liquefy for the considered event. Unless otherwise noted, it is assumed in all analyses that liquefaction is confined to the saturated portion of the loose sand layer.

5.1.2 Constitutive Modeling of Site Soils

The constitutive models of Elgamal et al. (2003) are used to simulate the response of each soil material in the 2D and 3D continuum models. These constitutive models use a nested yield surface approach and are available in pressure independent (J2 type) and pressure dependent (Drucker-Prager type) yield surfaces in OpenSees. The pressure dependent version of this constitutive model is capable of capturing contraction, dilation, and cyclic mobility for cohesionless soils. Figures 5.4, 5.5, and 5.6 demonstrate the constitutive response of the material models used for each soil layer, showing the relationships between the norm of the deviatoric stress, $\|\mathbf{s}\|$, mean stress, $p = \operatorname{tr}\boldsymbol{\sigma}$, volumetric strain, $\operatorname{tr}\boldsymbol{\varepsilon}$, norm of the deviatoric strain, $\|\mathbf{e}\|$, and excess pore pressure, u_e. These figures are developed using single element models of a conventional triaxial compression (CTC) test and a direct simple shear (DSS) test. The CTC test simulates drained conditions and is performed in a monotonic configuration only. The DSS test is simulated under undrained conditions and is performed in

monotonic and cyclic configurations.

Table 5.2: Contraction and dilation input parameters used in constitutive model for each soil type.

Soil Type	c_1	c_2	c_3	d_1	d_2	d_3
loose sand	0.087	5.0	0.18	0.0	0.0	3.0
dense sand	0.067	5.0	0.23	0.06	0.27	3.0
gravel	0.013	5.0	0.0	0.3	0.0	3.0
fill	0.013	5.0	0.0	0.3	0.0	3.0

The amount of contraction and dilation demonstrated in Figures 5.4, 5.5, and 5.6 are controlled by a series of input parameters that are related to the relative density of the model soils. The input parameters used for each soil type are summarized in Table 5.2. As would be expected, looser materials have larger contraction parameters and smaller dilation parameters, and these values get smaller and larger, respectively, with increasing relative density. The input parameters for the model soils beyond those referenced in Tables 5.1 and 5.2 are left as the default initialization values in all analyses.

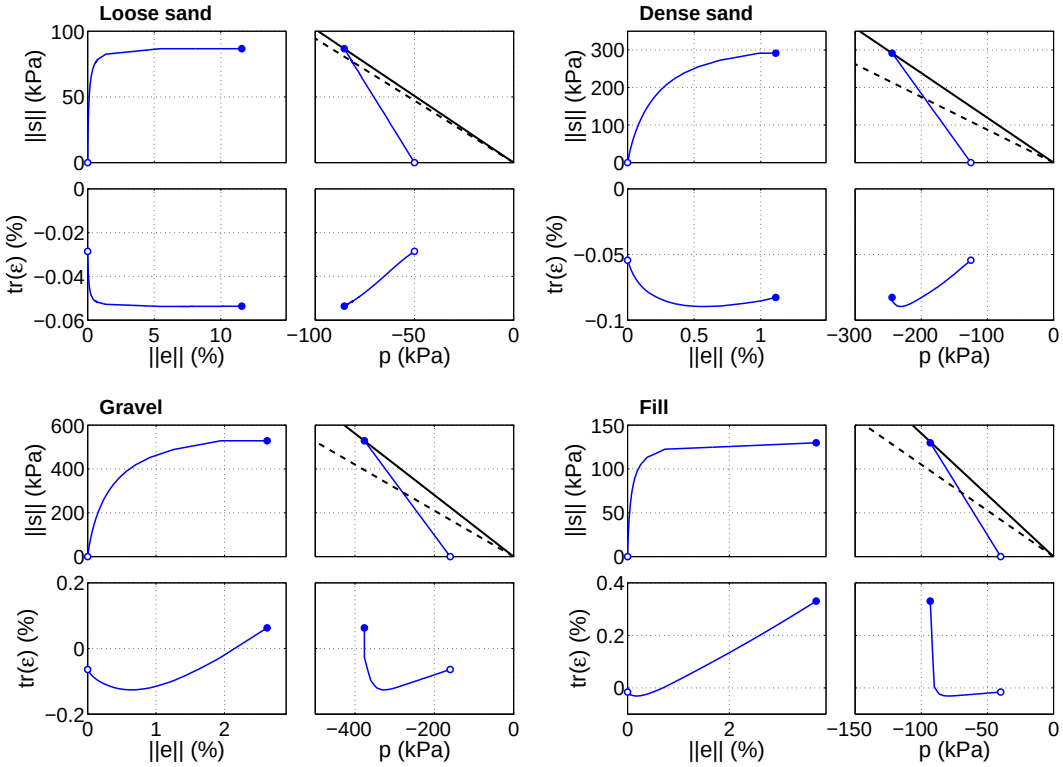

Figure 5.4: Constitutive response of model soils in simulated monotonic drained CTC test.

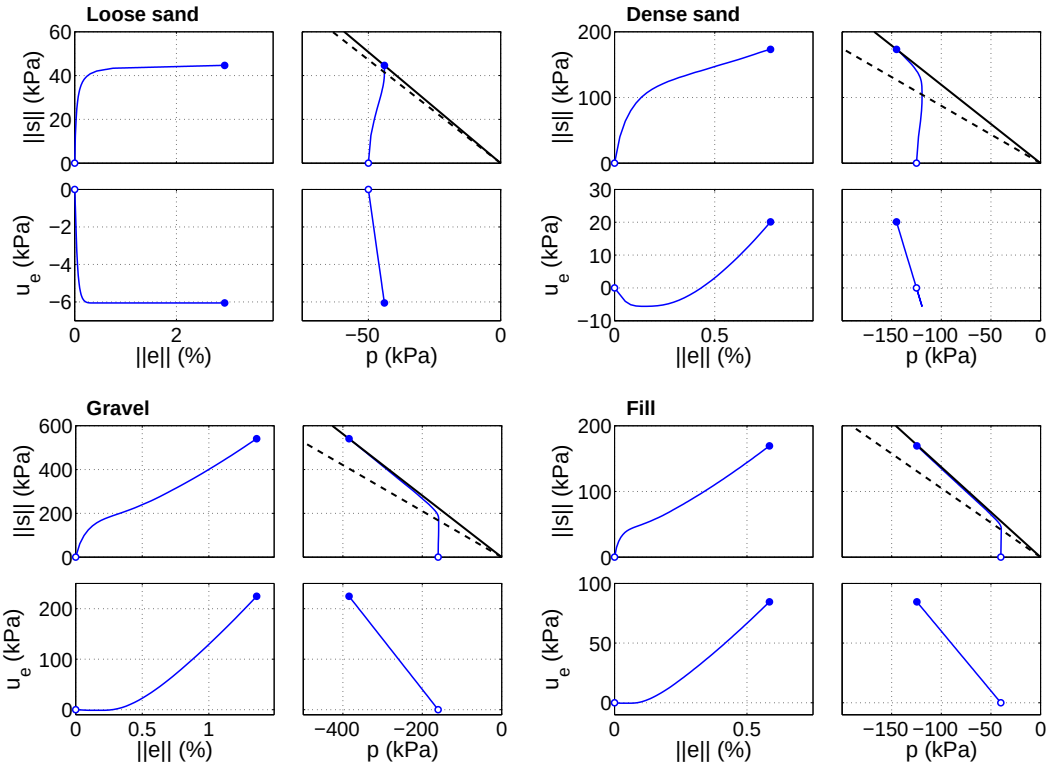

Figure 5.5: Constitutive response of model soils in simulated monotonic undrained DSS test.

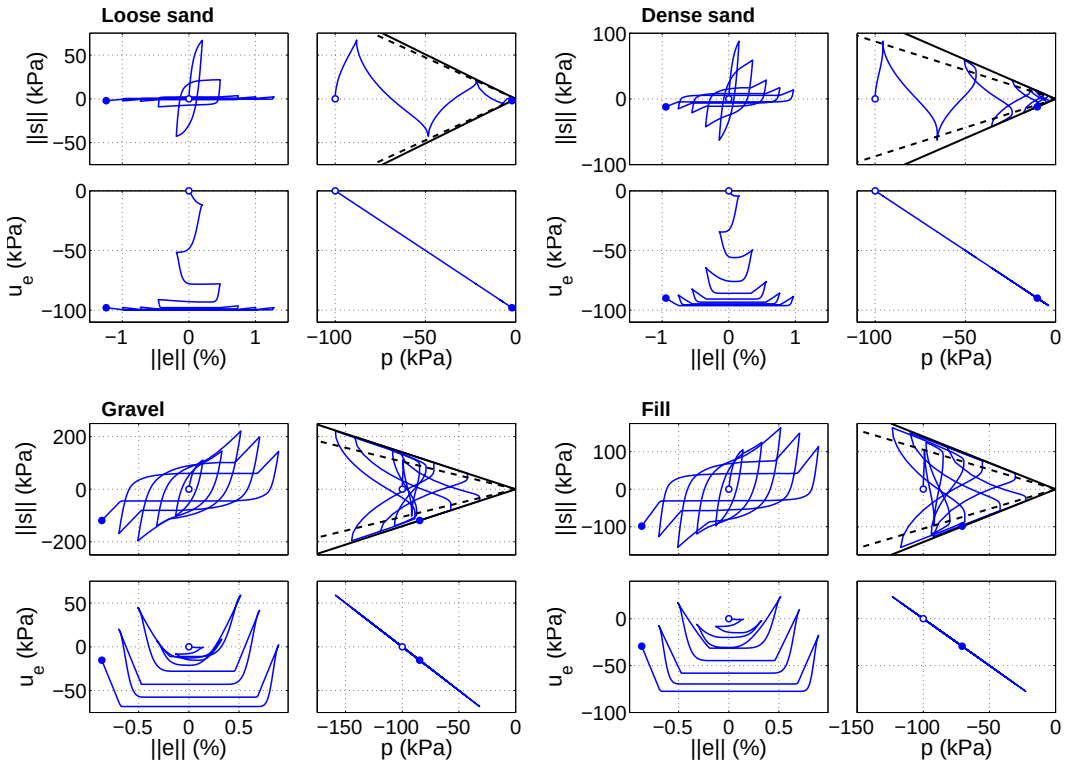

Figure 5.6: Constitutive response of model soils in simulated cyclic undrained DSS test.

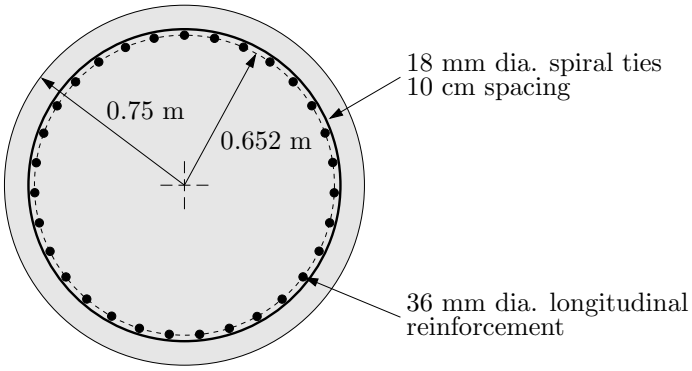

Figure 5.7: Dimensions and details of the model drilled shaft cross-section.

Table 5.3: Concrete and steel material properties in drilled shaft fiber section model. Refer to Figure 5.9 for definitions of terms.

Concrete Properties						Steel Properties		
f'_c (kPa)	ε_c	f'_{cu} (kPa)	ε_{cu}	f_t (kPa)	E_t (MPa)	σ_y (MPa)	E_s (GPa)	b
24525	0.003	4905	0.0368	3070	-2039	412	200	0.001

5.2 Foundation Modeling Approach

The abutments and pier foundations for Puente Mataquito are 1.5 m diameter reinforced concrete shafts. For modeling purposes, an idealized template cross-section, Figure 5.7, is assumed based on the typical reinforcement configuration used in the shaft foundations. There are 31 longitudinal bars, all 36 mm in diameter, and the central core of the shaft is confined with 18 mm diameter spiral ties spaced 10 cm apart.

A fiber section approach is used to incorporate the cross-sectional behavior of the foundations into the finite element models. The fiber section model is discretized into subregions, Figure 5.8, which are assigned uniaxial constitutive behavior corresponding to the type of material they represent. The uniaxial constitutive models used for the concrete and steel portions of the fiber section model are shown in Figure 5.9, with the corresponding model input parameters listed in Table 5.3.

The uniaxial constitutive model assumed for the reinforcing steel, Figure 5.9(b), is a bilinear plasticity model. The parameters defining the constitutive response of this model are the steel yield stress, σ_y, elastic modulus, E_s, and strain hardening ratio, b. The design steel yield stress (Ingeniería Cuatro Ltda., 2006) is used in the model, and the elastic modulus and strain hardening ratio are

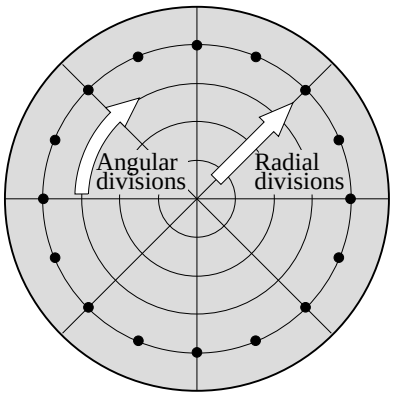

Figure 5.8: Typical discretization scheme for circular fiber section model.

assumed based on typical steel behavior.

The concrete constitutive model, Figure 5.9(a), has compressive behavior based on the work of Kent and Park (1971). The maximum compressive strength, f'_c, used in the model is the design compressive strength of the concrete used at Puente Mataquito (Ingeniería Cuatro Ltda., 2006). A strain at peak compressive stress, $\varepsilon_c = 0.003$, is assumed per ACI (2011) recommendations. The post-crushing behavior is defined after Park and Paulay (1975), where ε_{cu}, the strain at which the concrete is considered completely crushed, is based on the geometry of the core and amount of spiral confinement, and the residual compressive strength $f'_{cu} = 0.2f'_c$.

The tensile behavior for the concrete constitutive model is simplified, with a limited linear elastic capacity followed by linear softening. The tensile strength of the model, f_t, is defined based on the ACI (2011) recommended modulus of rupture for concrete in bending

$$f_r = 0.62\sqrt{f'_c} \tag{5.1}$$

where f_r and f'_c are in units of MPa. The tension softening stiffness, E_t, is determined from the fracture energy of the concrete using the technique discussed by McGann et al. (2012).

A moment-curvature analysis is conducted to verify proper implementation of the fiber section model and establish the capacity of the model shaft foundation. Figure 5.10 shows the moment-curvature response of a single model shaft foundation. The maximum bending moment of 9000 kN·m compares favorably with the nominal design moment capacity for the shaft foundations used in the construction of Puente Mataquito. In some of the models used in this research, the shafts are modeled using linear elastic section behavior. This linear elastic response is defined using the initial

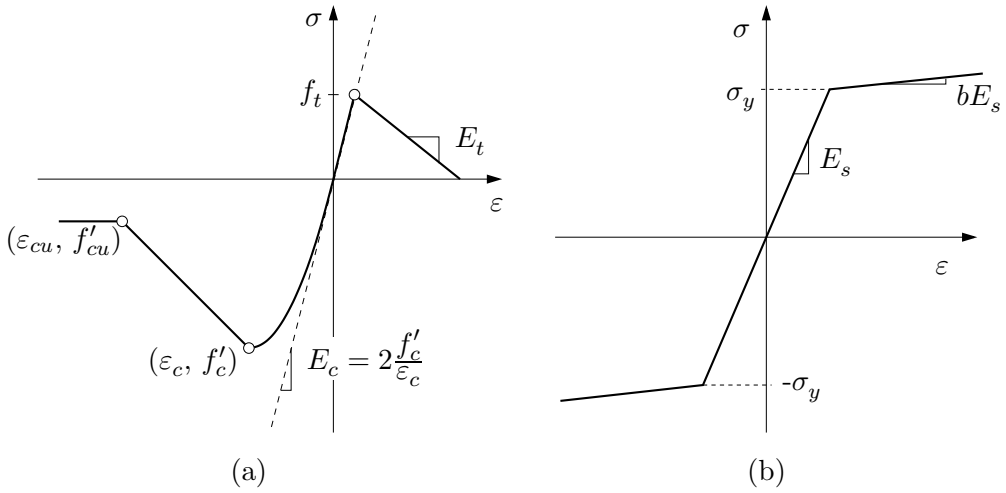

Figure 5.9: Uniaxial constitutive relations used in fiber section model for drilled shaft. (a) Concrete model. (b) Steel model. Refer to Table 5.3 for values used in the models.

tangent to the nonlinear moment-curvature response presented in Figure 5.10.

At the abutments, the shafts are grouped in a 4×2 layout with the dimensions and orientation shown in Figure 5.11. The short dimension of the pile cap corresponds to the longitudinal axis of the bridge. The shafts at the abutments are 17 m long, and extend from the pile cap down into the gravel soil layer, ending at a vertical elevation of -16.06 m (see Figure 5.3). The shafts are grouped in a 3×1 configuration at the seven interior piers with the layout and dimensions shown in Figure 5.12. The interior pier shafts are 28.6 m long and extend from a concrete cap just below the bridge girders into the gravel layer, ending at an elevation of -22.22 m.

The different types of numerical models used in this research vary in their treatment of the foundations. For the BNWF models, the grouped shafts at the bridge abutments are consolidated into a single equivalent shaft model following the procedure recommended by Caltrans (2011) and discussed in Section 3.1. The plane strain models consider a grouped pair of equivalent shaft models at the abutment which have the bending stiffness of a row of four shafts, and single equivalent shaft models at the interior piers with the stiffness of a row of three shafts. The 3D models consider the full geometry of the shaft group at the southern abutment, using beam-to-solid contact elements to model the soil-shaft interaction. Each of these specialized techniques are discussed further in the following sections.

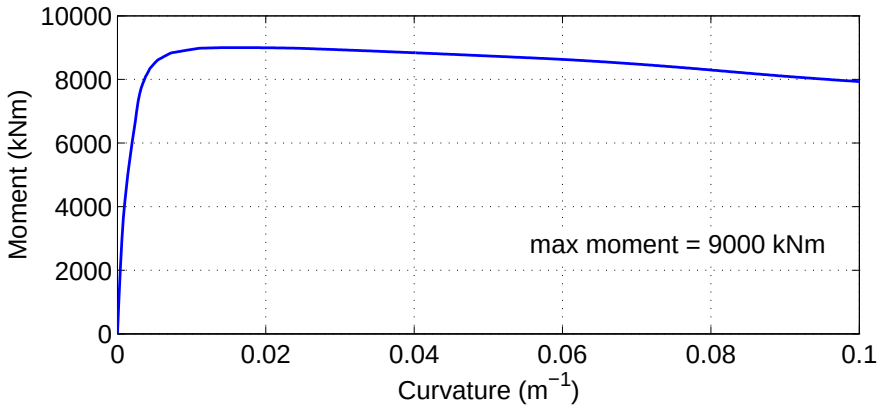

Figure 5.10: Model moment-curvature response for single drilled shaft foundation at design axial force.

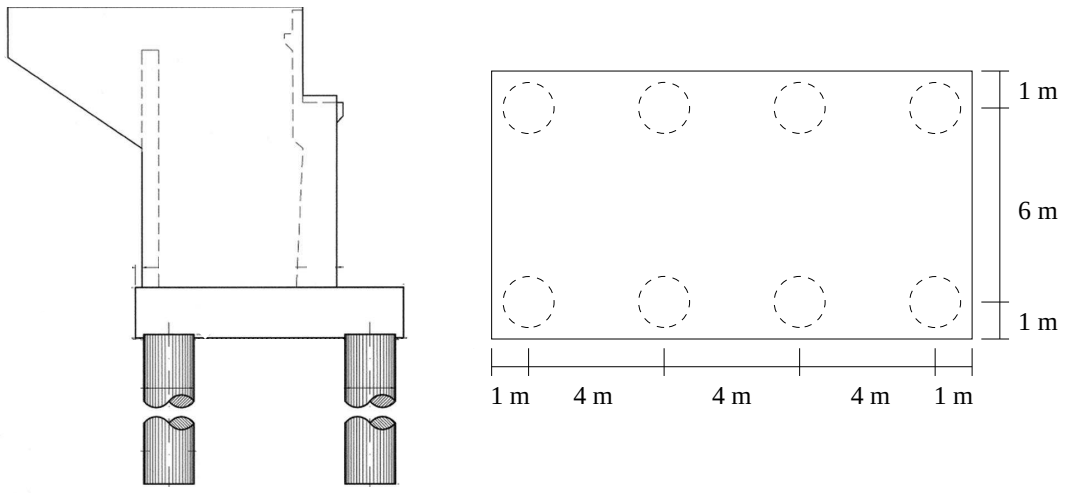

Figure 5.11: Elevation and plan views of typical abutment for Puente Mataquito (courtesy Ministerio de Obras Públicas, Chile).

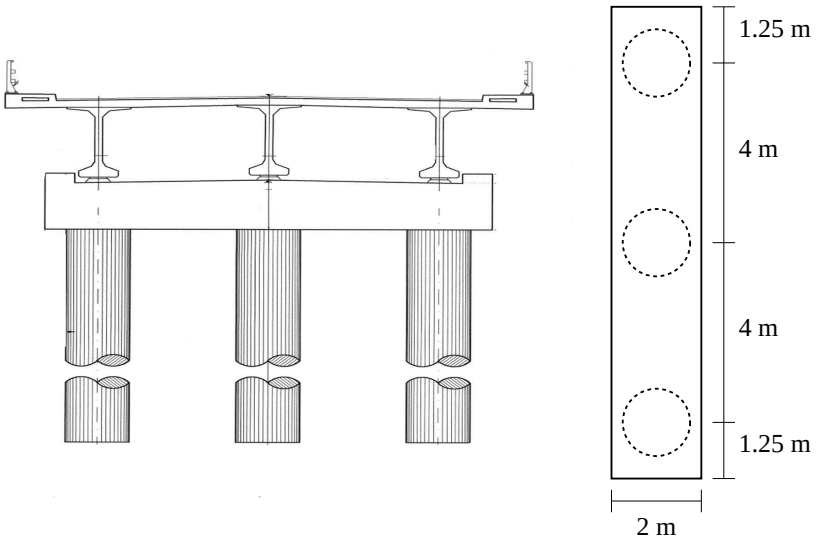

Figure 5.12: Elevation and plan views of typical interior pier shaft cap for Puente Mataquito (courtesy Ministerio de Obras Públicas, Chile).

5.3 Summary

To support the numerical modeling effort for the Puente Mataquito case study, an idealized soil profile is defined and a template section model of an individual shaft foundation is created. The idealized soil profile is used to inform the definition of the soil portion of the necessary models, and the template section model is the basis for all of the foundations considered in this work.

Chapter 6

DYNAMIC PLANE STRAIN MODELS: PUENTE MATAQUITO

A dynamic effective stress plane strain finite element model of the Puente Mataquito site is created to analyze the dynamic response of the bridge and underlying soils using two ground motion records. This model uses the idealized soil profile and shaft foundation models introduced in Chapter 5, and makes use of the efficient element formulations. This model is developed to gain a better understanding of the response of the bridge site to seismic excitation and to inform further modeling efforts.

Initially, two small parameter studies are performed to establish an appropriate soil domain thickness for use in subsequent models, and to assess the effects of variations in the assumed liquefiable layer configuration on the response of the site. This is done to verify that the assumptions made during development of the idealized site soil profile are reasonable. After the completion of this initial assessment and model verification, further analysis is performed using the Convento Viejo ground motion record from the 2010 Maule event. This final dynamic study provides insight into the response of the bridge and surrounding soils during seismic excitation, allowing for comparison with physical observations made following the earthquake, and for assessment of the structural demands resulting from any liquefaction and subsequent lateral spreading simulated by the model.

6.1 Plane Strain Model Development

The plane strain finite element model uses the **u**-p formulation of the SSP-uP element to represent the soil continuum, displacement-based beam elements to model the bridge foundations and superstructure, and uniaxial nonlinear force-displacement curves (p-y, t-z, Q-z springs) to consider soil-structure interaction effects. The commercial software GiD (CIMNE, 2008) is used as a pre- and post-processor for OpenSees to facilitate mesh creation and result visualization.

Figure 6.1 shows the finite element mesh for the plane strain model. Since the width of the model is far larger than the height, the central portion of the mesh is shown with increased resolution below a depiction of the full mesh. The colors in the soil domain represent separate layers within the soil profile. The boundaries and soil properties of these layers correspond with the idealized soil profile discussed in Section 5.1. Overall, the mesh is 795 m wide, with 237.5 m of soil on either side of the

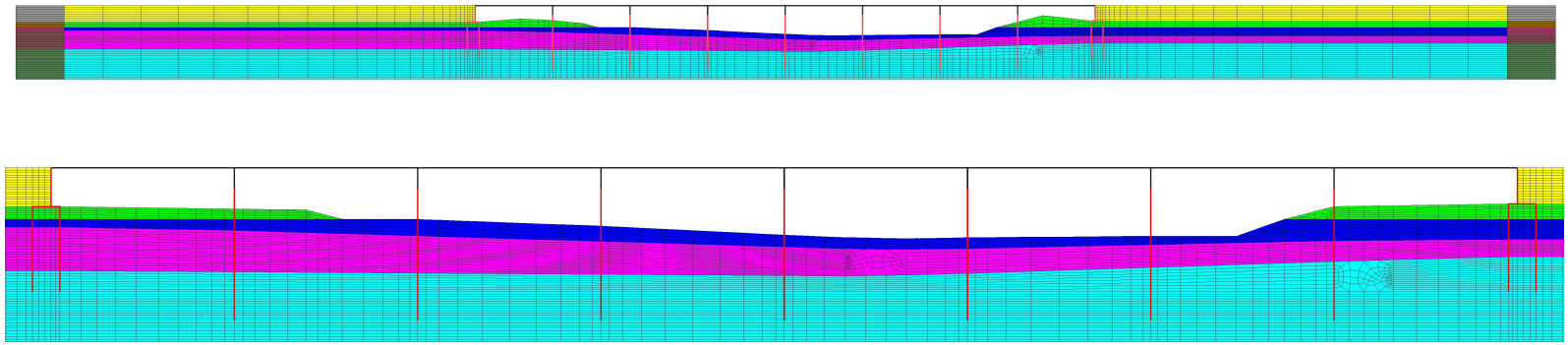

Figure 6.1: Finite element mesh for plane strain analysis of Puente Mataquito site.

bridge. The gravel layer is extended 4.78 m below the lower extremity of the interior pier shafts, ending at a vertical elevation of -27 m. Two levels of mesh refinement are considered for the plane strain model. The more refined version has 8031 solid elements and the less refined mesh has 3990 solid elements. Each mesh includes 360 beam elements and 252 soil-structure interaction elements. The less refined version of the mesh is used primarily for testing and comparative studies for which this level of refinement is adequate, while the refined mesh is used for more detailed analysis of the site.

6.1.1 Boundary and Loading Conditions

The mesh shown in Figure 6.1 represents only a portion of a large soil domain that extends far beyond practical limitations for the model. The boundary and loading conditions are implemented to reduce the error associated with this limited model domain as much as possible. In the vertical direction, the primary goal is to achieve an initial state of stress representative of the conditions at the site. In the horizontal direction, the emphasis is on applying the ground motions to the model in a way that is the most consistent with site conditions and in ensuring that free-field conditions exist at the extents of the model.

To achieve an appropriate initial state of stress in the model, the nodes along the base of the soil mesh are fixed against vertical translation, and elemental body forces are used to simulate the effect of gravity on the soil. For the beam elements representing the shaft foundations, t-z and Q-z springs provide vertical restraint through simulated skin friction and end bearing, respectively. A distributed loading equivalent to the self-weight of the bridge is applied to the beams representing the bridge deck.

The base of the model is not a physical boundary between the gravel and an underlying layer of bedrock, therefore, a rigid base approach to dynamic loading is not ideal. Instead, ground motions are applied to the model as equivalent force histories using the method of Joyner and Chen (1975), which considers the compliance of an underlying elastic halfspace, preventing all of the applied energy from becoming trapped inside the considered domain. To implement the Joyner and Chen (1975) approach, the nodes at the base of the mesh are constrained to have equal degrees-of-freedom in the horizontal direction with a control node at the lower left corner of the mesh. This control node is attached to a rate-dependent viscous damper element set with a dashpot coefficient

$$c = \rho_{\text{half}} v_{s\,\text{half}} A \tag{6.1}$$

where ρ_{half} and $v_{s\,\text{half}}$ are the mass density and shear wave velocity, respectively, of an assumed underlying elastic halfspace, and A is the base area of the model, accounting for the length of the model and the assigned thickness of the elements. The halfspace parameters are set as $\rho_{\text{half}} = 2.5$ Mg/m^3 and $v_{s\,\text{half}} = 750$ m/s for all analysis cases. A force history is obtained as

$$F_{\text{equiv}}(t) = \rho_{\text{half}} v_{s\,\text{half}} A v_{\text{record}}(t) \tag{6.2}$$

where $v_{\text{record}}(t)$ is the velocity time history of the recorded motion at that depth, and is applied dynamically at the control node. This approach for ground motion application considers the compliance of the soil and rock which exists below the extents of the model, and prevents energy from becoming trapped in the model domain.

The columns of elements at the horizontal extents of the soil mesh, depicted in distinct colors in Figure 6.1, are used to apply a free-field soil response to the interior of the model. The elements in these columns are assigned a thickness 100 times larger than that assigned to the interior elements to ensure that they are significantly more massive. When the ground motion is applied to the base of the model, these columns of elements respond in the manner of the free-field soils at the site, while simultaneously transmitting this response into the interior of the model. The horizontal extents of the mesh are defined such that these free-field columns are sufficiently removed from the areas of interest. This technique has been applied to dynamic plane strain analysis by Shin (2007), among others.

6.1.2 Additional Soil Properties for Effective Stress Analysis

The soil properties and constitutive models discussed in Section 5.1 are used in the plane strain model, however, several additional material properties must be defined for an effective stress analysis of the site soils. A fluid bulk modulus $K_{\text{fluid}} = 2.2$ GPa and fluid mass density $\rho_{\text{fluid}} = 1.0$ Mg/m^3 are used for all soil layers below the groundwater table. Isotropic permeabilities are assigned to each submerged soil layer, with values of 8.5×10^{-6} m/s, 5.0×10^{-3} m/s, and 1×10^{-2} m/s corresponding to the loose sand, dense sand, and gravel layers, respectively. The permeability values are selected to be as similar as possible to the expected values for each soil type, while producing the desired response in the numerical model.

6.1.3 Bridge Superstructure and Foundations

Displacement based beam-column elements are used to model the bridge superstructure, abutments, and shaft foundations. The beam elements representing the shaft foundations are assigned a section response based on the model drilled-shaft cross-section discussed in Section 5.2, and both elastic and elastoplastic section responses are considered. For the interior piers, the section properties of the shaft model are scaled by three to capture the bending stiffness of a 3×1 row of shafts. The beam elements in the piers transition from this foundation section model to an elastic girder section model at the base of the pier cap shown in Figure 5.12. The 4×2 grouped shaft foundations at the abutments are modeled with two columns of vertical beam elements, assigned the model shaft section properties scaled by four, connected at the top by a rigid horizontal beam representing the shaft cap. This configuration is shown in Figures 5.3 and 6.1.

The beam elements representing the bridge deck, interior piers above the pier caps, shaft caps, and abutment walls are assigned an elastic section response based on a composite cross-section defined by the bridge deck and girders. The second moment of area for this composite deck section is $I_{\text{deck}} = 4.58$ m^4 and the cross-sectional area is $A_{\text{deck}} = 7.25$ m^2. A modulus of elasticity $E_{\text{deck}} = 63.2$ GPa is chosen to represent a smearing of the reinforcement and concrete in the cross-section. The vertical location of the beam elements representing the bridge deck is the centroid of the composite deck girder cross-section.

6.1.4 Soil-Foundation Interaction Curves

The beam elements used to model the bridge foundations must be linked to the soil mesh in a manner that accounts for the disparity in what each element type represents in plane strain. Defining a direct link between the beam and soil nodes implies that the beam elements represent a wall with an infinitesimally small width in the plane and infinite thickness out of the plane. An appropriate link between the two element types is developed using interface elements assigned the constitutive response of commonly used soil-structure interaction curves that account for the three-dimensionality of the shaft foundations.

Zero-length elements are used for this purpose, with p-y curves defining the horizontal constitutive response and t-z and Q-z curves applied in the vertical direction. The use of zero-length elements allows for the beam and solid element nodes to share the same location within the mesh, thus simplifying mesh generation during pre-processing. Using this technique, the compatibility of displacements between the foundations and surrounding soil that occurred at the Puente Mataquito site cannot be directly captured, however, the mechanisms can still be identified. The modeled soil

will displace approximately in the manner expected for the embedded foundations, and the structural demands in the foundation elements will approximate those in the actual shaft foundations. Another potential issue with this modeling technique is that the soil response is effectively modeled twice. The interpretation of the *p*-*y*, *t*-*z*, and *Q*-*z* curves as the near-field soil response, and the continuum elements as more of a far-field response removes some of this concern, however, it is important to note the potential for error associated with this doubled soil response.

The *p*-*y*, *t*-*z*, and *Q*-*z* curves in the plane strain model are defined based on existing relations and previous experience. For the *p*-*y* curves, p_u values are defined using the method of Brinch Hansen (1961) and k_T values are defined using the API (2007) procedure corrected for overburden after Boulanger et al. (2003). The *t*-*z* curves are defined after the work of Mosher (1984) and Kulhawy (1991), and the *Q*-*z* curves are defined based on the work of Meyerhof (1976) and Vijayvergiya (1977). Since the beam elements in the model represent a row of shaft foundations, group effects are considered for the soil-foundation interaction curves using the *p*-multipliers of Mokwa and Duncan (2001).

The interface elements connecting the beam elements representing the abutment walls with the solid elements representing the embankment fill are assigned an elastic-perfectly plastic constitutive response in compression with zero tensile strength or stiffness. The ultimate capacity of these constitutive models is determined from the Rankine passive capacity of the soil in the embankments. The elastic stiffness values are set in a similar manner to the tri-linear curves discussed in Section 3.1.1, with $\Delta_{\max}$ set equal to 5% of the nodal depth. At the surface nodes, small non-zero ultimate force and displacement values are assigned for numerical purposes.

6.1.5 Ground Motions

Two ground motions are used during analysis of the plane strain model, the Convento Viejo record from the 2010 Maule event and the Gilroy No. 1 record from the Loma Prieta event. The Convento Viejo recording was made by a triaxial accelerograph located on rock inside a diversion tunnel for the Convento Viejo embankment dam (ARCADIS, 2010), which is approximately 100 km inland from Puente Mataquito. Figure 6.2 shows the location of the recording site in relation to Puente Mataquito and several cities. The horizontal acceleration, a, velocity, v, and displacement, u, time histories for the Convento Viejo motion are shown in Figure 6.3. The Convento Viejo ground motion record was obtained via personal correspondence with Christian Ledezma from Pontifica Universidad Católica de Chile. At the time of the analyses, the Convento Viejo dam was the nearest available recording site to Puente Mataquito with a rock ground motion record.

Figure 6.2: Location of the Convento Viejo recording site relative to Puente Mataquito.

Table 6.1: Maximum acceleration, velocity, displacement, and Arias intensity for Convento Viejo and Gilroy No. 1 ground motion records.

Record	$a_{\max}$ (g)	$v_{\max}$ (m/s)	$u_{\max}$ (m)	I_a (m/s)	duration (s)
Convento Viejo	0.147	0.246	0.081	1.74	299.97
Gilroy No. 1	0.473	0.267	0.081	1.68	39.945

The Gilroy Array No. 1 fault parallel record from the 1989 Loma Prieta event (NGA #765) from the PEER strong ground motion database (PEER, 2010) is used as an alternative ground motion. While this record does not possess the long duration and high frequency content characteristic to recorded motions from the Maule event, it is a significantly shorter motion with fewer recorded time steps, thus facilitating shorter analysis times more suitable for testing the model and producing comparative studies for different modeling decisions. The time histories for the Gilroy No. 1 record are shown in Figure 6.4.

Table 6.1 provides the maximum acceleration, velocity, and displacement along with the Arias intensity, I_a, for each ground motion record. The peak acceleration for the Gilroy record is significantly larger, however, the peak velocities, peak displacements and Arias intensities are similar for the two records. As shown in Figure 6.5, the Arias intensities develop differently for each motion. For the Gilroy record, there are several large amplitude waves early in the motion and these waves

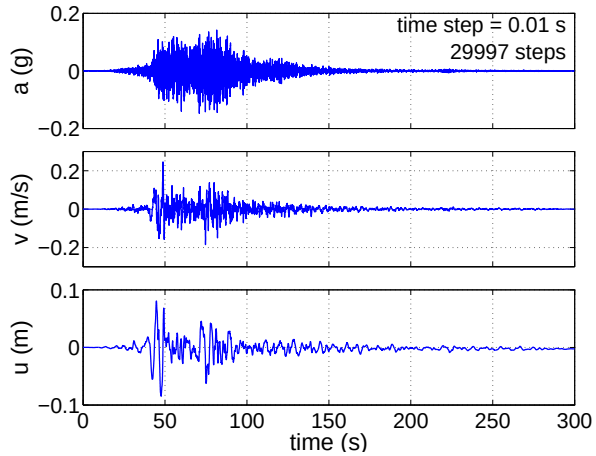

Figure 6.3: Acceleration, velocity, and displacement time histories for Convento Viejo ground motion record.

are the primary contribution to the Arias intensity for the record. The amplitudes for the Convento Viejo record are smaller in comparison, however, the high amplitude portion of this record lasts over a longer duration, leading to a slower rate of increase in the Arias intensity. For further comparison of the two ground motion records, the response spectra at 5% damping are shown in Figure 6.6. As expected, the two ground motion records produce very different response spectra.

6.2 Dynamic Plane Strain Analysis: Gilroy No. 1 Ground Motion Record

In order to determine a set of appropriate modeling parameters for use in subsequent models of the Puente Mataquito site, a series of initial simulations are performed using the Gilroy No. 1 ground motion record from the 1989 Loma Preita event. This record is shorter and more forgiving numerically than the Convento Viejo motion (see Section 6.1 for details), thus enabling a series of analyses to be performed efficiently. The results from these analyses are compared to each other to gain valid insights into the behavior of the Puente Mataquito site and to gauge the effect of various modeling choices on the results of the simulations. Two primary modeling choices are considered in this study: the effect of soil element domain thickness, and the effect of different liquefiable layer configurations.

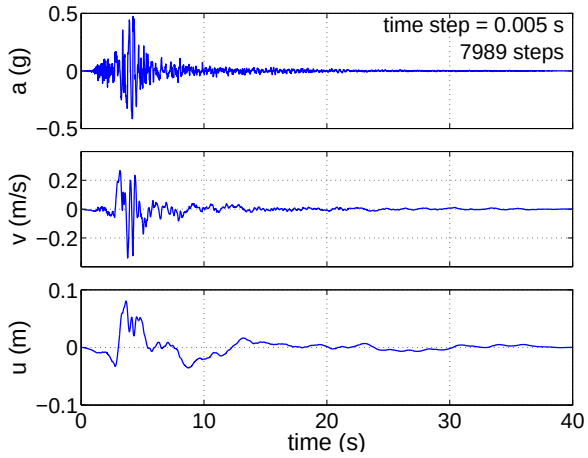

Figure 6.4: Acceleration, velocity, and displacement time histories for Gilroy No. 1 ground motion record.

6.2.1 Alternative Model Configurations

Several different configurations of the plane strain model are considered in order to assess the sensitivity of the results to different modeling choices. One set of alternative model configurations is chosen to evaluate the effects of solid element thickness. The incompatibility between the plane strain continuum elements used to model the soil and the beam-column elements used to model the bridge foundations necessitates care in the treatment of this thickness in order to gain appropriate results. This is especially true where the beam elements represent a row of grouped piles or shafts, as is the case for the Puente Mataquito model. Typically, plane strain continuum elements are assigned a unit thickness in the out-of-plane direction. It is likely that this definition does not achieve a realistic soil mass to foundation stiffness ratio, and as a result, the soil deformation and structural demands returned from the simulation may be underpredicted. To examine the effect of solid element thickness on the results, models are created that consider three element thickness values: 20 m, 90 m, and 1 km.

The 20 m thickness is based on the equivalent embankment width, w_t, proposed by Boulanger et al. (2006) for simplified analysis of piled bridge abutments subject to lateral spreading (see Section 3.1.1, step 5). This equivalent width is computed as the sum of the crest width with one-half of the width of the sloped sides as shown in Figure 6.7. The 90 m thickness is based on the surface width of a soil wedge developed over the full length of the abutment shafts as predicted using strain wedge theory (Ashour et al., 1998). The 1 km thickness is chosen as a maximum credible value.

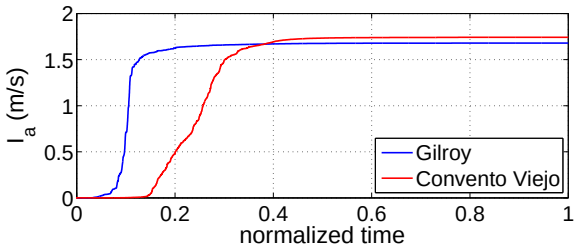

Figure 6.5: Arias intensity values over normalized motion duration for Convento Viejo and Gilroy No. 1 ground motion records.

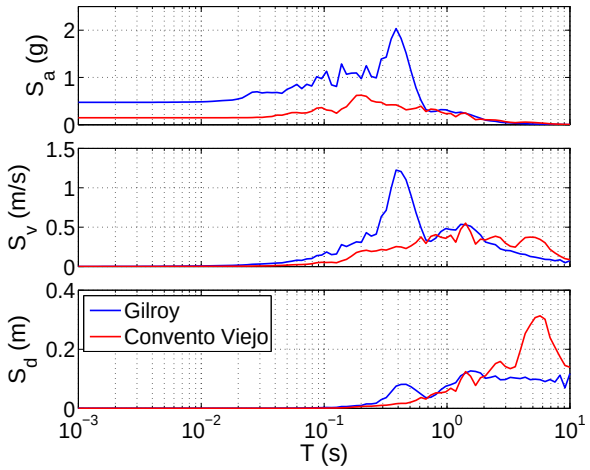

Figure 6.6: Response spectra (5% damping) for Convento Viejo and Gilroy No. 1 ground motion records.

Another set of model configurations is used to analyze the liquefaction behavior of the Puente Mataquito site, primarily with regards to uncertainty in the definition of the liquefiable layer for the idealized soil profile. To this purpose, three liquefaction configurations are considered for the plane strain model: no liquefaction, existing (idealized) liquefaction conditions, and thick liquefaction conditions. A 90 m soil domain thickness is assumed for these models. In the case without liquefaction, the permeabilities of the soil elements are set at 1.0 m/s, such that excess pore pressure will not develop. The existing liquefaction case considers the idealized soil profile discussed in Section 5.1, and the thick liquefaction case considers a soil profile in which the loose sand layer expands to replace the dense sand layer, resulting in a larger zone of liquefiable material. The results of these three cases are compared to each other and to observations made at the site to determine which liquefaction configuration is most representative of the Puente Mataquito site.

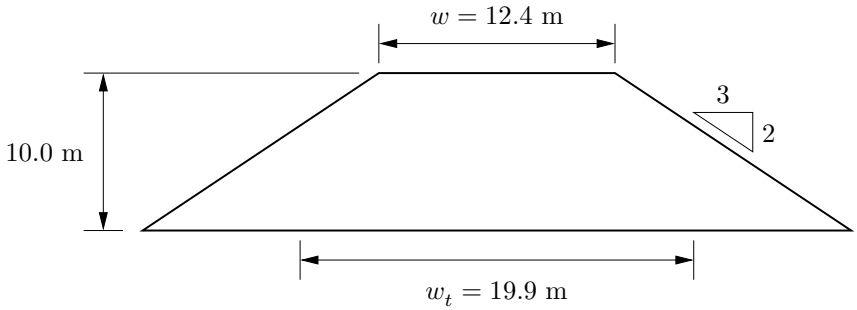

Figure 6.7: Idealized approach embankment dimensions for Puente Mataquito.

6.2.2 Effects of Soil Domain Thickness

Figure 6.8 demonstrates the effect of soil domain thickness on the residual horizontal displacement field returned by the model. Larger element thickness results in larger soil deformation, as the foundation stiffness is no longer sufficient to resist the movement of the increased soil masses. Figures 6.9, 6.10, and 6.11 show the progression of pore pressure ratio fields in the soil for for the 20 m, 90 m, and 1 km thick domains, respectively. As shown, there is little variation in pore pressure ratio with soil element thickness. The primary difference is in how long it takes for the large excess pore pressures to dissipate, and, as shown in Figure 6.8, how the build up of excess pore pressure is manifested in lateral soil deformation.

Figures 6.12 and 6.13 show the variation in pore pressure ratio with depth in the soil behind the two bridge abutments over the first half of the Gilroy ground motion. Significant excess pore pressures begin to develop at roughly the same point in the motion, and the dissipation of the express pore pressure tends to take longer as the soil domain thickness is increased. This is likely due to the lateral deformation of the soil above the liquefiable layer increasing the shear strain for the larger thickness values. Figures 6.14 and 6.15 verify this hypothesis, as significantly larger shear strains develop in the soil behind the abutments for the larger domain thickness values, especially on the southwest side.

The global response of the bridge is also affected by changing the thickness of the soil elements. Figures 6.16, 6.17, and 6.18 show the residual displaced shapes of the shaft foundations for the bridge, arranged in the same orientation used in previous plots of the bridge model. The general deformation patterns for the 20 and 90 m thick domains are similar, though the 90 m case sees larger shaft displacements, especially in the southwest abutment shafts and adjacent interior piers. The shaft displacements for the 1 km thick case are significantly larger than the other cases, and Pier

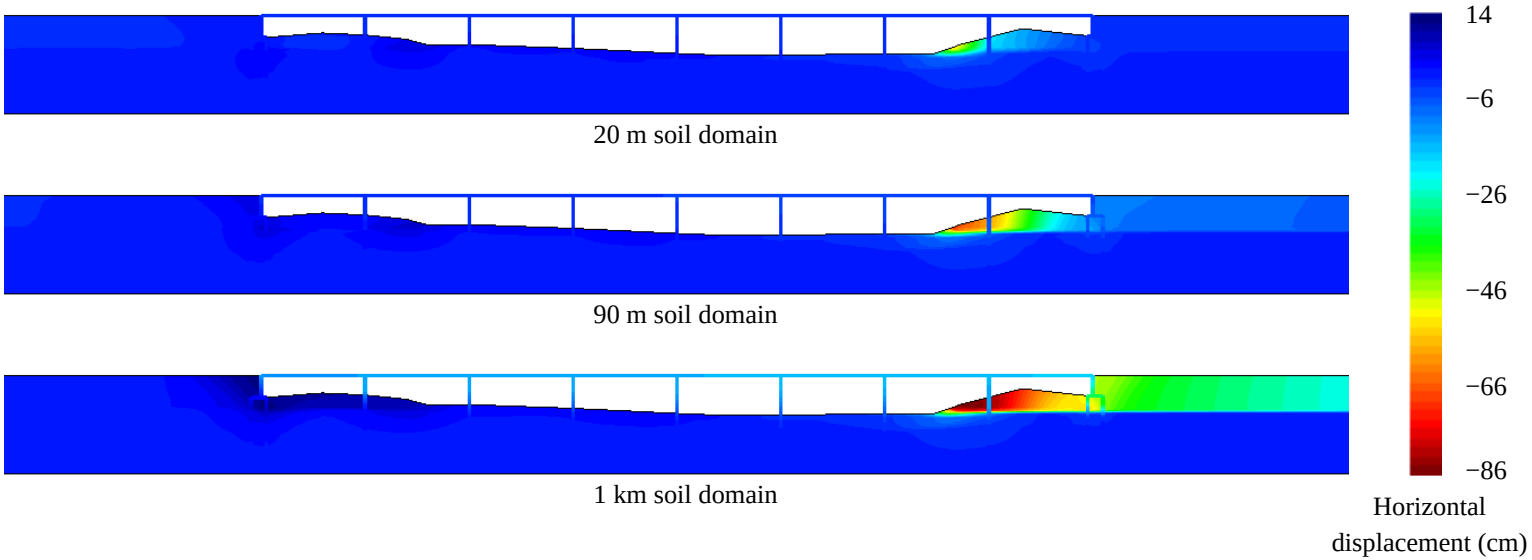

Figure 6.8: Residual displacement field for three soil domain thicknesses.

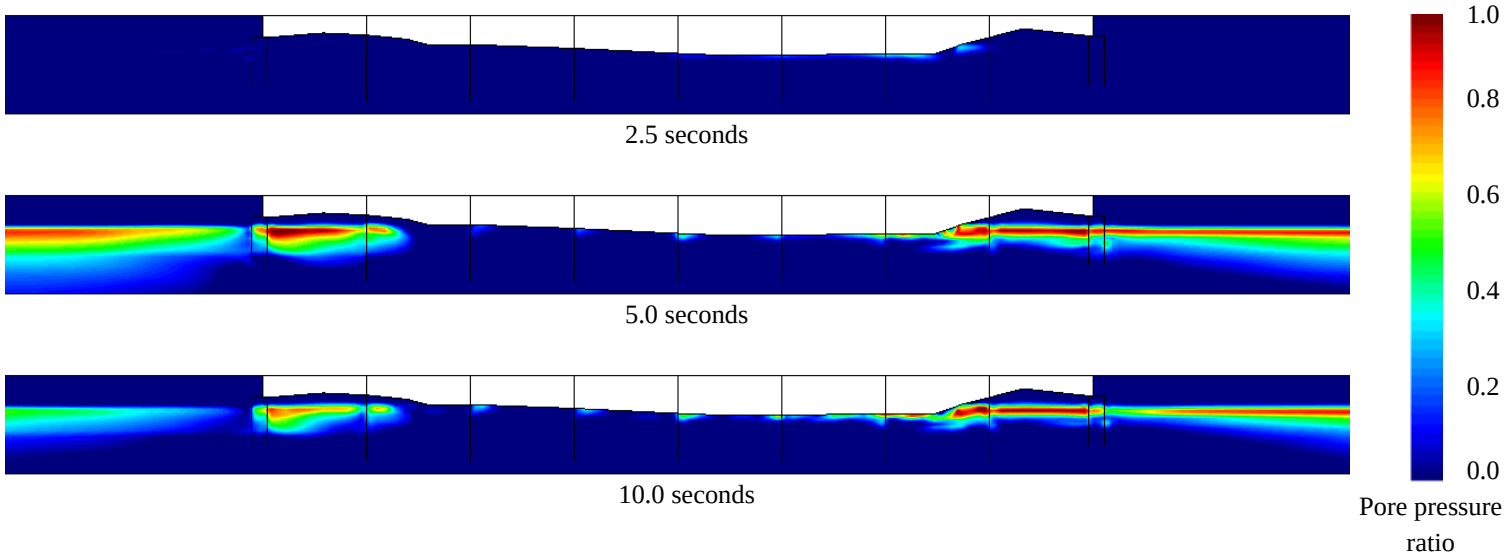

Figure 6.9: Progression of pore pressure ratio during analysis with Gilroy No. 1 motion and 20 m thick soil domain.

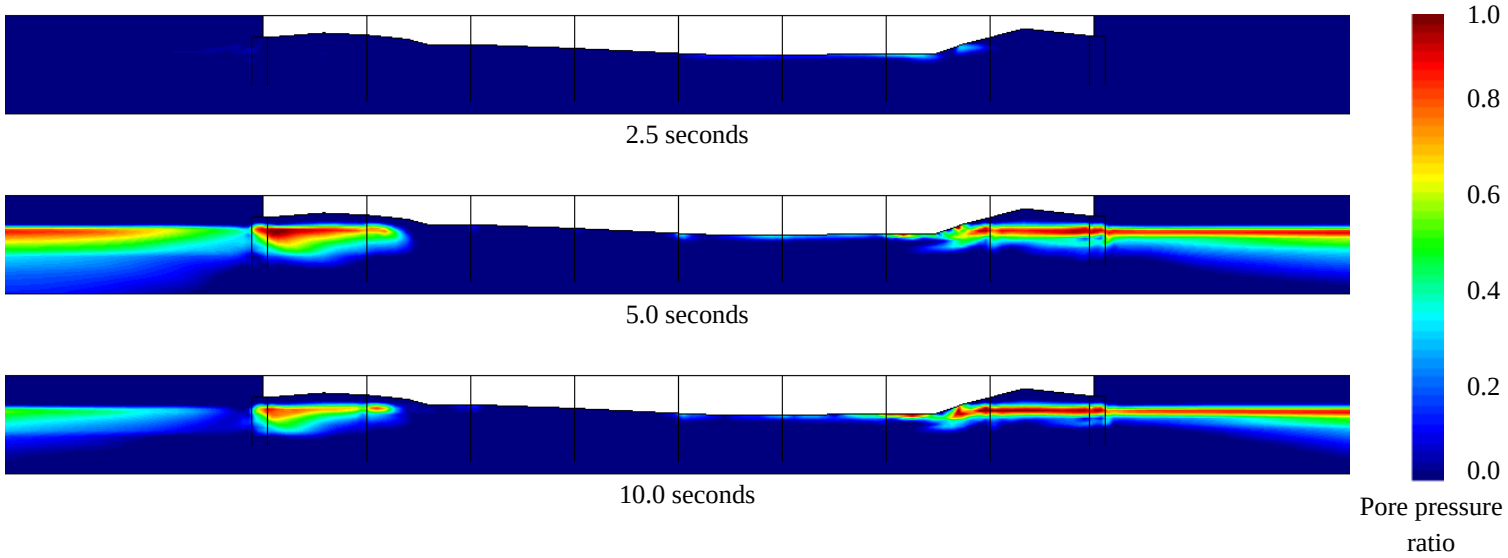

Figure 6.10: Progression of pore pressure ratio during analysis with Gilroy No. 1 motion and 90 m thick soil domain.

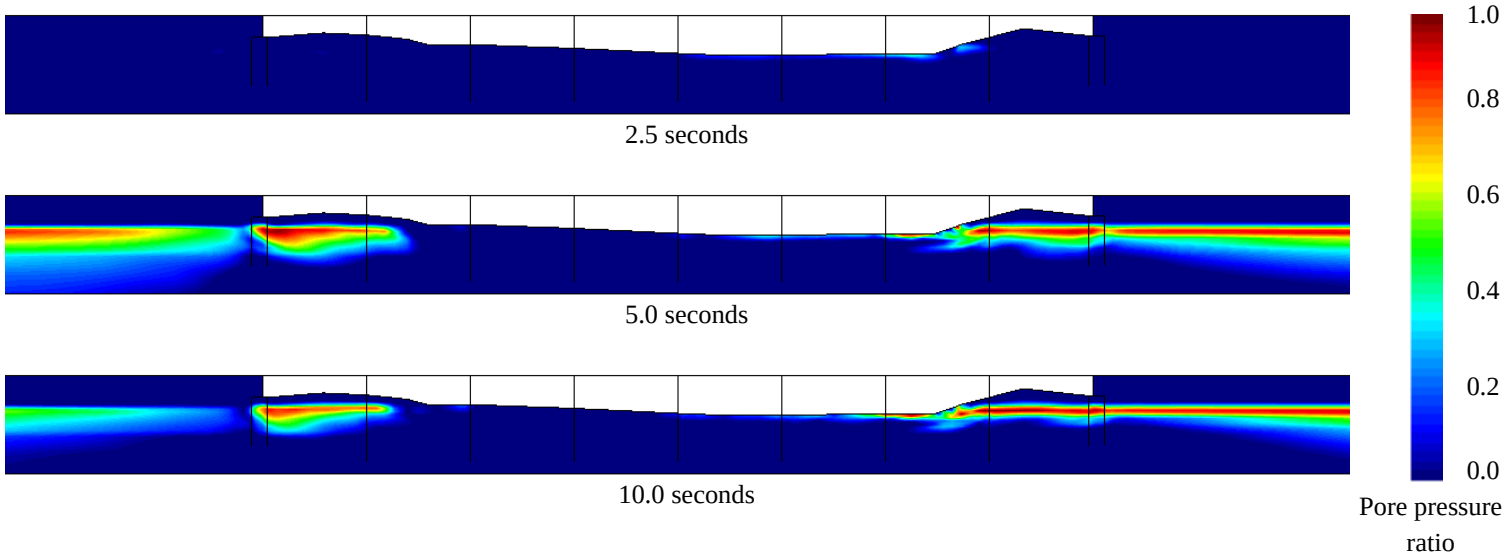

Figure 6.11: Progression of pore pressure ratio during analysis with Gilroy No. 1 motion and 1 km thick soil domain.

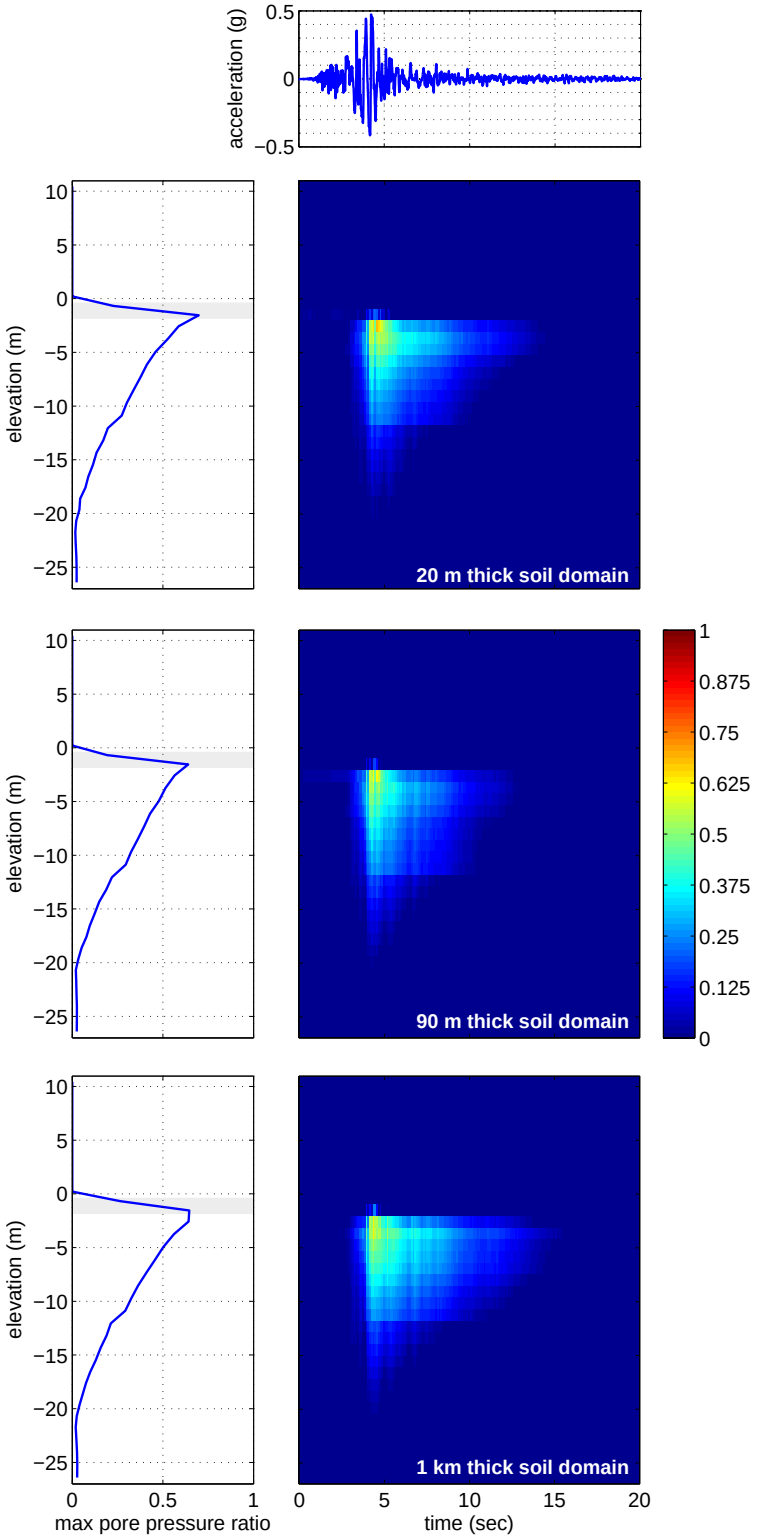

Figure 6.12: Spatial and temporal variation of pore pressure ratio in soil behind northeast abutment for three soil domain thicknesses.

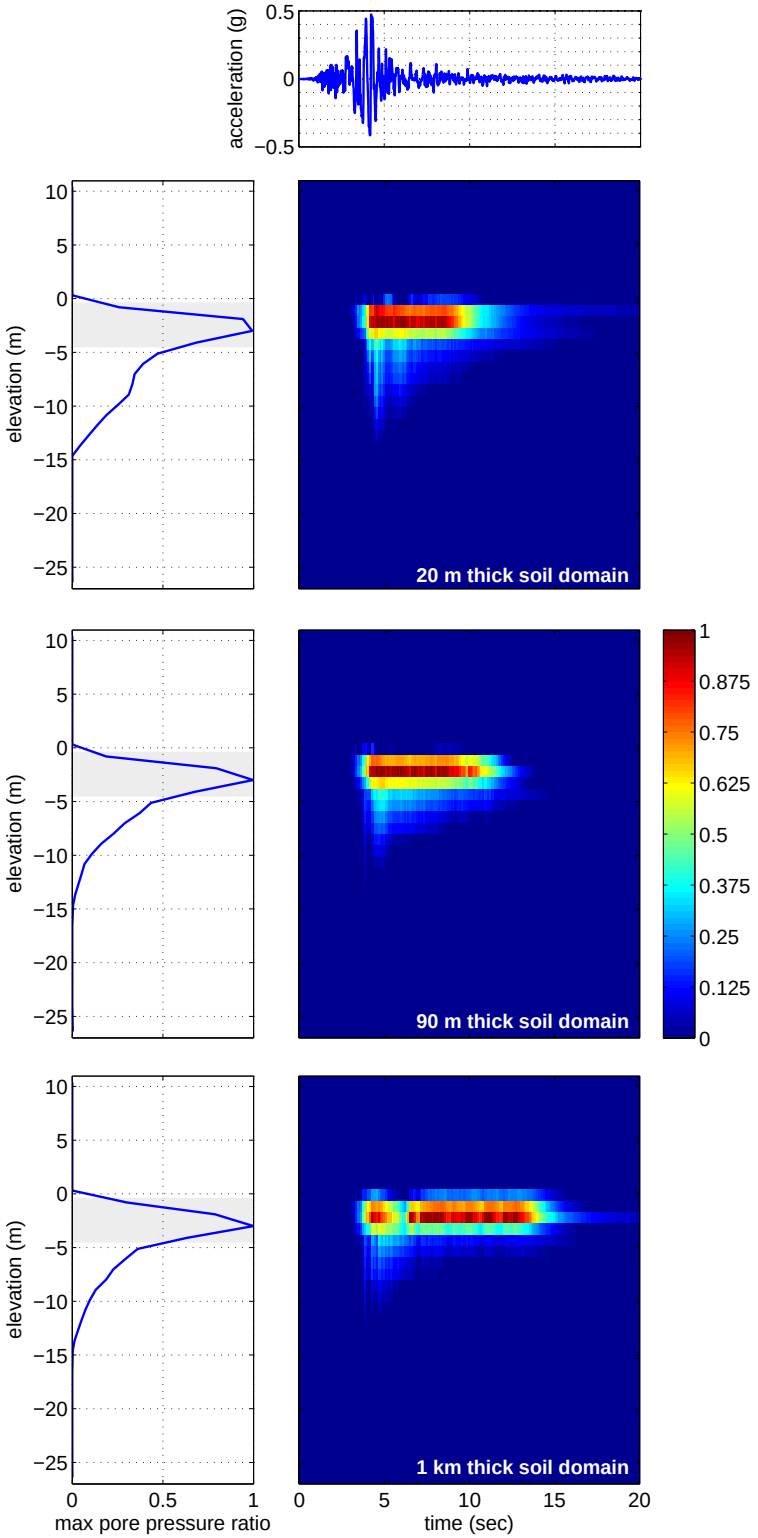

Figure 6.13: Spatial and temporal variation of pore pressure ratio in soil behind southwest abutment for three soil domain thicknesses.

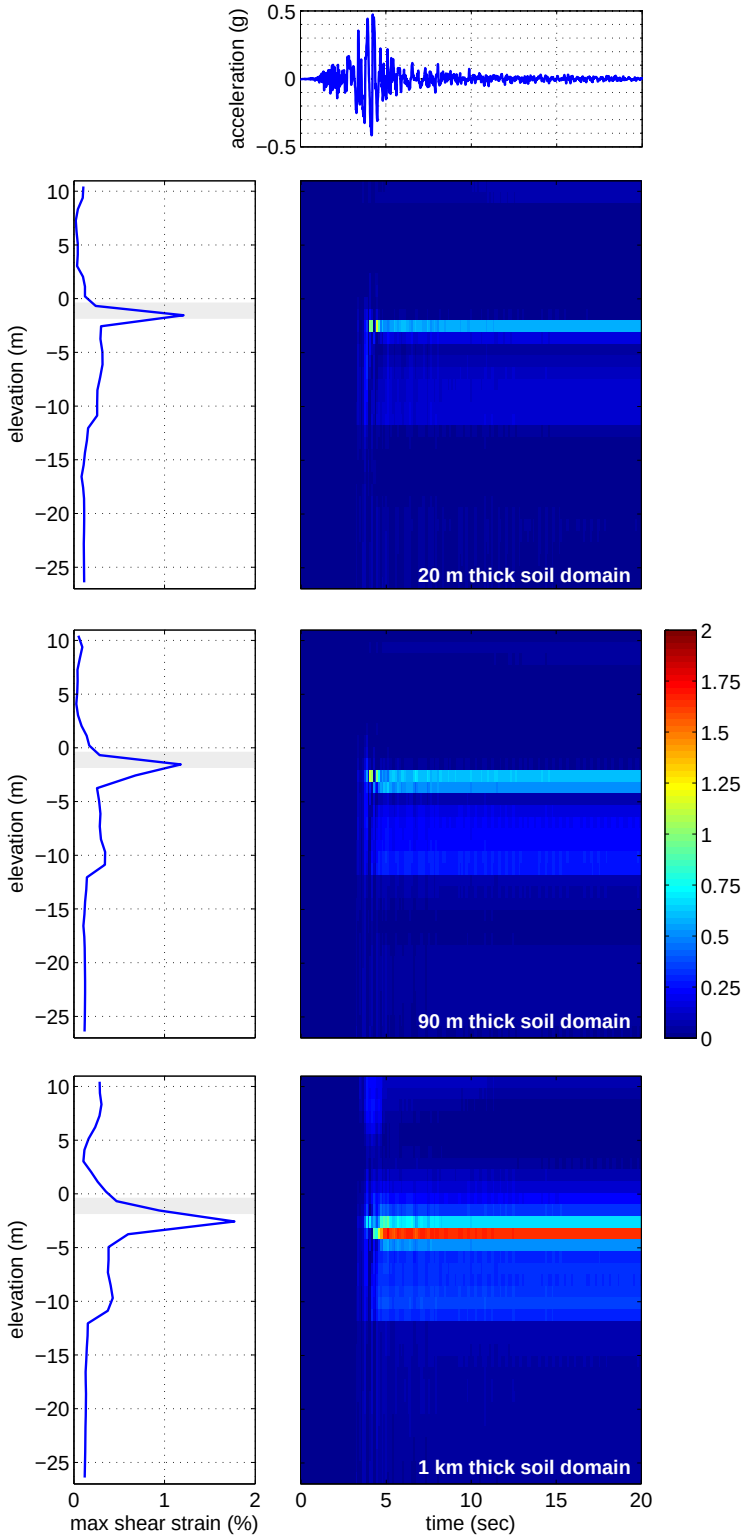

Figure 6.14: Spatial and temporal variation of shear strain in soil behind northeast abutment for three soil domain thicknesses.

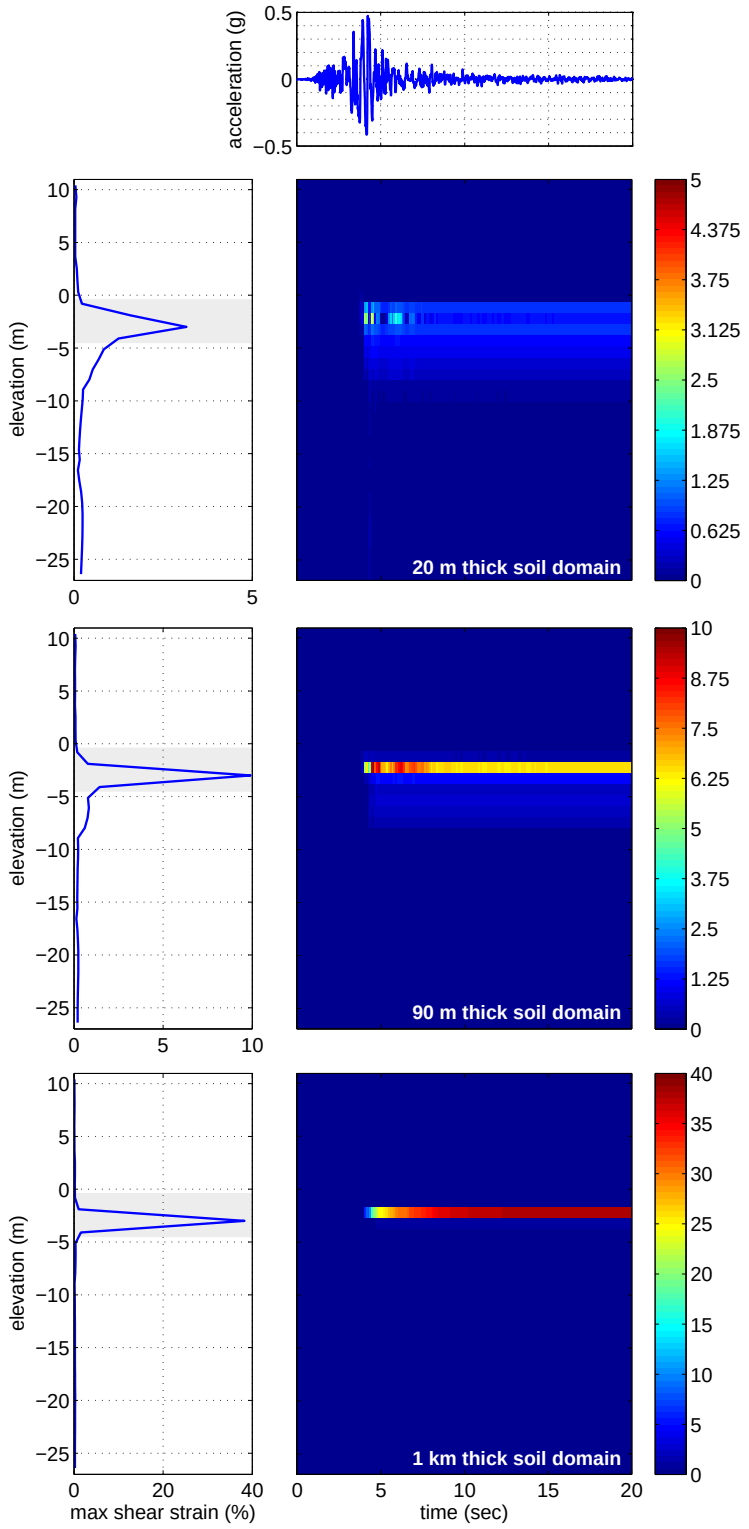

Figure 6.15: Spatial and temporal variation of shear strain in soil behind southwest abutment for three soil domain thicknesses.

7 displays a different bending mechanism that corresponds to the increased soil deformation in the vicinity of this foundation. For all three cases, the bridge deck moves towards the northeast side of the river. The shafts at the northeast abutment are subjected to a combined loading from the liquefaction-induced soil deformation and the bridge deck, resulting in relatively little displacement of the shaft cap.

Figure 6.19 shows the bending moment demands in each shaft foundation for all three soil domain thickness values. These moment diagrams agree with all previous observations, as the larger deformations resulting from increasing the mass of moving soil result in larger bending moments in the foundations. For the Gilroy motion, the model suggests that Pier 7 is likely to fail at the connection to the shaft cap for all three thicknesses, as the bending moment at this location is in excess of the 9 MN·m capacity of the shafts. Failure does not appear to be likely in any of the other foundations for the 20 and 90 m thick soil domains, while it appears that most of the foundations have failed for the 1 km thickness value.

For the geometry of the Puente Mataquito site, the 90 m thick soil domain appears to be the most appropriate choice of the three considered thickness values. Based on the results obtained from this small parameter study, it seems clear that a 1 km thick soil element domain is too large. The embankment and foundation deformations for this case far exceed the observations made at the site, and while this thickness may seem appropriate for the native portion of the soil profile, it is much too large for the embankment. The 20 m and 90 m thick element domains produce similar global results, and it is not immediately apparent from these results which is a better choice for this particular site. While the 20 m thickness accurately portrays the mass of the embankment fill, it may consider an insufficient mass of native soil in comparison to the foundation stiffness given the thickness of the grouped shafts, therefore, the 90 m thickness is selected for use in subsequent analyses.

6.2.3 Effects of Liquefiable Layer Thickness

The residual horizontal soil deformation fields for each liquefiable layer configuration are shown in Figure 6.20. There is a dramatic difference in the displacement magnitude between the three cases, with the larger liquefiable zone leading to significantly larger deformation. Figure 6.21 shows the progression of the pore pressure ratio field in the soil for the thick liquefiable layer configuration. As expected, increasing the scope of the liquefiable zone results in increased liquefaction throughout the soil profile.

The effects of the increased liquefiable zone are also clear in Figures 6.22 and 6.23, which show the variation of pore pressure ratio with depth and time in the soil behind the northeast and southwest

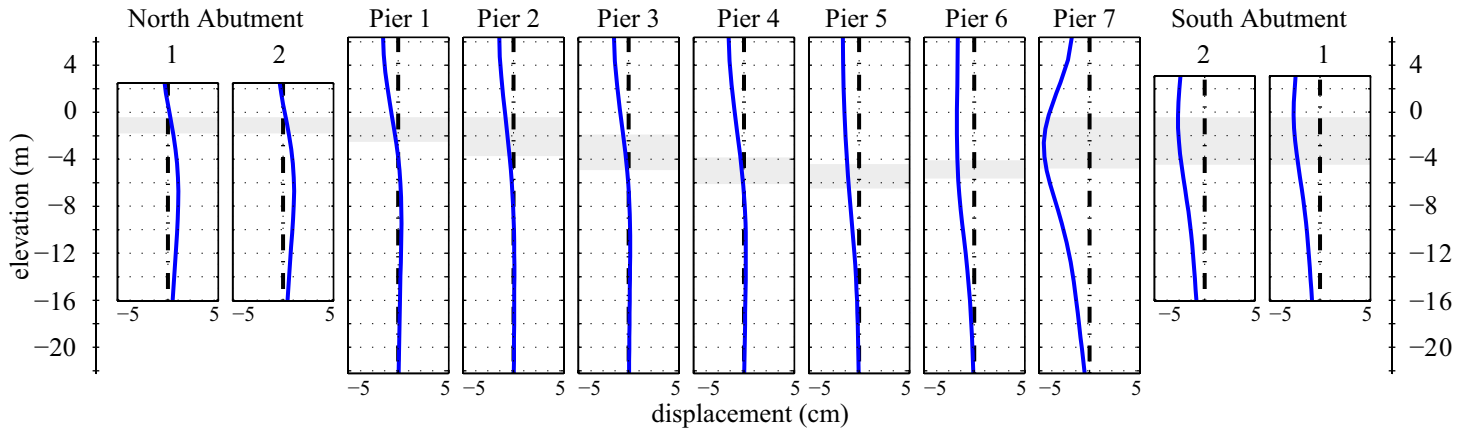

Figure 6.16: Residual shaft displacement profiles for 20 m thick domain.

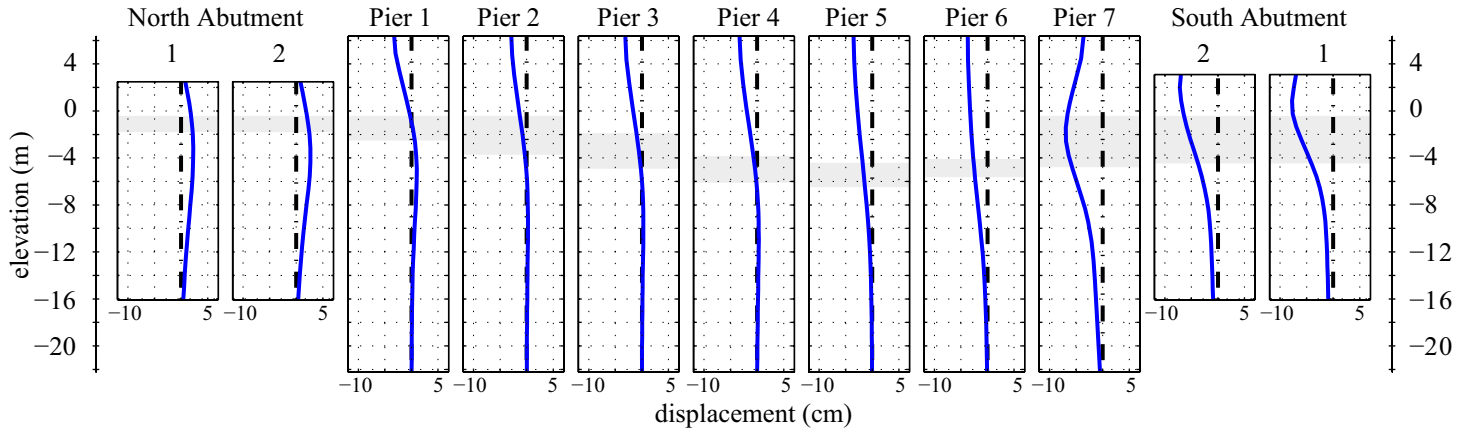

Figure 6.17: Residual shaft displacement profiles for 90 m thick domain.

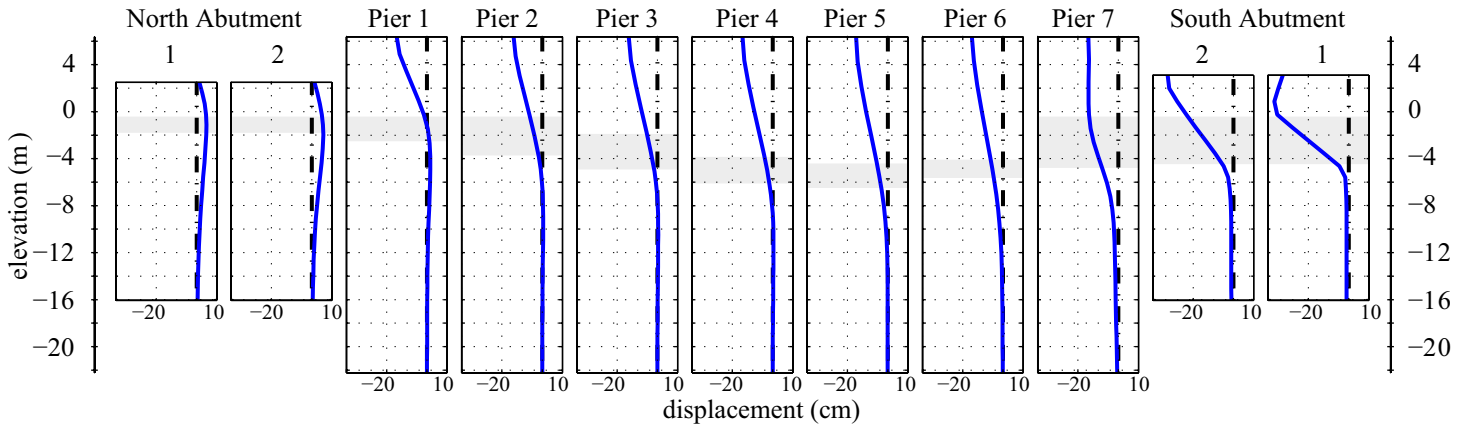

Figure 6.18: Residual shaft displacement profiles for 1 km thick domain.

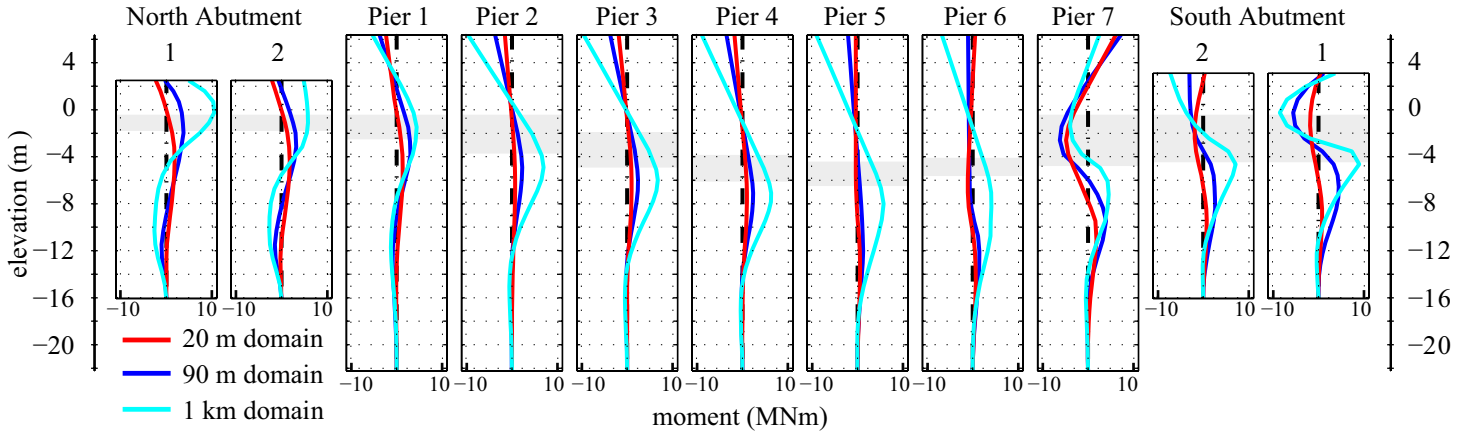

Figure 6.19: Residual bending moment profiles for three domain thicknesses.

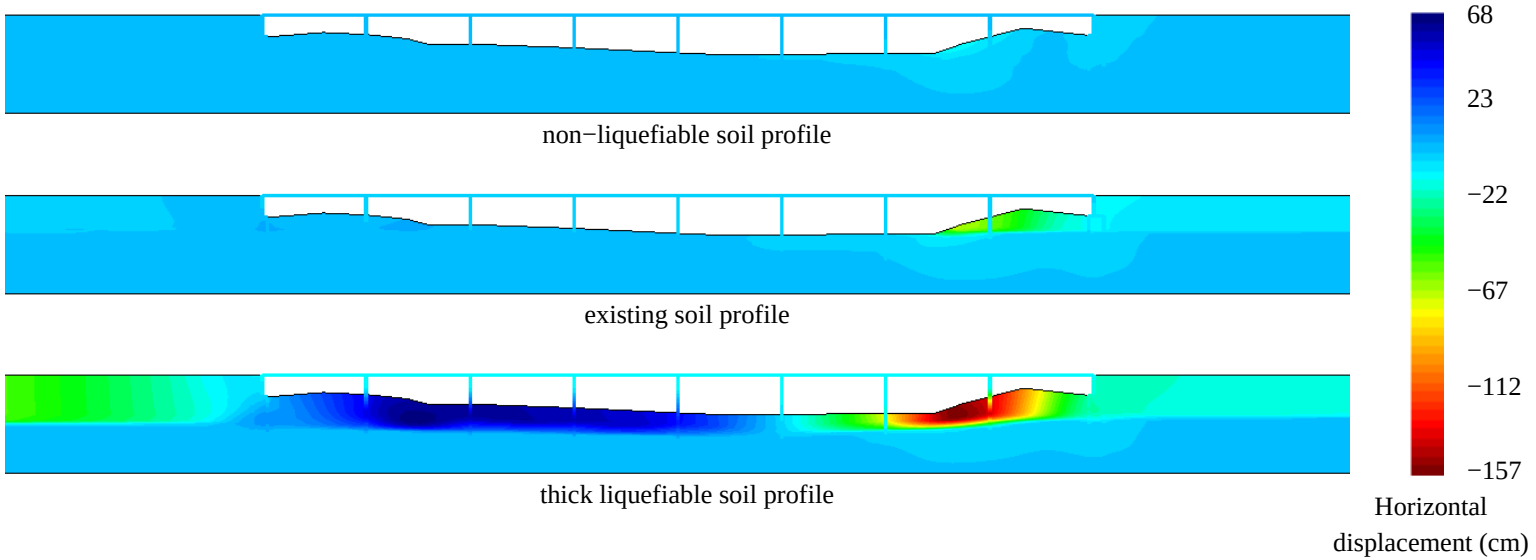

Figure 6.20: Residual displacement field for three liquefaction conditions.

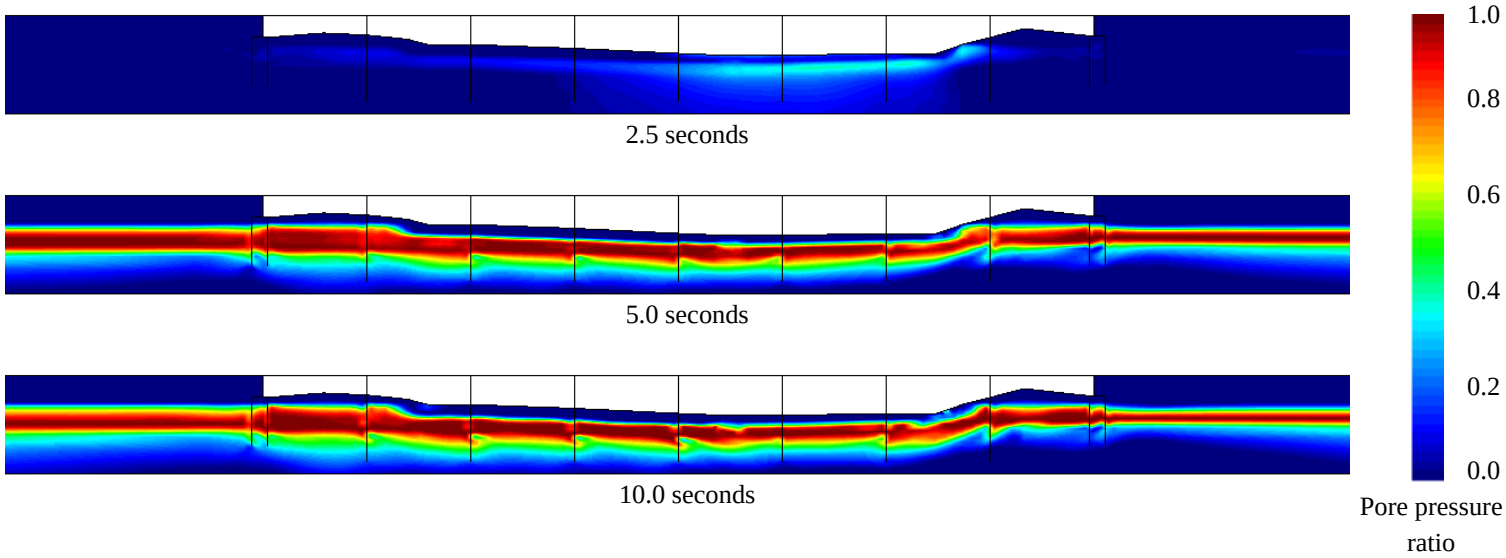

Figure 6.21: Pore pressure ratio field at three time steps during analysis for thick liquefiable soil profile.

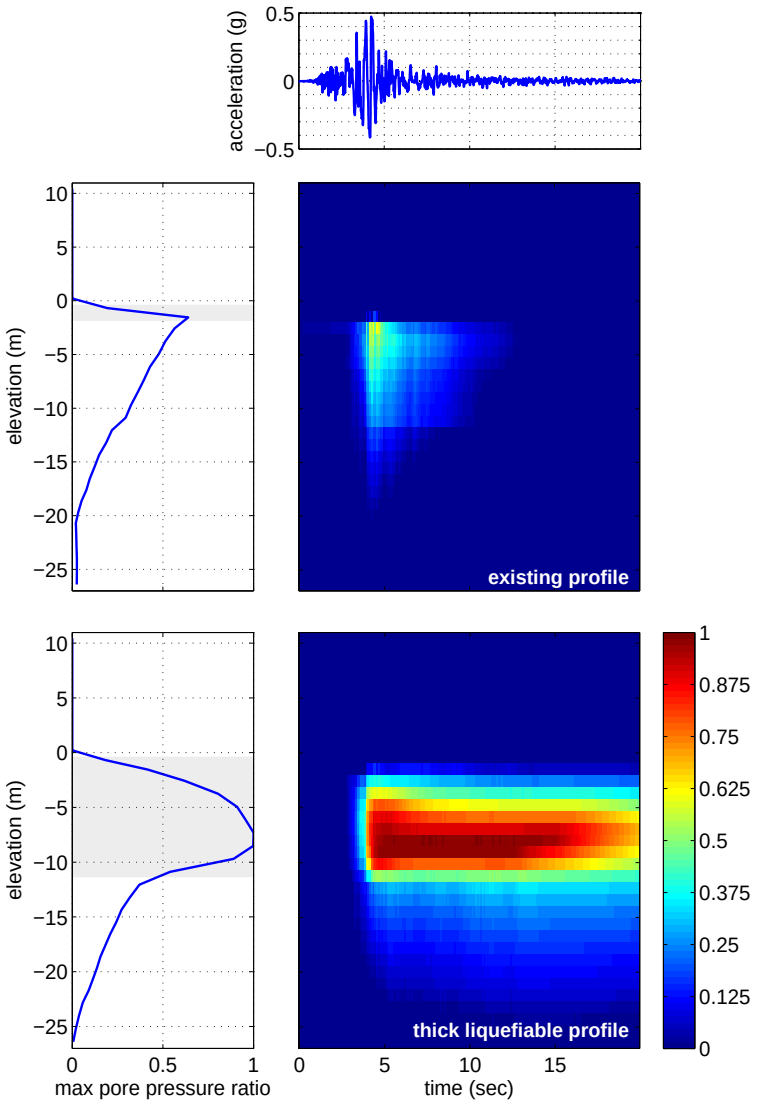

Figure 6.22: Spatial and temporal variation of pore pressure ratio in soil behind northeast abutment for two liquefaction configurations.

abutments, respectively, for the existing and thick liquefiable layer configurations. For the thick liquefaction configuration, the build up of significant excess pore pressure affects a larger amount of the soil profile, especially for the northeast side, and these excess pore pressures take much longer to dissipate. Figures 6.24 and 6.25 show the spatial and temporal variation of shear strain in the same locations behind the abutments for all three liquefiable layer configurations. For both sides, the maximum shear strains increase as the scope of liquefaction is increased. The shear strains on

the southwest side are larger than those on the opposite bank, corresponding to the soil deformation fields shown in Figure 6.20.

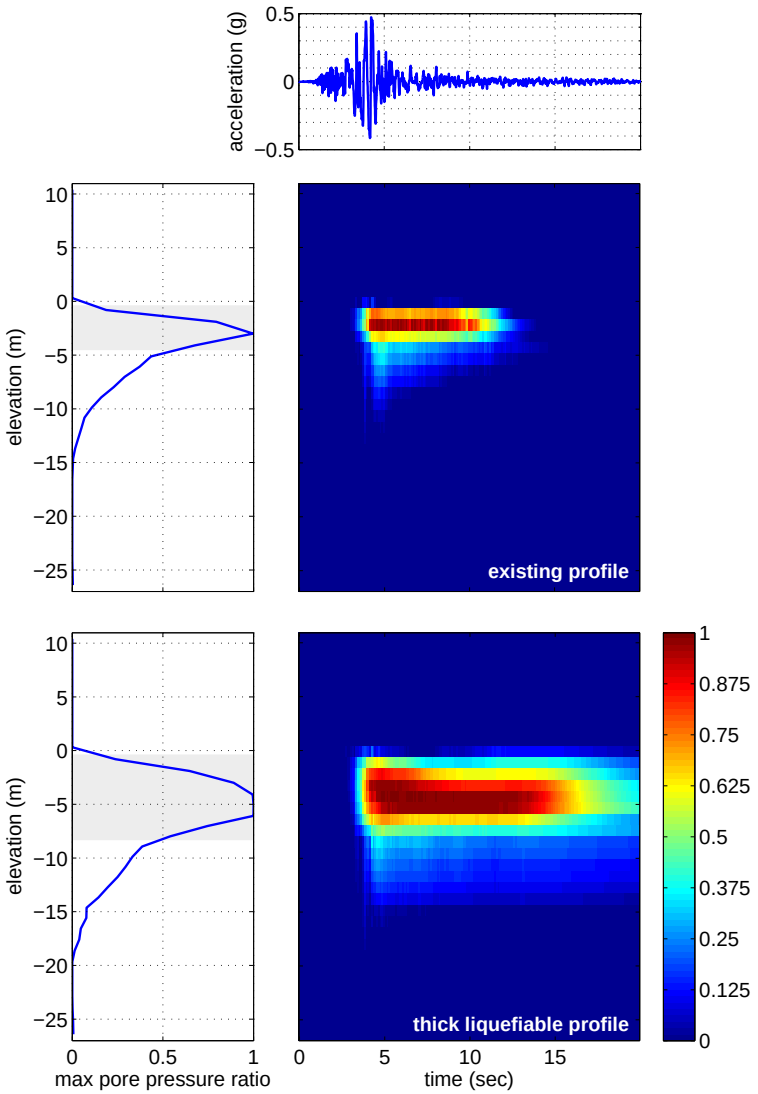

Figure 6.23: Spatial and temporal variation of pore pressure ratio in soil behind southwest bridge abutment for two liquefaction configurations.

Figures 6.26, 6.27, show the residual displaced shapes of the shaft foundations for the non-liquefiable and thick liquefiable layer configurations. Figure 6.17 shows the corresponding results for the existing liquefiable layer configuration. In the absence of liquefaction, the shaft deformations are relatively small, with a maximum value of 2.6 cm in Pier 7 and shaft cap displacements of

approximately 2.0 cm at each abutment. Very large shaft deformations are returned for the thickened liquefiable layer configuration. For this case, the southwest abutment shaft cap translates 19 cm towards the river, pushing the bridge deck in the same direction and causing the northeast shaft cap to move 5.5 cm away from the river. The interior piers are severely deformed with the thick configuration, and as shown in Figure 6.28, based on the bending moment demands in the shafts, failure or near-failure is predicted for all of the bridge foundations.

Based on the results for the three considered liquefiable layer configurations, it appears the layer configuration used in the idealized soil profile best represents the Puente Mataquito site response. The soil deformation in the absence of liquefaction is too minor in comparison to the site observations, while the shaft bending demands and deformations are too severe for the thickened liquefaction configuration. This small parameter study provides confidence that the idealized soil profile adequately describes the soil conditions at for the case study site.

6.3 Dynamic Plane Strain Analysis: Convento Viejo Ground Motion Record

The response of the Puente Mataquito soils to the Convento Viejo ground motion record are examined in order to gain an understanding of how the site may have responded during the Maule earthquake. It is important to establish whether or not the model predicts liquefaction to occur for this motion, and to determine the consequences of liquefaction if it does occur. This initial numerical study is used, along with the observations made during post-earthquake reconnaissance at the site, to inform the remainder of the numerical work for Puente Mataquito.

6.3.1 Global Soil Response

The residual soil deformation profiles are assessed to determine if the model predicts the development of lateral spreading due to the Convento Viejo motion. Figure 6.29 shows the residual horizontal and vertical displacement fields that exist after the ground motion has been applied to the model. As shown, the large horizontal soil deformation (> 3.0 m) occurs between the two abutments on the banks of the river and along the river bed. In comparison, relatively little horizontal deformation occurs behind the abutments, indicating that the bridge deck and foundations provided sufficient restraint. The residual vertical deformation is more uniform over the soil domain shown in Figure 6.29, with approximately 30 cm of downward displacement at the top of the embankment fill behind each abutment. The largest vertical deformations occur on the slopes of the river bank, and the horizontal and vertical soil deformation here causes the uplift of material on the southwest river bed.

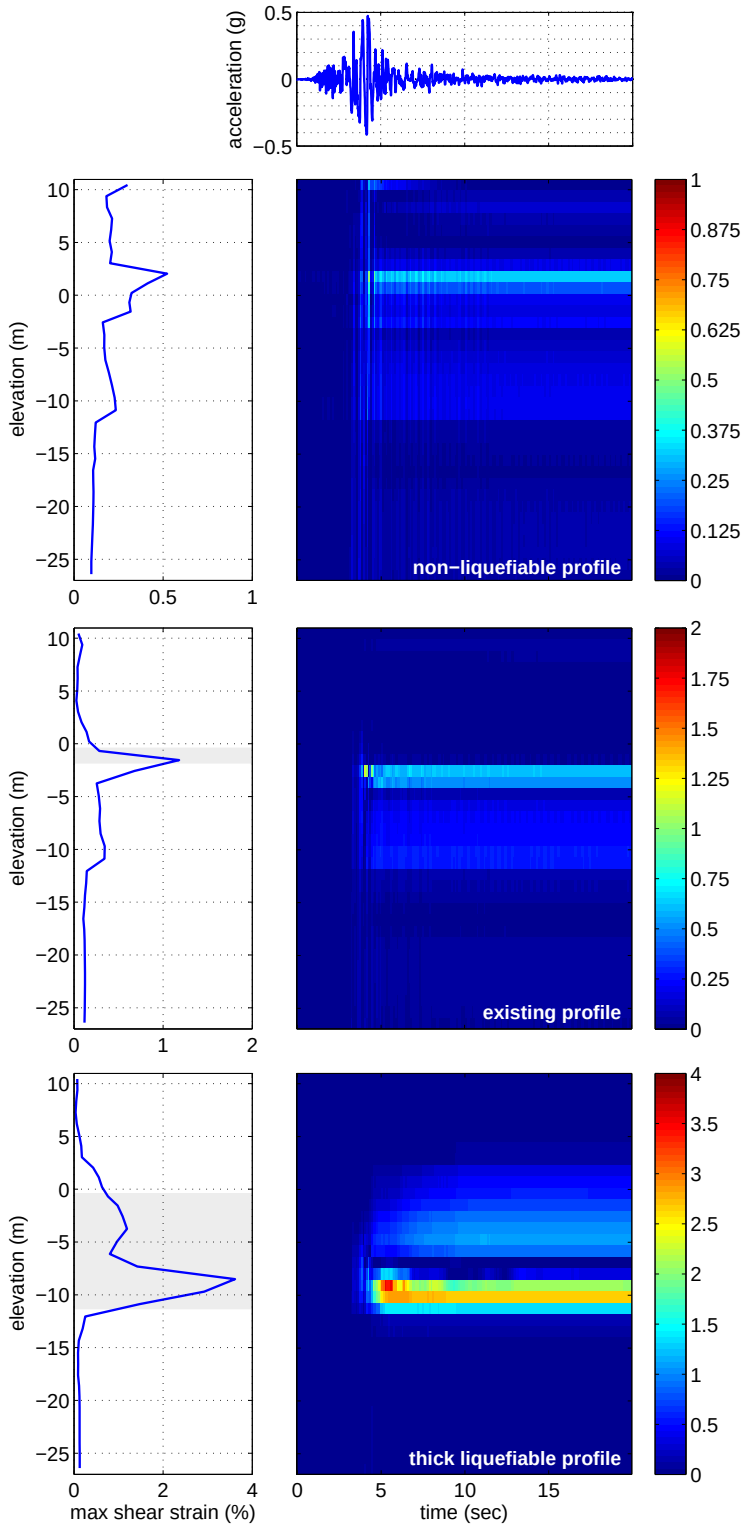

Figure 6.24: Spatial and temporal variation of shear strain in soil behind northeast abutment for three liquefaction configurations.

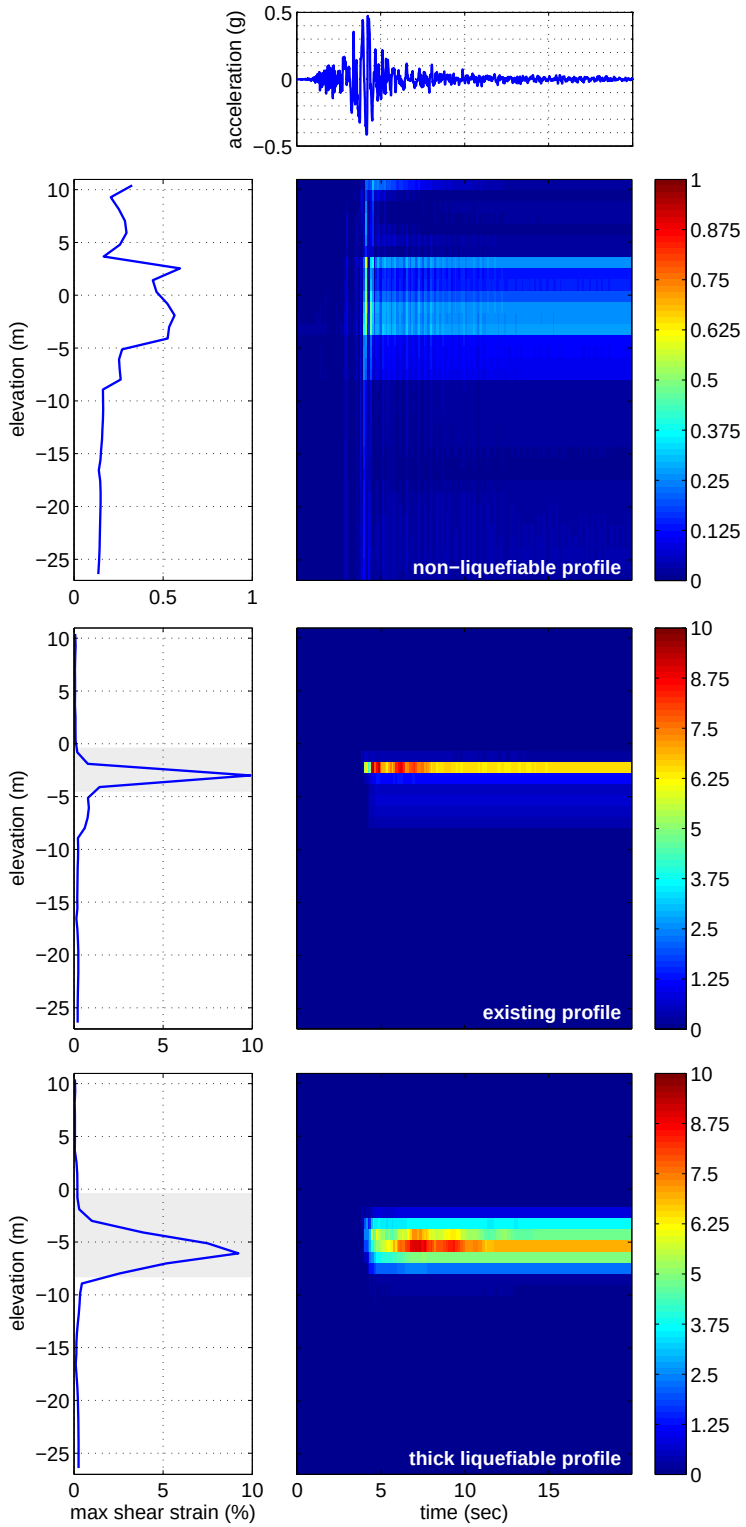

Figure 6.25: Spatial and temporal variation of shear strain in soil behind southwest abutment for three liquefaction configurations.

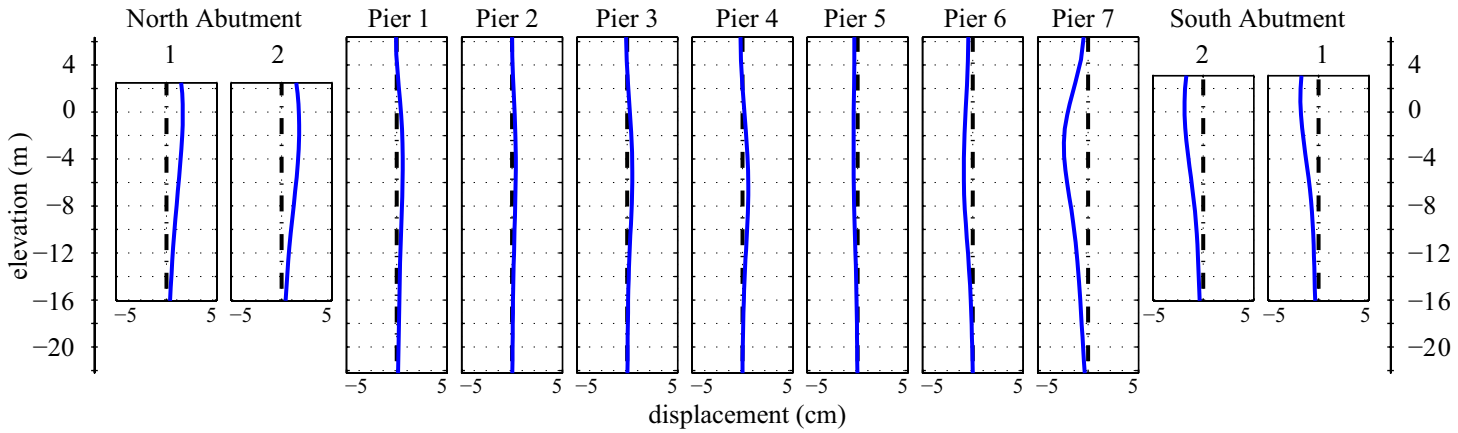

Figure 6.26: Residual shaft displacements for non-liquefiable soil profile.

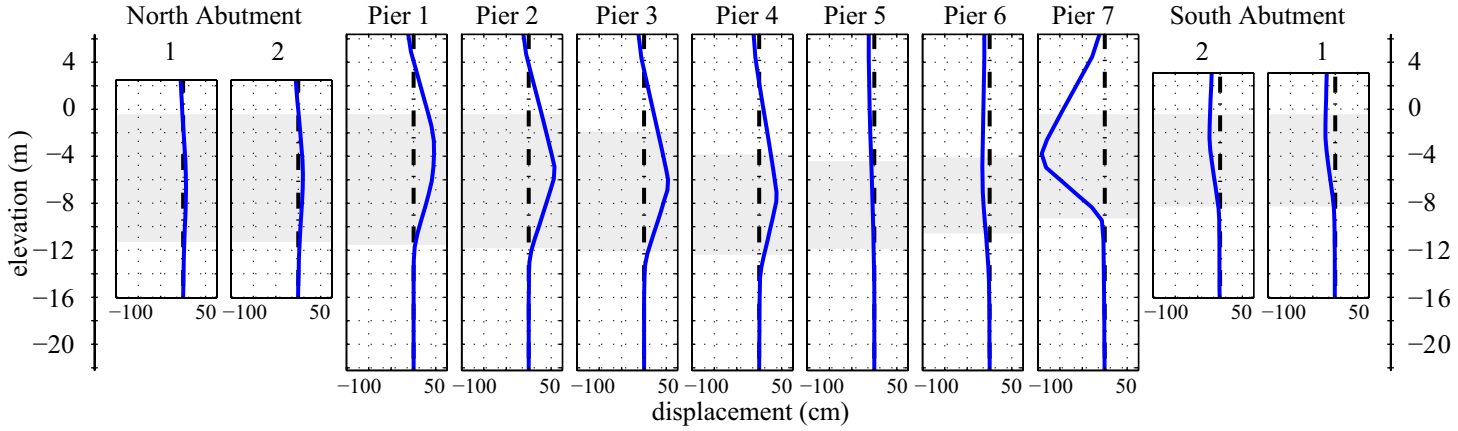

Figure 6.27: Residual shaft displacements for thick liquefiable soil profile.

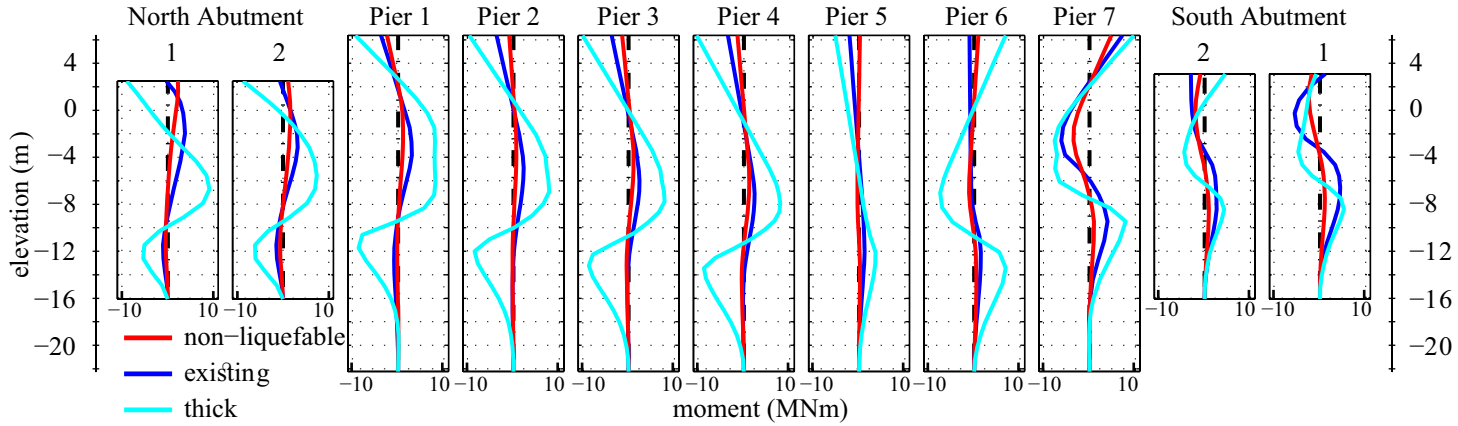

Figure 6.28: Residual bending moment profiles for three liquefaction conditions.

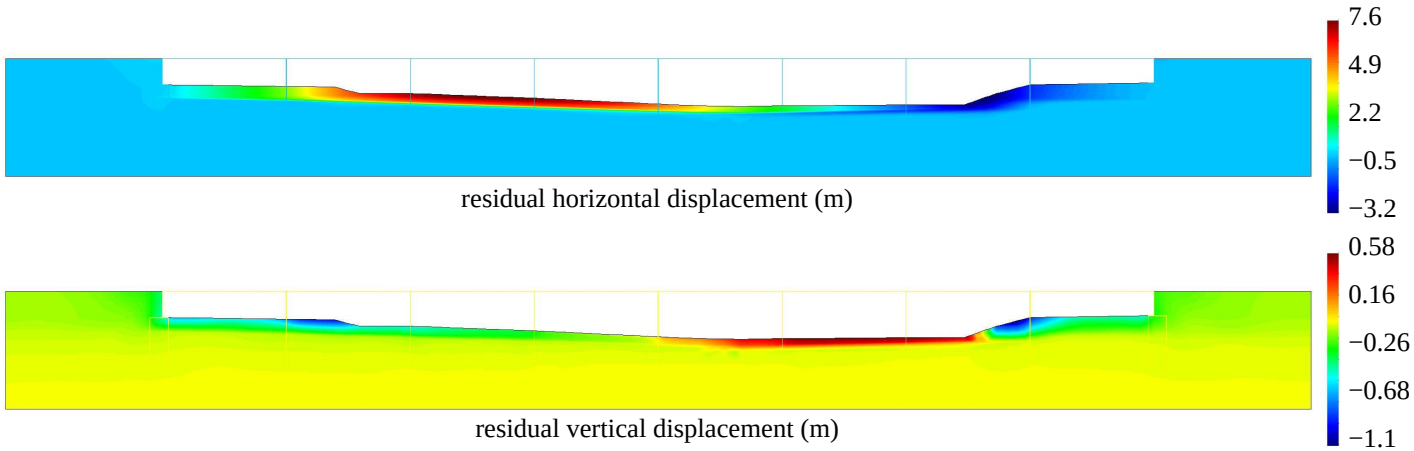

Figure 6.29: Residual horizontal and vertical displacement fields.

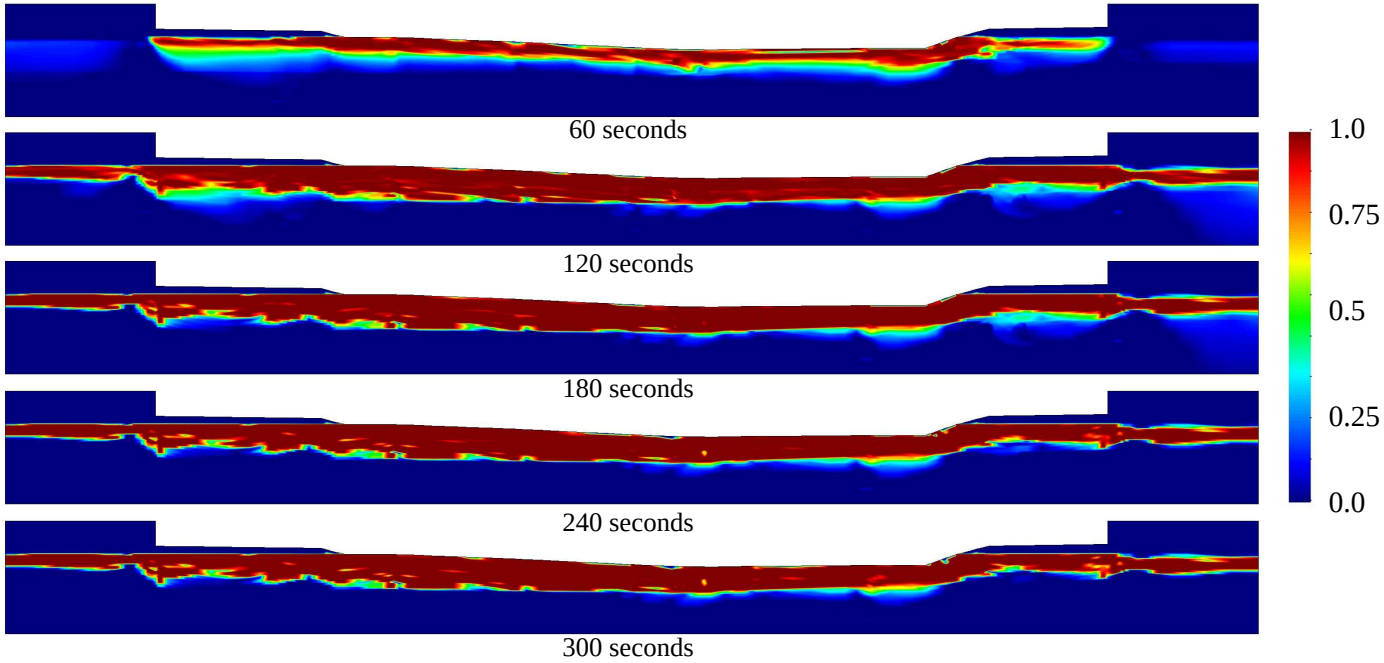

Figure 6.30: Progression of pore pressure ratio during analysis with Convento Viejo Motion.

The residual deformation profiles of Figure 6.29 suggest that lateral spreading has occurred due to liquefaction-induced loss of strength in the underlying soils, however, an examination of the pore pressure response in the soil is necessary to confirm this observation. Figure 6.30 shows a sequence of pore pressure ratio profiles during the application of the Convento Viejo motion. After 60 s, the material along the river bed has reached pore pressure ratios at or near 1.0, indicating that excess pore pressure has become approximately equal to the mean effective stress, and little strength remains in this region. At 120 s, the liquefiable material below the approach embankments display pore pressure ratios indicative of liquefaction, and this pore pressure ratio profile remains essentially constant for the remainder of the motion. Figure 6.31 shows the progression of horizontal soil deformation over the first 180 s of the motion. Lateral deformation between the abutments gradually increases over this portion of the motion, and essentially reaches a steady state value after 180 s with very little change over the remaining duration.

The pore pressure response of Figure 6.30 demonstrates a flaw in the modeling approach for this site and ground motion. When the elements in the liquefiable loose sand layer reach a strength state corresponding to $r_u \approx 1.0$, the elements deform such that the excess pore pressure does not dissipate as would be expected after the conclusion of the strong shaking in the ground motion record. The cause of this behavior is likely due to the numerical difficulty in capturing the build-up of excess pore pressure and corresponding soil shear strength loss due to the large number of high frequency cycles present in the Convento Viejo ground motion record. The results obtained using the Gilroy No. 1 record, which has a considerably lower frequency content, do not display this type of response for the same site geometry and element formulations. Additionally, this behavior is not isolated to the Q1-P1ssp element, as a secondary analysis using a standard Q1-P1 element displays a similar response.

The consequences of this undesirable element response are relatively minor in terms of the desired outcomes for this study. The absence of pore pressure dissipation likely increases the magnitude of the residual displacements in the model, however, the trends shown in the results are still valid. A soil deformation pattern and pore pressure response indicative of liquefaction-induced lateral soil deformation (lateral spreading) is evident in the results of Figures 6.29 through 6.31. Large lateral displacements in the soil in and adjacent to the river, and vertical slumping of the embankments are predicted by the model, corresponding with observations made at the site. Details of the response in the foundations and adjacent embankment fill obscured in this global view of the results are examined following discussion of the global structural response for the bridge.

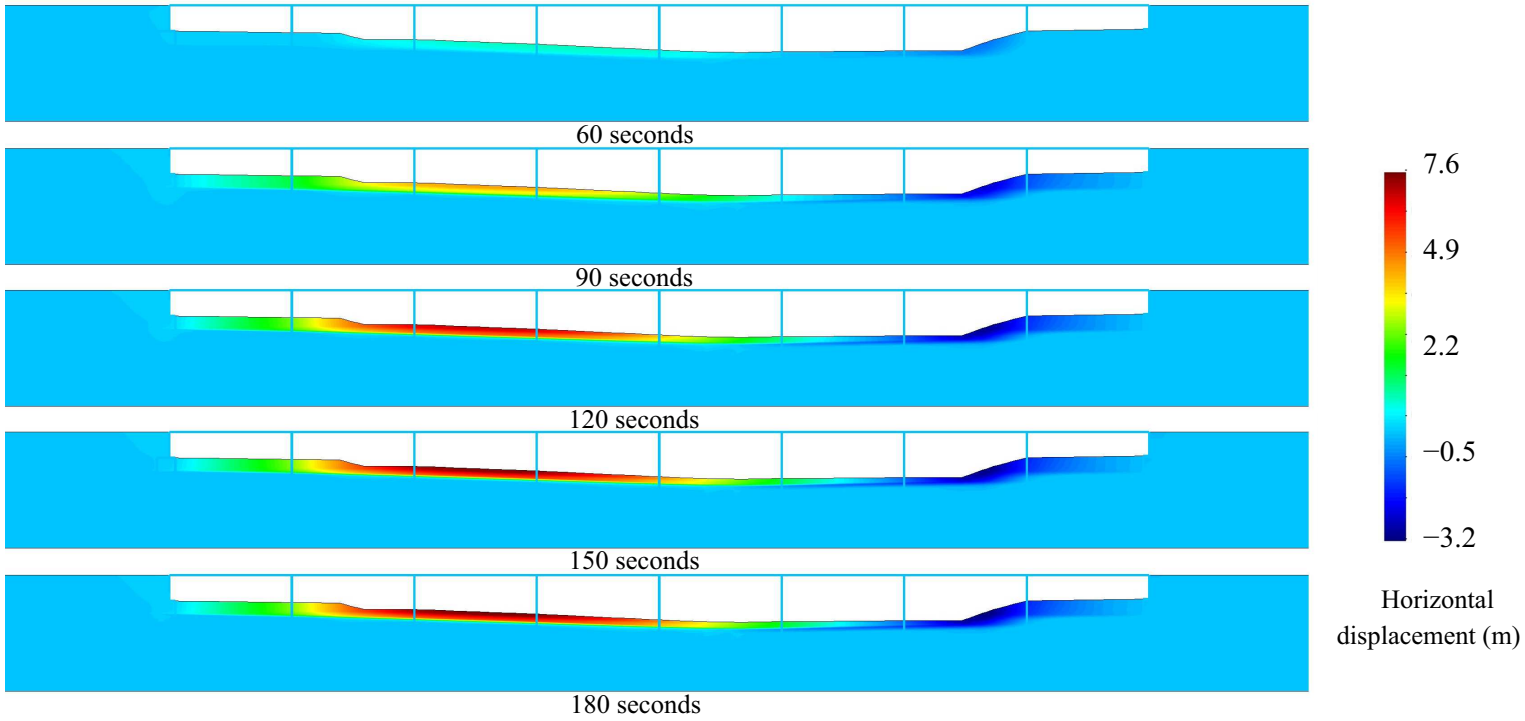

Figure 6.31: Progression of horizontal displacement during analysis with Convento Viejo motion.

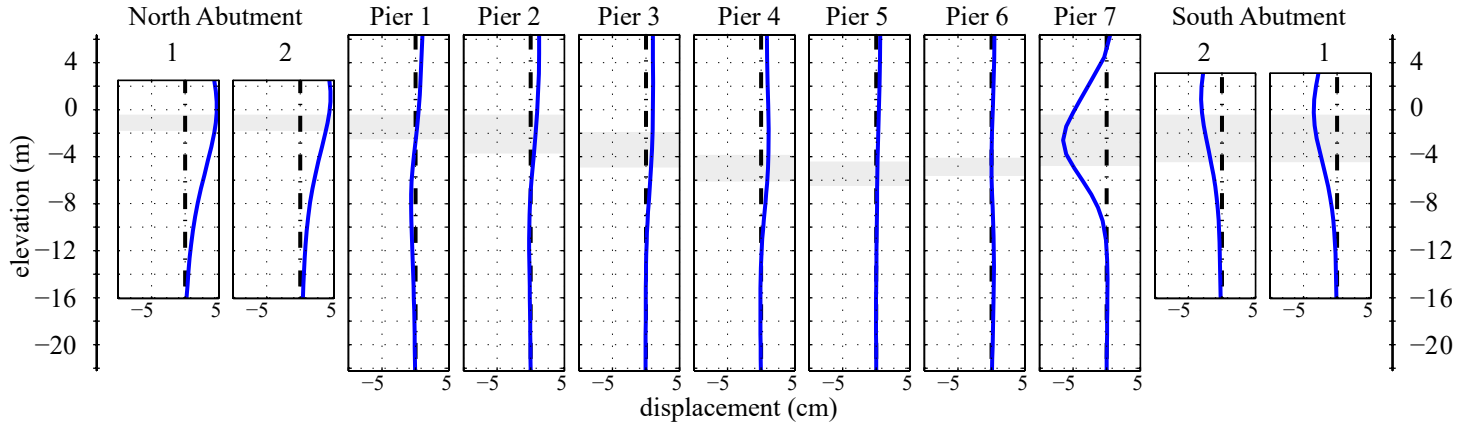

Figure 6.32: Residual shaft displacement profiles.

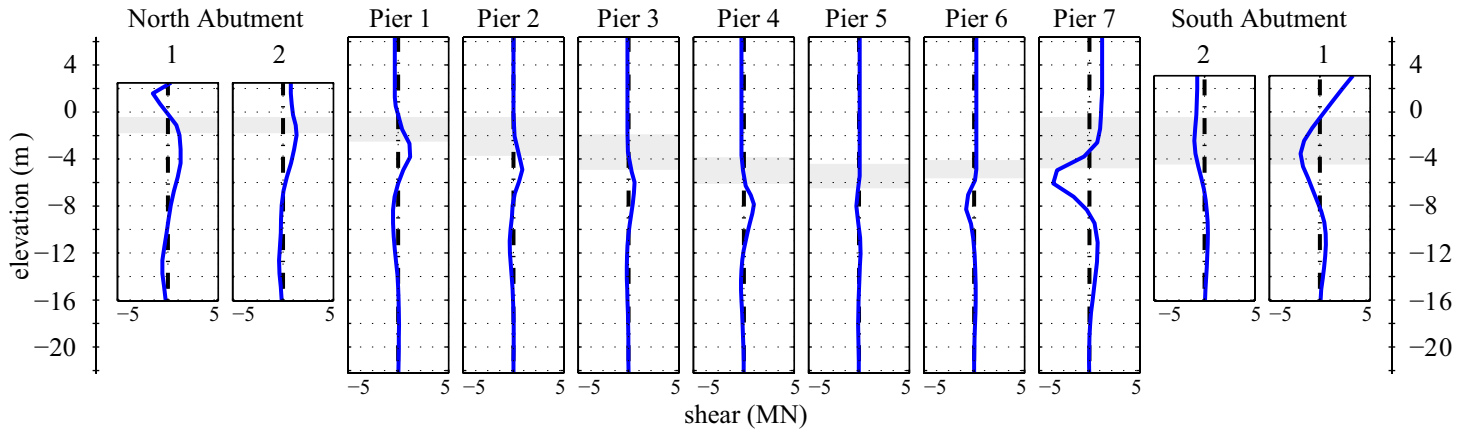

Figure 6.33: Residual shaft shear force profiles.

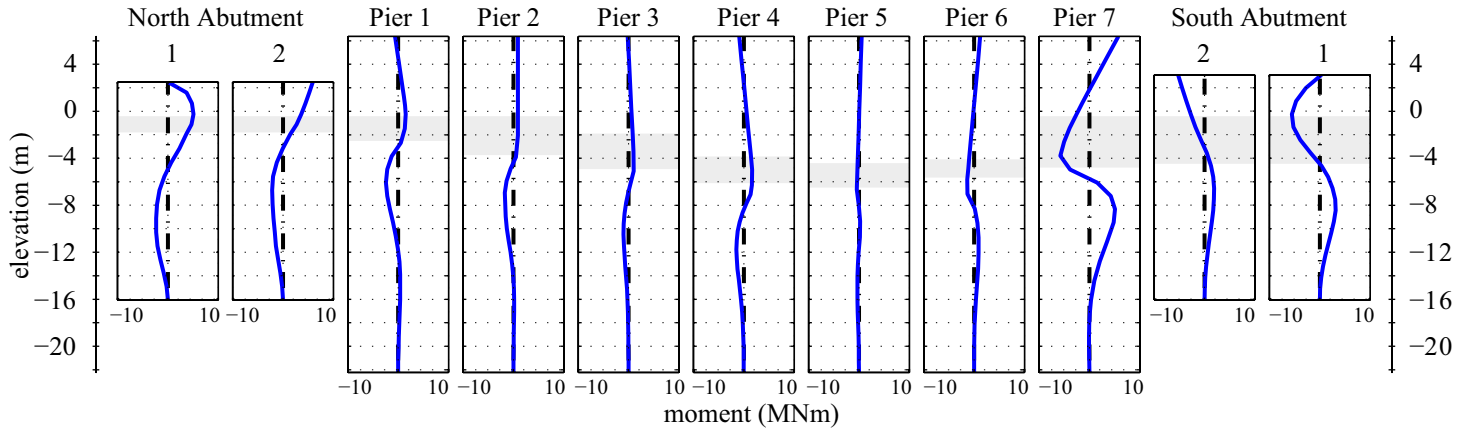

Figure 6.34: Residual shaft bending moment profiles.

Table 6.2: Maximum in-span displacement, shear force, and bending moment demands in abutment shaft foundations for Convento Viejo analysis.

shaft group	max disp (cm)	max shear (MN)	max moment (MN·m)
north abutment 1	4.7	1.5	5.1
north abutment 2	4.5	1.3	5.2
south abutment 1	3.5	1.0	5.3
south abutment 2	3.1	1.9	5.5

6.3.2 Global Structural Response

The build-up of excess pore pressure and subsequent soil deformation observed in Figures 6.29 through 6.31 place kinematic demands on the bridge abutments and embedded shaft foundations. The residual displaced shapes of the shaft foundations for the bridge are shown in Figure 6.32, arranged to correspond with the spatial location of each pier and abutment shaft. The corresponding shear force and bending moment demands are shown in Figures 6.33 and 6.34. The extents of the liquefiable loose sand layer at each location are shown in gray in these plots. Though the soil deformation on the northeast bank is larger, Pier 7 displays the largest displacement demand of the interior piers. This makes sense in the context of the soil profile, as the large soil deformations on the northeast bank are shallow, indicating that the soil can flow around the piers, while the soil deformation on the southwest bank extends deeper and thus engages more resistance from the embedded foundation.

The abutments have similar maximum residual displacements, 4.7 cm at the northeast abutment and 3.5 cm at the southwest abutment, though slightly different mechanisms appear to govern their response. The shaft cap at northeast abutment tends to displace purely in a horizontal manner with only minor rotation, while the southwest shaft cap shows more rotation due to resistance from the bridge deck. These observations, along with the deformation patterns for the interior piers, which all exhibit positive displacement at the top, show that the entire bridge is translating in the positive x-direction (to the right in the plots). The moment and shear demands in the abutment shaft foundations are also reasonably similar, though, as shown in Table 6.2, the maximum in-span shear and moments are somewhat larger on the southwest side.

The observed shaft displacements correlate well with observations made at Puente Mataquito. Deformation of the northeast abutment was assumed to be around 5 cm based on superficial concrete cracking/spalling, and shear cracks in the cap for Interior Pier 1 suggest the river-ward displacement

of this foundation. Measurable or visible deformation of the southwest abutment was not noted, however, displacement could have occurred without visible damage. The rotation of the southwest abutment observed in the model could also have reasonably occurred without attendant damage. Overall, it is encouraging that the trends observed in the plane strain model correlate roughly with observations made during the reconnaissance effort.

6.3.3 Abutment and Embankment Response

It is of interest to examine the response of the soil near the abutment foundations more closely in order to confirm observations made at the global level. Of particular interest is to assess the evidence of lateral spreading and associated embankment failure that may be obscured by the magnitude of the soil deformation along the river. Figure 6.35 shows the variation of pore pressure ratio with depth over the course of the motion in the soil behind the two abutments. Figures 6.36 and 6.37 show the spatial and temporal variation of shear strain behind the northeast and southwest abutments, respectively. As shown in these plots, nearly half of the higher amplitude portion of the motion has elapsed before significant excess pore pressure begins to develop, with larger shear strains developing 10 to 20 s after the onset of liquefaction. As expected, the largest shear strains are found at the boundary of the liquefiable loose sand and denser sand layers.

To assess how the pore pressure ratio and shear strain profiles shown in Figures 6.35 through 6.37 are manifested as soil deformation, the displacement fields near the abutments are computed and plotted in Figure 6.38. In this plot, the size and color of the vectors indicate magnitude, and the directions of the vectors correspond with the direction of displacement. As shown, the primary component of embankment deformation is downward, and significant horizontal deformation is limited to the immediate vicinity of the abutment wall. Each of these displacement fields suggest the formation of a failure surface in the embankment, especially if the deformation in front of the abutments is considered as a part of the failure mass.

6.4 Summary

Two small parameter studies performed using the Gilroy No. 1 ground motion record have demonstrated the effects of soil element thickness and liquefiable layer configuration on the response of the Puente Mataquito plane strain model. This work has established the importance of defining a soil domain that has sufficient mass in comparison to foundation stiffness, and determined that for the site conditions used in the model, a 90 m thick soil domain appeared to be the most applicable definition for the continuum elements in this model. This work also verified that the liquefiable layer

definition assumed in the idealized soil profile appropriately reflects the site conditions based on a comparison of the results in the model with observations made at the bridge site.

The results of the Convento Viejo analysis establish the susceptibility of the site to liquefaction for a ground motion that is representative of that experienced by the bridge, demonstrate that the plane strain model is able to predict trends that correspond to physical observations made at the site, demonstrate some of the mechanisms leading to liquefaction and lateral spreading, and reveal the consequences of these phenomena. Based on these results, both bridge abutments appear to be strong candidates for future study using a combination of the pile pinning approach and a 3D finite element model, but since only one will be considered, the southwest abutment is selected for further inspection. Both the Gilroy and Convento Viejo analyses predict liquefaction and attendant lateral soil deformation at this location, and the Convento Viejo analysis reveals a more interesting deformation mechanism with the rotation of the shaft cap observed at the southwest abutment. The interaction of the bridge deck, abutment walls, and shafts during lateral spreading has been identified as an important factor in determining the structural response during this type of event (Franke, 2011), a 3D model of this abutment will allow for a detailed study of these effects.

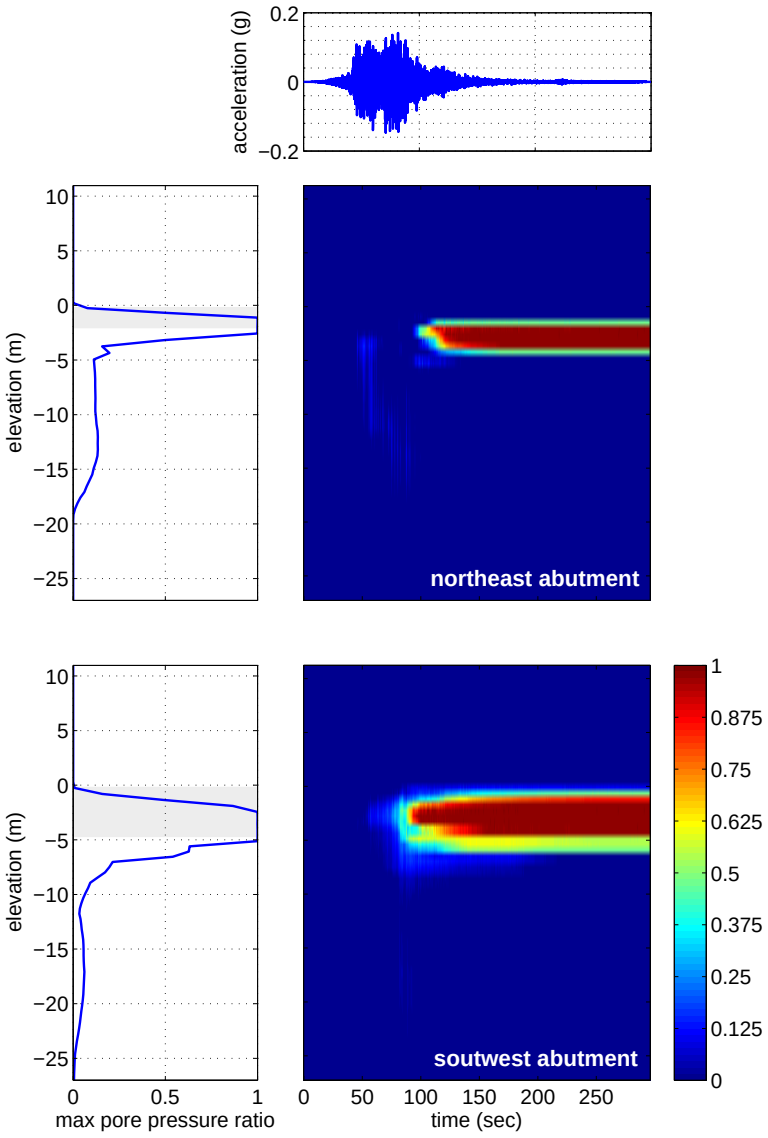

Figure 6.35: Spatial and temporal variation of pore pressure ratio in soil behind abutments.

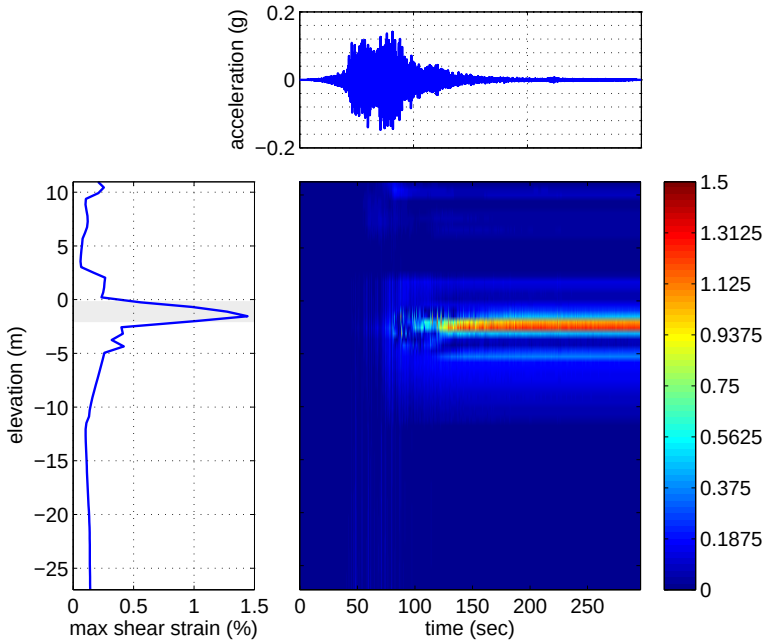

Figure 6.36: Spatial and temporal variation of shear strain in soil behind northeast abutment.

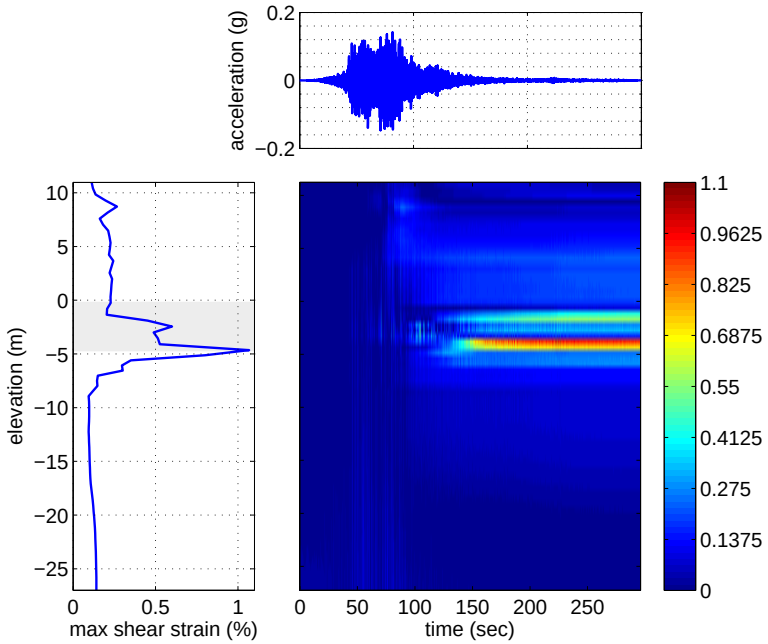

Figure 6.37: Spatial and temporal variation of shear strain in soil behind southwest abutment.

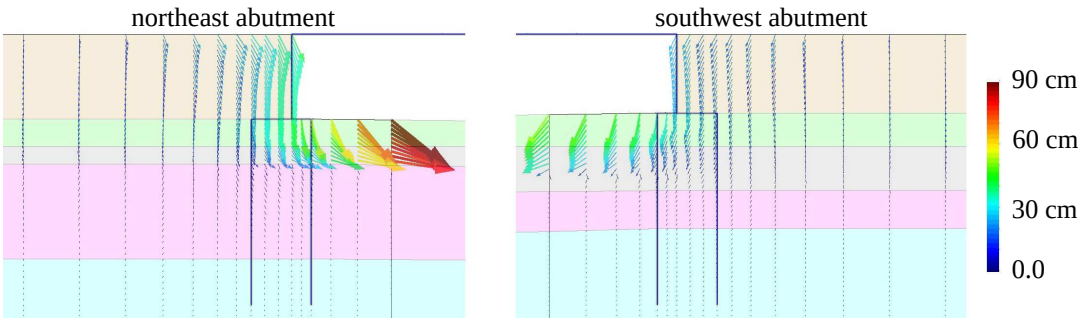

Figure 6.38: Residual displacement fields at abutments.

Chapter 7

SIMULATION AND ASSESSMENT OF EFFECTS OF LATERAL SPREADING ON SOUTHWEST ABUTMENT TO PUENTE MATAQUITO

The dynamic plane strain models discussed in the previous chapter confirmed the susceptibility of the site to both liquefaction and lateral spreading, and identified the southwest abutment for use in further evaluation of the effects of lateral spreading on bridge foundations. Two very distinct methods are used for this purpose: (1) the pile pinning analysis procedure adopted by Caltrans (2011) involving a combination of a BNWF model of the foundation and a slope stability model of the site, and (2) a series of 3D finite element models of the grouped shaft foundation, abutment, and surrounding soils. The results obtained through the application of these modeling approaches to the southwest abutment are presented and analyzed following discussions on the development of the necessary numerical models.

7.1 Pile Pinning Model Development

The pile pinning model of the southwest bridge abutment is created following the Caltrans (2011) procedure for the restrained ground displacement case presented in Section 3.1. This model is considered in order to assess the viability of this design approach through comparison with the observations made at the bridge site and the bending demands resulting from 3D finite element models. To this purpose, a BNWF model of the foundation is developed by converting the 4×2 pile group (Figure 5.11) into an equivalent single shaft model, and through the definition of soil-shaft interaction (p-y) curves that appropriately represent the idealized soil profile and account for group effects. In addition to this BNWF model of the foundation, a limit equilibrium slope stability model is developed for use in determining the compatible force-displacement state which defines the final design displacement in the pile pinning approach.

7.1.1 Development of Foundation Model

The southwest abutment foundation is converted into an equivalent beam model using the Caltrans recommendations for the pile pinning analysis procedure. Two versions of the equivalent beam model are created, one which considers a linear elastic shaft response, and one which considers the

Table 7.1: Properties of linear elastic equivalent beam model for grouped shaft foundation.

Parameter	Single Shaft	Equivalent Shaft
E	21.3 GPa	21.3 GPa
I	0.2485 m^4	1.988 m^4
A	1.7671 m^2	14.137 m^2
G	8.52 GPa	8.52 GPa

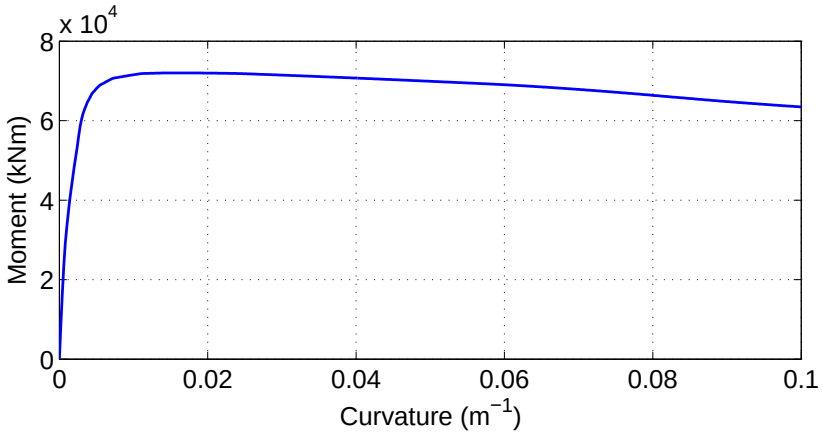

Figure 7.1: Model moment-curvature response for nonlinear equivalent beam model of grouped shaft foundation.

nonlinear section response of the shaft foundations. The properties of the equivalent linear elastic shaft section are determined using the geometry of the shaft and the initial bending stiffness indicated in the moment-curvature plot of Figure 5.10, which, for a single shaft, is $EI = 5.295$ GN·m^2. A gross second moment of the area for a single shaft, $I_g = 0.2485$ m^4, suggests an elastic stiffness $E = 21.3$ GPa, and, for an assumed Poisson's ratio $\nu = 0.25$, a shear stiffness $G = 8.52$ GPa. The section parameters for a single shaft are scaled by the number of shafts in the group to obtain values for use in the equivalent beam model. The properties of this linear elastic equivalent beam model are provided in Table 7.1. The nonlinear equivalent beam model is defined by scaling the single shaft moment-curvature response by the number of shafts in the group, resulting in the equivalent beam model moment-curvature response shown in Figure 7.1. The stiffness of the shaft group is likely underrepresented by the scaling approach adopted for use by Caltrans, however, the intention of this study is an evaluation of the approach, thus, the modeling recommendations involved in its use are followed here.

A rotational spring is used to simulate the rotational stiffness of the shaft cap following the procedure of Mokwa and Duncan (2003). For an axial load of $P = 4120$ kN, and assuming that the

axial capacity is achieved with 0.25 in of vertical displacement, the axial stiffness for a single pile is computed as

$$k_a = \frac{0.75 \cdot 4120 \text{ kN}}{0.0063 \text{ m}} = 490 \text{ MN/m} \tag{7.1}$$

The rotational stiffness for the pile group is based on the number of rows in the shaft cap, n_{row}, the number of shafts in each row, n_{pile}, and the distance from the center of the row to the center of the shaft cap, d_c, as

$$k_\theta = n_{\text{row}} n_{\text{pile}} d_c^2 \, k_a \tag{7.2}$$

For the geometry of the abutment group at Puente Mataquito,

$$k_\theta = 2 \cdot 4 \cdot (3 \text{ m})^2 \cdot 490 \text{ MN/m} = 35.3 \text{ GN} \cdot \text{m} \tag{7.3}$$

This rotational spring is applied to the equivalent beam model at the location of the shaft cap. Above this point, the beam model is given a bending stiffness that is many times larger than the rest of the beam in order to incorporate the abutment into the equivalent beam model. This relatively rigid abutment portion of the beam is assigned linear elastic behavior for both the linear elastic and nonlinear equivalent beam models.

It should be noted that the equivalent beam models defined using the Caltrans (2011) procedure under-represent the bending stiffness of the pile group, which should fall somewhere between the values reported above and the assumption that the group acts as a single beam during the application of lateral loads. The addition of the rotational spring to the model provides some compensation, but even with this spring, the equivalent model may represent an oversimplification of the true foundation response.

7.1.2 Definition of p-y Curves

In the BNWF model, the soil response is represented by a series of *p-y* curves defined based on the idealized soil profile with the properties presented in Table 5.1. These curves are defined with ultimate lateral resistance, p_u, values computed using the method of Brinch Hansen (1961) and initial stiffness, k_T, values computed using the API (2007) recommendations corrected for overburden stress after Boulanger et al. (2003).

Group effects are incorporated into the BNWF model using the group efficiency factors of Mokwa and Duncan (2001) and the procedure recommended by Caltrans (2011). The efficiency factors for the leading and trailing rows are 0.88 and 0.67, respectively. The group effect *p*-multiplier for the

equivalent shaft model is computed as the product of the number of piles with the average of the leading and trailing row values

$$p_{\text{group}} = \frac{8 \cdot (0.88 + 0.67)}{2} = 5.88 \tag{7.4}$$

The residual strength of the liquefiable soil is computed using the undrained shear strength expression recommended by Ledezma and Bray (2010)

$$\frac{S_{ur}}{\sigma'_v} = \exp\left(\frac{N_{1,60\ \text{cs}}}{8} - 3.5\right)\left(1 + \frac{\left(0.3N_{1,60\ \text{cs}}\right)^2}{128}\right) \qquad 0 \leq N_{1,60\ \text{cs}} \leq 20 \tag{7.5}$$

where S_{ur} is the undrained shear strength, σ'_v is the vertical effective stress, and $N_{1,60\ \text{cs}}$ is the clean sand corrected SPT blowcount. This expression is a weighted average of the procedures proposed by Seed and Harder (1990), Olson and Stark (2002), Kramer and Mayfield (2007), and Idriss and Boulanger (2007). In their approach, Ledezma and Bray assigned a weight of 3 to methods that give S_u/σ'_v (i.e. Olson and Stark (2002) and Kramer and Mayfield (2007)) compared to a weight of 2 assigned to methods that only give S_u. A weight of 5 was assigned to the most recent method of Idriss and Boulanger (2008). The undrained shear strength is used to define the p_u values of the p-y curves within the liquefiable loose sand layer, and is computed using the average SPT value assumed for this layer when defining the idealized soil profile of the site. Using this approach, the average undrained strength for the layer is 11.7 kPa, and the undrained strength varies with overburden pressure as $S_u/\sigma'_v = 0.11$. A linear smearing is used to reduce the p_u values for the p-y curves within one shaft diameter of the liquefiable layer boundaries per the recommendations of Caltrans (2011) and Ashford et al. (2011).

7.1.3 Definition of Abutment-Soil Interaction Curve

A tri-linear force-displacement curve is used to model abutment-embankment interaction in the BNWF model. As shown in Figure 3.3, this tri-linear curve is defined in terms of two variables, the ultimate passive force and the displacement at which this force is assumed to be fully developed. Using the geometry and properties of the embankment fill assumed for the idealized soil profile of the site, an ultimate lateral force $F_{\text{ult}} = 94$ MN is computed assuming the development of a Rankine passive wedge at a displacement of $\Delta_{\text{max}} = 0.51$ m.

7.1.4 Pseudostatic Slope Stability Model

The determination of the compatible force-displacement design state for the restrained ground displacement case requires the comparison of the results obtained from a pushover analysis of the BNWF model described in the preceding sections with the results of a slope stability analysis of the abutment site. For this purpose, a pseudostatic slope stability model is developed using Slide 6.0 (Rocscience, 2010) for the geometry and properties assumed in the idealized soil profile. This model is used to compute the horizontal resisting force required at the center of the liquefiable layer to reach a factor of safety FS = 1.0 for a series of horizontal yield accelerations $k_y = 0.05$, 0.1, 0.15, 0.2, 0.25, 0.3, 0.35, 0.4.

To assess the sensitivity of the final design result to choices made during the analysis steps, several versions of this model are developed and analyzed. Two limit equilibrium methods are considered, the simplified Bishop method (Bishop, 1955) and the simplified Janbu method (Janbu, 1973). The failure surfaces are restricted such that they do not extend more than four times the embankment thickness behind the abutment to eliminate complex effects related to a very large slide mass per the suggestion of Ashford et al. (2011). Four cases are considered for each limit equilibrium approach:

- $F_{\text{deck}} = 0$ kN/m with constant $S_u = 11.7$ kPa in the liquefiable layer.
- $F_{\text{deck}} = 377$ kN/m with constant $S_u = 11.7$ kPa in the liquefiable layer.
- $F_{\text{deck}} = 0$ kN/m with $S_u/\sigma'_v = 0.11$ in the liquefiable layer.
- $F_{\text{deck}} = 377$ kN/m with $S_u/\sigma'_v = 0.11$ in the liquefiable layer.

The non-zero F_{deck} value is determined from the full passive resistance of the embankment fill acting over the 2.74 m depth of the bridge deck, and is applied at the centroid of the bridge deck/girder cross-section. The constant undrained strength values are the average value for the layer, and the overburden dependent values correspond to the SPT profiles assumed for the idealized soil profile.

7.2 Application of Pile Pinning Analysis Procedure to Southwest Abutment

The BNWF equivalent shaft foundation and limit equilibrium slope stability models developed for the southwestern abutment of Puente Mataquito are used to determine compatible force-displacement states for the bridge abutment and approach embankment. The viability of this design approach is assessed through comparison with observations made at the site, and in subsequent sections, with the structural demands resulting from plane strain and 3D models of the bridge. The variability in the estimated compatible state is demonstrated by considering various modeling decisions and

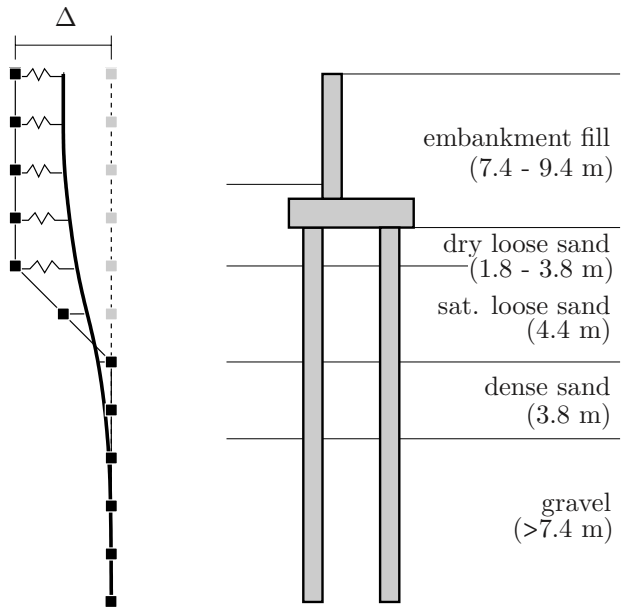

Figure 7.2: Applied displacement profile for equivalent shaft BNWF model of Puente Mataquito southwestern abutment.

assumptions throughout the procedure, and an approach for estimating an appropriate compatible state amidst the observed variability is proposed.

7.2.1 Initial Pushover Analysis of Foundation Model

The equivalent shaft BNWF model of the southwestern abutment is analyzed in a pushover analysis simulating the kinematic demands of lateral spreading. As discussed in Section 3.1.1, this pushover analysis is conducted by applying a set displacement profile to the soil end of the *p-y* springs supporting the foundation. The applied displacement profile used for this purpose is set at a constant 1.0 m in the upper layers, linearly-increasing from zero to 1.0 m across the liquefiable layer, and zero in the underlying material as shown in Figure 7.2.

The purpose of this analysis is to obtain a curve defining the relationship between the applied surface displacement and the foundation shear force at the center of the liquefiable loose sand layer. The unmodified shear force, V_{unmod}, recorded at this location for each step in the analysis is used to compute a corresponding running average shear force, V_{run}, which, at recorded step j, is computed as

$$V_{\text{run}}(j) = \frac{\sum_{i=1}^{j} V_{\text{unmod}}(j)}{j} \tag{7.6}$$

This running average shear force, introduced by Boulanger et al. (2006), is recommended for use in

Table 7.2: Foundation resisting forces (in kN/m) necessary to reach FS = 1.0.

	constant S_u				varying S_u			
	$F_{\text{deck}} = 0$		$F_{\text{deck}} = 377$ kN/m		$F_{\text{deck}} = 0$		$F_{\text{deck}} = 377$ kN/m	
k_y (g)	Bishop	Janbu	Bishop	Janbu	Bishop	Janbu	Bishop	Janbu
0.05	25	136	45	0	0	42	45	0
0.10	192	403	55	38	0	88	46	0
0.15	426	716	223	340	65	344	48	0
0.20	697	1047	476	695	290	649	87	272
0.25	973	1321	747	1039	571	996	339	619
0.30	1229	1693	1025	1325	865	1341	624	986
0.35	1511	1884	1286	1643	1216	1639	919	1352
0.40	1913	2201	1602	1911	1627	1982	1314	1651

subsequent analysis steps to account for a discrepancy in how the force in the middle of the liquefied layer is treated in the pushover and slope stability phases of the procedure. In the current work, the unmodified and running average values are both considered in order to assess how each definition affects the compatible force-displacement state determined at the end of the procedure.

7.2.2 Slope Stability and Deformation Analysis

The slope stability model is used to compute the horizontal resisting force required at the center of the liquefiable loose sand layer to reach a factor of safety FS = 1.0 for a series of horizontal accelerations. As discussed in Section 7.1.4, several configurations of this model are considered in order to assess the sensitivity of the results to different modeling decisions. Table 7.2 shows the foundation resisting force values determined for each slope stability analysis approach (Bishop, 1955; Janbu, 1973) with various model parameters.

As expected, using a variable strength in the liquefiable layer or a non-zero deck resistance requires less foundational resistance to achieve FS = 1.0 than the corresponding cases with constant S_u or $F_{\text{deck}} = 0$. An interesting aspect of the results in Table 7.2 is that the choice of analysis method makes a significant difference in the stabilizing force returned for a given yield acceleration. In general, the Janbu approach returns larger forces for a given combination of k_y, F_{deck}, and S_u than those computed using the Bishop approach. With $F_{\text{deck}} = 377$ kN/m, the passive force of fill acting over the depth of the bridge deck, the Bishop approach appears to have issues at lower yield accelerations, especially for the variable S_u cases, as the required resisting forces are larger than for $F_{\text{deck}} = 0$.

The displacements necessary for determination of the compatible state for the foundation are estimated using a Newmark rigid sliding block approach for each considered acceleration value. The

Table 7.3: Displacements estimated using Bray and Travasarou (2007) procedure.

k_y (g)	$d_{16\%}$ (cm)	d (cm)	$d_{84\%}$ (cm)
0.05	42.0	80.9	155.9
0.10	13.8	26.8	51.6
0.15	3.9	10.9	22.3
0.20	0.0	3.3	9.8
0.25	0.0	0.0	3.8
0.30	0.0	0.0	0.0
0.35	0.0	0.0	0.0
0.40	0.0	0.0	0.0

predictive model of Bray and Travasarou (2007) is used for this purpose. Using this model, the nonzero displacement d in centimeters can be estimated for the Newmark rigid sliding block case as

$$\begin{aligned}\ln(d) = &-0.22 - 2.83\ln(k_y) - 0.333(\ln(k_y))^2 + 0.566\ln(k_y)\ln(\text{PGA}) \\ &+ 3.04\ln(\text{PGA}) - 0.244(\ln(\text{PGA}))^2 + 0.278(M-7) \pm \epsilon \end{aligned} \tag{7.7}$$

where PGA is the peak ground acceleration of the ground motion, M is the moment magnitude of the event, and ϵ is a normally distributed random variable with zero mean and a standard deviation of 0.66. The variability in this estimated displacement is considered by computing the 16 and 84% exceedance values from (7.7), thus establishing a range of estimated displacement values for each foundation resisting force. Because the standard deviation for the natural logarithm of displacement is 0.66, these values are computed as as $d_{16\%} = \exp(d - 0.66)$ and $d_{84\%} = \exp(d + 0.66)$, respectively. Table 7.3 lists the 16%, mean, and 84% displacements estimated from (7.7) using the magnitude, $\text{M}_w = 8.8$, and peak ground acceleration, PGA = 0.4 g, of the 2010 Maule event.

7.2.3 Determination of Compatible Force-Displacement State

The foundation displacement used for design purposes is determined by finding the compatible state indicated by the initial foundation pushover and slope stability/deformation analyses. This is accomplished by plotting the force-displacement data returned from each analysis type and noting the intersection of the two curves. The foundation resisting force values determined in the slope stability analysis represent the resisting force per unit width of soil, thus, in order to compare the two data sets, the shear force values computed in the pushover analysis must be divided by an appropriate width. Two widths are considered for this purpose, the embankment crest width, $w = 12.4$ m, taken from the actual geometry at Puente Mataquito, and the tributary embankment

width, $w_t = 19.9$ m, computed per the recommendations of Boulanger et al. (2006) (see Figure 3.6 for further information).

Figure 7.3 shows the compatibility plots for pushover curves defined with both the running average and unmodified shear forces, V_{run} and V_{unmod}, respectively, scaled by w and w_t and slope stability/deformation curves computed using the Janbu method with overburden dependent strength in the liquefiable layer and $F_{\text{deck}} = 377$ kN/m. The curve for the mean displacement, d, is shown as a solid line, and the $d_{16\%}$ and $d_{84\%}$ curves are shown as dashed lines. The compatible states resulting from the same set of parameters, but with the Bishop method of slope stability analysis, are shown in Figure 7.4. These plots represent only a portion of the considered cases, however, they provide and example of how the compatible state is determined for actual data, and demonstrate the variability of the compatible state for a series of modeling decisions. Tables 7.4 and 7.5 provide the compatible displacement values determined for each considered combination of model parameters. The maximum values for $F_{\text{deck}} = 0$ and $F_{\text{deck}} \neq 0$ and the minimum overall value are highlighted. The boxed values represent the range of displacements corresponding to the modeling decisions recommended by Martin et al. (2002) as modified by Boulanger et al. (2006) and Ashford et al. (2011).

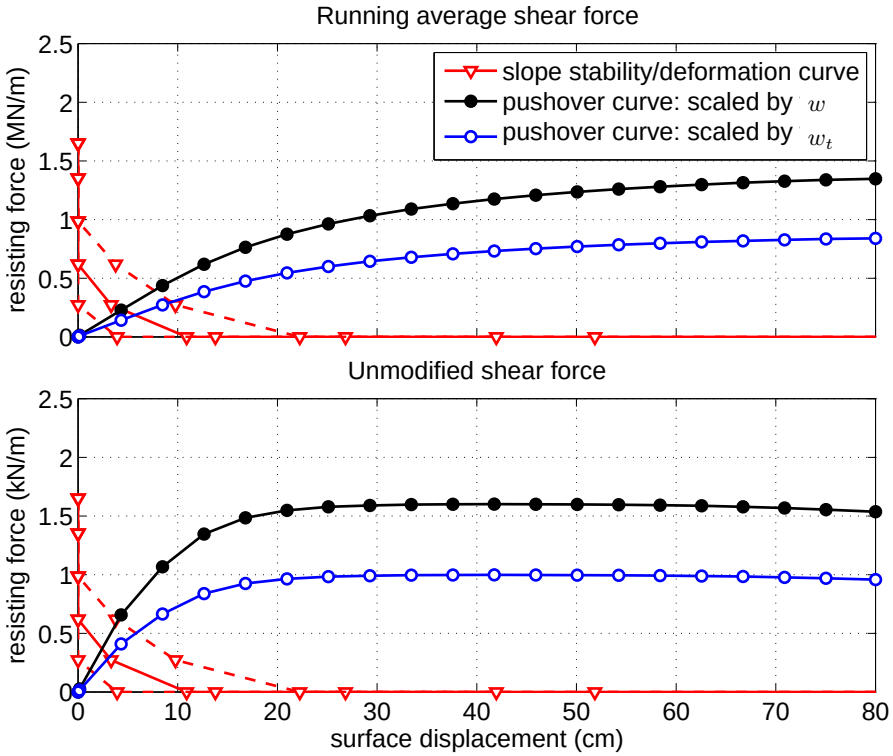

Figure 7.3: Compatible force-displacement states using the Janbu (1973) method for slope stability analysis with a varying S_u in the liquefied layer and $F_{\text{deck}} = 377$ kN/m.

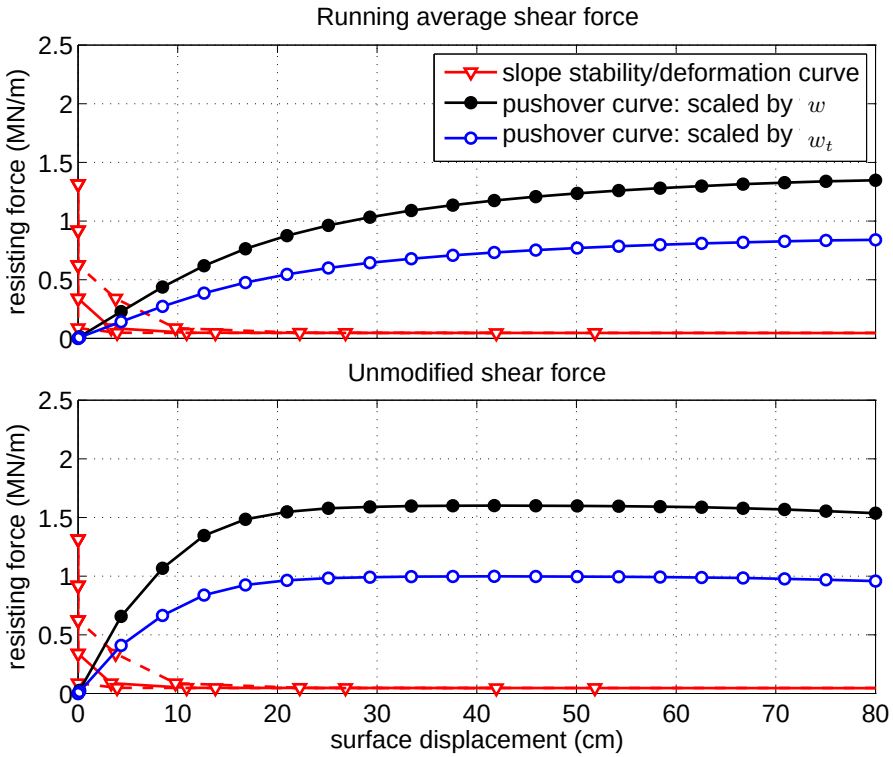

Figure 7.4: Compatible force-displacement states using the Bishop (1955) method for slope stability analysis with a varying S_u in the liquefied layer and $F_{\text{deck}} = 377$ kN/m.

Table 7.4: Compatible displacements (in cm) for various pushover and slope stability/deformation curves using the method of Janbu (1973).

16th percentile displacements – $d_{16\%}$

	$F_{\text{deck}} = 0$		$F_{\text{deck}} = 377$ kN/m	
pushover curve	constant S_u	varying S_u	constant S_u	varying S_u
V_{run}/w	10.3	5.7	5.6	2.2
V_{run}/w_t	13.6	7.7	7.3	2.6
V_{unmod}/w	4.7	2.8	2.9	1.2
V_{unmod}/w_t	7.5	3.8	3.8	1.7

mean displacements – d

	$F_{\text{deck}} = 0$		$F_{\text{deck}} = 377$ kN/m	
	constant S_u	varying S_u	constant S_u	varying S_u
V_{run}/w	13.8	8.5	8.7	4.4
V_{run}/w_t	20.2	11.0	10.9	5.7
V_{unmod}/w	6.8	4.1	4.3	2.4
V_{unmod}/w_t	10.3	6.3	6.5	3.1

84th percentile displacements – $d_{84\%}$

	$F_{\text{deck}} = 0$		$F_{\text{deck}} = 377$ kN/m	
	constant S_u	varying S_u	constant S_u	varying S_u
V_{run}/w	18.6	12.1	12.6	7.6
V_{run}/w_t	29.2	16.8	17.2	9.4
V_{unmod}/w	8.8	6.3	6.6	4.0
V_{unmod}/w_t	15.5	9.1	9.5	5.8

Table 7.5: Compatible displacements (in cm) for various pushover and slope stability/deformation curves using the method of Bishop (1955).

16^{th} percentile displacements – $d_{16\%}$

	$F_{\text{deck}} = 0$		$F_{\text{deck}} = 377$ kN/m	
pushover curve	constant S_u	varying S_u	constant S_u	varying S_u
V_{run}/w	6.9	2.6	4.2	1.3
V_{run}/w_t	9.4	3.2	5.9	2.0
V_{unmod}/w	3.2	1.4	2.2	0.5
V_{unmod}/w_t	4.4	1.9	3.0	0.8

mean displacements – d

	$F_{\text{deck}} = 0$		$F_{\text{deck}} = 377$ kN/m	
	constant S_u	varying S_u	constant S_u	varying S_u
V_{run}/w	9.4	4.7	6.9	2.6
V_{run}/w_t	13.1	6.3	9.0	3.1
V_{unmod}/w	4.4	2.4	3.2	1.5
V_{unmod}/w_t	6.9	3.2	4.7	2.0

84^{th} percentile displacements – $d_{84\%}$

	$F_{\text{deck}} = 0$		$F_{\text{deck}} = 377$ kN/m	
	constant S_u	varying S_u	constant S_u	varying S_u
V_{run}/w	12.9	7.6	9.6	5.3
V_{run}/w_t	18.6	9.5	13.4	6.7
V_{unmod}/w	6.3	3.8	4.8	2.7
V_{unmod}/w_t	9.5	5.6	7.3	3.7

There is significant variability in the compatible displacements for the different combinations of slope stability modeling decisions and pushover curve definition techniques. Estimated displacements range from 0.5 to 29.2 cm over the full spectrum of considered cases, and from 0.5 to 17.2 cm for those cases that consider the resistance provided by the bridge deck. This variability is apparent within the context of the boxed values in Tables 7.4 and 7.5, which range from 3.1 to 10.9 cm. Even if the scope of the study is restricted to the mean displacement cases with overburden dependent strength for the liquefied layer, as shown in Figures 7.3 and 7.4, there is variability depending on the particular slope stability analysis procedure used in the slope stability/deformation analysis.

Figures 7.5 shows the compatibility plot for all of the considered cases and 7.6 shows the compatibility plot for only the $F_{\text{deck}} \neq 0$ cases. The shaded portions of these plots represent the range of compatible displacements implied by the application of the procedure to the Puente Mataquito southwest abutment foundation and approach embankment. It is not practical to assess the foundation performance at all of the compatible states shown in these plots, however, a range of structural demands can be obtained through consideration of the minimum and maximum estimated displacements, and the average structural demands can be estimated by defining an average compatible displacement value. In order to determine a single displacement that is representative of each data set, the centroid of the shaded areas defined in the compatibility plots are computed and plotted as solid dots in Figures 7.5 and 7.6. The average displacement states computed with this approach are 11.4 cm for the full data set and 7.5 cm for the $F_{\text{deck}} \neq 0$ cases. The latter value corresponds well with the boxed displacement values of Tables 7.4 and 7.5.

7.2.4 Assessment of Foundation Performance

With a range of compatible displacements defined using the results of the initial pushover and slope stability/deformation analysis phases, the final step in the pile-pinning analysis procedure is the assessment of the foundation performance at the compatible displacement. This is accomplished using a pushover analysis with the equivalent shaft BNWF model where the applied surface displacement is set equal to the minimum, average, and maximum compatible displacement values discussed in the previous section and shown in Figures 7.5 and 7.6. Consideration of these values defines a range of estimated foundation demands that can be compared to the observed site displacements as well as the results of the 3D foundation model.

The shaft displacement profiles, shear force diagrams, and bending moment diagrams resulting from lateral spreading pushover analyses of the BNWF model for each considered surface displacement are shown in Figures 7.7 and 7.8. The shear forces and bending moments in these plots are

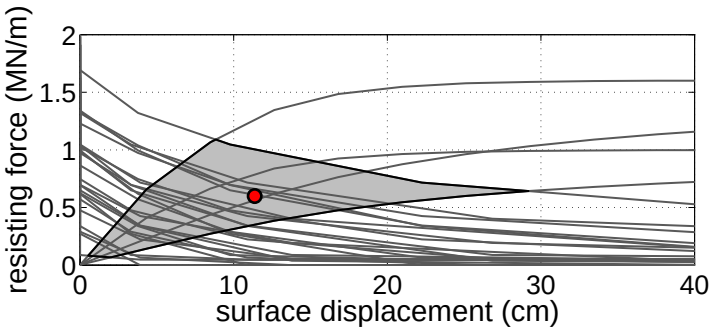

Figure 7.5: Variability in compatible state for all considered cases.

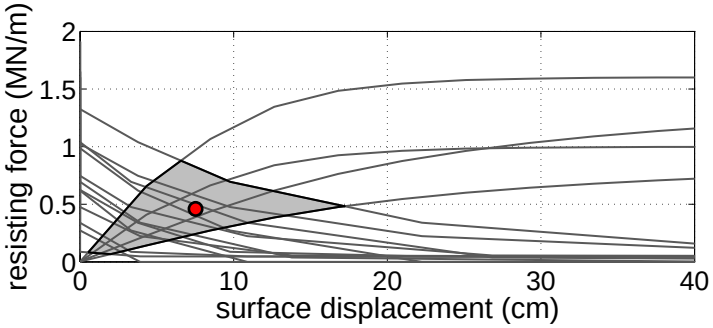

Figure 7.6: Variability in compatible state for cases with $F_{\text{deck}} \neq 0$

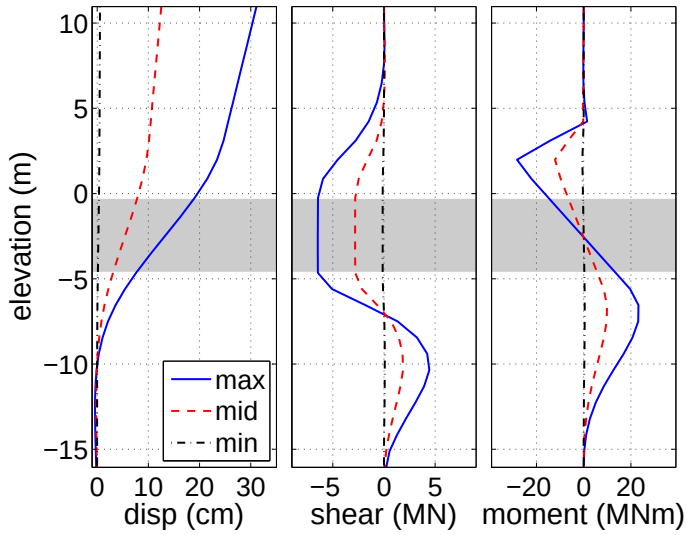

Figure 7.7: Shaft displacement, shear, and moment demands for minimum (0.5 cm), mean (11.4 cm), and maximum (29.2 cm) compatible states for full data set.

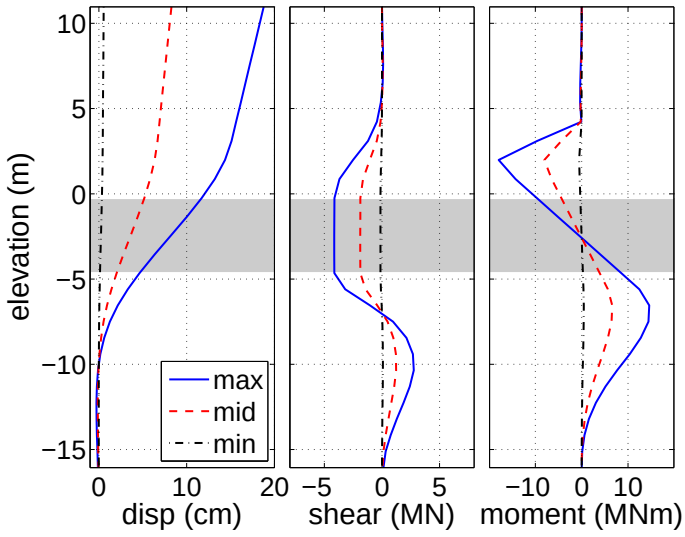

Figure 7.8: Shaft displacement, shear, and moment demands for minimum (0.5 cm), mean (7.5 cm), and maximum (17.2 cm) compatible states for $F_{\text{deck}} \neq 0$ data set.

average shaft values computed by dividing the demands returned by the equivalent foundation model by the number of shafts in the group. As expected, the wide range of compatible displacements results in a wide range of estimated foundation demands, with larger applied displacements leading to larger shear and moment demands. Table 7.6 provides the maximum shaft displacement, shear force, and bending moment returned by the foundation model for each compatible displacement value.

Aside from the 0.5 and 7.5 cm cases, the maximum moments returned from this study are in excess of the 9.0 MN·m design capacity for the Puente Mataquito shaft foundations. Of the considered displacements, the average for the $F_{\text{deck}} \neq 0$ cases, 7.5 cm, is the most representative of the recommendations of Martin et al. (2002), Boulanger et al. (2006), and Ashford et al. (2011). It is encouraging that the foundation performance for this displacement correlates at least roughly with the observed foundation performance under lateral spreading. Observations at the southwest abutment indicated little or no lateral displacement of the abutment, which suggests that the shafts were able to restrain the movement of the foundation while remaining primarily in the elastic regime. For a 7.5 cm applied displacement, the BNWF model suggests shaft performance in line with the likely foundation behavior, with the shafts approaching but not reaching the plastic moment capacity. The estimated and reported abutment displacements are not in direct agreement, however, the estimated displacement is small enough for the bridge to have experienced while sustaining little visible damage, and as discussed in Section 4.2 the abutment displacement may have been underreported.

The discrepancy between the foundation demands for the average displacements resulting from full data set and the $F_{\text{deck}} \neq 0$ data set highlights the importance of the lateral resistance provided by

Table 7.6: Maximum shaft displacement, shear, and moment demands for five considered compatible soil displacement states.

compatible disp	max disp (cm)	max shear (MN)	max moment (MN·m)
0.5 cm	0.55	0.13	0.54
7.5 cm	8.3	1.88	8.06
11.4 cm	12.5	2.82	12.11
17.2 cm	18.8	4.14	17.92
29.2 cm	31.1	6.47	28.20

the bridge deck in determining the foundation response to the kinematic demands of lateral spreading. This is evident in the results of this analysis, as the inclusion or omission of F_{deck} in the slope stability analysis phase significantly changes the compatible displacement state, and is confirmed by the results from the 3D model of the southwest abutment discussed in the following sections. The inclusion of the bridge deck resistance as a constant force equal to the full passive resistance of soil acting over the area of the deck is a convenient approach, but the full passive force may not develop for all displacements and this practice may overestimate the lateral resistance provided by the bridge deck. Additionally, other site-specific factors may affect the available lateral deck resistance. Expansion gaps are typically included at the connection of the deck to the abutment, and a certain amount of displacement must occur before significant deck resistance is available. It is also possible for the deck to become unseated at larger displacements and, as discussed by Franke (2011), the factors leading to this response are obscure, as similarly constructed bridges have displayed opposing deck behavior for similar lateral spreading demands.

Further research is necessary to fully understand all of the factors contributing to the available deck resistance during lateral spreading, however, there are simpler approaches that can be incorporated into the pile pinning analysis procedure to consider the uncertainty in the contribution of the deck resistance to the compatible displacement for the foundation. One such approach is the use of a running average shear force in the definition of the pushover curve as proposed by Boulanger et al. (2006). The use of this technique adds some conservatism to the final result by lowering the pushover curve, which returns a larger compatible displacement than would be estimated for an unmodified shear force. Another approach is the consideration of multiple compatible states for which F_{deck} is set to both zero and nonzero values. The pushover and slope stability analyses used in this design procedure are relatively inexpensive in terms of time and computational effort, therefore, performing them multiple times is feasible in practice. The range of compatible displacements resulting from this

approach can be used to determine a final displacement estimate, perhaps similar to the centroidal approach discussed above, or to define a range of foundation demands for use in design.

7.3 3D Finite Element Model Development

3D finite element models are created to analyze the response of the southwest approach embankment, abutment, and grouped shaft foundation to the kinematic demands of lateral spreading. A schematic of the considered domain for the southwest abutment model is shown in Figure 7.9, and the basic mesh used for the 3D model is shown in Figure 7.10. Symmetry is considered to reduce computational demand, and the mesh is selectively refined such that the elements are smaller near the foundation and the ground surface, and become larger with increasing distance from these features. Figure 7.11 shows the model with the solid bodies made transparent to demonstrate how the abutment, embankment, and shaft cap fit together, and to expose the embedded shaft foundations. For simplicity, the layer boundaries beneath the abutment in the idealized soil profile are assumed to extend horizontally over the full model domain, and the gravel layer extends only to the bottom of the shaft foundations.

The soil is modeled using the SSP elements developed by McGann et al. (2015) and the constitutive models of Elgamal et al. (2003) introduced in Section 5.1. Total stress analysis is assumed as the SSP element makes no consideration for pore pressure effects. The bridge deck is considered using a linear elastic spring element, the abutment and shaft cap are modeled using a combination of beam-column and solid elements, and the shafts are modeled with beam-column elements that interface with the surrounding solid nodes via beam-solid contact elements.

7.3.1 Boundary and Loading Conditions

The boundary conditions for the 3D model are defined to minimize the error associated with representing only a portion of a very large soil domain. Capturing the response of the foundations and their immediate surroundings is the primary objective of the model, therefore, the locations of the mesh boundaries are selected to minimize their effect on this area. The nodes along the base of the gravel layer (light blue in Figure 7.10) are fixed against vertical translation, and elemental body forces are used to simulate the effect of gravity on the soil. The nodes on the symmetry plane are fixed against translation normal to this plane, and the nodes on the vertical boundary opposite the symmetry plane are fixed against all horizontal translation. The nodes on the two remaining vertical boundaries are fixed against out-of-plane translation only. The nodes at the base of the beam-column elements representing the shaft foundations are supported on Q-z springs to consider

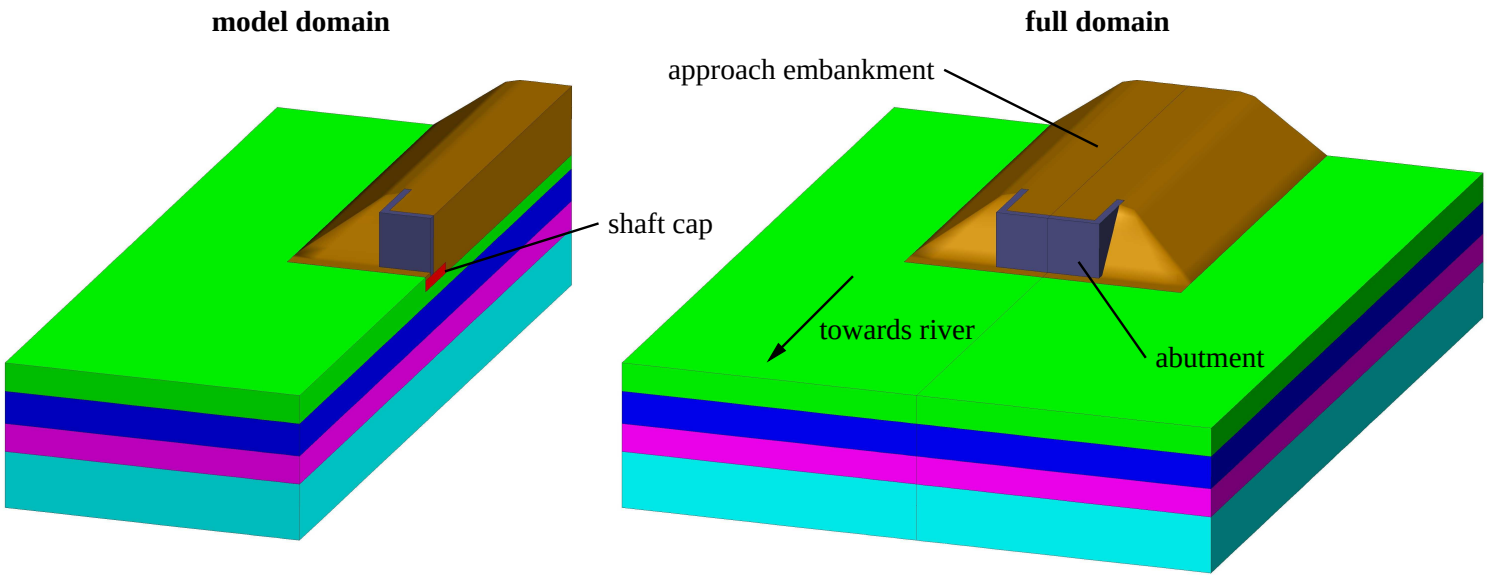

Figure 7.9: Schematic of Puente Mataquito southwest abutment demonstrating symmetry considerations.

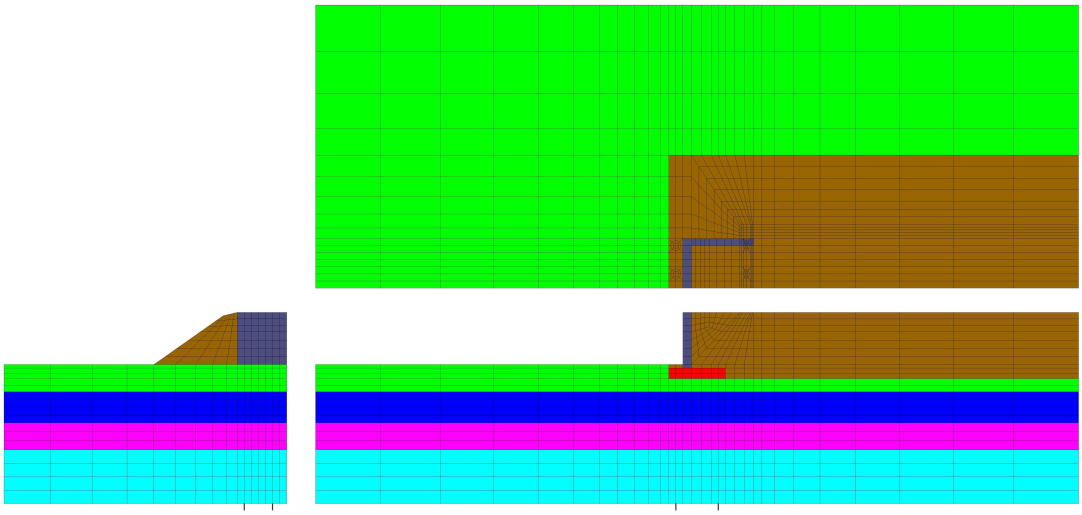

Figure 7.10: Base 3D finite element mesh for southwest abutment of Puente Mataquito.

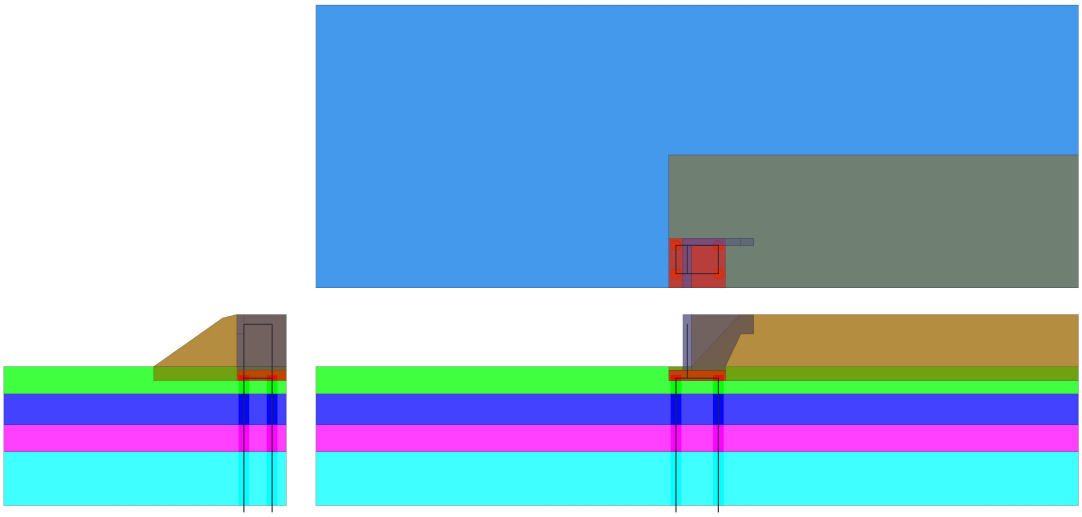

Figure 7.11: Transparent view of base 3D finite element mesh.

end bearing effects.

The kinematic demands of lateral spreading are achieved in the model by gradually imposing a set displacement profile to the vertical mesh boundaries as shown in Figure 7.12. This displacement profile represents the free-field kinematic demands on the soil system, with the material above the liquefiable layer translating laterally in relation to the material below. Applied displacements are constant on the boundaries of the dry loose sand and embankment fill layers, linearly increasing across the liquefiable saturated loose sand layer, and held at zero in on the boundaries of the dense sand and gravel layers. No displacements are imposed on the nodes in the symmetry plane not

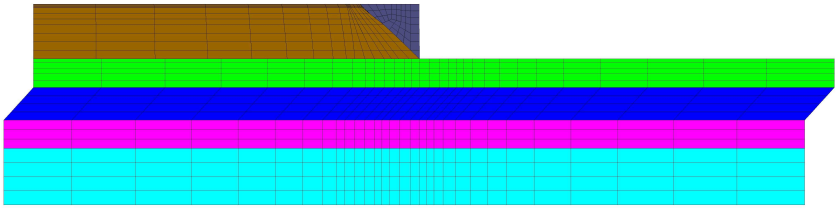

Figure 7.12: Displacement profile applied to mesh boundaries used to simulate kinematic demands of lateral spreading.

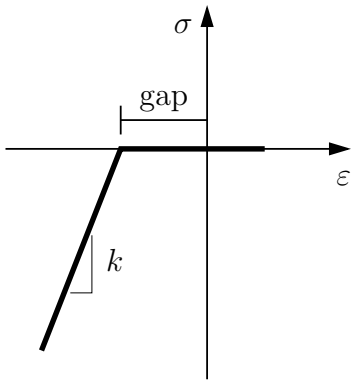

Figure 7.13: Linear elastic constitutive model with gap used in bridge deck spring.

shared with other vertical boundaries.

7.3.2 Modified Soil Properties

The focus of the 3D modeling effort is to simulate the response of the bridge foundation to the kinematic demands of a lateral spreading event. It is assumed that effects related to the initiation of liquefaction are irrelevant to this goal, therefore, the properties of the liquefiable loose sand are modified to reflect the reduction in strength and stiffness associated with a liquefied state. This layer is modeled as a pressure independent (J2) material with a reduced shear modulus $G = 6000$ kPa, and an undrained shear strength of 18.0 kPa. The bulk modulus is unmodified, resulting in a nearly incompressible state that reflects the incompressibility of water. The remaining soil layers in the 3D model (embankment fill, dry loose sand, dense sand, and gravel) are assigned the soil properties discussed in Section 5.1.

7.3.3 Consideration of the Bridge Deck

The bridge deck is not explicitly considered in the 3D model for Puente Mataquito, instead the presence of the deck is modeled using a linear elastic spring. An elastic constitutive model with a gap, Figure 7.13, is used to define the response of the deck spring. This constitutive model considers zero

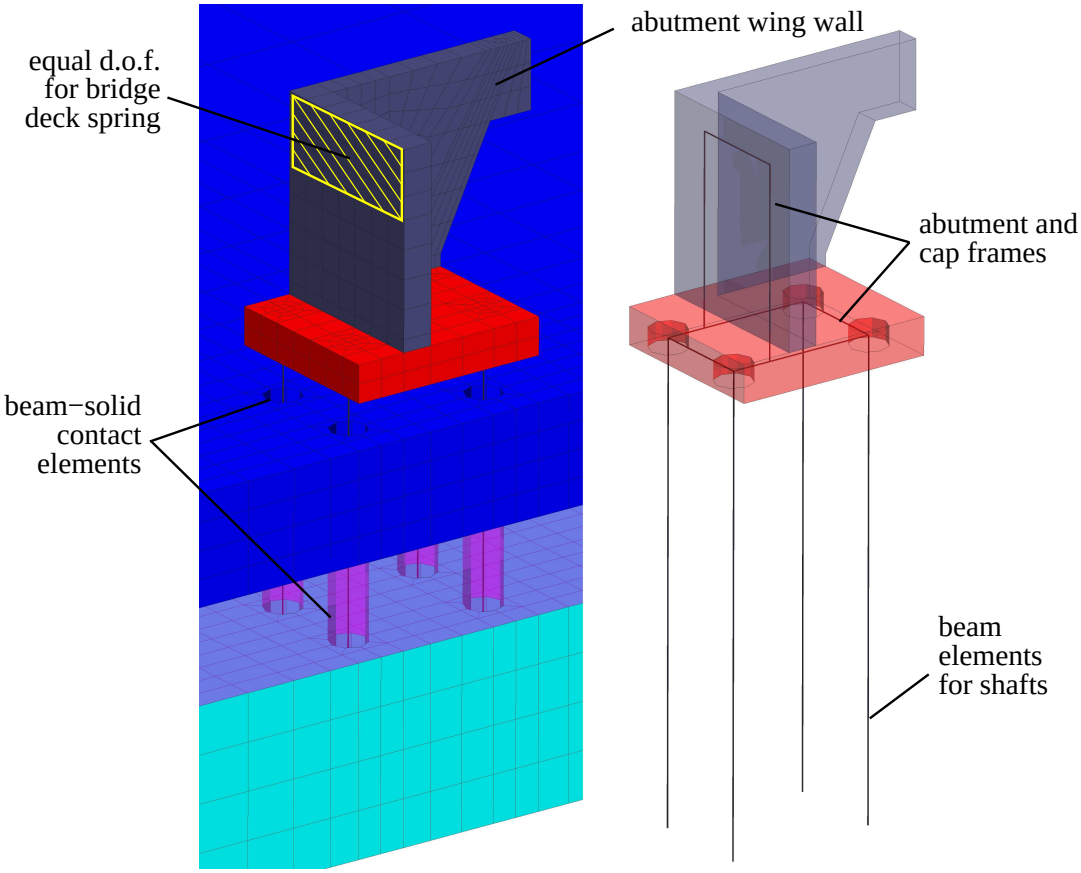

Figure 7.14: Incorporation of grouped shaft foundation into 3D model.

tensile stiffness and zero compressive stiffness prior to gap closure. The spring stiffness, $k = EA/L$, is assigned based on a smeared reinforced concrete elastic modulus, $E_{\text{deck}} = 63.2$ GPa, the bridge deck gross cross-sectional area, $A_{\text{deck}} = 7.25$ m^2, and the span length $L = 40$ m. The nodes on the abutment coinciding with the location of the bridge deck, see Figure 7.14, are constrained to have equal degrees-of-freedom in the direction of loading, and are connected to the free end of the spring element. The sensitivity of the results to the magnitude of the expansion gap is assessed by considering a series of expansion gap values.

7.3.4 Abutment and Grouped Shaft Foundation

Figure 7.14 shows how the grouped shaft foundation is incorporated in to the 3D model. Displacement-based beam-column elements are used to model the shaft foundations, with the foundation model discussed in Section 5.2 used to describe the section response. The shaft foundations consider linear elastic section response in order to determine the theoretical structural demands independent of strength. No scaling of the section behavior is necessary in the 3D model, as each column of beam

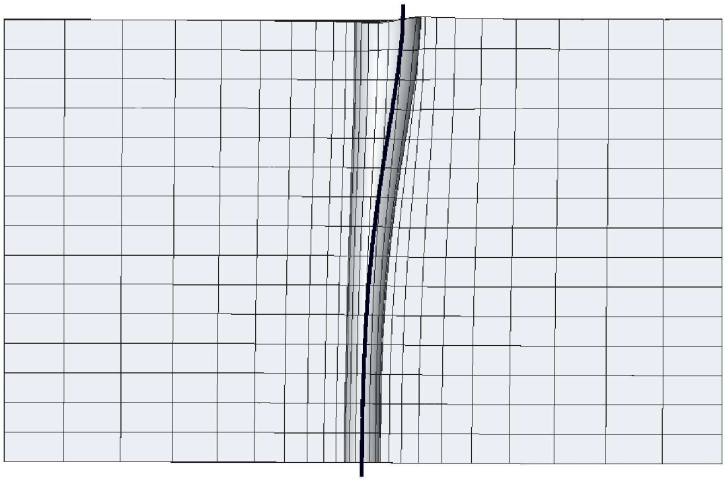

Figure 7.15: Example of gapping behavior simulated with beam-solid contact elements.

elements represents a single shaft foundation. Each shaft is loaded vertically with the foundation design axial load $P = 4120$ kN and supported at the base by a Q-z spring with parameters computed based on the vertical stress and soil properties at the base of the shafts. A circular space surrounding the beam-column elements is built into the mesh to represent the size of the foundation modeled using the beam-column elements. The beam-solid contact elements of Petek (2006) are used to enforce a contact condition with the solid element nodes on the outer circumference of this space. The beam elements are extended beyond the bottom of the solid element mesh to ensure contact is enforced with the nodes at the base of the mesh.

The shaft cap and abutment are modeled primarily using solid elements. These elements are assigned a linear elastic constitutive response, with elastic parameters $G = 1.3$ GPa and $K = 2.5$ GPa. As shown in Figure 7.14, beam elements are used to form a frame inside of the cap and abutment bodies. The beam elements inside the shaft cap serve to rigidly tie the shafts together within the cap. The beam elements inside the front wall of the abutment are used to transmit forces acting on the abutment into the grouped shaft foundation, and the nodes at the top of these elements are constrained to have equal degrees-of-freedom in the direction of loading with the bridge deck spring. All of the beam elements in the abutment/cap frame are assigned linear elastic behavior with a large enough bending stiffness such that these elements are rigid in comparison to the shaft section model.

The beam-solid contact element of Petek (2006) is very advantageous in the context of the 3D model. This element allows the shaft foundations to be modeled using beam-column elements, thus enabling the use of fiber section models and the interpretation of results in the context of traditional beam theory, and creates a contact interface capable of capturing frictional stick-slip and gapping behaviors. Figure 7.15 shows an application of this element to a pile pushover analysis. As shown,

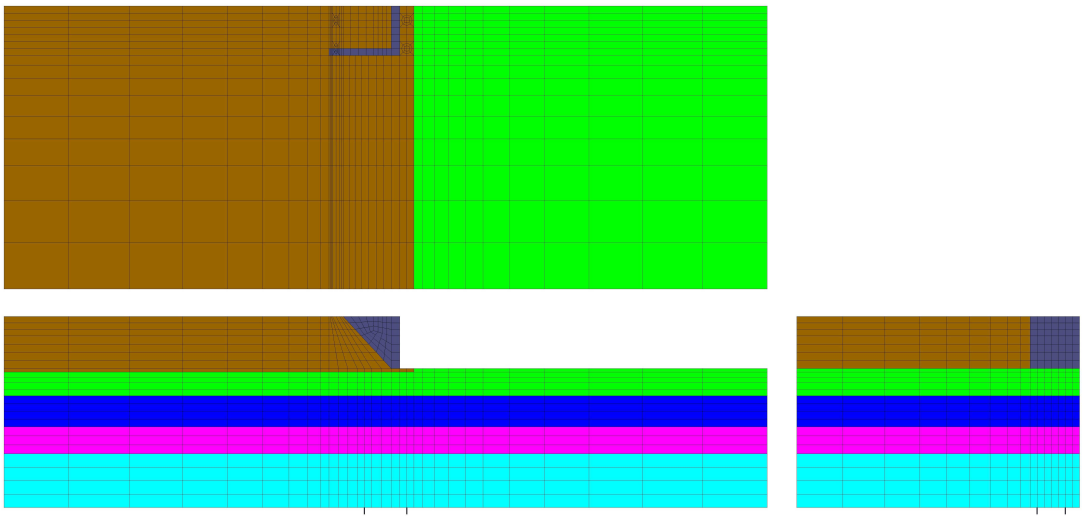

Figure 7.16: Mesh for wide embankment geometry intended to simulate 2D assumptions.

the beam elements do not come into direct contact with the surrounding solid elements, and a gap develops on the trailing edge of the pile while the soil deformation on the leading edge matches the pile deformation. For the purposes of efficiency, the original beam-solid contact elements of Petek (2006) are extended to include a penalty formulation in the enforcement of the contact condition. This extended version of the element is used in all of the 3D modeling presented in this work, and the necessary modifications are summarized in the following discussion.

7.3.5 Alternative Configurations

One alternative mesh configuration is considered for the 3D model. This mesh, shown in Figure 7.16, is identical to the base mesh for the site with the exception of the embankment geometry. Instead of using the embankment geometry existing at the bridge site, the alternative mesh considers an embankment that extends to the boundary of the model. This wide embankment geometry is intended to simulate the assumptions made in a plane strain treatment of the site, and is used to compare the foundation demands due to lateral spreading to those resulting from the existing embankment geometry. The kinematic demands of lateral spreading are simulated in the manner described previously, with a set displacement profile imposed on the non-symmetry vertical boundaries of the mesh. Displacements are not imposed on the side of the embankment across from the symmetry plane, and these nodes are left free to displace in the loading direction.

For each embankment geometry, lateral spreading analyses are conducted for two deck expansion gap values to test the sensitivity of the results to this parameter. According to construction drawings of the bridge, a 20 cm expansion gap is built in to the connection of the bridge deck and abutment. The two gap magnitudes considered in the applied kinematic model are based on this value. The

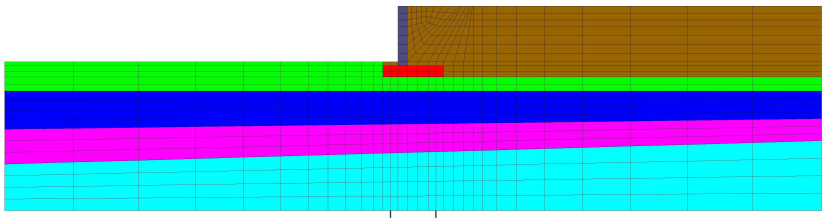

Figure 7.17: Mesh for bridge foundation strength reduction model.

first gap, 5 cm, is chosen on the assumption that the deck is moving towards the abutment due to lateral spreading on the opposite river bank as observed in the plane strain models. The second gap, 25 cm, is based on the assumption that the bridge deck may be moving slightly away from the abutment as lateral soil movement affects the interior piers.

7.3.6 Strength Reduction Model

A second approach to simulating the kinematic demands of lateral spreading on the embedded bridge foundation is considered to provide verification of the results obtained from the applied kinematic model, and to aid in the identification of lateral load reduction mechanisms that may be obscured by the applied kinematic approach. In this second model, instead of applying a set displacement profile to the model boundaries, the shear strength and stiffness of the liquefiable layer are gradually reduced to nearly zero (G = 1.0 kPa and S_u = 0.05 kPa) over a series of analysis steps, with the model being allowed to reach equilibrium for each new set of parameters before proceeding to the next state. Using this approach, the effects of liquefaction in the saturated loose sand layer on the soil-foundation-bridge system can be considered in a simplified manner. This new model is referred to as the strength reduction model in all subsequent discussion in reference to the technique used to simulate the kinematic demands of lateral spreading. Based on similar reasoning, the 3D model discussed in the preceding sections is referred to as the applied kinematic model.

The strength reduction model is created with a slightly modified soil geometry to facilitate the alternative approach to simulating the kinematic demands associated with lateral spreading. The mesh for this case, shown in Figure 7.17, considers soil layer boundaries that slope down towards the river. The orientations of these sloped boundaries are defined by extrapolating the slopes of the layers at the center of the foundation in the idealized soil profile to the model boundaries. Two additional complementary meshes are considered for the strength reduction model, one without an embankment, bridge, or foundation, Figure 7.18, and one with an embankment but no foundation

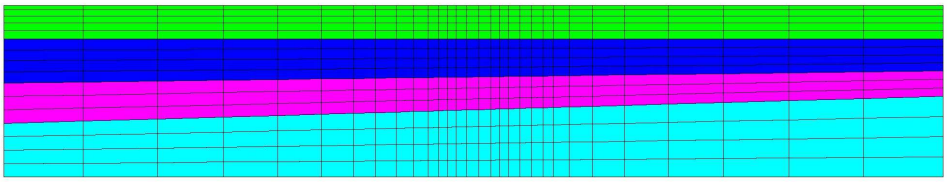

Figure 7.18: Mesh for soil-only strength reduction model.

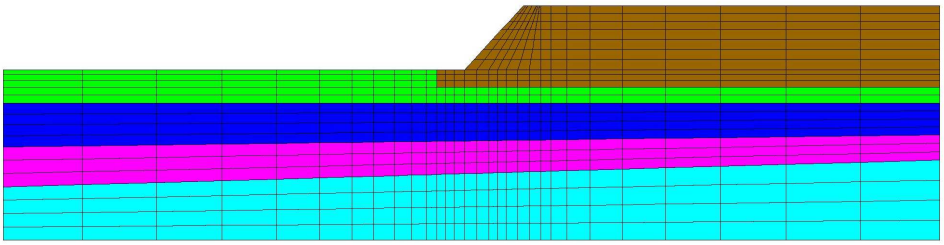

Figure 7.19: Mesh for embankment-only strength reduction model.

or bridge deck, Figure 7.19. The mesh extents and layer geometry of the native soils in both models, and the embankment in the latter model, match those of the base bridge mesh of Figure 7.17.

In all three meshes, the soil nodes above the bottom of the liquefiable layer on the boundary away from the river and the boundary opposite the symmetry plane are allowed to translate towards the river, but are held fixed against translation is the opposite direction. All other boundary conditions are as previously defined. Three global slopes are considered for the strength reduction model. These slopes are simulated by applying gravitational body forces consistent with 0°, 2.5°, and 5.0° rotations of the mesh. These rotated body forces are applied only to the solid elements above the liquefied layer. The lower soil layers consider vertical body forces as in the applied kinematic model. The non-zero global slopes are not intended to simulate conditions at the site, but they are useful in that they encourage the soil above the liquefiable layer to move towards the river, placing larger kinematic demands on the embedded foundations, and allowing deformation mechanisms to be more clearly identified.

7.4 3D FEA of Southwest Abutment with Applied Kinematic Model

The applied kinematic model is used to examine the response of the southwest abutment and approach embankment to the kinematic demands of lateral spreading, and to compare these demands

to those predicted by a plane strain description of the problem. To accomplish this, two embankment geometries are considered: the embankment geometry existing at the site shown in Figure 7.10, and a widened embankment geometry where the embankment fill extends to the boundary of the mesh as shown in Figure 7.16. In addition to the these two geometries, two expansion gap values are considered in order to assess the effect of the size of the gap between the bridge deck and abutment on the response of the model. The results of the lateral spreading simulations for each embankment geometry and expansion gap value are compared to each other in terms of the global response of the soils and foundations, the overall behavior of the abutment and foundation, and the displacement, shear force, and bending moment demands developed in the shaft foundations.

7.4.1 Global Model Response

Figures 7.20 and 7.21 show the deformed mesh at the end of the analysis for the 5 cm and 25 cm gap applied kinematic models with the existing embankment geometry. The deformed meshes are magnified 4 times for visualization, and contours of displacement magnitude (units of cm) are plotted on each mesh. Figures 7.22 and 7.23 are the corresponding plots for the wide embankment geometry. For all cases, the displacements in the direction of loading are generally larger than those in other directions, and the deformation magnitude contours shown in these figures are primarily influenced by this displacement component.

The deformation fields for these models show that with the existing embankment geometry, the bridge foundation provides more resistance to riverward deformation in the immediately adjacent soil and affects a larger lateral expanse of soil. With the wide geometry, there is increased overburden stress at the lateral free-field boundary due to the presence of the embankment. This increases the available shear strength and stiffness of the soil in this location, leading to a larger kinematic demand on the foundation as the free-field displacement is propagated closer to the bridge. This is manifested in the smaller lateral zone of foundation influence for these cases, and in the larger deformations present below the connection of the bridge deck to the abutment.

7.4.2 Abutment and Foundation Response

Figure 7.24 shows how the displacement at the top of the abutment changes over the course of the free-field displacement application. Prior to gap closure for both gap magnitudes, the abutment displacement in the wide geometry case is essentially equal to the free-field displacement, indicating that the foundation is unable to provide significant resistance to the lateral soil deformation. In contrast, the abutment displacements for the existing embankment geometry are less than the

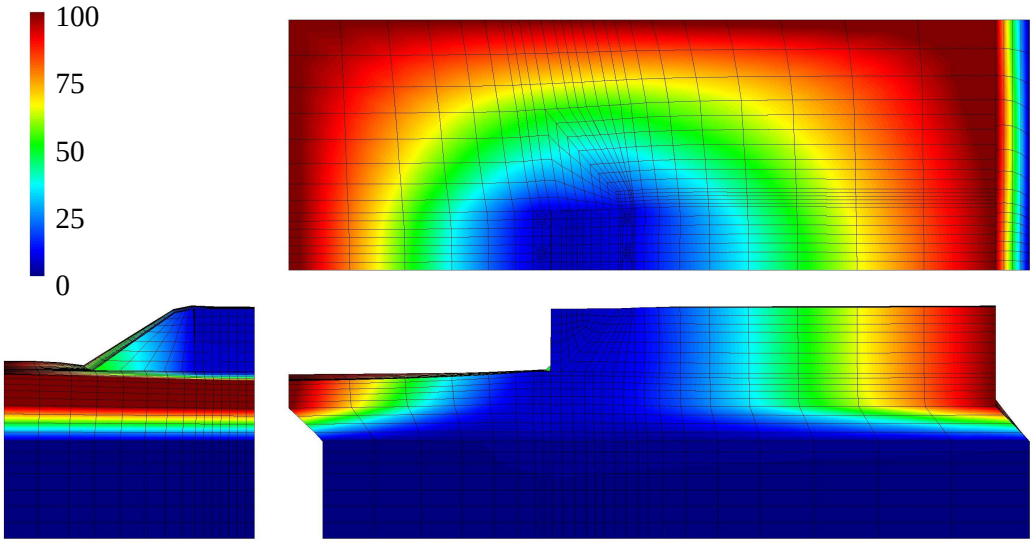

Figure 7.20: Deformed mesh (magnified 4 times) for existing geometry 5 cm gap applied kinematic model with contours of displacement magnitude (in cm).

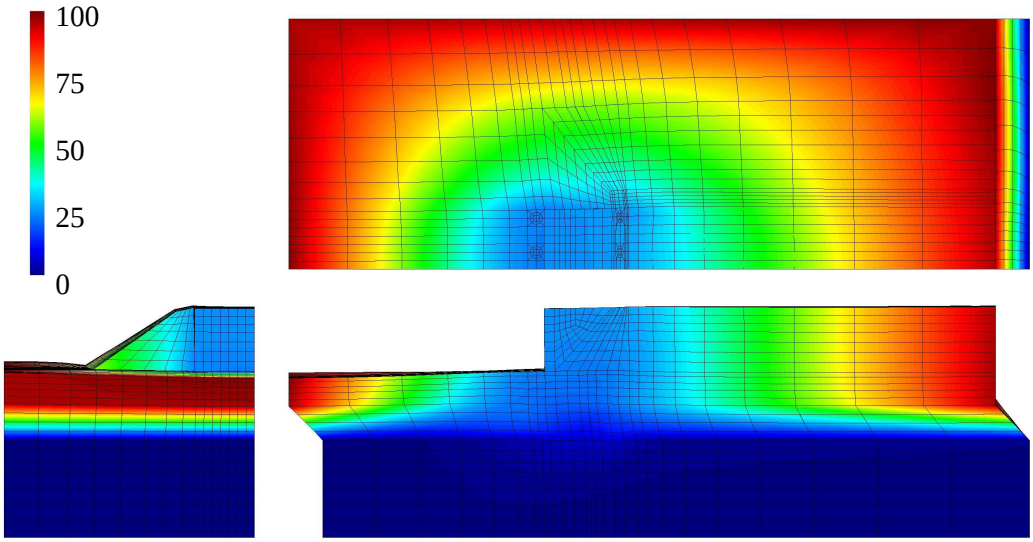

Figure 7.21: Deformed mesh (magnified 4 times) for existing geometry 25 cm gap applied kinematic model with contours of displacement magnitude (in cm).

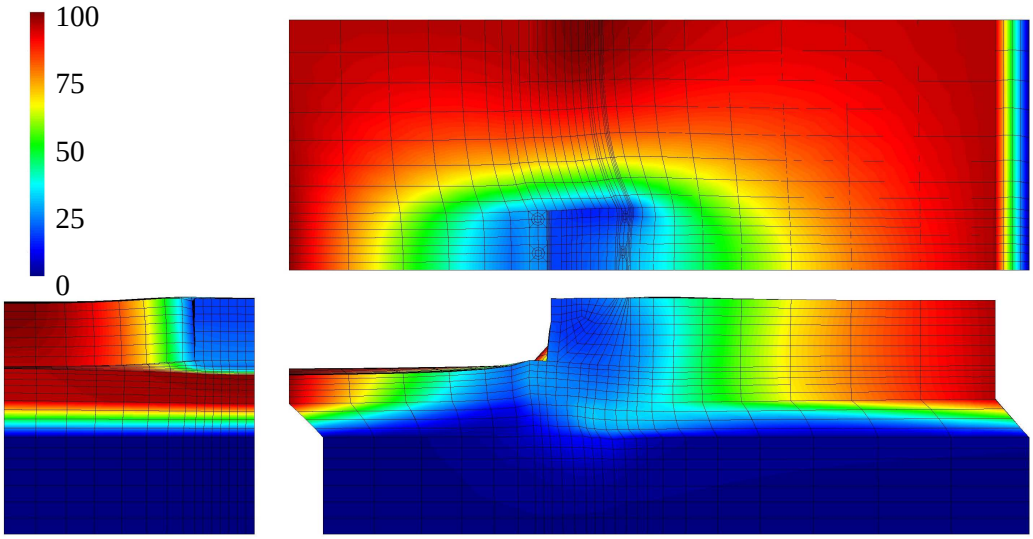

Figure 7.22: Deformed mesh (magnified 4 times) for wide geometry 5 cm gap applied kinematic model with contours of displacement magnitude (in cm).

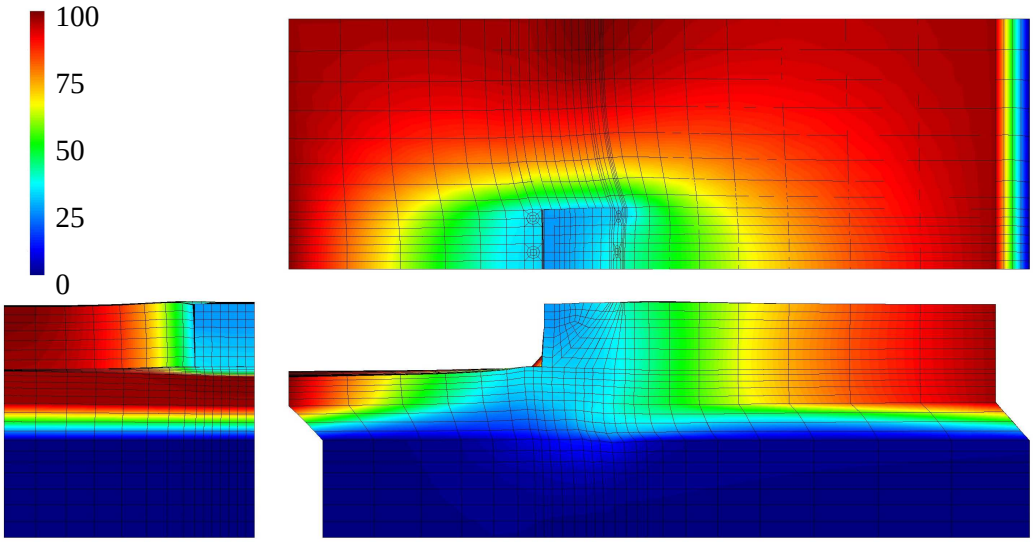

Figure 7.23: Deformed mesh (magnified 4 times) for wide geometry 25 cm gap applied kinematic model with contours of displacement magnitude (in cm).

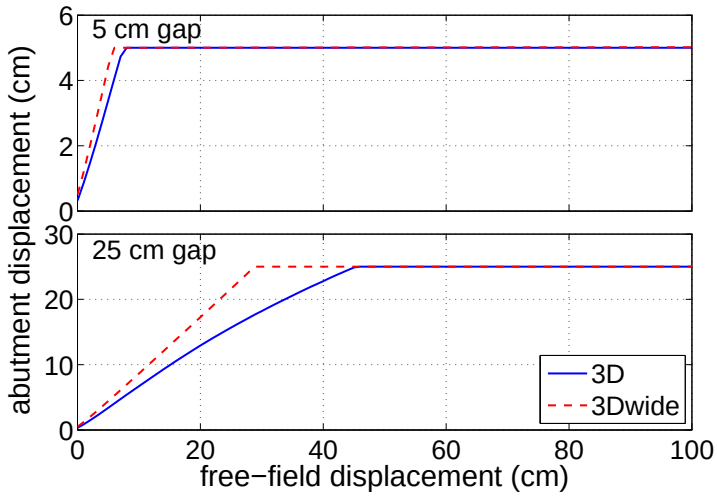

Figure 7.24: Evolution of abutment displacement in direction of loading for 5 cm and 25 cm gap cases.

applied values, indicating that the foundation is resisting the lateral soil demands. The difference between the free-field and abutment displacement for this geometry increases with increasing free-field displacement. After the gap has closed, the displacement at the top of the abutment remains essentially constant due to the resistance provided by the bridge deck spring.

The deformation mechanism for the foundation changes after the closure of the gap. Figures 7.25 and 7.26, which show the deformed shapes of the model foundations for the 5 cm and 25 cm gap cases, respectively, demonstrate this difference in deformation mechanism. After the gap has closed, the lateral deformation of the shaft cap continues to increase, resulting in a rotation about the bridge deck connection point. This effect is most clearly observed for the wide embankment geometry cases, though it is present in all considered configurations. This type of rotational foundation response to lateral spreading corresponds to observations made at numerous bridge sites, including the New Zealand bridges discussed in Chapter 1, and demonstrates the importance of the bridge deck in defining the overall foundation response. It also demonstrates the need for 3D (or 2D) simulation, as a simplified analysis may not capture this effect.

The effects of approach embankment geometry are also evident from the deformed foundations of Figures 7.25 and 7.26. Prior to gap closure, the foundation deformations for each embankment geometry are similar, with the existing geometry inducing slightly less lateral movement in the foundation. After the gap has closed, the differences in how the embankment configuration affects the bridge foundation become apparent, as the end of analysis foundation deformations for the widened embankment cases are significantly larger than those for the corresponding existing geometry cases.

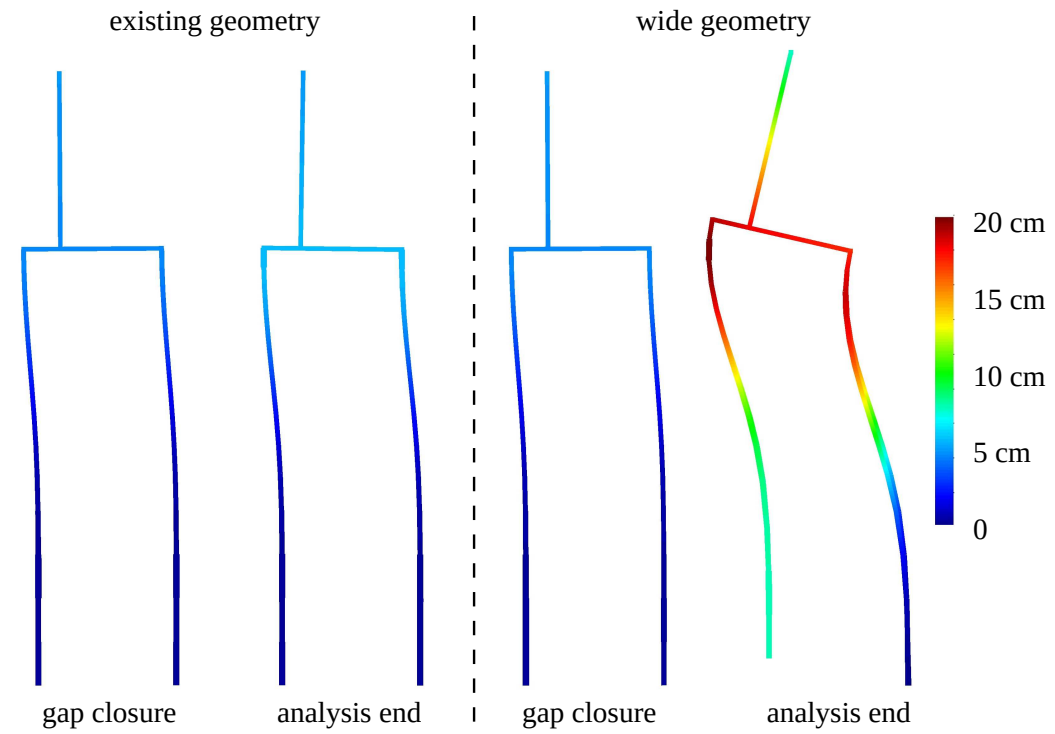

Figure 7.25: Foundation deformations (magnified 15 times) at gap closure and analysis end for 5 cm gap models.

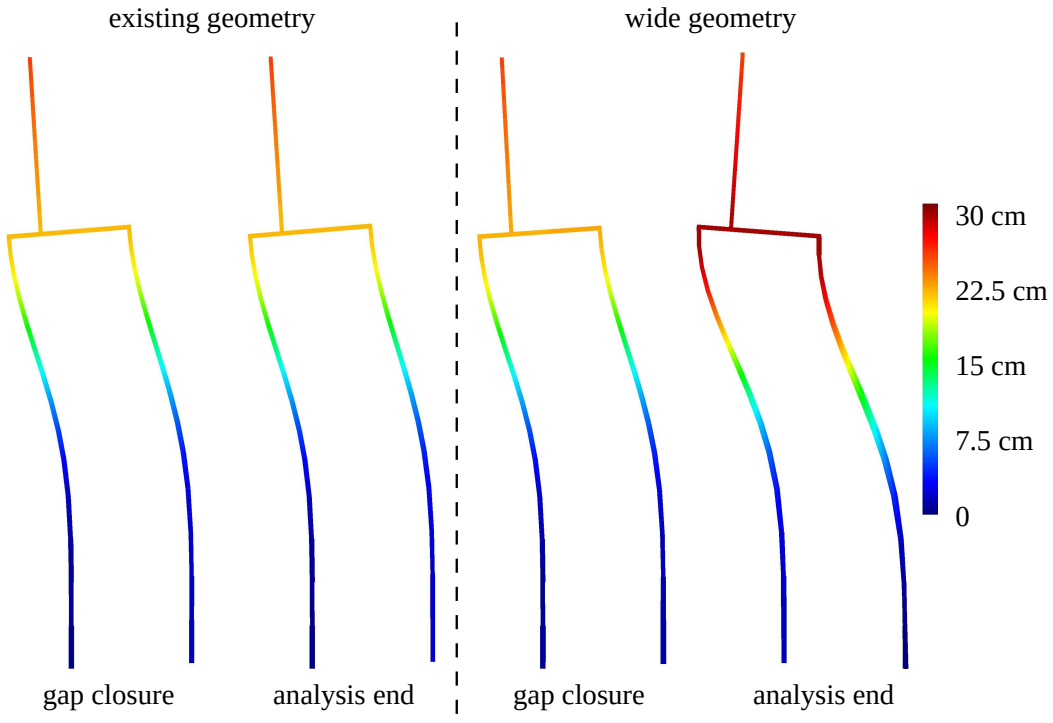

Figure 7.26: Foundation deformations (magnified 15 times) at gap closure and analysis end for 25 cm gap models.

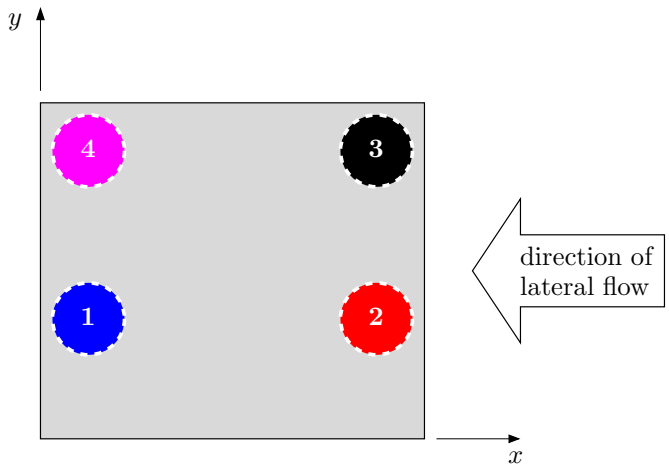

Figure 7.27: Numbering and color scheme used for foundation shafts.

7.4.3 Foundation Bending Demands

The shaft bending demands developed in the applied kinematic model vary for each of the four shafts in the foundation, especially at larger displacements. To aid in identifying these shafts in the subsequent discussion, Figure 7.27 establishes a numbering and color coding scheme for the shaft group. The shaft displacement profiles, shear force diagrams, and bending moment diagrams at the closure of the 5 cm and 25 cm gaps are shown in Figures 7.28 and 7.29. These plots demonstrate that prior to gap closure, the foundation demands for the existing and wide embankment geometries are nearly the same, though it is important to note that, as shown in Figure 7.24, gap closure occurs at different levels of free-field displacement for the two geometries.

Figures 7.30 and 7.31 show summaries of the shaft bending demands at the end of the analysis (i.e., 1 m free-field displacement in upper layers) for the 5 cm and 25 cm gaps, respectively. These plots demonstrate the importance of the bridge deck resistance in defining the magnitude of the shaft bending demands due to lateral spreading, especially with respect to three-dimensional effects. For the existing embankment geometry, the bending demands at the end of the analysis are only slightly larger than at gap closure. This indicates that the lateral resistance provided by the grouped shaft foundation and bridge deck is sufficient to resist the kinematic demands imposed by the soil given the limited footprint of the approach embankment. In contrast, for the wide embankment geometry the foundation rotates about the essentially horizontally stationary deck connection as the free-field displacements increase past the gap closure point. As shown in Figures 7.30 and 7.31 this results in significantly larger shear and moment demands in the shafts.

The change in the foundation deformation mode after the gap has closed also results in a change in

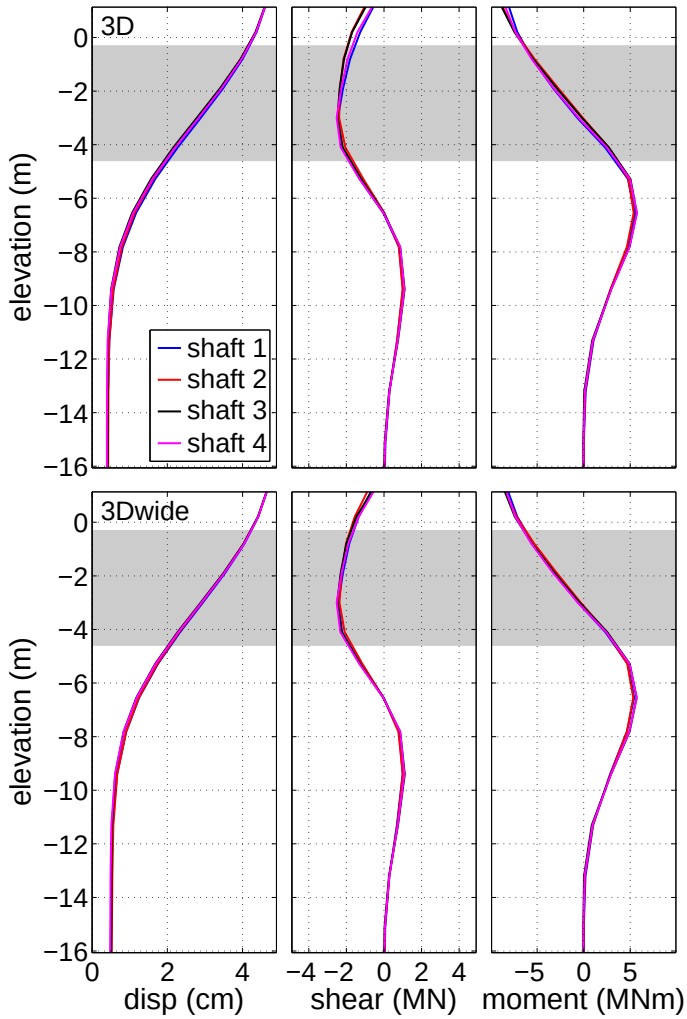

Figure 7.28: Shaft bending demands for existing and wide embankment geometries at closure of 5 cm gap.

the individual shaft response within the group. Whereas initially all four shafts responded similarly, after gap closure two distinct responses appear, with shafts 2 and 3 sharing one response, and shafts 1 and 4 sharing the other. The leading shafts (2 and 3) display larger displacements with depth than the trailing shafts (1 and 4), resulting larger shear force demands in the lower soil layers and slightly lower moment demands overall. In both cases, the outer shafts (3 and 4) develop somewhat larger shear and moment demands than the inner shafts (1 and 2), with shaft 4 typically displaying the largest bending demands of the four shafts.

To further examine the difference between the bending demands for the two embankment geome-

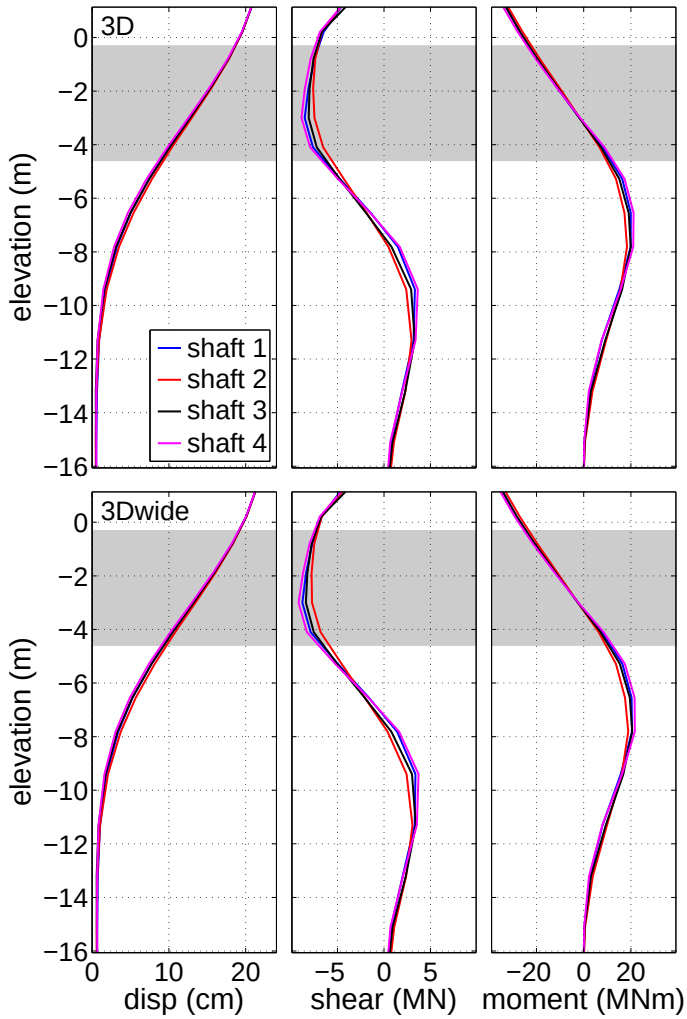

Figure 7.29: Shaft bending demands for existing and wide embankment geometries at closure of 25 cm gap.

tries, the progressions of maximum shear force and bending moment above (or within) and below the liquefied layer are shown in Figures 7.32 through 7.35 for the 5 cm gap, and in Figures 7.36 through 7.39 for the 25 cm gap. These plots confirm and clarify several observations made from the previously discussed bending demand summary plots. For the existing geometry, the maximum bending demands level off after the gap has closed, reaching ultimate values that are not significantly larger than those at the closure of the gap. For the wide embankment geometry, the maximum shear and moment demands do not level off after gap closure. These demands continue to increase with increasing free-field displacement, though at a lesser rate of increase than in the pre-closure regime.

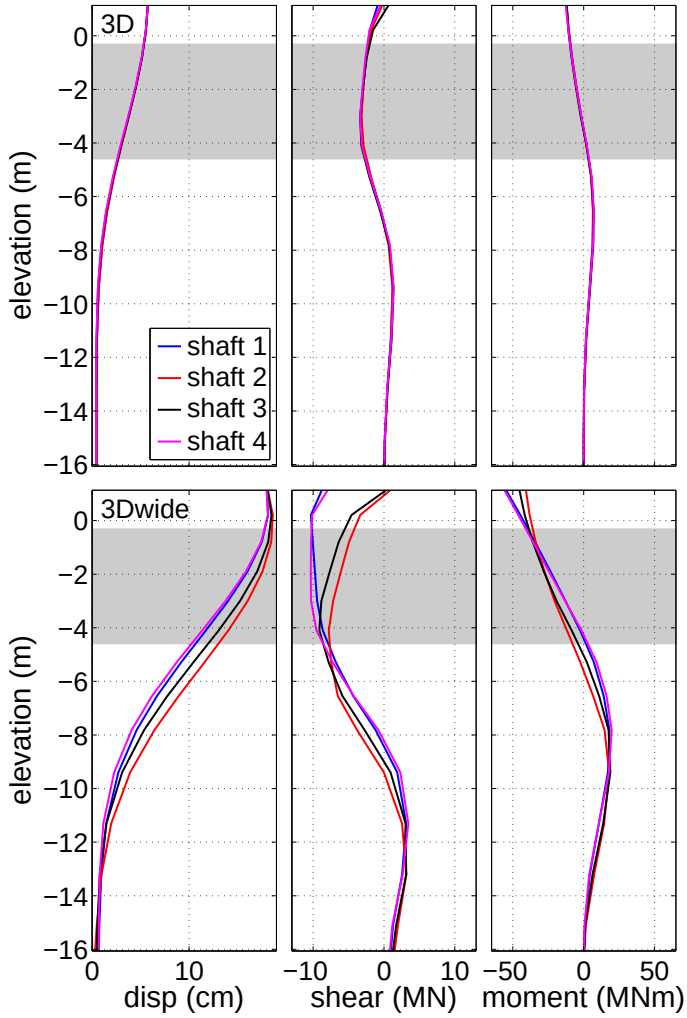

Figure 7.30: Shaft bending demands for existing and wide embankment geometries at analysis end for 5 cm gap.

The group effects noted in Figures 7.30 and 7.31 are also apparent in these maximum demand evolution plots, and as clearly indicated in Figures 7.36, 7.38, and 7.39, the group effects are manifested prior to gap closure in certain cases.

7.4.4 Summary of Applied Kinematic Model Results

The results obtained from the various configurations of the applied kinematic model have established that there is a tangible difference in the foundation response depending on the geometry of the approach embankment. The soil deformation near the foundation, the general foundation response, and the shaft bending demands are all significantly larger for the wide embankment case, especially after the closure of the deck expansion gap. This indicates that consideration for the 3D geometry

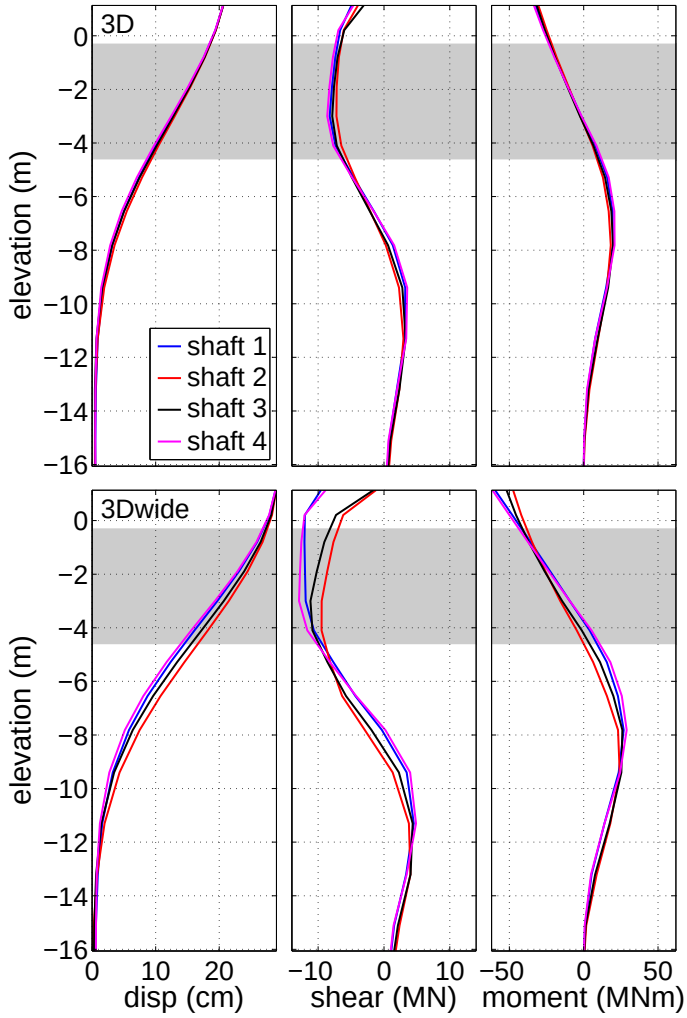

Figure 7.31: Shaft bending demands for existing and wide embankment geometries at analysis end for 25 cm gap.

of the embankment is critical in order to determine appropriate structural foundation demands for the lateral spreading load case.

These results also highlight the importance of the bridge deck and expansion gap in defining the response of the foundation to lateral spreading. Prior to expansion gap closure, the differences between the two geometries are less significant, as the lateral soil movement imposes nearly matching movement in the foundation. After expansion gap closure, the three-dimensional effects become more prominent. The addition of the lateral deck stiffness to the bending stiffness of the foundation is sufficient to resist most of the remaining kinematic demands for the existing embankment geometry, leading to relatively minor increases in the structural foundation demands as the free-field displacement continues past the closure of the gap. This is not the case for the simulated 2D conditions of

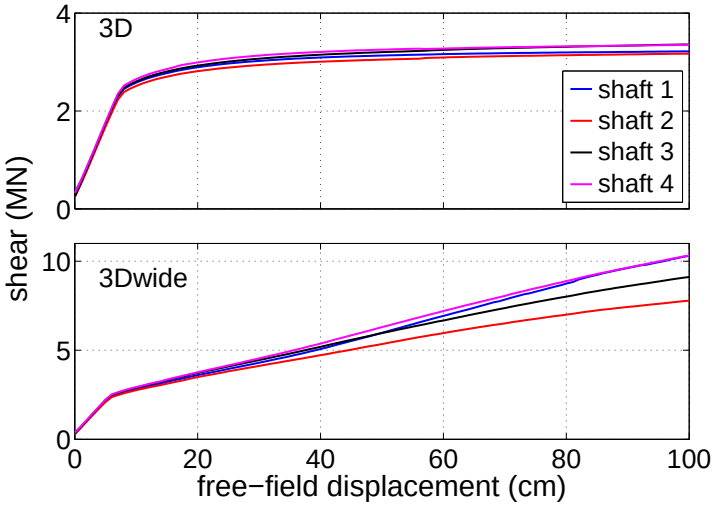

Figure 7.32: Evolution of maximum shear force above the liquefiable layer for existing and wide embankment geometries with 5 cm gap.

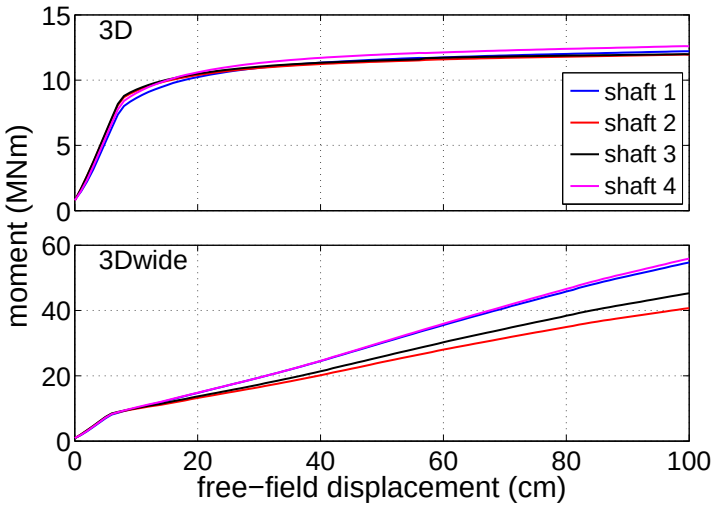

Figure 7.33: Evolution of maximum moment above the liquefiable layer for existing and wide embankment geometries with 5 cm gap.

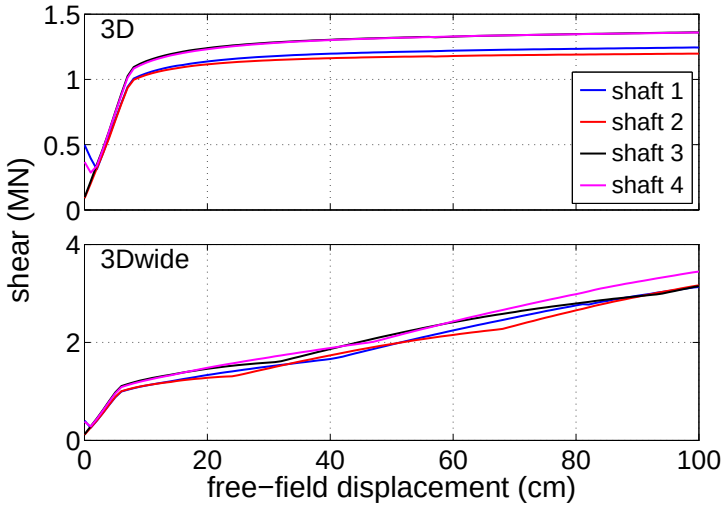

Figure 7.34: Evolution of maximum shear force below the liquefiable layer for existing and wide embankment geometries with 5 cm gap.

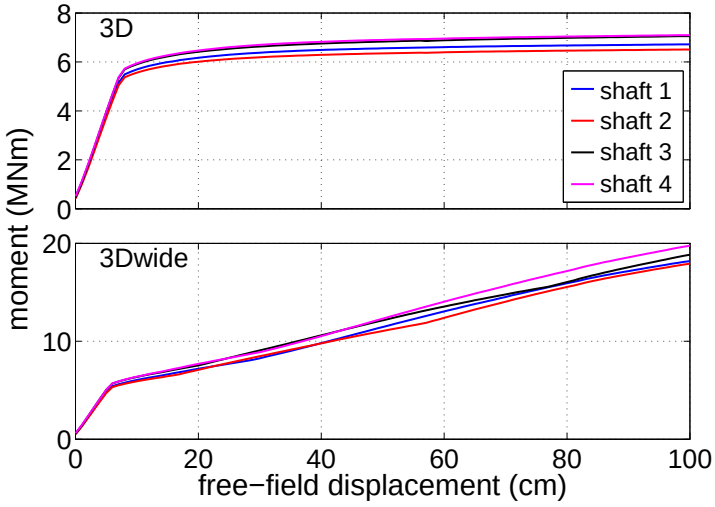

Figure 7.35: Evolution of maximum moment below the liquefiable layer for existing and wide embankment geometries with 5 cm gap.

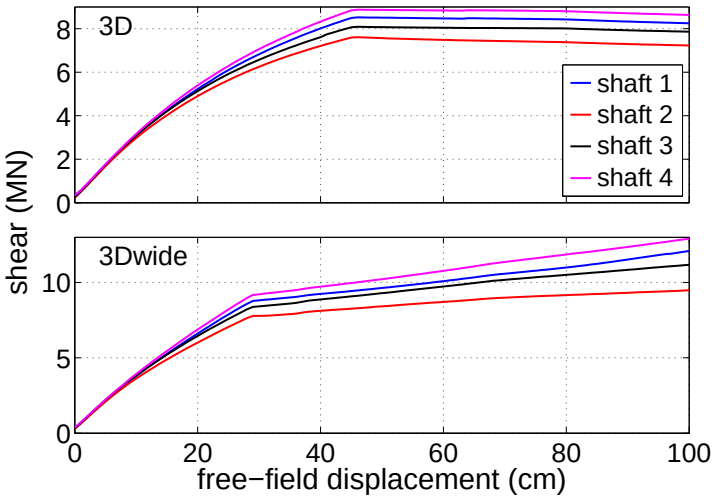

Figure 7.36: Evolution of maximum shear force above the liquefiable layer for existing and wide embankment geometries with 25 cm gap.

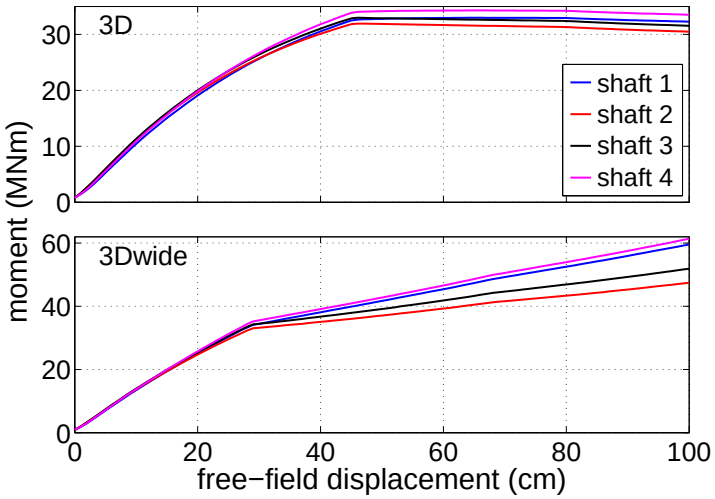

Figure 7.37: Evolution of maximum moment above the liquefiable layer for existing and wide embankment geometries with 25 cm gap.

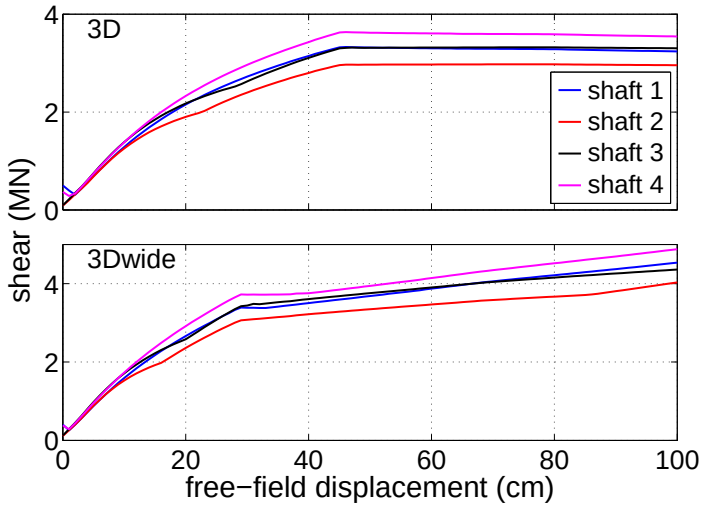

Figure 7.38: Evolution of maximum shear force below the liquefiable layer for existing and wide embankment geometries with 25 cm gap.

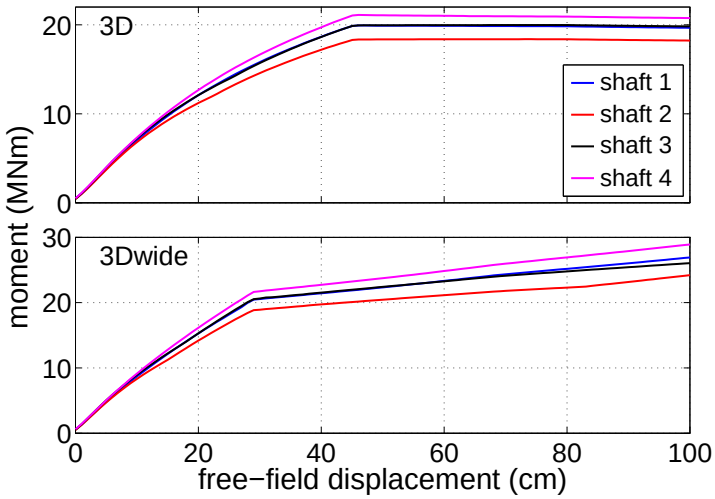

Figure 7.39: Evolution of maximum moment below the liquefiable layer for existing and wide embankment geometries with 25 cm gap.

the wide embankment geometry, as significant foundation demands develop after gap closure.

7.5 3D FEA of Southwest Abutment with Strength Reduction Model

The strength reduction models are advantageous in that they allow for an evaluation of how the system responds as the saturated loose sand layer loses shear strength and stiffness. Consideration of the three model configurations (foundation and embankment, soil-only, embankment-only) shown in Figures 7.17, 7.18, and 7.19 allows for an assessment of the impact of the embankment and foundation on the response of the site. This set of models also serves as an independent evaluation of the results of the applied kinematic model, especially with respect to the foundation bending demands. The kinematic demands of lateral spreading are simulated in a completely different manner for these models, and correlation between the bending demands obtained from each approach increases confidence in the observations and conclusions made from the models.

7.5.1 Global Model Response

Figures 7.40 and 7.41 show the deformed mesh at the end of the analysis for the bridge foundation and embankment only model configurations with flat slope conditions. The mesh deformations are magnified 25 times for visualization purposes, and displacement magnitudes (units of cm) are indicated as contours with the same scale in each figure. A similar figure for the soil-only case is not included here, as the deformations for the flat slope condition are negligible in comparison. The results shown in Figures 7.40 and 7.41 reflect the general trends indicated for all considered slopes. The loss of shear strength and stiffness in the loose sand layer results in a tendency for the embankment to slump downward and expand laterally in both directions as shown in Figure 7.41. With the bridge foundation in place, the riverward deformation of the embankment is resisted, which results in less overall slumping. The bridge foundation also reduces lateral deformation in the second lateral direction in the adjacent embankment fill, however, the free-field lateral deformation is much less affected.

Table 7.7 shows the maximum soil displacements in the x-, y-, and z-directions ($u_{\max}$, $v_{\max}$, and $w_{\max}$, respectively) for each of the considered strength reduction model configurations. For these models, the x-axis is oriented towards the river and corresponds with the primary direction of the kinematic soil demands, the y-axis is oriented perpendicularly to the symmetry plane, and the z-axis is oriented vertically. These maximum displacements provide further evidence of how the presence of the embankment and bridge foundation affect the overall deformation pattern for the site. Adding the approach embankment without a foundation to restrain its deformation results in the largest

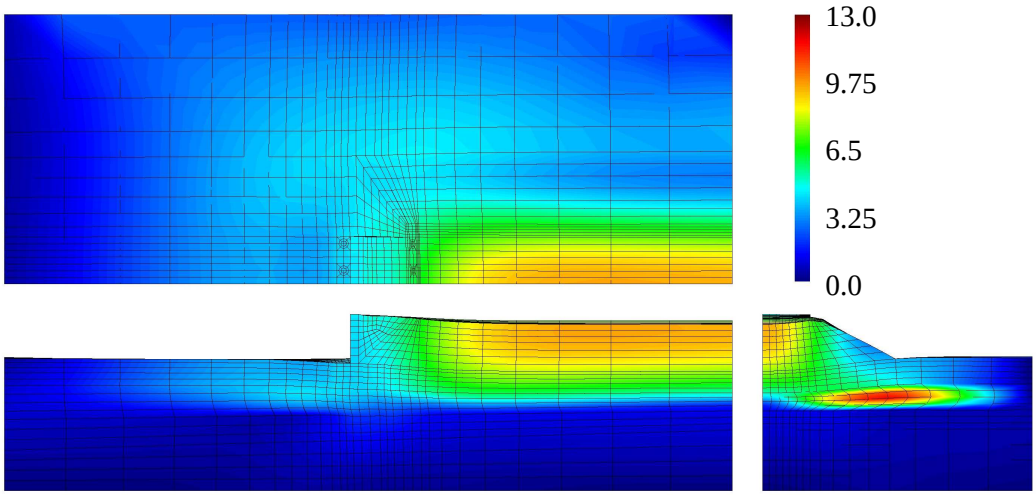

Figure 7.40: Deformed mesh (magnified 25 times) for flat slope foundation strength reduction model with contours of displacement magnitude (in cm).

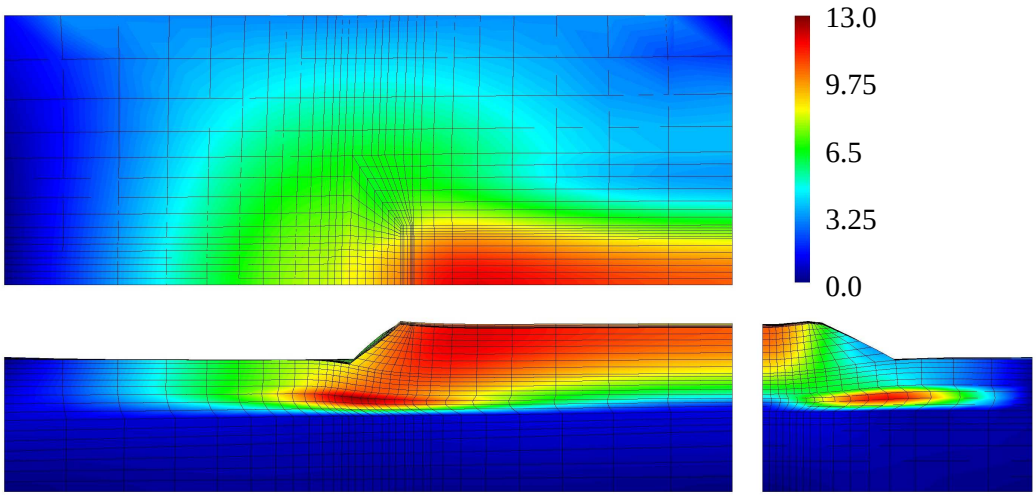

Figure 7.41: Deformed mesh (magnified 25 times) for flat slope embankment-only strength reduction model with contours of displacement magnitude (in cm).

deformations in all three directions. The unbalanced loading applied by the embankment causes relatively large deformation out from the embankment centerline, and these deformations are only slightly reduced by the presence of the foundation. Vertical slumping of the embankment is more significantly affected by the addition of the foundation, likely due to reductions in the deformations in both lateral directions. The most dramatic effect of the bridge foundation on the site is in reducing

Table 7.7: Maximum soil displacements for three strength reduction model configurations at each considered slope.

model type	slope	$u_{\max}$ (cm)	$v_{\max}$ (cm)	$w_{\max}$ (cm)
soil-only	0°	0.5	0.0	1.1
	2.5°	13.4	0.0	4.0
	5°	23.2	0.0	5.0
embankment	0°	12.6	12.3	11.2
	2.5°	22.2	13.1	16.9
	5°	32.8	13.5	22.9
foundation	0°	4.4	12.0	9.5
	2.5°	8.8	12.7	13.1
	5°	13.6	13.1	16.8

the riverward displacements of the soil. As expected, the $u_{\max}$ values in the foundation model for each slope are smaller than the corresponding results in the embankment model, but perhaps unexpectedly, these deformations are also smaller than those for the native soil alone at the larger slopes.

The global model results for three strength reduction model configurations demonstrate the importance of the bridge foundation in defining the overall lateral displacement of the system, lending credence to the compatibility-based approach used in the pile pinning analysis procedure. These models also show that the outward displacement of the soil away from the bridge centerline is largely due to the approach embankment alone. The slumping mechanism displayed by these models is a response that was observed at the Puente Mataquito site, and appears to be due primarily to the overall settling of the embankment as the liquefiable layer loses strength, though there is likely an additional component of loss in embankment height due to material moving laterally. This vertical slumping is present in the applied kinematic models, however, the magnitude is small in comparison to the lateral deformations, and the compression of the embankment under the applied displacement profile further obscures any slumping in that set of models.

7.5.2 Foundation Bending Demands

Figures 7.42, 7.43, and 7.44 show the shaft foundation displacement, shear force, and bending moment demands developed for the flat, 2.5°, and 5° slope cases in the strength reduction model. The bending demands shown in these plots are averaged across the four shafts to get a single set of demands for each case that is representative of the whole. As expected, the larger slopes lead to larger abutment displacements and correspondingly larger shear and moment demands in the shaft

foundations.

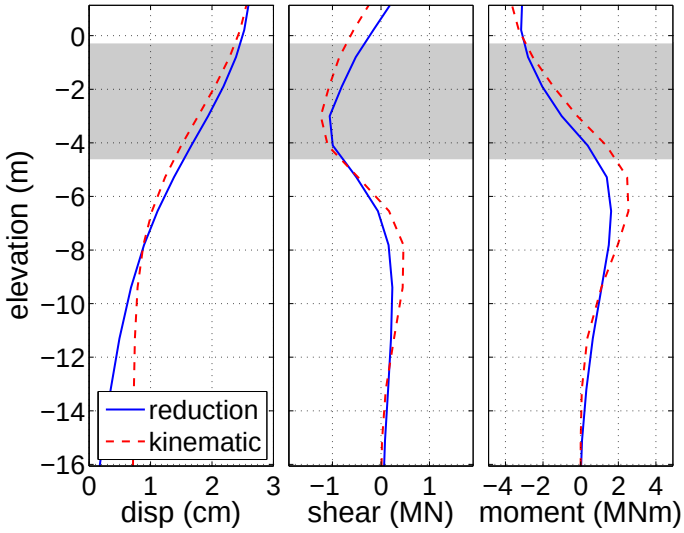

Figure 7.42: Average shaft bending demands for flat strength reduction model. Demands at matching abutment displacement in applied kinematic model are shown for reference.

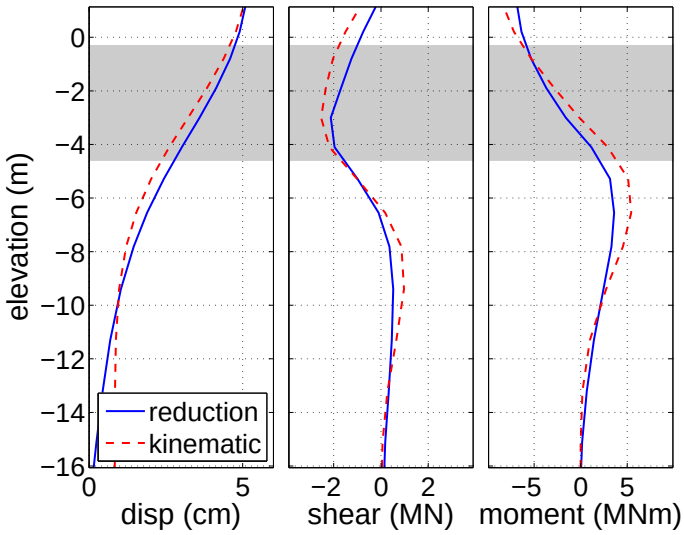

Figure 7.43: Average shaft bending demands for 2.5° strength reduction model. Demands at matching abutment displacement in applied kinematic model are shown for reference.

The bending demands at equivalent abutment displacements in the applied kinematic model are provided in these plots to compare how the two approaches for modeling lateral spreading affect the foundation response. The displacement profiles shown in Figures 7.42, 7.43, and 7.44 demonstrate the primary difference between the two approaches. In the strength reduction models, there is more of a rigid body rotation aspect to the shaft deformation profile. This serves to lessen the shear

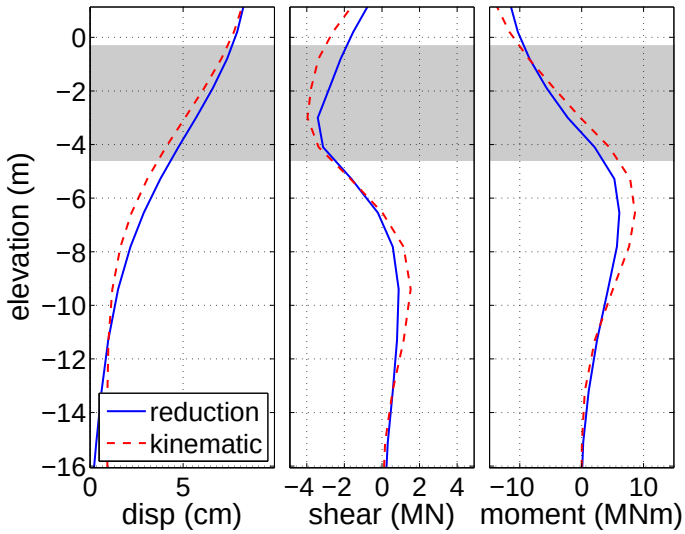

Figure 7.44: Average shaft bending demands for 5° strength reduction model. Demands at matching abutment displacement in applied kinematic model are shown for reference.

force and bending moment demands as compared to the applied kinematic model, even though the displacement at the top of the abutment is the same in each case. However, the overall form of shear and moment diagrams correspond between the two approaches, and the maximum demands are of the same order of magnitude.

The evolution of the maximum shear force and bending moment demands in the shaft foundations in the strength reduction model are compared to the corresponding demands in the applied kinematic model in Figures 7.45 through 7.50. These plots reveal some differences between the two lateral spreading modeling approaches that are obscured by considering only the average shaft demands as in Figures 7.42 through 7.44. Group effects are more prominent in the reduction model results, with shafts 2 and 3 on the leading row carrying consistently larger maximum moment demands, and shafts 3 and 4 on the outside of the group carrying larger shear force demands. The form of the maximum shear and moment evolution for the flat case differs from that displayed by the applied kinematic model, however, the difference is minor, and as the abutment displacement increases, the overall similarity between the two data sets increases. Overall, the two modeling approaches return very similar foundation demands for corresponding abutment displacements.

7.5.3 Summary of Strength Reduction Model Results

The results obtained from the strength reduction models have identified several significant features related to how a bridge foundation responds to the kinematic demands of lateral spreading, as well

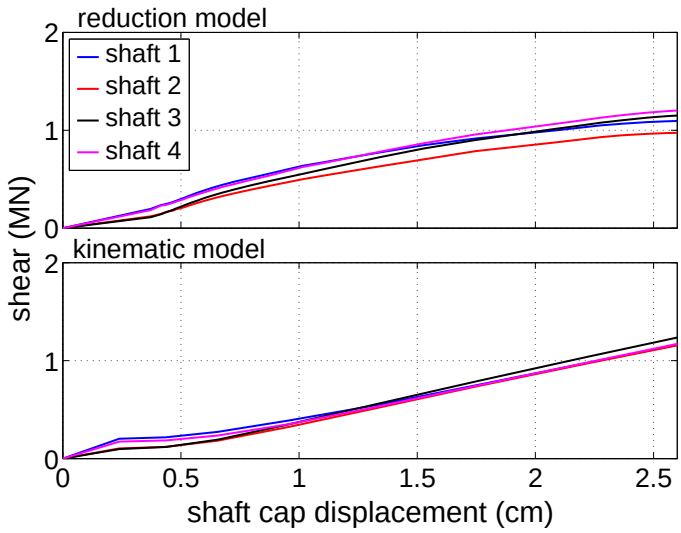

Figure 7.45: Evolution of maximum shear forces for flat strength reduction model and applied kinematic model at matching cap displacement.

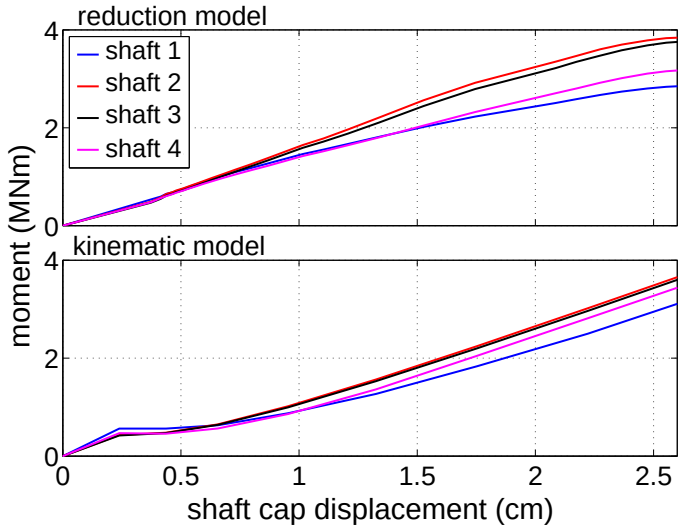

Figure 7.46: Evolution of maximum bending moments for flat strength reduction model and applied kinematic model at matching cap displacement.

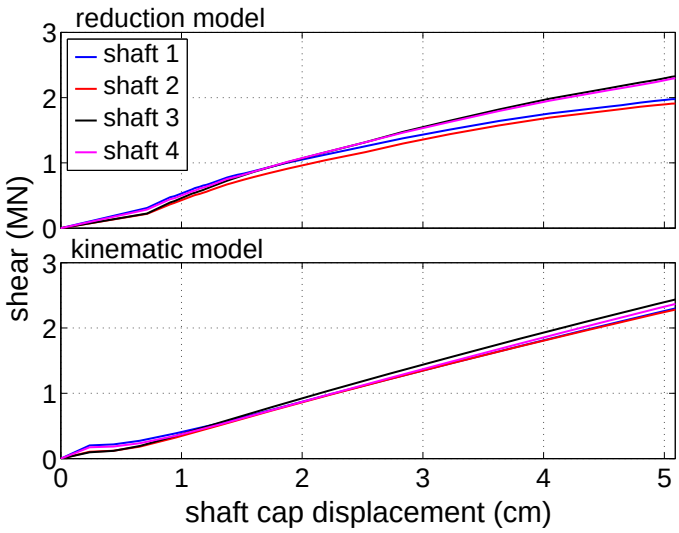

Figure 7.47: Evolution of maximum shear forces for 2.5° slope strength reduction model and applied kinematic model at matching cap displacement.

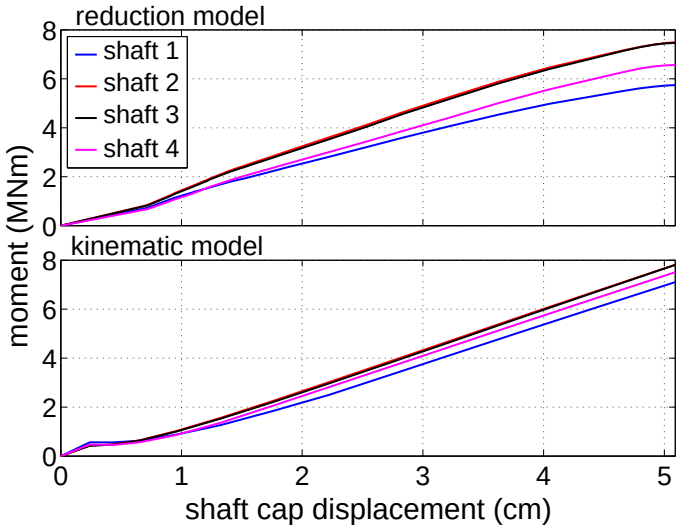

Figure 7.48: Evolution of maximum bending moments for 2.5° slope strength reduction model and applied kinematic model at matching cap displacement.

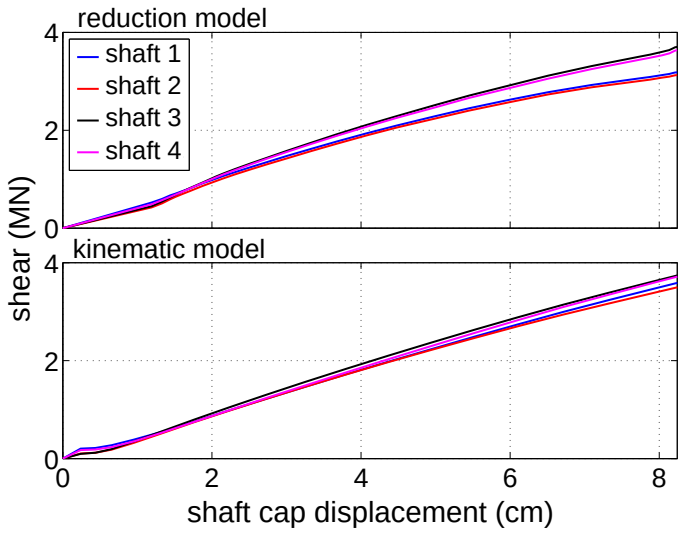

Figure 7.49: Evolution of maximum shear forces for 5° slope strength reduction model and applied kinematic model at matching cap displacement.

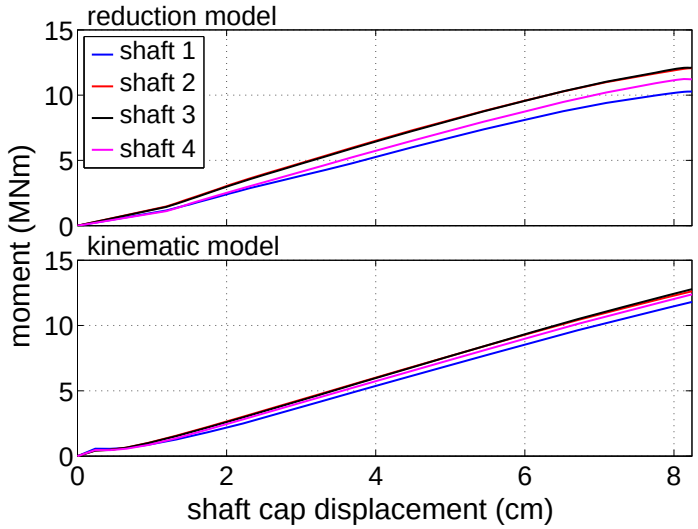

Figure 7.50: Evolution of maximum bending moments for 5° slope strength reduction model and applied kinematic model at matching cap displacement.

as how the presence of the foundation alters the global response of the site. The foundation bending demands obtained from the strength reduction models are essentially the same as those returned from the applied kinematic model at corresponding abutment displacements. This provides increased confidence in the results and observations obtained from the 3D modeling effort.

7.6 Comparison of 3D FE and Pile Pinning Analysis Approaches

The pile pinning model discussed in Section 7.2 and the applied kinematic version of the 3D finite element model discussed in Section 7.4 represent two separate approaches to model the effects of lateral spreading on the southwest abutment and grouped shaft foundation for Puente Mataquito. The shaft foundation bending demands obtained from these two modeling approaches are compared to each other in order to comment on their relative similarities and differences, to demonstrate positive aspects of the pile pinning analysis procedure, and to identify potential flaws or shortcomings of the simplified approach as compared to the 3D model.

7.6.1 Comparison to 5 cm Gap Applied Kinematic Model

Figure 7.51 shows the average shaft bending demands at the closure of the 5 cm gap in the existing and wide embankment geometry cases alongside the shaft bending demands determined from lateral spreading pushover analyses with the BNWF model for the minimum and maximum compatible displacements (0.5 and 29.2 cm, respectively) resulting from all of the cases considered in the pile pinning analysis (see Section 7.2.4). The shaded zones in this plot are the shaft displacement, shear force, and bending moment demands bounded by the minimum and maximum compatible states, and represent the range of demands suggested by the pile pinning analysis. The demands for the mean (11.4 cm) compatible displacement are shown for reference and labeled as *1Davg*. Figure 7.52 shows a similar comparison between the two analysis approaches, however, here the minimum, mean, and maximum compatible displacements for those cases in which $F_{\text{deck}} \neq 0$ (compatible displacements of 0.5, 7.5, and 17.2 cm, respectively) are used to determine the bending demands for the pile pinning approach. Figures 7.53 and 7.54 are constructed similarly, however, the bending demands from the 3D applied kinematic model are those at the end of the analysis when the full 1 m free-field displacement profile has been applied.

The bending demands at the closure of the 5 cm gap in the 3D model fall within the range of demands suggested by the pile pinning analysis, and as shown in Figure 7.52, these demands are reasonably similar to the mean compatible displacement results from the cases with $F_{\text{deck}} \neq 0$. As previously discussed, and as shown in Figures 7.51 and 7.52, at the closure of the gap, there is little

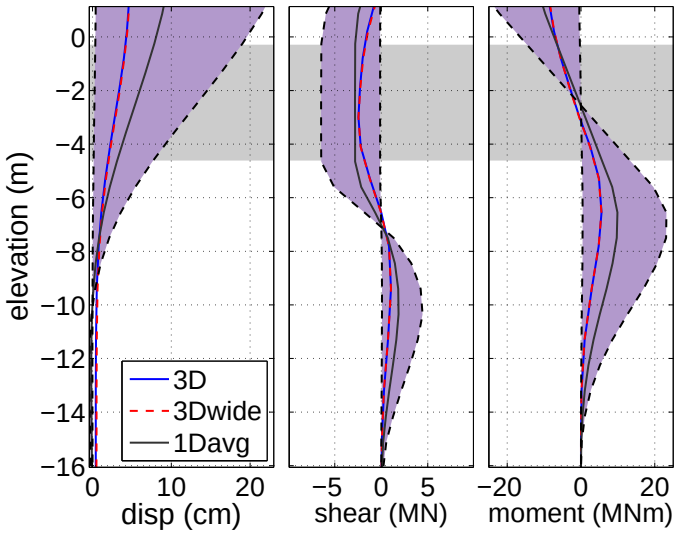

Figure 7.51: Average shaft bending demands at closure of 5 cm gap in applied kinematic model with zone of bending demands suggested by all cases considered in pile pinning model.

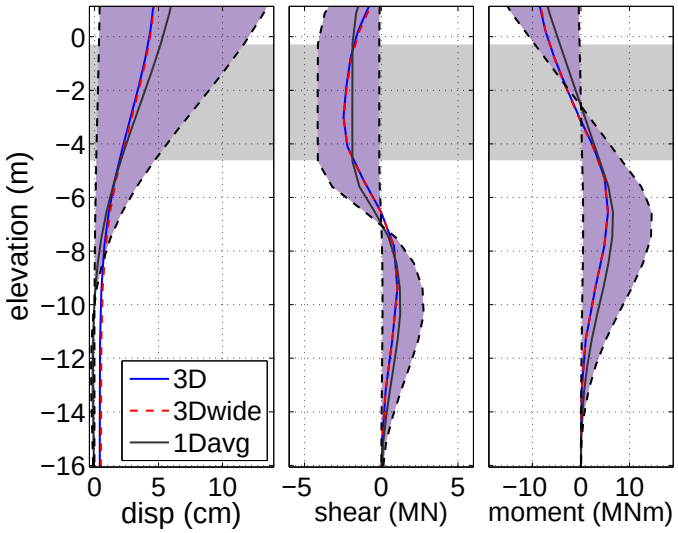

Figure 7.52: Average shaft bending demands at closure of 5 cm gap in applied kinematic model with zone of bending demands suggested by $F_{\text{deck}} \neq 0$ cases considered in pile pinning model.

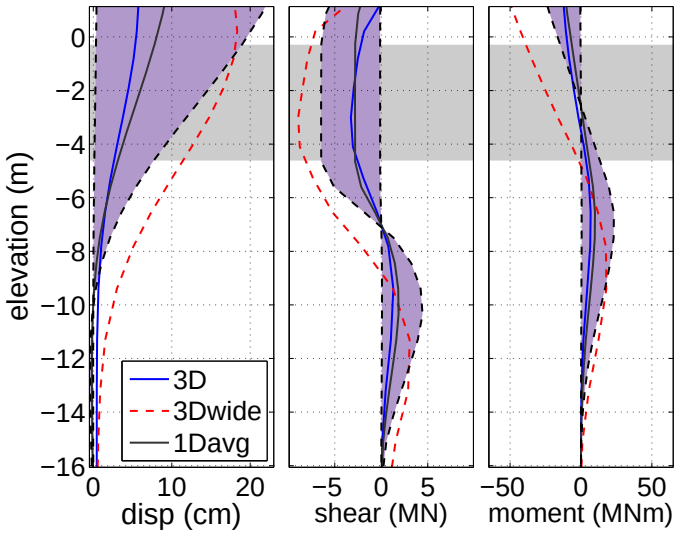

Figure 7.53: Average shaft bending demands at analysis end with 5 cm gap in applied kinematic model with zone of bending demands suggested by all cases considered in pile pinning model.

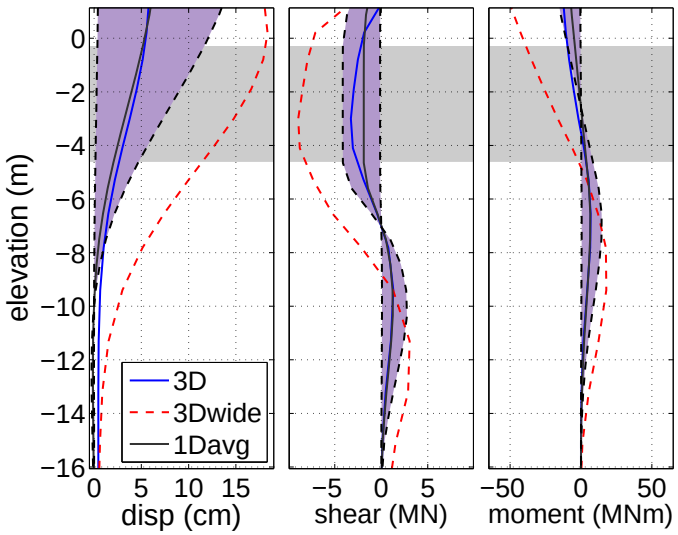

Figure 7.54: Average shaft bending demands at analysis end with 5 cm gap in applied kinematic model with zone of bending demands suggested by $F_{\text{deck}} \neq 0$ cases considered in pile pinning model.

difference between the foundations demands for the two embankment geometries, and both sets of curves correspond reasonably well with the mean pile pinning results. Neither of these observations apply to the end of analysis bending demands shown in Figures 7.53 and 7.54, where the results for the wide embankment geometry fall outside the range of pile pinning demands for both data sets, while the existing embankment geometry demands remain within the suggested ranges and retain their similarity to the mean compatible state for the $F_{\text{deck}} \neq 0$ cases. It is encouraging that the bending demands at the end of the free-field displacement application for the wide embankment geometry, which are similar to what would be expected from a 2D description of the problem, do not correspond to the pile pinning results. This indicates that the pile pinning analysis procedure is capable of estimating foundation bending demands that are consistent with three-dimensional embankment geometry effects.

7.6.2 Comparison to 25 cm Gap Applied Kinematic Model

The pile pinning results do not compare as favorably to the 25 cm gap cases in the applied kinematic model. Figures 7.55 and 7.56 show the bending demand comparisons at the closure of the gap, and Figures 7.57 and 7.58 show these comparisons at the end of the free-field displacement application. At gap closure, the 3D bending demands are slightly larger than those for the maximum considered compatible displacement (29.2 cm), and are well outside of the range defined by the $F_{\text{deck}} \neq 0$ cases. After gap closure, the existing embankment geometry results remain essentially the same relative to the ranges obtained in the pile pinning analysis, while the wide geometry demands become even larger in comparison.

The discrepancies between the two modeling approaches demonstrated in Figures 7.55 through 7.58 emphasize the importance of consideration for the presence of an expansion gap when determining foundation demands developed during lateral spreading. The 25 cm of displacement required to close the gap in the 3D models is larger than all but one of the compatible displacements considered in this comparison, therefore, even the most conservative estimate of foundation bending demands obtained from the pile pinning procedure may be too small when the magnitude of the gap is relatively large. For bridges where the foundation alone does not provide sufficient lateral resistance to embankment deformation, it is likely that the expansion gap will be closed due to lateral movement of the foundation. In this case, a better estimation of the foundation bending demands may be obtained by considering the magnitude of the expansion gap in the compatible displacement used for the final evaluation of the foundation.

A potential solution to this problem may be to consider $F_{\text{deck}} \neq 0$ in the determination of the

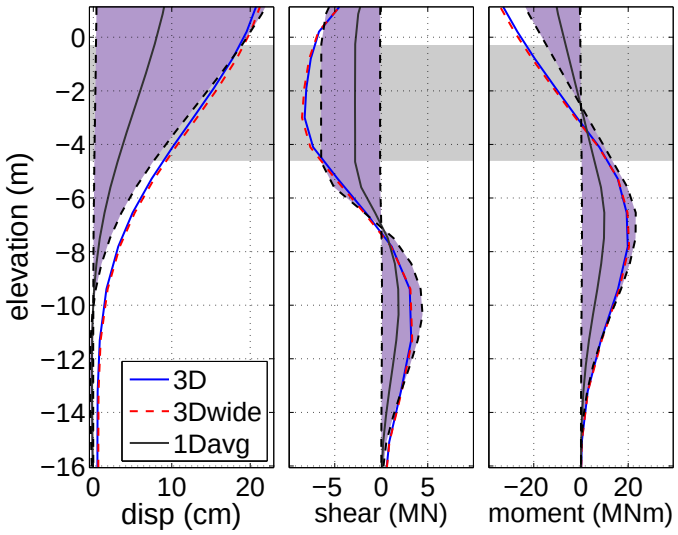

Figure 7.55: Average shaft bending demands at closure of 25 cm gap in applied kinematic model with zone of bending demands suggested by all cases considered in pile pinning model.

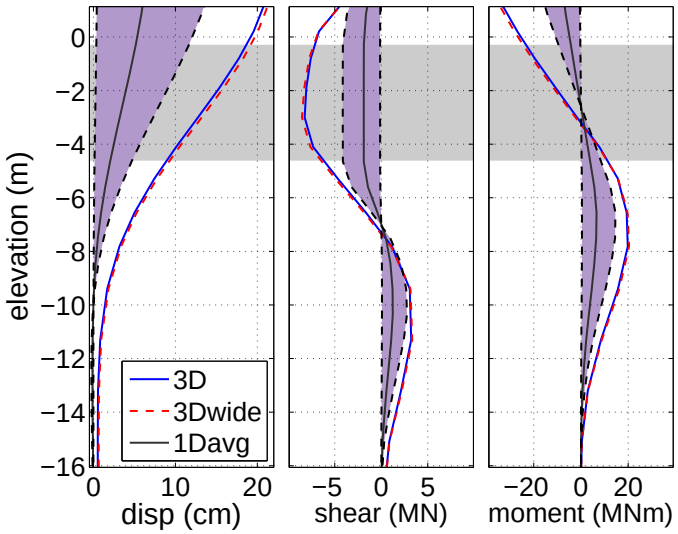

Figure 7.56: Average shaft bending demands at closure of 25 cm gap in applied kinematic model with zone of bending demands suggested by $F_{\text{deck}} \neq 0$ cases considered in pile pinning model.

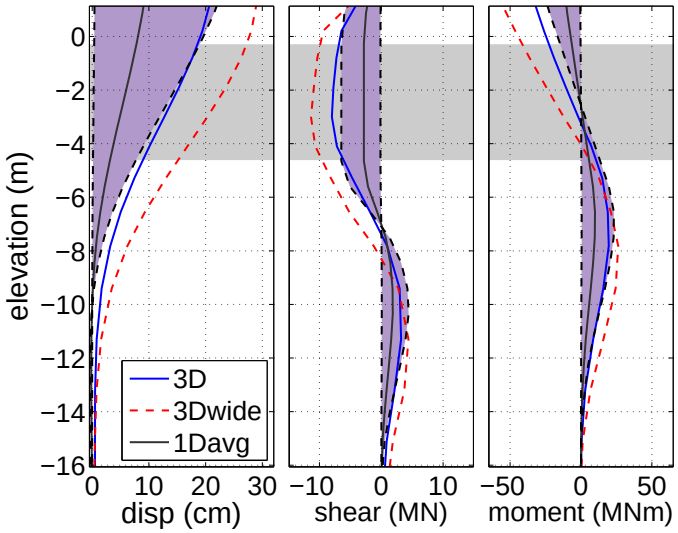

Figure 7.57: Average shaft bending demands at analysis end with 25 cm gap in applied kinematic model with zone of bending demands suggested by all cases considered in pile pinning model.

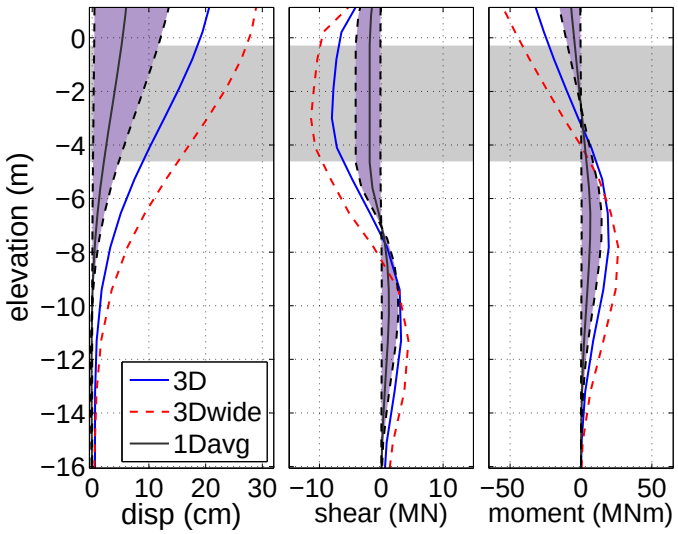

Figure 7.58: Average shaft bending demands analysis end with 25 cm gap in applied kinematic model with zone of bending demands suggested by $F_{\text{deck}} \neq 0$ cases considered in pile pinning model.

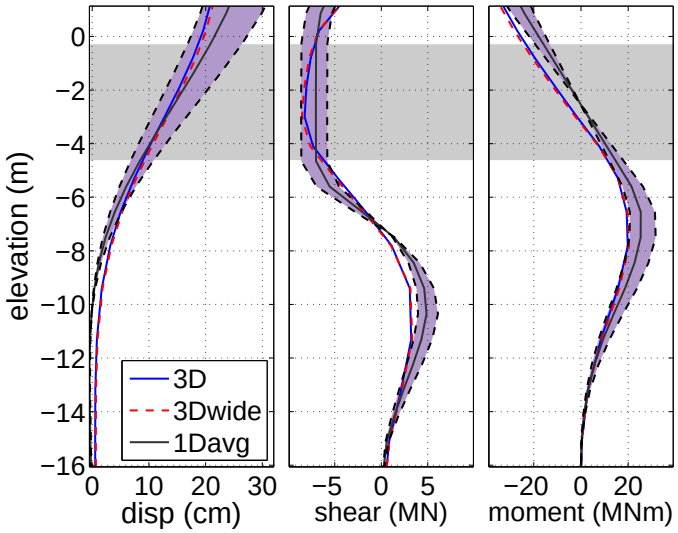

Figure 7.59: Average shaft bending demands at closure of 25 cm gap in applied kinematic model with zone of bending demands suggested by the sum of the compatible displacements for the $F_{\text{deck}} \neq 0$ cases with the gap magnitude.

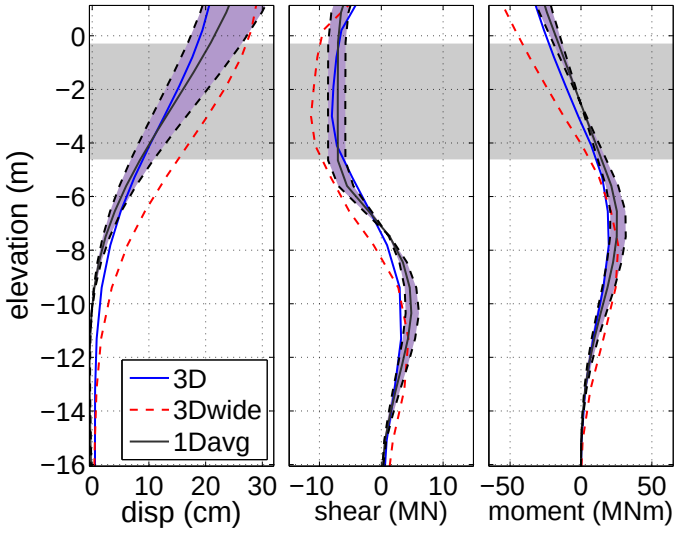

Figure 7.60: Average shaft bending demands analysis end with 25 cm gap in applied kinematic model with zone of bending demands suggested by the sum of the compatible displacements for the $F_{\text{deck}} \neq 0$ cases with the gap magnitude.

compatible state, then simply add the gap magnitude to the estimated compatible displacement and use the resulting displacement to determine the design foundation bending demands in the final BNWF analysis phase. Figures 7.59 and 7.60 demonstrate an application of this approach to the Puente Mataquito foundation. These plots compare the 3D results at the closure of the gap and the end of the analysis, respectively, to the bending demands resulting from adding 25 cm to the compatible displacements for the $F_{\text{deck}} \neq 0$ cases. With this modification to the pile pinning analysis, the shear force and bending demands moment for the 3D embankment geometry now compare more favorably to the pile pinning demands. Figure 7.60 also shows that the structural demands resulting from the wide embankment geometry in the 3D model remain larger than those predicted by the modified pile pinning approach, though the difference is not as great as for the unmodified pile pinning results and the smaller expansion gap.

The potential solution demonstrated here is rather simplistic, and further comparative studies are required to determine if this is a viable solution for general use, however, it appears to effectively introduce the effects of the 25 cm expansion gap into the pile pinning analysis for the foundation and site geometry at Puente Mataquito. With further research, the proposed solution of adding the gap distance to the compatible displacement value may prove to be a successful approach for dealing with lateral spreading design of bridges with larger expansion gaps.

7.7 Summary

The response of the southwest abutment at Puente Mataquito to lateral spreading was evaluated using two analysis approaches: simplified pile pinning analyses in which the foundation is represented using a BNWF approach, and 3D finite element analyses that consider the full geometry of the site. The results from these analyses were used to gain insights into the mechanisms that govern the response of abutment and foundation during the kinematic loading of lateral spreading.

The 3D FEA for the abutment demonstrated that there is a tangible difference in the foundation demands and soil deformation due to consideration of the three-dimensional embankment geometry. These analyses identified important mechanisms leading to this reduction in demands. During the simulated lateral spreading events, rather than pushing directly into the abutment and foundation, the embankment slumps vertically and deforms in the outward lateral direction, thus reducing the foundation demands. The pinning resistance of the foundation was also demonstrated using 3D models that considered gradual loss of shear strength and stiffness in the liquefied layer. The 3D modeling effort also showed how the presence of a bridge deck expansion gap affects the response of the system and the foundation, and identified the importance of the lateral resistance of the bridge

deck on the response of the site during lateral spreading.

The pile pinning analysis for the abutment was used to demonstrate that the application of this approach to an actual problem is not quite as simple as it may seem from a theoretical viewpoint, as seemingly minor changes in modeling choices, e.g., the chosen method of slope stability analysis, resulted in different compatible solutions. To overcome the observed variability in the compatible displacements predicted by this procedure, an approach is proposed in which the final design displacement is obtained as an average value from an array of compatible states computed using different assumptions. This proposed method requires many individual analyses for the design of a single foundation, however, the pushover and slope stability analyses involved in the pile pinning procedure are relatively inexpensive in terms of time and computational resources. Through comparison to the results from 3D FEA, it was shown that when applied carefully, the pile pinning procedure is able to predict foundation bending demands that correspond to a three-dimensional description of the problem, especially for smaller deck expansion gaps.

When performing the design of a bridge foundation using the pile pinning analysis procedure, it would be useful to have an independent prediction of how much pinning resistance can be expected for a particular combination of foundation, soil profile, and embankment geometry. The parameter study introduced in the following chapter addresses an approach to estimating the expected difference between the foundation displacement, shear force, and bending moment demands resulting from 2D and 3D descriptions of the problem. This difference can be interpreted as an indication of the amount of lateral pinning resistance available for a particular site.

Chapter 8

GENERAL MODEL DEVELOPMENT: LLACOLÉN BRIDGE

The Llacolén bridge was chosen as a representative case where soil embankment three dimensional effects are not present. In contrast the geometry of the bridge approach introduces structural three dimensional aspects to response to lateral spreading. Numerical models are therefore developed to assess these three dimensional effects. For this purpose beam on Nonlinear Winkler Foundation (BNWF) models are developed to test and compare simplified lateral spreading analysis procedures and 3D finite element models of the northeast approach are used to simulate the local response to lateral spreading kinematic demands and assess the potential 3D effects. Both of these models share certain aspects of model development which are described in this chapter. Specific considerations for development of each of these models are explained in Chapter 9.

8.1 Development of Idealized Soil Profile

Subsurface information available at the Llacolén bridge site are two series of pre-event Standard Penetration Test (SPT) blow counts and the information gathered after the event by reconnaissance teams and other institutes. First series of pre-event tests were conducted by the Japanese International Cooperation Agency (JICA) in 1993 at four locations along the bridge alignment. A consultant consortium of Systra-Sofretu/Cade Idepe performed six additional standard penetration tests in 1996. Figures 8.1a and 8.1c show the result profiles for these two series of standard penetration tests.

The GEER team conducted three Dynamic Cone Penetration Tests (DCPT) at the bridge site. They reported that the soil above 2^{m} deep was loose and the penetration was refused at the depth of $2.2\text{-}3.0^{m}$. They also performed a LIDAR (Light Detection and Ranging, Terretrial Laser Scanning) scan of the bridge and an SASW (Spectral Analysis of Surface Waves) test. The GEER team categorized the soil at the site as relatively uniform, consisting of very dark gray to black, medium to coarse grained sand with traces of fine gravel. Figure 8.2 depicts the data from their explorations.

Requested by University of California at Berkeley, el Centro de Investigación Desarrollo e Innovación de Estructuras y Materiales, IDIEM (the Center for Research, Development and Innovation of Structures and Materials), performed an additional SPT and two CPT tests. Figure 8.1b shows

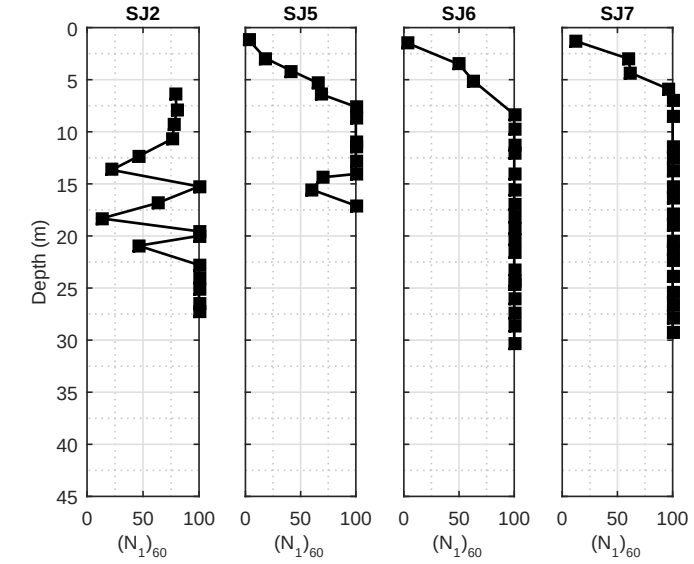

(a) JICA (1993)

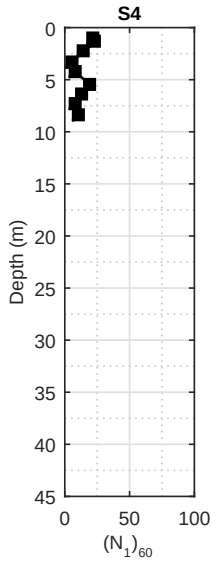

(b) IDIEM (2010)

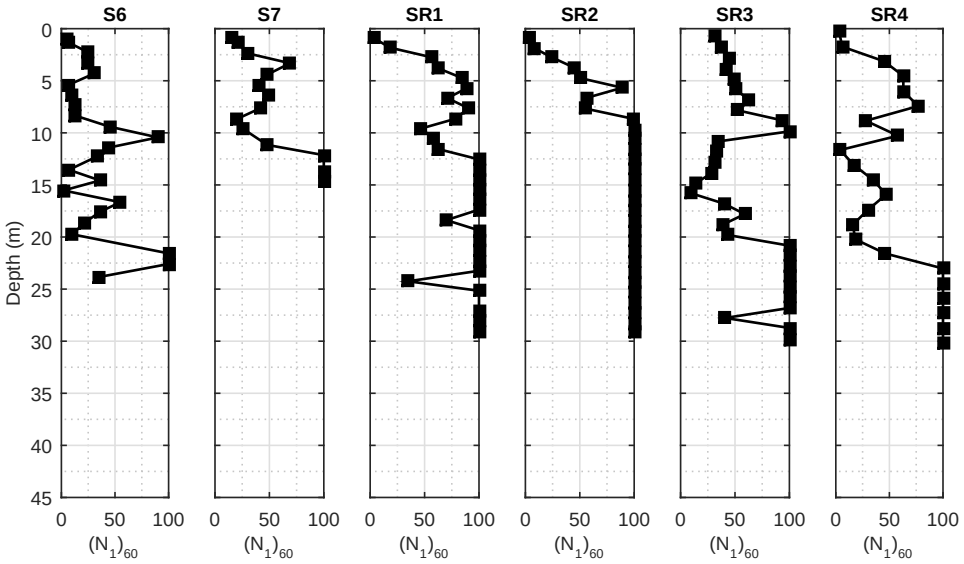

(c) Consultant consortium (1996)

Figure 8.1: SPT resistance profiles for subsurface explorations at Llacolén bridge site.

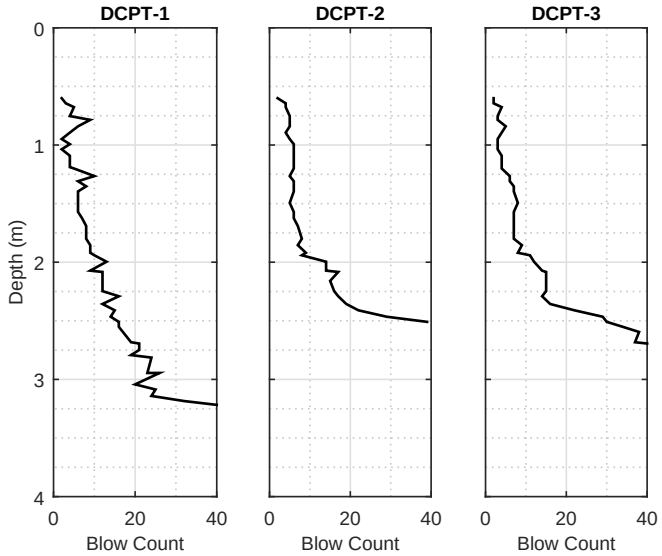

Figure 8.2: Dynamic Cone Penetration Test (DCPT) resistance profiles at Llacolén bridge site after the Maule earthquake.

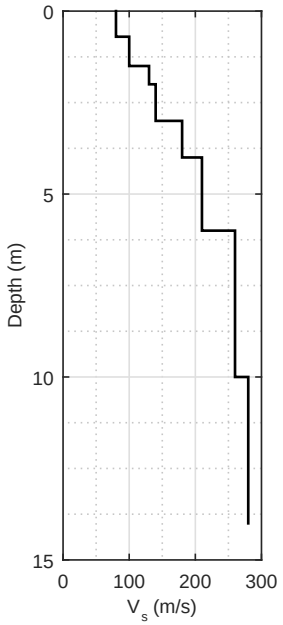

Figure 8.3: Shear wave velocity profile at Llacolén bridge site after the Maule earthquake obtained using SASW Method.

Table 8.1: Soil description at Llacolén bridge site (GEER, 2010a).

Height		Description
Top (m)	Bottom (m)	
0.00	3.00	Gray medium sand, homogeneous structure, average compactness
3.00	5.00	Brown medium sand, homogeneous structure, brick particles are observed at 5.00 m
5.00	7.45	Gray medium sand, homogeneous structure, low compactness, no plasticity.

No water table detected.

Table 8.2: Grain size distribution of the soil samples at Llacolén bridge site (GEER, 2010a).

Sample Depth (m)	1.00-1.45	1.75-2.20	4.00-4.45	4.75-5.20	7.00-7.45
USCS Class	SP-SM	SP	SP-SM	SM	SM
D_{10} (mm)	1.03	0.93	-	-	-
D_{30} (mm)	0.40	0.37	0.35	-	0.37
D_{50} (mm)	0.61	0.58	0.61	0.33	0.59
D_{60} (mm)	0.72	0.71	0.74	0.46	0.68
C_u	0.70	0.76	-	-	-
C_c	0.22	0.21	-	-	-

the SPT resistance profile and Figure 8.4 shows CPT penetration resistance profiles obtained by IDIEM. In order to perform the CPT tests, they needed to excavate the dense sand layers to allow for the penetration of the cone. This gave IDIEM an opportunity to get samples from the soil and perform grain size distribution analysis as well. It is worth mentioning that the CPT test at this site ended at a depth of 3.25^{m} because the cone resistance reached higher than $30.0\ ^{\mathrm{MPa}}$ indicating a granular material was encountered. Based on their observations, stratification of the soil layers are summarized in Table 8.1.

Using this information an idealized soil profile is obtained to be used in the development of the numerical models of the Llacolén bridge's northeast bent. Pre-event information is used for soil profile generation to disregard any soil disturbance due to liquefaction densifications. Some of the post-event information is used in different aspects of parameter identification for the soil as

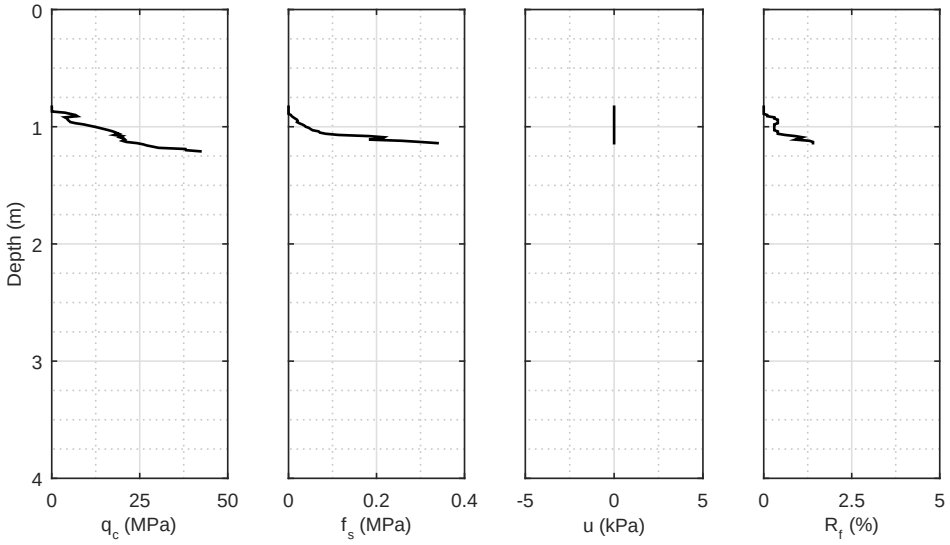

(a) CPT-9

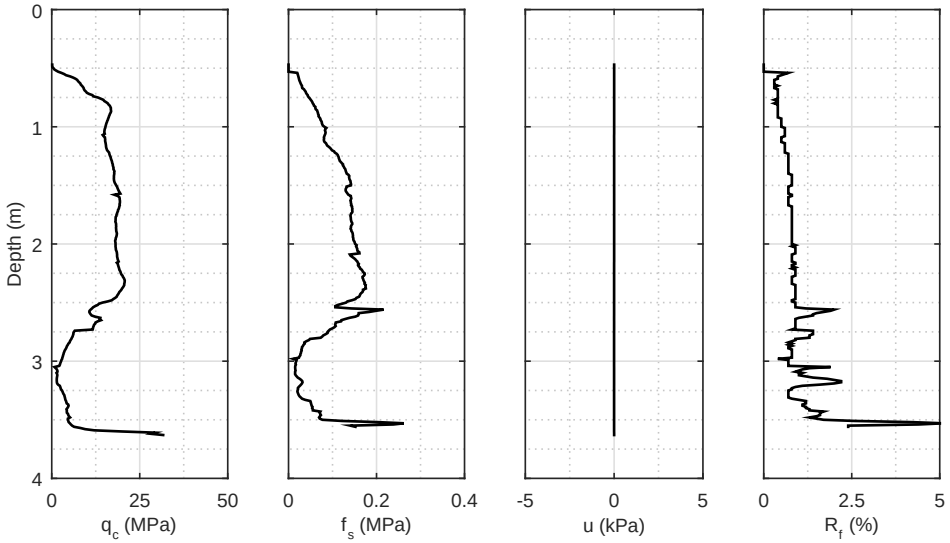

(b) CPT-10

Figure 8.4: Cone Penetration Test (CPT) resistance profiles at Llacolén bridge site obtained by IDIEM.

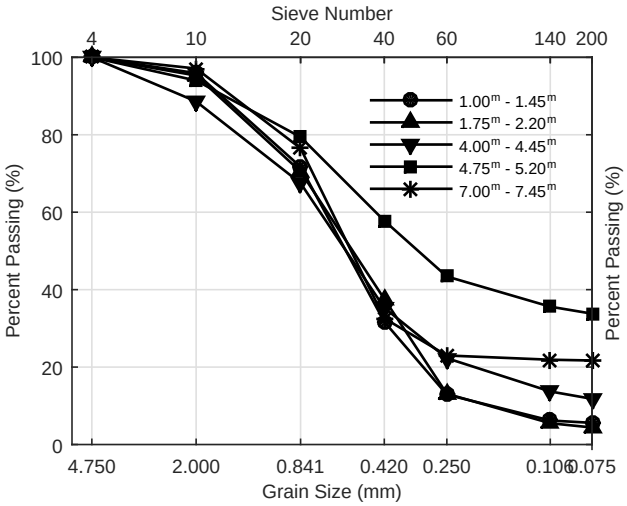

Figure 8.5: Grain size distribution of the soil samples at Llacolén bridge site (GEER, 2010a).

well. Figure 8.6b shows a longitudinal profile of the subsurface strata along the bridge axis and the location of the pre-event SPT experiments. The corresponding SPT resistance profiles are shown in Figure 8.1. The soil description provided by IDIEM (Table 8.1) indicates that the shallower parts of the soil are predominantly cohesionless. Although boring logs are not available for deeper soils at the site, boring logs at the adjacent bridge, Puente Juan Pablo II, indicate that the soil profile is generally non-plastic and cohesionless. For the purposes of the numerical models, minor variations in the soil profile are ignored and all materials are assumed to be cohesionless. The groundwater table is assumed to be at the average annual level of the river flow and all of the soil below the groundwater table is assumed to be saturated.

Based on the available subsurface information, the profile can be divided roughly into four soil layers, an upper loose sand layer, a middle layer of denser sand over a layer of medium dense sand and an underlying dense gravel layer. A weighted average SPT resistance value is calculated for each layer from the data illustrated in Figure 8.1. Representative friction angles, ϕ, for each layer are estimated from the SPT values using the correlation proposed by Kulhawy and Mayne (1990). Estimated properties for the site soils are summarized in Table 8.3.

8.1.1 Liquefaction Potential Assessment

Susceptibility of the soil to liquefaction at the Llacolén bridge site is assessed using the procedure proposed by Youd et al. (2002). The nearest available ground motion to Llacolén bridge site recorded

Table 8.3: Model properties for soil layers in idealized soil profile.

Soil Type	ρ (Mg/m^3)	ϕ (°)	$G_{\max}$ (MPa)	$K_{\max}$ (MPa)	e	ϕ_{pt} (°)
Loose sand	1.7	33	10.3	30.8	0.77	29
Dense sand	2.0	35	20.5	44.4	0.65	26
Med. dense sand	1.8	32	10.3	26.7	0.77	26
Gravel	2.1	42	41.0	80.0	0.55	26

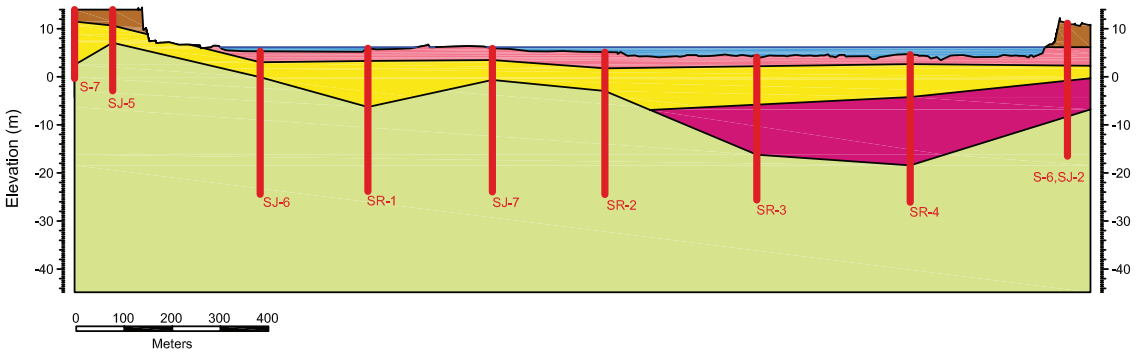

(a) Elevation view of the idealized soil profile with the location of SPT locations.

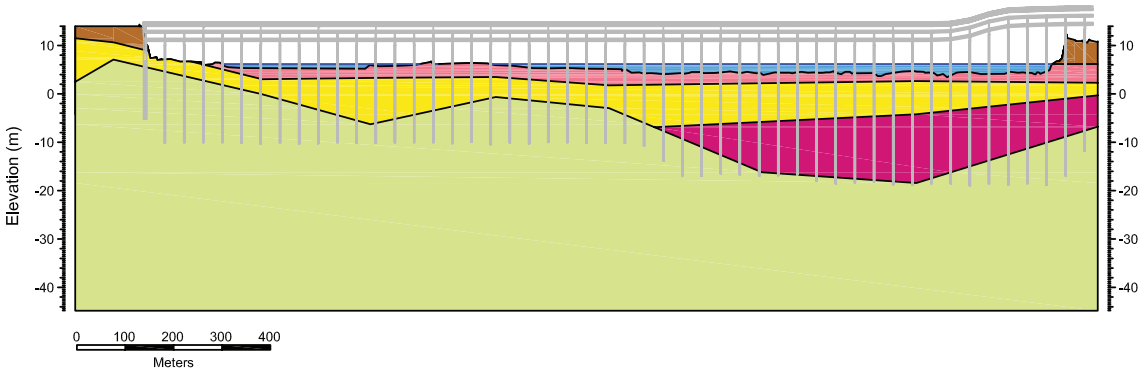

(b) Elevation view of the idealized soil profile with the longitudinal view of the bridge.

Figure 8.6: Elevation view of the idealized soil profile along with the location of SPT boreholes and the longitudinal bridge profile (Vertical scale increased).

a peak ground acceleration (PGA) of 0.65 g (Boroschek et al., 2010). Based on the available grain size distribution data for the upper parts of the soil profile, fines content fall in the range of 5% to 33%. An SPT resistance of 26 is shown to be the threshold value indicating if a soil in this site is susceptible to liquefaction. Based on this analysis, the saturated portion of the upper loose sand layer is shown to be susceptible to liquefaction. The assessment procedure by Youd et al. is only valid up to depths of 15 meters. Therefore the points below 15 meters are not considered in this analysis although they might be subject to liquefaction. This assumption is not necessarily representative of actual conditions at the Llacolén bridge site but for the purposes of this research is acceptable.

8.1.2 Constitutive Modeling of Site Soils

The same constitutive models described in Section 5.1.2 are used for the analysis of northeast approach of the Llacolén bridge. The Pressure independent constitutive model (J2 type) is used for the liquefiable layer to represent an almost incompressible soil layer, and pressure dependent (Drucker-Prager type) models are used to represent the behavior of all cohesionless soil. The input parameters for each soil type are summarized in Table 8.4.

Table 8.4: Contraction and dilation input parameters used in constitutive model for each soil type.

Soil Type	c_1	c_2	c_3	d_1	d_2	d_3
Loose sand	0.067	5.0	0.23	0.06	0.0	0.27
Dense sand	0.028	5.0	0.05	0.1	0.0	0.05
Med. dense sand	0.067	5.0	0.23	0.06	0.0	0.27
Gravel	0.013	5.0	0.0	0.3	0.0	0.0

8.2 Foundation Modeling Approach

Foundation shafts and pier columns are modeled taking the same approach as explained in Section 5.2. As shown in Figure 8.7, the pier consists of 11 columns and an inverted-T beam on which the girders are seated. This beam is modeled with displacement-based beam-column elements using properties that are calculated based on the geometry of the beam shown in Figure 4.15b. The same type of element is used to model the columns and foundation shafts. Pier columns are made of 1.35^{m}

circular sections with two different reinforcement layout (Figure 8.8a). The moment-curvature behavior of these sections under the assumed axial force is shown in Figure 8.9a. The foundation shafts are 1.5^{m} diameter circular sections with four different types of reinforcement arrangement(Figure 8.8b). Figure 8.9b depicts the moment-curvature diagrams of each of these sections. An empty circular region along the columns and piles representing the area occupied by the these elements is incorporated into the 3D finite element models. The interface between these elements and the surrounding soil elements is modeled using beam-solid contact elements (Petek, 2006). The cap beam which connects the piles to the columns is modeled with solid elements and an elastic constitutive model is assigned to these elements.

The bridge deck geometry (Figure 4.16) is not explicitly modeled in the numerical models, instead a linear elastic spring is used to represent the effects of the presence of the bridge deck. The constitutive behavior of the spring considers the existence of a gap which when closed acts in compression. The spring considers zero tensile and compressive stiffness if the gap is open. Based on the deck geometry and the reinforcement details of the deck shown in Figure 4.16, a gross cross-sectional area and a composite stiffness can be calculated for the bridge deck. Assuming a smeared reinforced concrete elastic modulus of $E_{deck} = 63.2^{\text{GPa}}$, and using the span length of 21 meters, a stiffness of $k = EA/L$ can be calculated for the deck spring. Assuming equal tributary area for each of the pier columns, the area A is divided by the number of columns and a spring is defined for each column. These springs are connected to the head of the columns on one side and are assumed fixed in the other side. The gap is assumed to be almost equal to the sum of the openings of the expansion joints on each side of the pier which is 10^{cm}.

8.3 Summary

An idealized subsurface soil profile is developed for the purpose of developing numerical models of the Llacolén bridge northeast approach. Details of the foundation elements and their modeling technique are described and used as a basis for all the foundations considered in this study.

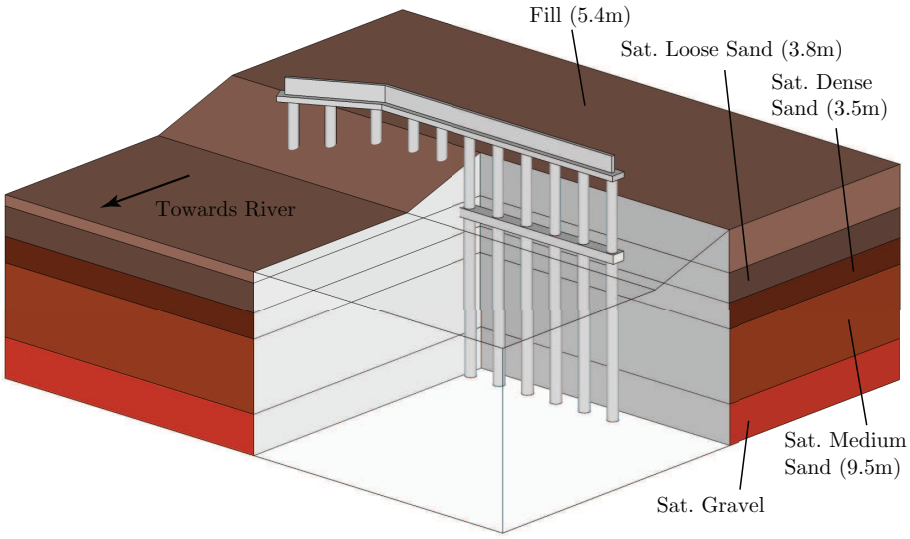

Figure 8.7: Schematic of the northeast approach of the Llacolén bridge with the idealized soil profile.

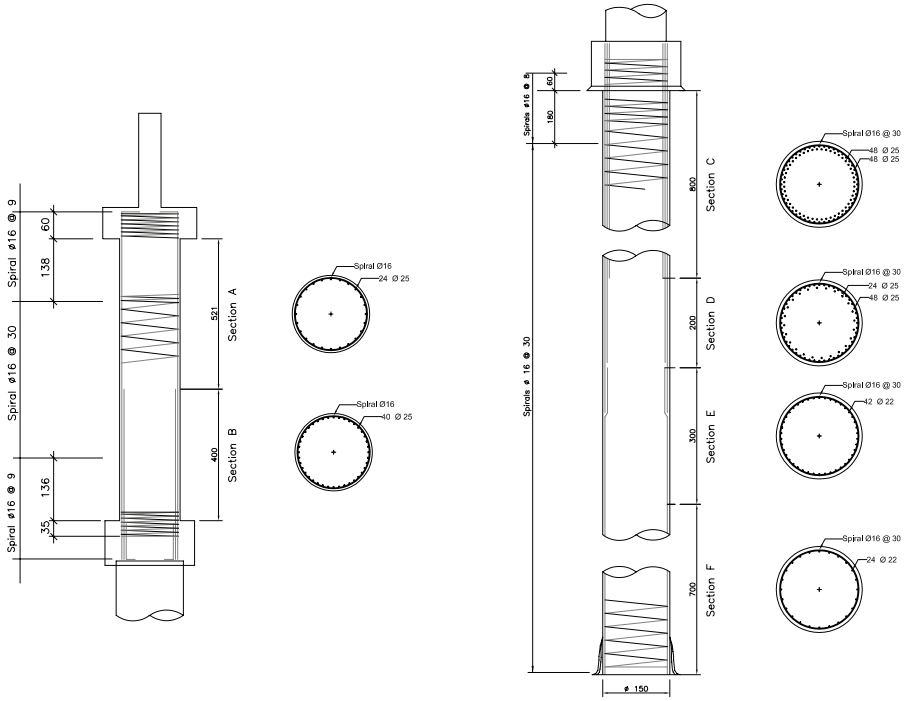

(a) (b)

Figure 8.8: Construction detail of the Llacolén bridge foundation shafts and pier columns.

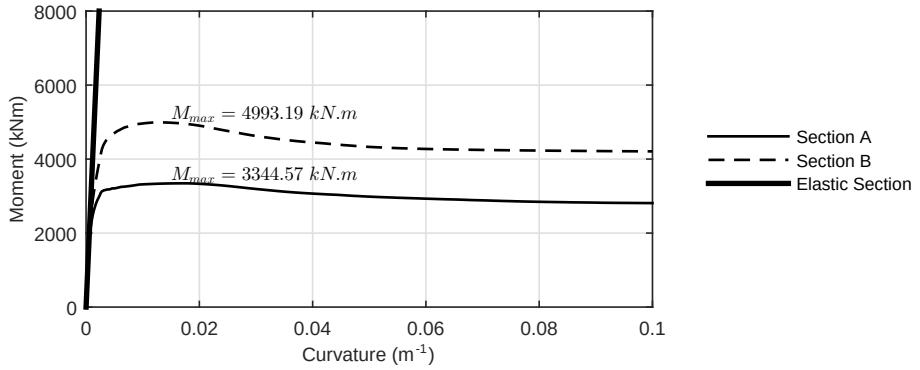

(a) Pier column sections A and B.

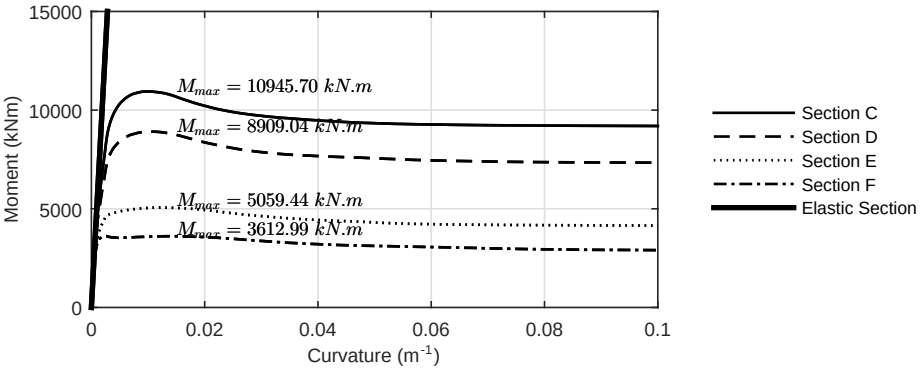

(b) Foundation pile sections C, D, E and F.

Figure 8.9: Model moment-curvature response for different sections of the Llacolén bridge foundation pile and pier column at design axial force. Equivalent elastic section stiffness is shown as initial tangent to moment-curvature response.

Chapter 9

SIMULATION AND ASSESSMENT OF EFFECTS OF LATERAL SPREADING ON NORTHEAST APPROACH TO LLACOLÉN BRIDGE

As discussed in Section 4.3 extensive evidences of liquefaction and lateral spreading were observed on the eastern bank of the Bío Bío river in the vicinity of Llacolén bridge. Moreover, the shape of the northeast approach provides an opportunity to assess three dimensional structural effects on the response of the bridge approach to lateral spreading. For this purpose, two types of numerical models are used: (1) the pile pinning analysis procedure involving a BNWF model of the foundation system, and (2) a 3D finite element model of the bridge approach. This chapter discusses details on the development of these models and presents results from the numerical simulations. Analysis and comparison of the results from the simplified and 3D numerical simulations are also included at the end of the chapter. Due to the length of the bridge and the large number of bridge spans two-dimensional plane strain simulations are not included in this study.

9.1 Pile Pinning Model Development

As indicated before, the Llacolén bridge fits the case where three-dimensional soil effects are not applicable. Therefore, following the Caltrans (2011) procedure for unrestrained ground displacement case presented in Section 3.1, the pile pinning model of the northeast approach is created. The purpose for development of this model is to assess the viability of this design procedure through comparison with the observations made at the bridge site and results of the 3D finite element models. Therefore a BNWF model of the foundation is developed using a representative shaft model and definition of p-y curves that appropriately captures the soil-shaft interaction for the idealized soil profile, liquefied layer and group effects.

9.1.1 Development of Foundation Model

The northeast approach pier foundation consists of 11 piles located side-by-side, 3 diameters apart and tied together with a cap beam. The cap beam is located in the liquefiable layer and is not likely to provide much resistance to lateral spreading. Each pile is made of reinforced concrete with 4 different reinforcement arrangement along their length resulting in 4 sections with different

Table 9.1: Properties of linear elastic equivalent beam model for grouped shaft foundation.

	Parameter	Single Shaft	Equivalent Shaft
Pier Columns	E	21.3 GPa	21.3 GPa
	I	0.163 m^4	1.793 m^4
	A	1.431 m^2	15.745 m^2
	G	8.52 GPa	8.52 GPa
Foundation Piles	E	19.0 GPa	19.0 GPa
	I	0.249 m^4	2.734 m^4
	A	1.767 m^2	19.439 m^2
	G	7.6 GPa	7.6 GPa

capacities and moment-curvature diagrams. The approach bent is made of 11 pier columns which are partly embedded and each consist of 2 different sections (Figure 8.9). The moment-curvature diagrams of these sections are scaled per Caltrans recommendations to convert the foundation system into an equivalent shaft.

Both linear elastic shaft response and nonlinear inelastic shaft response are considered and a separate model is created for each case. The properties for the linear elastic shaft are determined using the initial bending stiffness seen in the moment-curvature plots of Figure 8.9, and geometry of the sections. For a single pier column section the initial bending stiffness is $EI = 3.473\text{GN.m}^2$ which along with the gross second moment of area for a single shaft, $I_g = 0.163\text{m}^4$, results in an elastic stiffness $E = 21.3\text{GPa}$. Assuming a Poisson's ratio of 0.25, this elastic stiffness gives a shear modulus of $G = 8.52\text{GPa}$. These values for the foundation piles are $EI = 4.722\text{GN.m}^2$, $I_g = 0.249\text{m}^4$ resulting in $E = 19.0\text{GPa}$ and $G = 7.6\text{GPa}$. Table 9.1 presents a summary of the linear elastic equivalent shaft properties. The moment-curvature diagrams of single nonlinear shaft sections are scaled by the number of piles in the group.

Since the group of piles in the northeast approach of Llacolén bridge is a side-by-side arrangement except for the 3 northern piles that are located eccentric to the group axis, no rotational spring is considered in the BNWF analyses to represent the rotational stiffness due to group effects. Eccentricity of the northern 3 piles introduces some local rotational stiffness however it is assumed that this stiffness is negligible compared to global response of the bridge bent.

A linear compressional spring is used at the column head to represent the existence of the bridge deck. This spring incorporates a gap, before which closure no force is exerted to the foundation system. As the gap is closed, the spring acts in compression and simulates a linear elastic deck

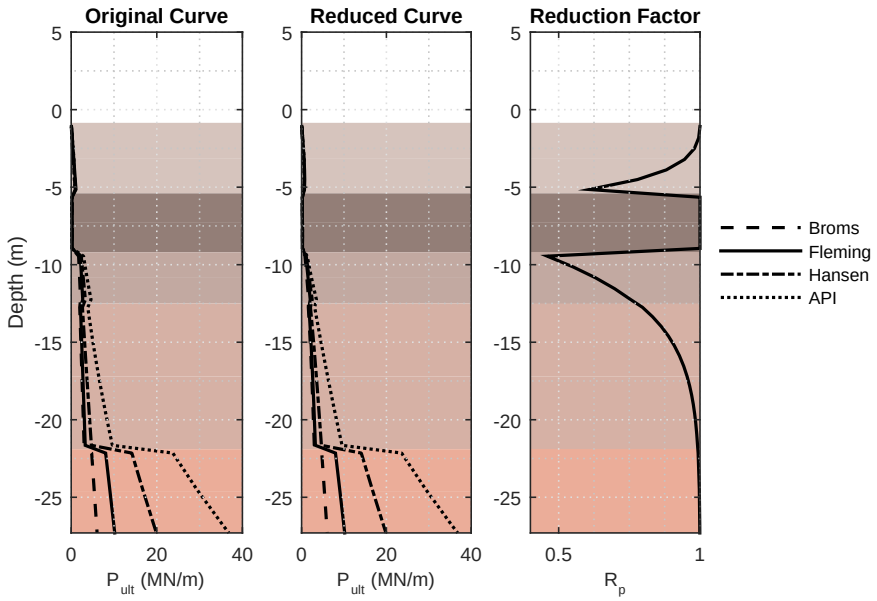

Figure 9.1: Calculated p_u for definition of p-y curves. Effects of liquefied soil layer on neighboring layers p_u is applied based on the procedure proposed by McGann et al. (2012).

section. Stiffness of this spring is calculated using the elastic properties of the deck and its geometry.

9.1.2 Definition of p-y curves

Soil-pile interaction in BNWF analysis is represented through series of p-y curves defined based on the idealized soil profile. Necessary parameters to define these curves are the ultimate lateral resistance, p_u, and initial stiffness, k_T. Four distinct methods for calculation of p_u based on the idealized soil profile properties are used here: (1) method by Broms (1964), (2) method by Fleming et al. (1985), (3) method by Brinch Hansen (1961) and (4) method by API (1987). Figure 9.1 shows the calculated values of p_u for each of these methods along with the reduced values due to the presence of a liquefiable layer as recommended by McGann et al. (2012). Although there is a great discrepancy among the values of p_u calculated using each of these methods specially at depth, since most of the deformations happen close to the surface, the results are less impacted by the variance of p_u values.

API (1987) presents an empirical relationship for the initial stiffness, k_T, of $p-y$ curves. Another method for calculating this parameter is using the modulus reduction of the idealized soil material and relating the strain at which the shear stiffness is reduced to half the original value, γ_{50}, to ϵ_{50}

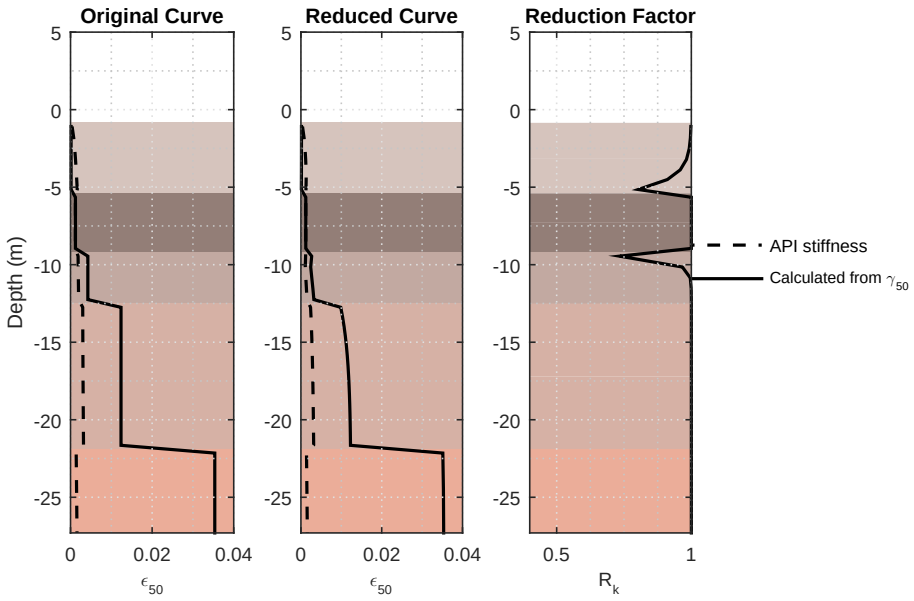

Figure 9.2: Comparison of the ϵ_{50} values based on the stiffness proposed by API and calculated based on γ_{50}, Effects of liquefied soil layer on neighboring layers ϵ_{50} is applied based on the procedure proposed by McGann et al. (2012).

which is the strain at which half the strength is mobilized in a conventional triaxial compression test. Then the initial stiffness is calculated using the semi-empirical equation $y_{50} = 2.5D\epsilon_{50}$ and the definition of the p-y curve, where y_{50} is the displacement at which half the p_u is mobilized and D is the pile diameter. Figure 9.2 illustrates the comparison between these two methods along with the reduced curves as proposed by McGann et al. (2012).

Caltrans (2011) recommends group efficiency factors of Mokwa and Duncan (2001) to incorporate the loss of efficiency of piles due to group effects. However this procedure is less applicable to side-by-side pile groups where only one row of piles exist. For side-by-side pile groups, Reese and Van Impe (2010) suggests using an efficiency factor of

$$e = \begin{cases} 0.64\,(s/D)^{0.34} & 1 \leq s/D \leq 3.75 \\ 1.0 & s/D \geq 3.75 \end{cases}$$

where s is the spacing between the piles. The group effect p-multiplier for the equivalent shaft model is computed as the product of number of piles with the group efficiency factor

$$p_{group} = 11 \times 0.93 = 10.23$$

Table 9.2: Displacements estimated using Bray and Travasarou (2007) procedure.

k_y (g)	$d_{16\%}$ (cm)	d (cm)	$d_{84\%}$ (cm)
0.05	88.7	171.6	332.1
0.1	35.8	69.3	134.0
0.15	18.1	35.1	67.9
0.2	10.5	20.3	39.3
0.25	6.6	12.8	24.7
0.35	3.1	6.0	11.5
0.45	1.7	3.2	6.2
0.55	1.0	1.9	3.7
0.65	0.6	1.2	2.3

The residual strength of the liquefiable soil is computed using the undrained shear strength hybrid expression presented by Kramer (2008) per Caltrans recommendation

$$S_{ur} = 2116 \exp\left(-8.444 + 0.109(N_{1,60}) + 5.379\left(\frac{\sigma'_v}{2116}\right)^{0.1}\right)$$

where S_{ur} is the undrained shear strength, σ'_v is the vertical effective stress, and $N_{1,60}$ is the corrected SPT blow count. For $N_{1,60} = 10$ and $\sigma'_v = 106^{\text{kPa}}$, the undrained shear strength of the liquefiable layer is computed equal to $S_{ur} \approx 15^{\text{kPa}}$.

9.1.3 Deformation Analysis

Ground crust displacement due to liquefaction of the subterranean layers is needed to define the displacement profile resulting in lateral spreading. (Caltrans, 2011) recommends using either the Newark-based method by Bray and Travasarou (2007) or the procedure by Faris et al. (2006) which is based on strain potential. Estimated ground displacements using the expression presented by Bray and Travasarou (2007)

$$\begin{aligned}\ln(d) = &-0.22 - 2.83\ln(k_y) - 0.333(\ln(k_y))^2 + 0.566\ln(k_y)\ln(\text{PGA}) \\ &+ 3.04\ln(\text{PGA}) - 0.244(\ln(\text{PGA}))^2 + 0.278(M-7) \pm \epsilon \end{aligned} \tag{9.1}$$

using a peak ground acceleration, PGA $= 0.65g$ and moment magnitude, $M = 8.8$ are summarized in Table 9.2. The value of k_y needs to be estimated using some slope stability analysis method.

The second method by Faris et al. (2006) requires computation of the Displacement Potential

Index (DPI) which is the integral of the strain potential within the liquefiable layer, that is $DPI = \int_{liq\ layer} \gamma_{max}\, dz$ where z is the depth measure. The amount of ground deformation is then estimated as

$$d_{max}(m) = [DPI(m)]^{1.07}$$

Wu (2002) gives a relationship between $N_{1,60}$ and the estimated cyclic stress ratio, CSR, corrected for earthquake magnitude. Using a magnitude corrected CSR of 0.3 and a corrected SPT blow count of 10, this relationships results in a $\gamma_{max} = 0.36$. This results in a maximum ground displacement of $d = 140.0^{\text{cm}}$. Such large displacements mobilize the passive resistance of the soil completely and the structural demands become insensitive to the amount of displacement. Therefore a displacement of 100^{cm} is considered for the BNWF analyses.

9.1.4 Assessment of Foundation Performance

The final stage in pile-pinning analysis is applying the displacement profile to the equivalent BNWF model and assess the foundation performance under such loading conditions. Estimated p_u values using different methods result in slightly different foundation demands. Figure 9.3 shows the shaft displacement profile, shear force diagram and bending moment diagram resulting from lateral spreading pushover analysis of the BNWF model developed using each of the methods for estimating p_u values. In this figure a deck spring with a 10^{cm} gap is considered and initial stiffness of p-y curves are calculated using γ_{50}. This figure shows that BNWF results are relatively insensitive to the method chosen for definition of the ultimate lateral resistance of the p-y curves. Figure 9.4 depicts the effects of choosing initial stiffness using any of the two methods described previously. In this case no deck spring is considered to emphasize the effect of the choice of stiffness on the results. Behavior of the shafts are linear elastic in this case to remove any side effects caused by the nonlinear behavior of the shafts. The effects are relatively small and are even smaller in the case a 10^{cm} gap deck spring is considered. From this point on, all the presented results are from cases using p_u calculated from Brinch Hansen (1961) and initial stiffnesses calculated using γ_{50}.

Figure 9.5 compares BNWF results for linear elastic versus nonlinear cases and also cases with a 10^{cm} gap deck versus cases with no deck considered. The importance of considering nonlinear behavior of the shafts is obvious since in the case with no deck, a plastic hinge is formed and the bending moments are redistributed. The shear force and bending moment diagrams are quite different in this case. However in the case where a deck spring is present, linearity of shaft behavior plays a less important role and there is no meaningful difference between them. In cases where a deck spring is considered the bending moment demands are different in nature. In these cases a

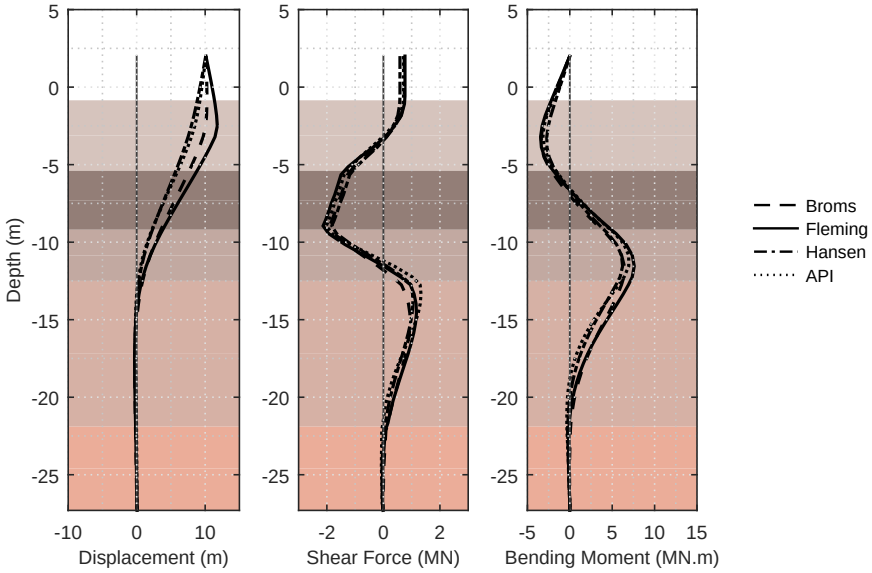

Figure 9.3: Effect of different p_u calculation methods on shaft bending demands at the end of analysis for 1-D BNWF model with 10^{cm} gap using back-calculated stiffness from γ_{50}.

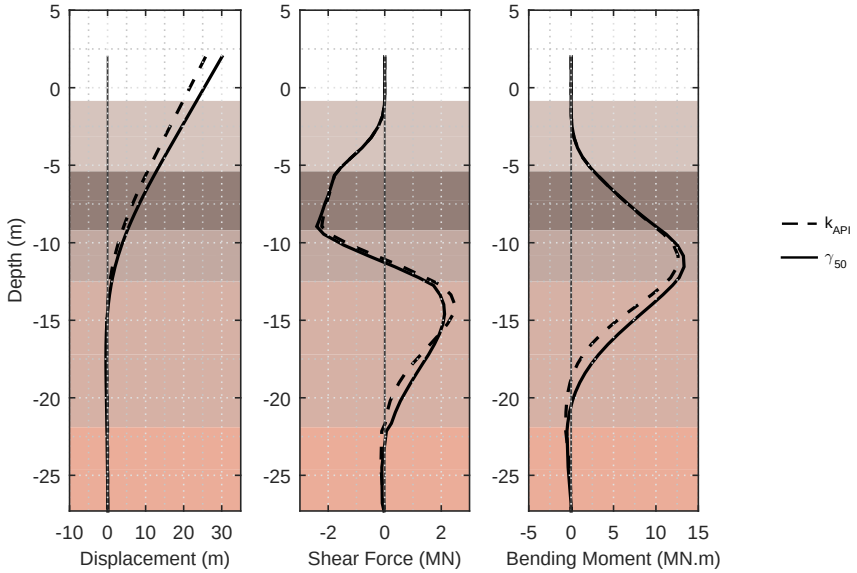

Figure 9.4: Effect of different initial stiffness calculation methods on shaft bending demands at the end of analysis for 1-D BNWF model with no deck using Hansen formulation.

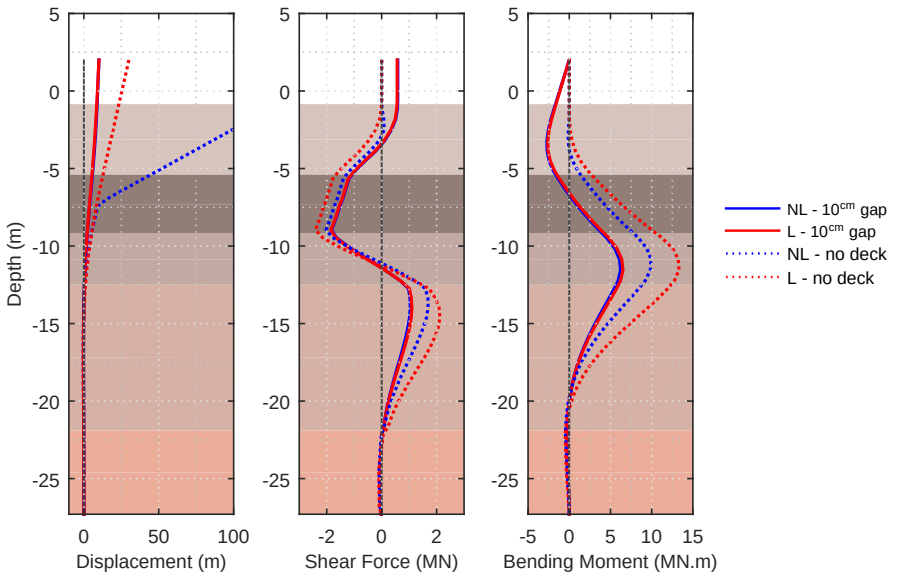

Figure 9.5: Effect of linear vs. nonlinear structural response on shaft bending demands at the end of analysis for 1-D BNWF model.

negative moment demand is seen close to the surface due to the lateral force applied by the deck while decreasing the positive demands at depth.

The amount of lateral spreading observed in the bridge site is reported about 25^{cm}. Figures 9.6 and 9.7 depict the evolution of demand profiles with increasing free field displacements. It is obvious that at a 25^{cm} free field displacement the strength of the soil springs is fully mobilized close to the surface where most of the lateral spreading displacement profile exists. Comparing the result profiles from the case with no deck for 25^{cm} and 100^{cm} ground displacements, it is apparent that formation of the plastic hinge results in redistribution of the bending moments. Figure 9.7 however shows that as soon as the deck gap is closed, further application of free field displacement has minimal effect on the structural demands.

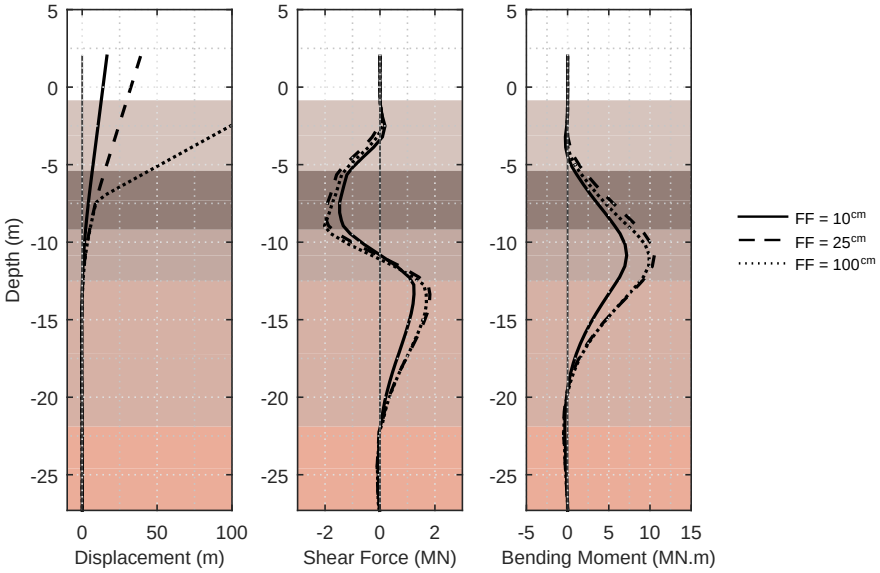

Figure 9.6: Effect of free field displacement on shaft bending demands for 1-D BNWF model with no deck.

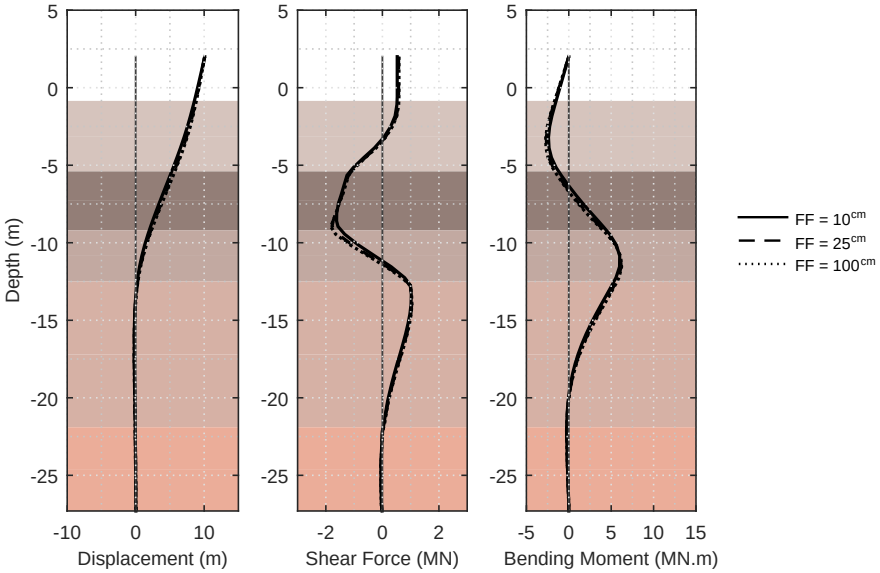

Figure 9.7: Effect of free field displacement on shaft bending demands for 1-D BNWF model with 10^{cm} gap.

9.2 3D Finite Element Model Development

Figure 9.8a depicts the domain considered for finite element analysis of the northeast approach pier of the Llacolén bridge along with a simple representation of the bridge pier with its foundation system. The foundation structure consists of the 11 piles connected to each other by means of a cap beam. The end of 11 bridge pier columns embed into the cap beam to transfer the loads to the foundation. Bridge girders are simply seated on an inverted-T beam which transmits the loads of the superstructure to the pier. The bank slope is protected from erosion with a rock rip-rap. A 4V:13H slope is assumed based on the information available and material properties of the upper dry sand layer is applied to this layer for simplicity. For the sake of simplicity, soil layering is assumed to be horizontal and extend to the boundaries of the model. Also since the gravel layer in which the pile toes are embedded is very stiff ($N_{SPT} > 100$), it is assumed that this layer extends only to the bottom of the shaft foundations and, as explained in the following sections, pile toes are assumed to be fixed against translation in vertical direction. A representative three dimensional mesh is created for this domain to analyze the response of bridge piers to kinematic demands due to lateral spreading. As shown in Figure 9.9, the mesh is selectively refined near the foundation and element size becomes larger with increasing distance from the foundation.

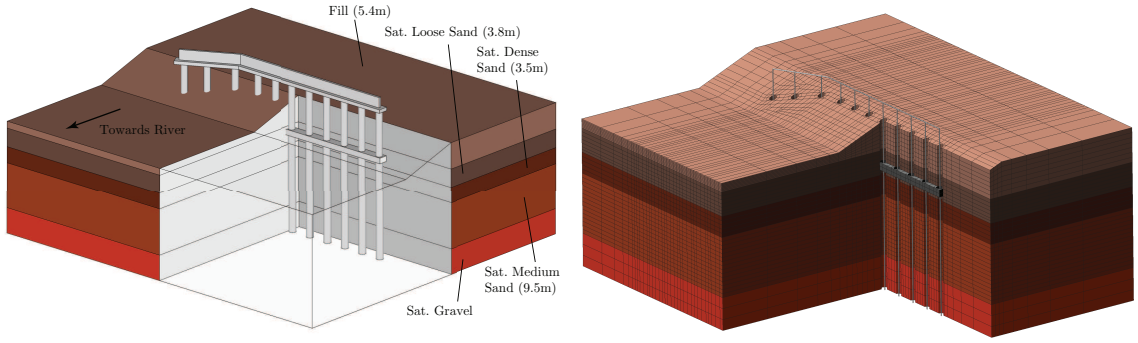

(a) Schematic of the bridge approach.

(b) 3D finite element mesh.

Figure 9.8: Schematic of the northeast approach of Llacolén bridge and generated 3D finite element mesh.

Stabilized single-point integration solid elements (McGann et al., 2015) are used to model the soil and the embedded cap beam. This type of element uses a stabilization technique to minimize effects of hourglass locking with a single integration point and provides a fast and at the same time reliable computational analysis. Constitutive models proposed by (Elgamal et al., 2003) are

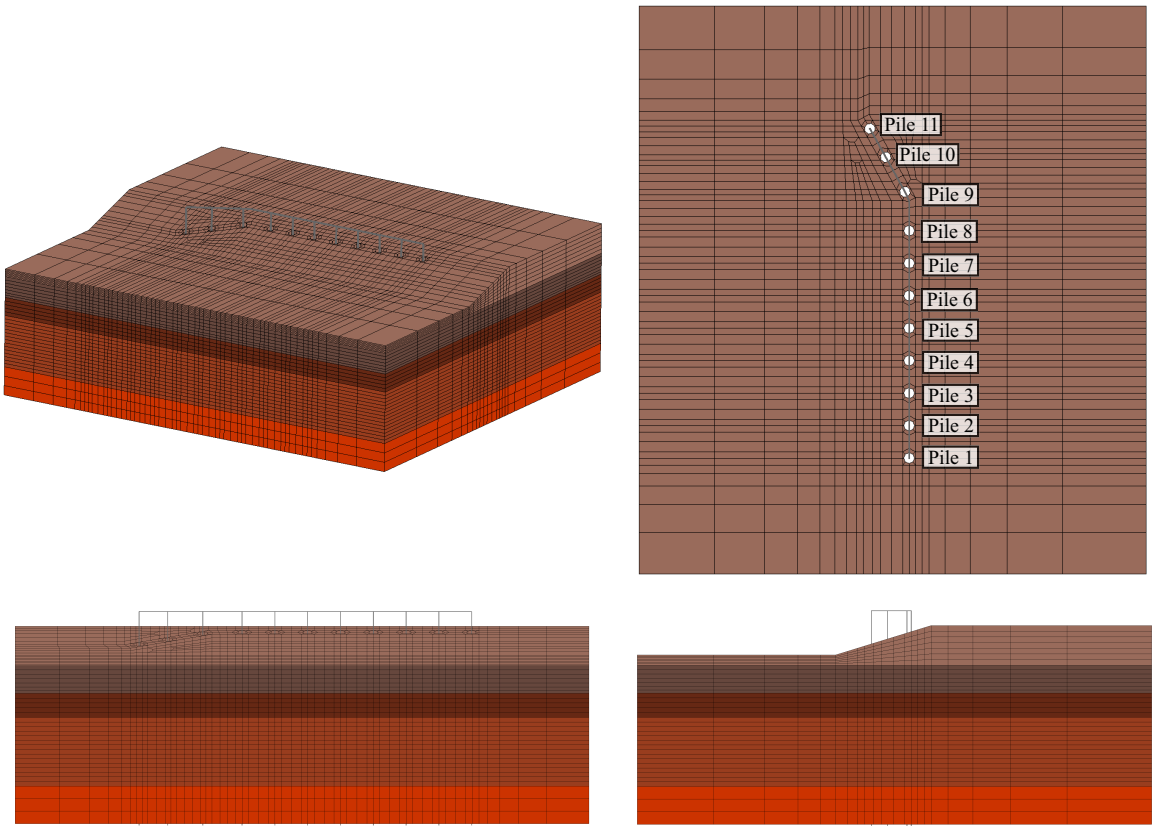

Figure 9.9: 3D finite element mesh for northeast approach of Llacolén bridge.

used to model the soil behavior. Total stress analysis assumptions are used for the purposes of this research and therefore no consideration for pore water pressure effects is made. Piles, columns and the inverted-T beam are all modeled using beam-column elements. The interface between the piles and the surrounding solid nodes is modeled using beam-solid contact elements (Petek, 2006).

All numerical models are developed and analyzed using the OpenSees computational framework (McKenna, 1997; McKenna et al., 2010; OpenSees, 2007). OpenSees (Open system for Earthquake Engineering Simulations) is an open source, object-oriented finite element platform maintained by Pacific Earthquake Engineering Research (PEER).

9.2.1 Boundary and Loading Conditions

Size of the model and foundation proximity to model boundaries are chosen to minimize boundary effects and to eliminate the errors associated with modeling only a portion of a very large soil domain.

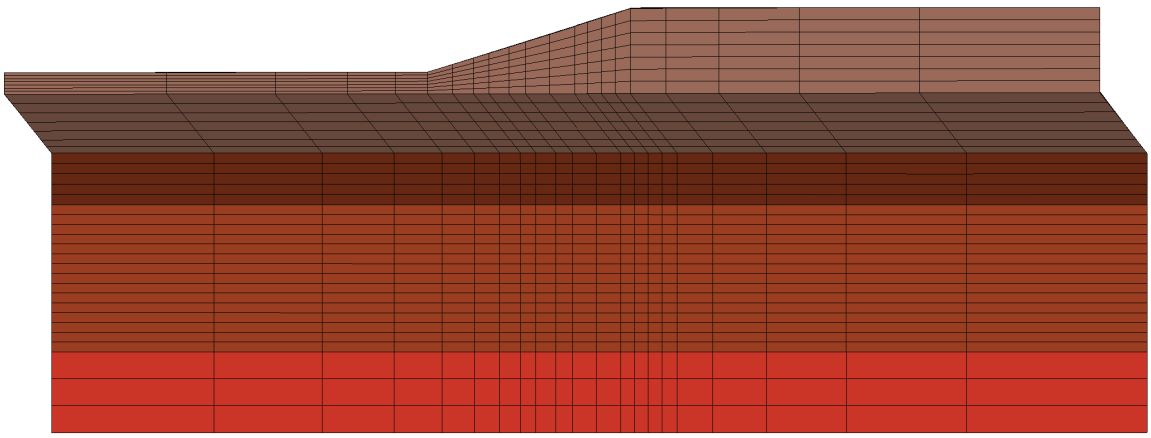

Figure 9.10: Displacement profile applied to mesh boundaries used to simulate kinematic demands of lateral spreading.

All the nodes on the vertical boundary planes are fixed against out-of-plane translation. The gravel layer at the bottom of the model is a very stiff soil which is assumed to be almost incompressible below the foundation. Therefore all the nodes at the base of the model, including both solid and beam nodes are restrained in vertical translation. As a result toe bearing effects on the piles are ignored.

Weight of the deck portion corresponding to the tributary area for each column and span is calculated and applied to the columns. Weight of the columns and shafts at different sections are calculated and applied along the elements in order to represent the actual axial loads in these elements. Application of these loads is necessary to account for the nonlinearity in the foundation elements.

Kinematic demands of lateral spreading are applied using a gradually increasing displacement profile to the vertical boundaries. This type of displacement profile represents the free-field kinematic demands on the soil system. It is assumed that layers above the liquefiable layer move a constant amount laterally with respect to the underlying material. The transition between the translation of above-liquefiable-soil layers and below-liquefiable-soil layers is assumed linear over the thickness of the liquefiable layer.

9.2.2 Modified Soil Properties

The effects related to the liquefaction initiation process are irrelevant to the objectives of this research. The goal here is to assess the foundation response to the kinematic demands of lateral

spreading. Therefore it is assumed that the kinematic demands are applied while the properties of the liquefied layer is modified so that this layer has a low shear stiffness and nearly incompressible volumetric response associated with a liquefied state. Also an undrained strength value representing the ultimate residual strength of the liquefied soil is used for this layer. The properties of the remaining soil layers is kept the same as their assumed properties discussed in Section 8.1.

9.2.3 3D FEA of Northeast Approach with Applied Kinematic Model

As discussed in the previous sections, effects of lateral spreading on the bridge foundation is modeled using a kinematic displacement pattern applied to the boundaries of the model in a quasi-static manner. Reconnaissance teams estimated the amount of spreading to be around 25^{cm} based on their measurements done at the site. Given the extent of damage and structural deformation, it is probable that the amount of lateral spreading was more than the measured accumulation of ground cracks on the surface. In this study, a 1^{m} lateral spreading is applied and the results are contrasted to the 25^{cm} observed lateral spreading response.

To evaluate the effects of the bridge deck on the foundation response, the deck is modeled using a compressional spring with an assigned gap. There is a 10^{cm} expansion gap between the bridge deck and the pier structure on each side. Models with different gap values (10, 20, 30^{cm} and ∞) are created and the results are shown in the following sections.

As an initial analysis, elastic behavior was assigned to the pier columns and the foundation structural elements. However it turns out that the nonlinear response of these elements is of high importance and in some cases may change the mechanism totally. Effects of nonlinear material behavior of the columns and piles are assessed through contrasting the initial model results with linear behavior to an additional model with nonlinear material behavior.

9.2.4 Global Model Response

Figures 9.11–9.13 show the deformed mesh with horizontal displacement contours for 10^{cm} gap, 20^{cm} gap and no deck conditions. Deformations are magnified 5 times for better visualization. In all these figures, nonlinear pile and column behavior is considered and the results correspond to the maximum applied kinematic boundary condition equal to 1^{m}. The horizontal displacements shown in these figures are the component of the displacement in the direction of lateral spreading. Figure 9.14 depicts the component of the displacement perpendicular to the direction of lateral spreading. Results shown in this figure are from the case with a 10^{cm} gap.

The effect of the bridge foundation resistance is obvious in all Figures 9.11–9.13. This effect is

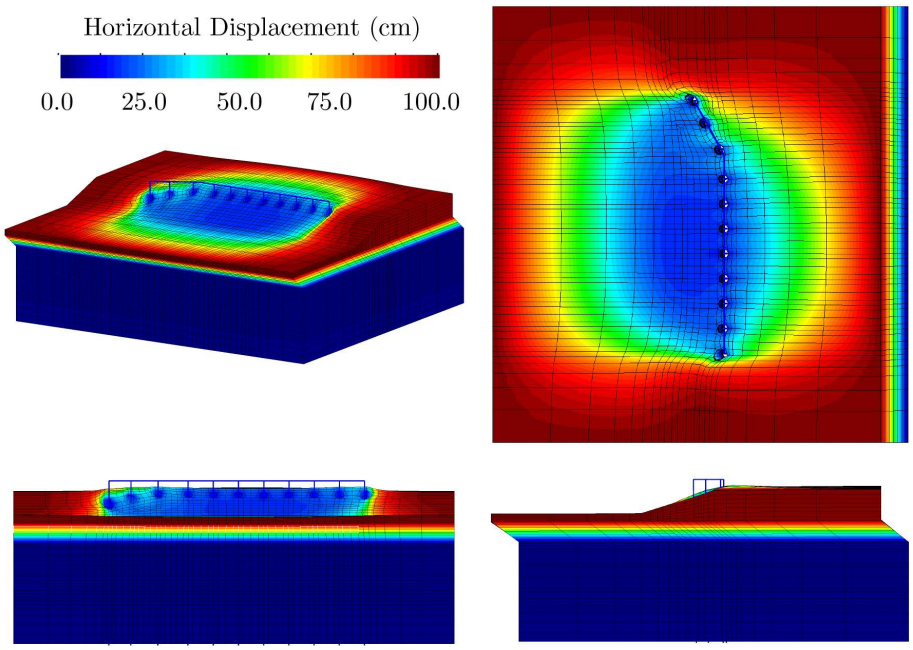

Figure 9.11: Deformed mesh (magnified 5 times) for 10^{cm} gap applied kinematic model with contours of river-ward horizontal displacement.

more pronounced in cases where a smaller gap is considered for the bridge deck. Figure 9.11 shows displacement results for the model with a 10^{cm} gap deck spring. In comparison with Figure 9.12 showing the results for a 20^{cm} gap model, the near-field displacements are more affected since the bridge deck stiffness provides more resistance at earlier stages of the loading program, leading to more contrast in the near field displacements versus the free field displacements. Figure 9.13 shows the results for a case without bridge deck. In this case the resistance comes from the structural stiffness of the foundation system and the superstructure does not affect the response.

Contours of displacement in the transverse direction (perpendicular to the direction of lateral spreading) are shown in Figure 9.14. This figure shows that due to the resistance of the bridge foundation, the soil mass is forced to flow around the bridge foundation, specially on the northern side. This relative more concentration of displacement is due to the shape of the bridge pier in this location where the bridge pier is angled at about 29° relative to the pier axis. The three-dimensional effects resulting from the geometry of the bridge pier cannot be captured in any one or two dimensional analysis methods and is of high importance. A closer look in the same region in this figure shows that near the piles located at the angled part of the bridge, the soil is forced to flow around the individual piles more than around any other pile at the straight part.

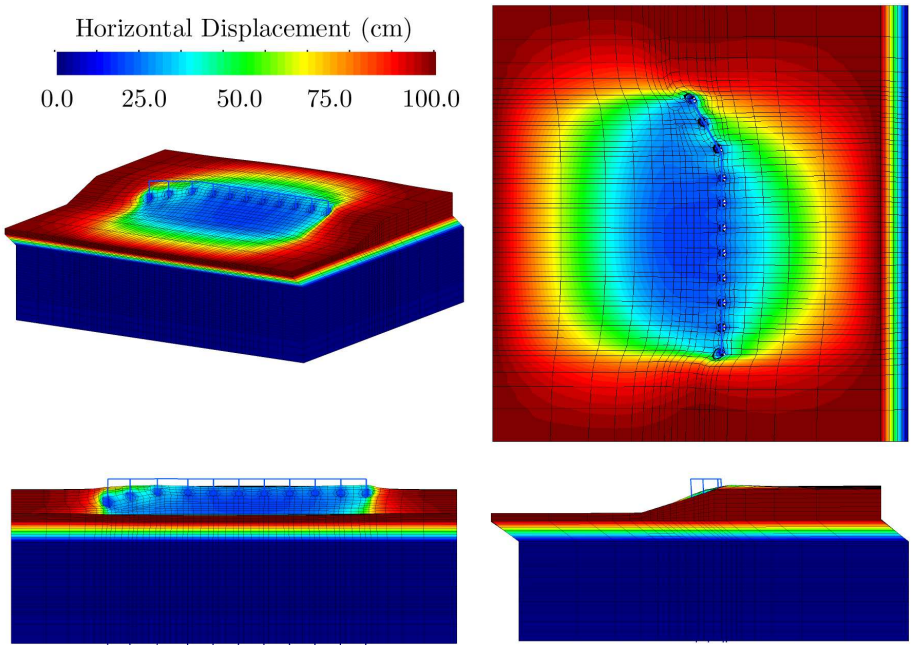

Figure 9.12: Deformed mesh (magnified 5 times) for 20^{cm} gap applied kinematic model with contours of river-ward horizontal displacement.

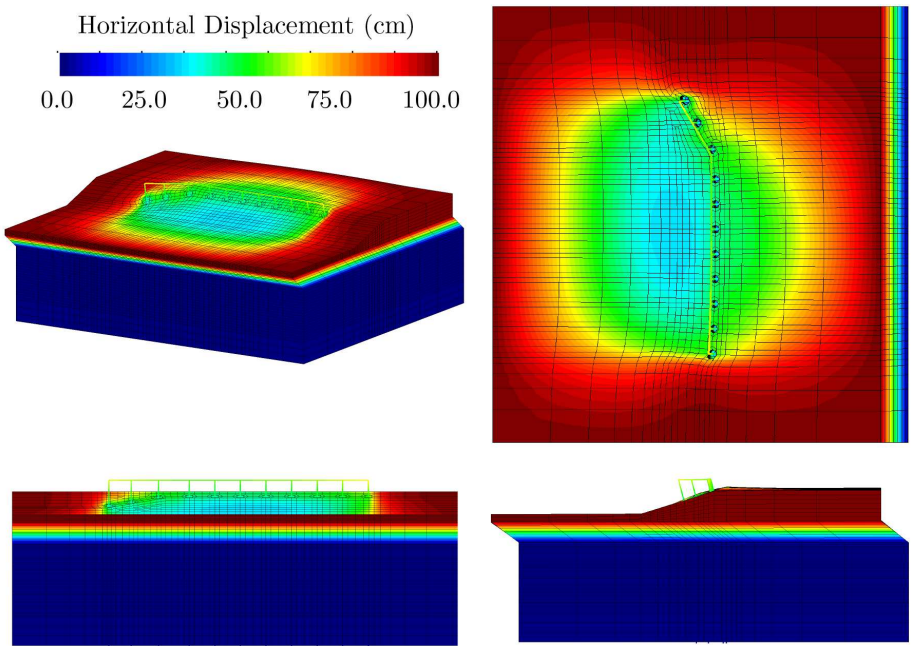

Figure 9.13: Deformed mesh (magnified 5 times) for no deck applied kinematic model with contours of river-ward horizontal displacement.

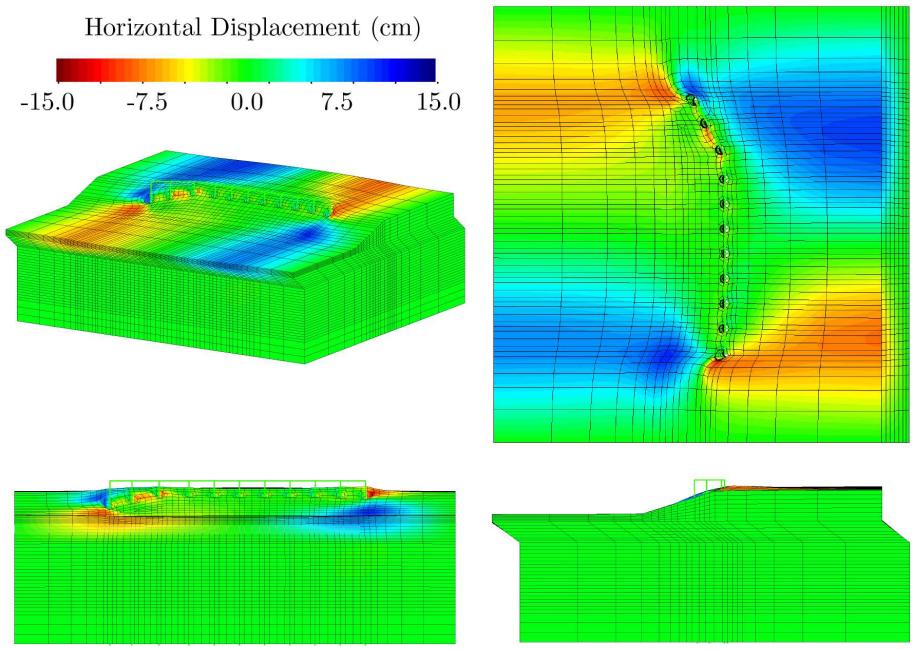

Figure 9.14: Deformed mesh (magnified 5 times) for 10^{cm} gap applied kinematic model with contours of transverse horizontal displacement.

9.2.5 Pier and Foundation Response

Figure 9.15 shows the displacement of the bridge pier at the top of the pier column 1 over the course of the free field displacement application. Results from models with 10^{cm} gap, 20^{cm} gap and 30^{cm} gap are shown in this figure. Figure 9.15a shows the results when elastic behavior is assigned to the shafts and Figure 9.15b shows the results when elastoplastic behavior is considered for the shafts. The 1: 1 bisection line is shown for reference. For all these cases, after the closure of the expansion gap, the displacement of the pier is effectively impeded by the stiffness provided by the bridge deck and is essentially constant. Prior to closure of the gap, pier movement is closer to the free field displacement indicating that the foundation provides much less resistance. It is important to consider the rotation of the column in this observation as the location of the the top of the bridge pier is several meters above the ground surface and small rotations at the ground surface elevation of the shafts result in larger displacements at the top of the column.

In cases where no deck spring is considered, the elastoplastic shafts show larger displacements due to their softer responses. Specifically the response shows a sudden increase in the displacements at free field displacements of around 75^{cm}. At this point, a plastic hinge is formed along the shaft

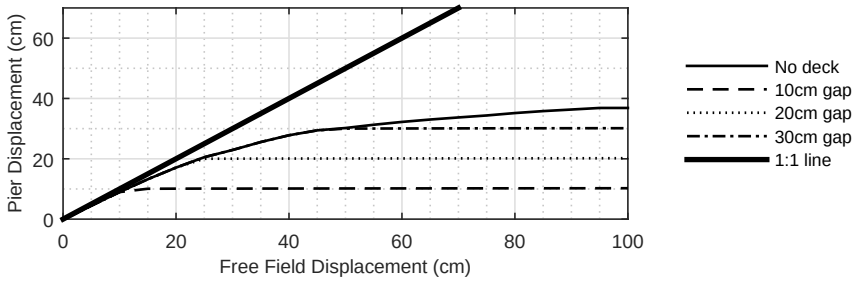

(a) Linear elastic beam elements.

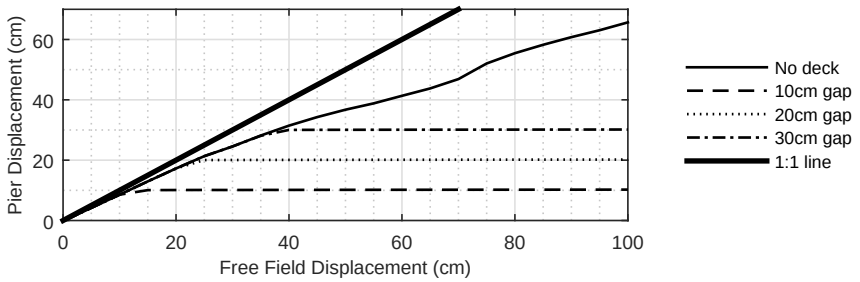

(b) Nonlinear beam elements.

Figure 9.15: Evolution of pier beam displacement in direction of loading for various gap sizes.

and a mechanism forms leading to larger displacements.

As mentioned before, the stiffness of the bridge deck spring is simply calculated based on the young modulus of the concrete, the cross-sectional area of the deck and length of the span. Calculation of the actual stiffness is more complicated. In order to consider the effect of the deck stiffness, models with deck spring stiffnesses based on different span lengths are created and the results are shown in Figure 9.16. Prior to closure of the gap these models are essentially the same and the responses are equal. Even after the gap is closed, the response is not very sensitive to the stiffness of the deck. This is expected since axial stiffness of the deck is much higher than the lateral flexural stiffness of the pier.

Figure 9.17 compares the displacement of the pier at different locations. Also shown in this figure is the displacement of the pier in the transverse direction. Displacements in the direction perpendicular to the lateral spreading direction are much smaller compared to the other direction. This is expected due to the direction of the kinematic loading. Also, the stiffness of the pile group in the transverse direction is much greater. Complimentary to these results, shown in Figures 9.18 and 9.19 are the displacement of the pier beam at the end of the application of 1^{m} free field displacement

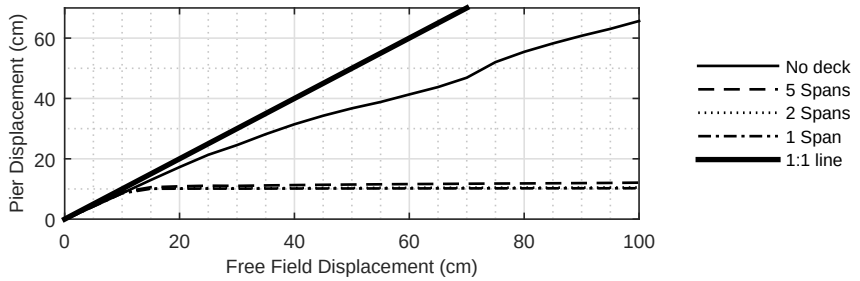

Figure 9.16: Evolution of pier beam displacement in direction of loading for 10^{cm} gap with various deck stiffnesses.

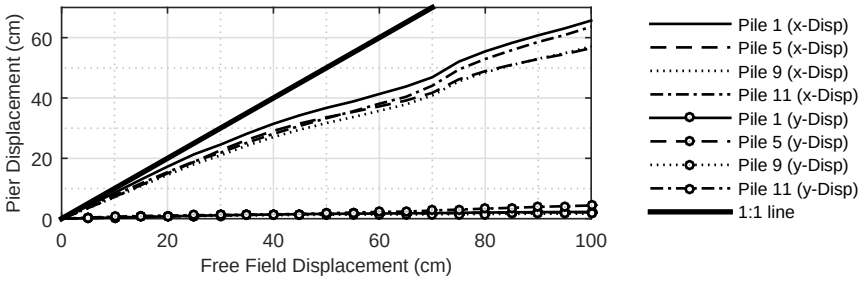

Figure 9.17: Evolution of pier beam displacement in direction (x-disp) and perpendicular (y-disp) to loading for no deck case. Refer to Figure 9.9 for pile numbering.

for a case with a 10^{cm} gap and a case with no bridge deck. Figure 9.18 shows relatively uniform displacements in both directions parallel and perpendicular to the direction of lateral spreading. Less uniform displacements at the distal locations are expected due to less structural stiffness at these locations. This effect is more pronounced in Figure 9.19 where the bridge deck is not modeled. Displacements are less uniform in both directions. Transverse displacements are mostly uniform in the straight portion of the pier. However in the angled part of the pier an obvious hinge mechanism is formed.

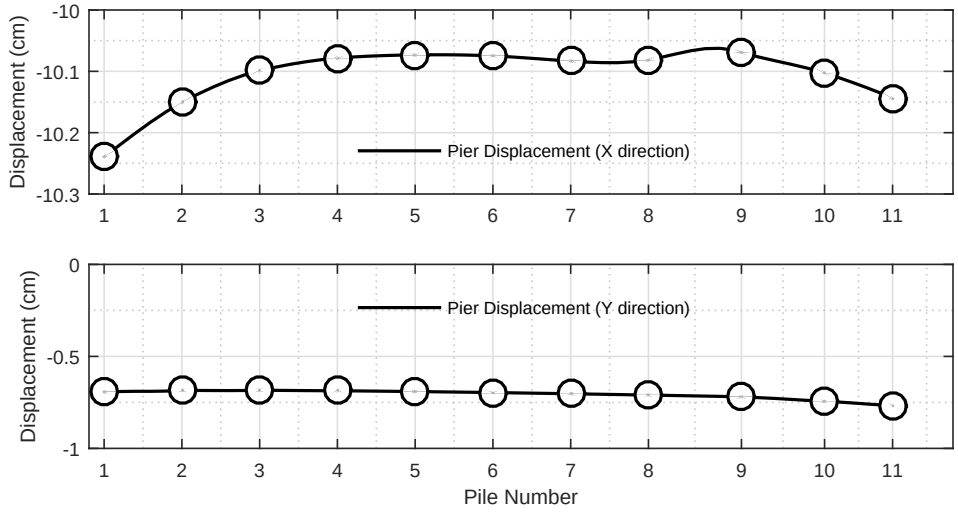

Figure 9.18: Pier Displacements parallel (X) and perpendicular (Y) to the direction of lateral spreading for 10^{cm} gap case. Refer to Figure 9.9 for pile numbering.

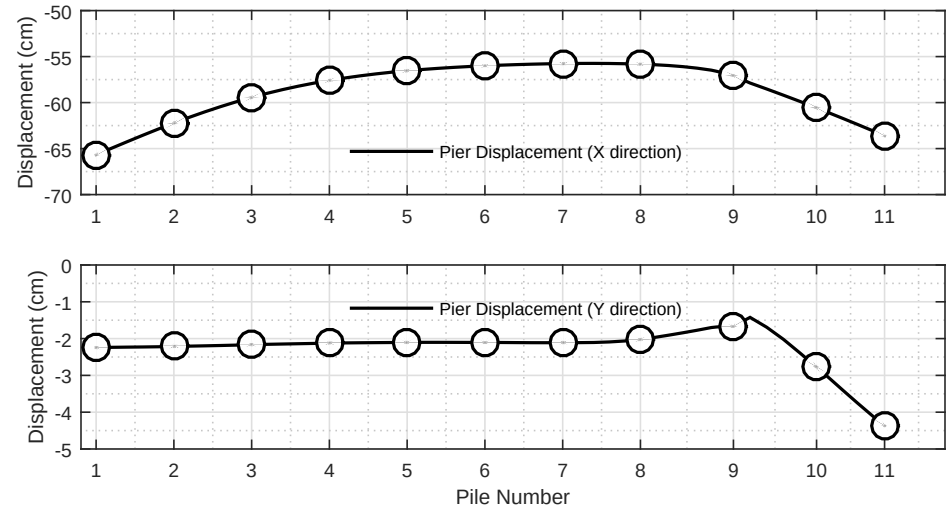

Figure 9.19: Pier Displacements parallel (X) and perpendicular (Y) to the direction of lateral spreading for no deck case. Refer to Figure 9.9 for pile numbering.

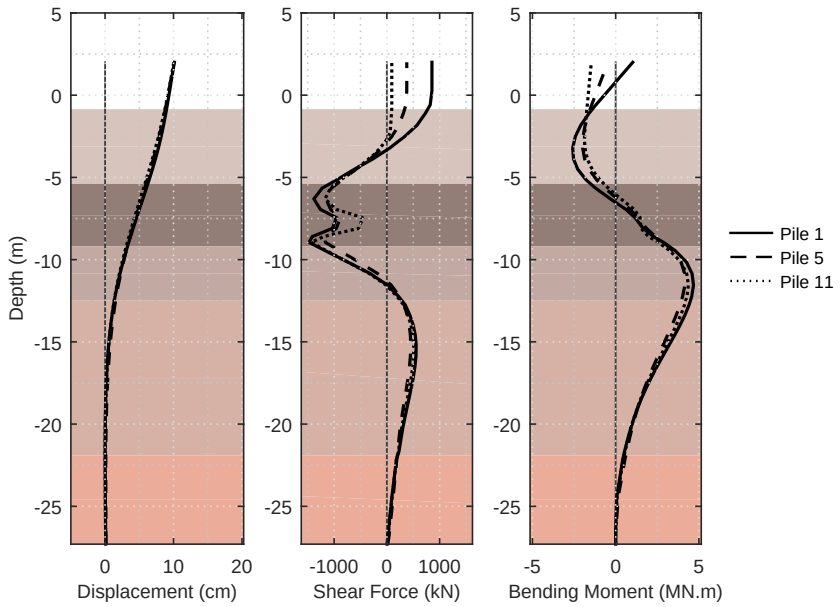

Figure 9.20: Shaft bending demands at 25$^{\text{cm}}$ free field displacement for 10$^{\text{cm}}$ gap case for various piles. Refer to Figure 9.9 for pile numbering.

9.2.6 Foundation Bending Demands

The shaft displacement, shear force and bending moment profiles of 3 shafts are shown in Figures 9.20 and 9.21 for free field displacements of 25$^{\text{cm}}$ and 1$^{\text{m}}$ respectively. Results shown in these figures are from models with a 10$^{\text{cm}}$ gap and elastoplastic shafts. Bending moment demands vary for each of the piles in both cases. This variability is more pronounced for larger displacements.

The rough irregularity seen in the shear force and bending moment diagrams at about 8$^{\text{m}}$ deep is due to the stiffness provided by the cap beam connecting pile heads to each other. This beam resists a portion of the demands due to its high stiffness. Figure 9.22 shows the result profiles from a case in which the cap beam was removed and the results are contrasted with the case which considers the existence of the cap beam. This figure shows that if the pile structure were to resist the soil passive forces alone, the result profile would be smooth as expected.

Figures 9.23 and 9.24 show the evolution of demands as the free field displacement increases. Results shown in these figures correspond to 10$^{\text{cm}}$, 25$^{\text{cm}}$ and 1$^{\text{m}}$ free field displacements. Figure 9.23 displays the results for the case with no deck while Figure 9.24 shows the results for a case with a 10$^{\text{cm}}$ gap model. In the case with of a deck spring absent, the demands increase to the point a plastic hinge is formed. The deformation mechanism is different when a deck spring is considered.

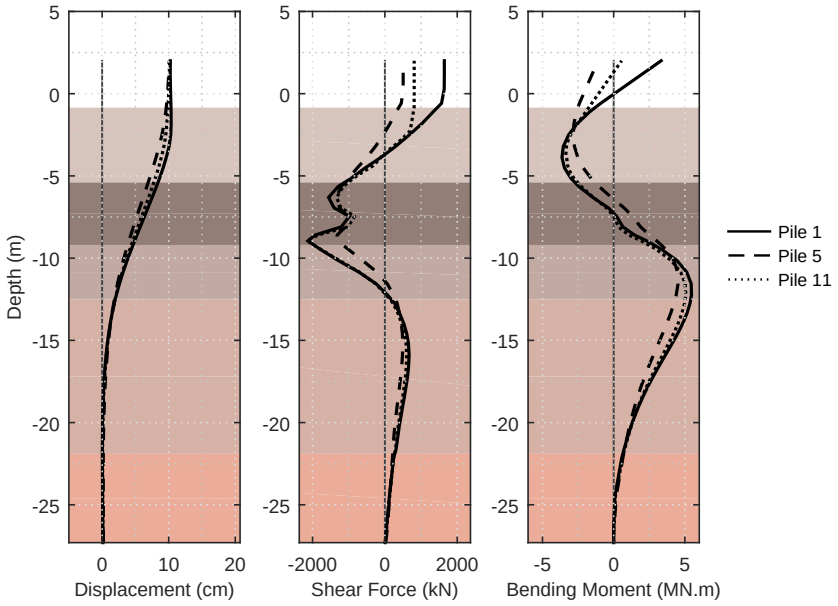

Figure 9.21: Shaft bending demands at 100$^{\text{cm}}$ free field displacement for 10$^{\text{cm}}$ gap case for various piles. Refer to Figure 9.9 for pile numbering.

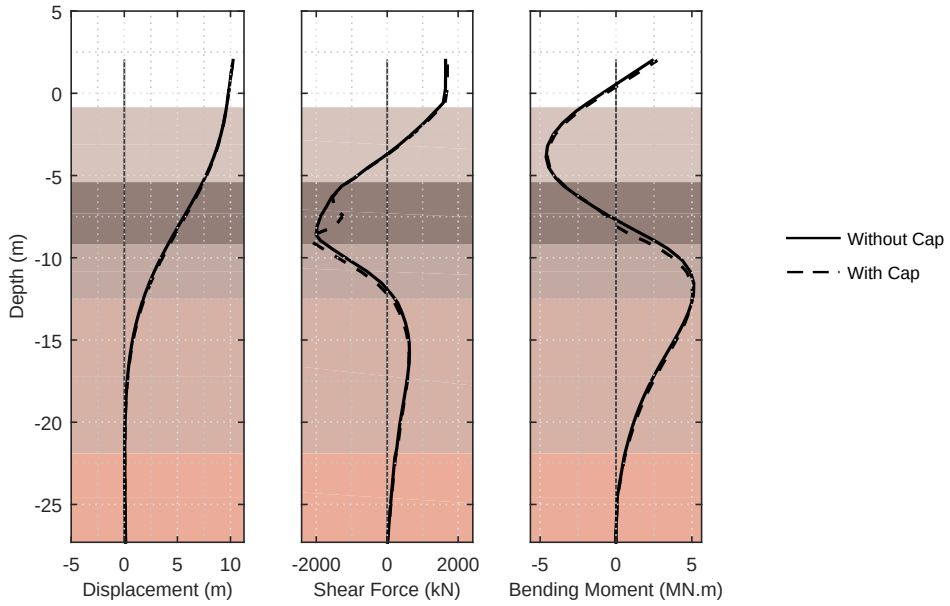

Figure 9.22: Effect of foundation cap on shaft bending demands at for 10$^{\text{cm}}$ gap case.

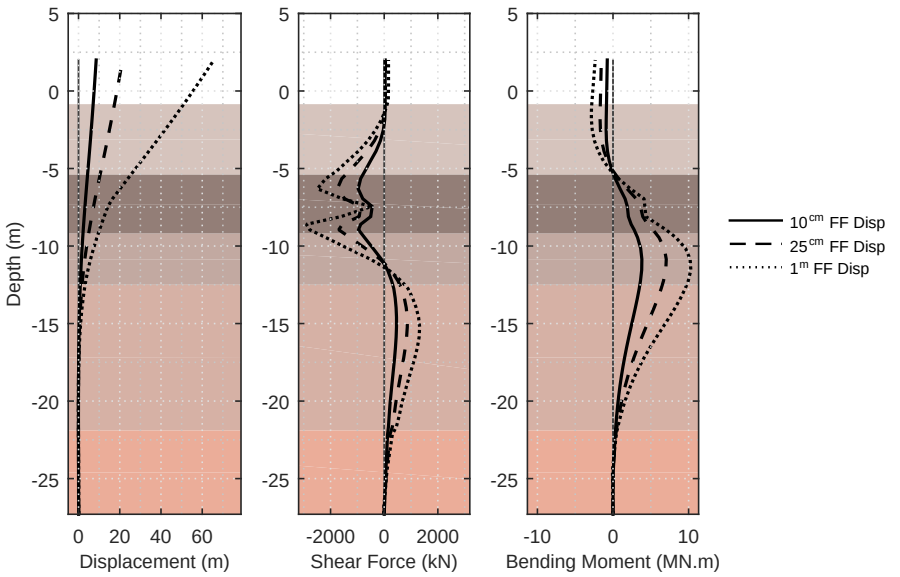

Figure 9.23: Effect of free field displacement on shaft bending demands at for no deck case.

As a result the moment distribution along the shafts are different between these two cases. In Figure 9.23 there is not considerable amount of negative moment demand, while this is not the case in Figure 9.24.

Figure 9.25 compares the response of the system when linear and nonlinear shafts are used. As expected, since structural demands due to passive forces exerted on the shafts are shown to be larger than the capacity of pile sections in the linear analysis, formation of a plastic hinge is clear in the results from nonlinear analysis at the corresponding location. This is consistent with the observations made in the field and shown in Figure 4.17. Figure 9.25 shows that the linear elastic shaft compares well with the elastoplastic shaft behavior prior to formation of a plastic hinge. For the case with a 20^{cm} gap, displacements and structural demands are reasonably close. However, for the no deck case, the response of a linear shaft deviates from the nonlinear shaft due to formation of a plastic hinge and redistribution of the bending moments and stresses.

The evolution of maximum shear force and maximum bending moment along three shafts for linear and nonlinear behavior are shown in Figures 9.26 through 9.28. Bending capacity of these shafts changes during the kinematic loading due to change in axial forces. This change in axial force is discussed later however these figures show that the bending demands are generally higher when a linear elastic shaft is used. The reason being that for the nonlinear cases, the maximum moment capacity (as shown in Figure 8.9) is reached and further demands are redistributed along the shafts

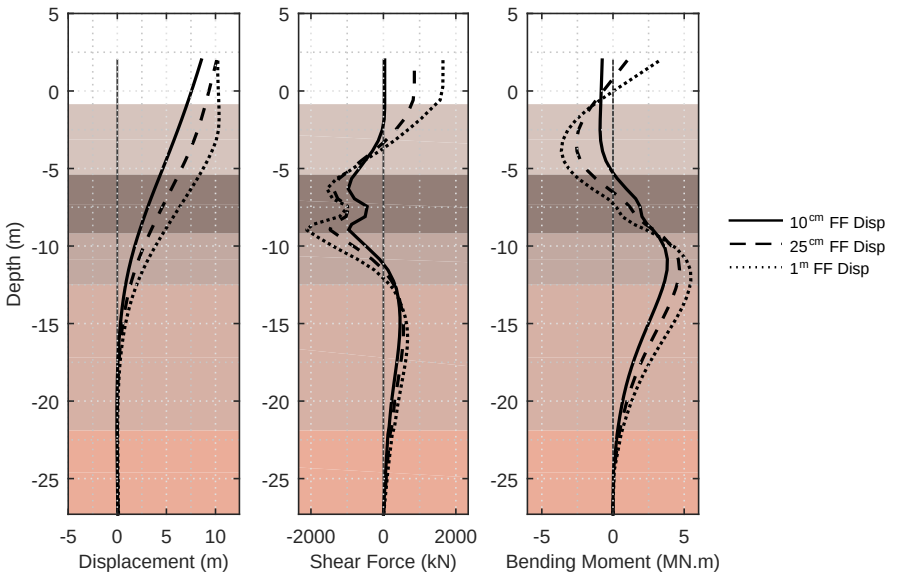

Figure 9.24: Effect of free field displacement on shaft bending demands at for 10^{cm} gap case.

accordingly. For the linear cases on the other hand, the capacity of the shafts are not capped and therefore the response of the shaft is defined completely from the soil reaction demands.

The effect of considering the deck resistance manifests in the change of axial forces in the shafts over the course of the loading. Figures 9.29 and 9.30 show the evolution of the change in maximum axial forces over the course of the application of the free field displacement. One of the non-intuitive three-dimensional effects seen in these figures is the evolution of the axial forces in shafts 9 and 11. These shafts are located with an offset from the pier axis and because of this, a group rotation effect is seen in their axial response. For the no-deck case (Figure 9.29) shaft 11 has additional compressional forces while shaft 9 has additional tensile forces. Although the overall axial force in shaft 9 remains in compression, the reduction in axial force increases the bending capacity of the shaft while the opposite is true for shaft 11. This effect is something that cannot be captured by any simplified model of a three-dimensional case like the Llacolén bridge pier. These effects are less pronounced in the case with a 10^{cm} gap deck (Figure 9.30) probably because of the impediment in the displacements.

The 3D geometric effects can also be seen in Figure 9.31. In this figure the evolution of the maximum shear forces and bending moments along the shafts are shown for piles 1, 5, 9 and 11. For comparison, the same quantities in the transverse direction are also depicted. Demands in the

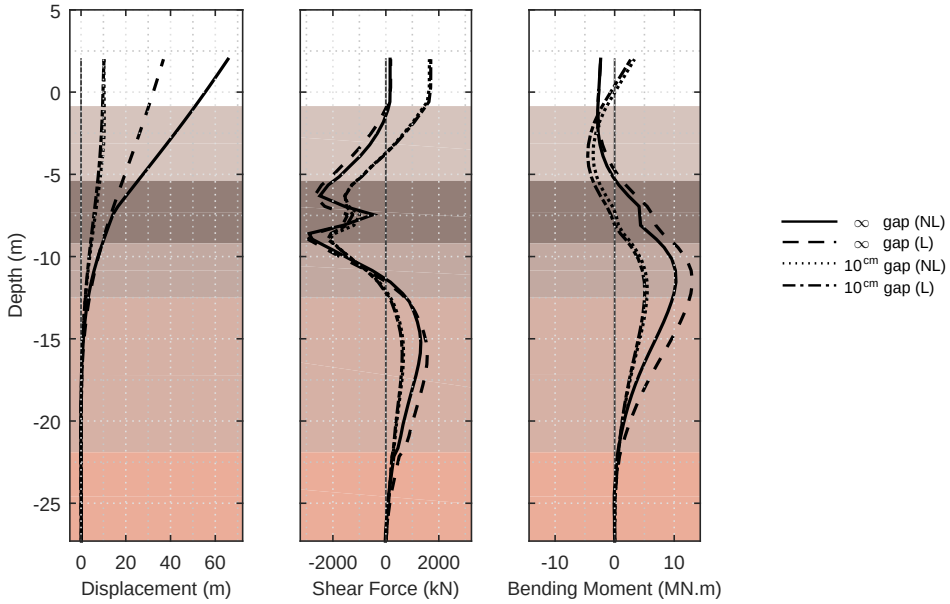

Figure 9.25: Effect of linearity of structural elements on shaft bending demands at the end of analysis.

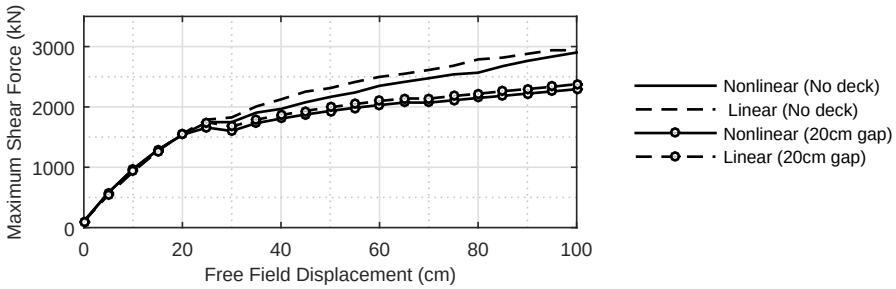

(a) Evolution of maximum shear force.

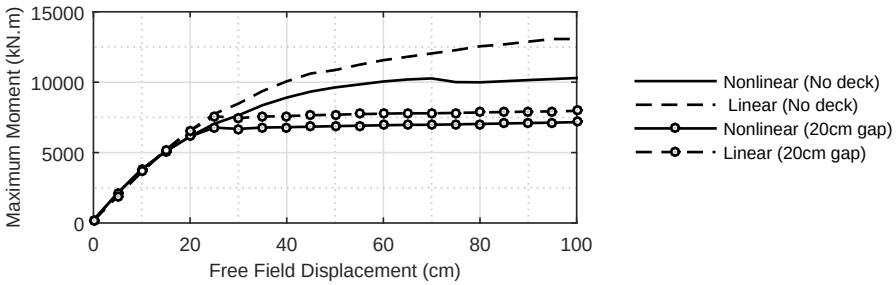

(b) Evolution of maximum bending moment.

Figure 9.26: Effect of linearity of structural elements on evolution of structural demands (Pile 1).

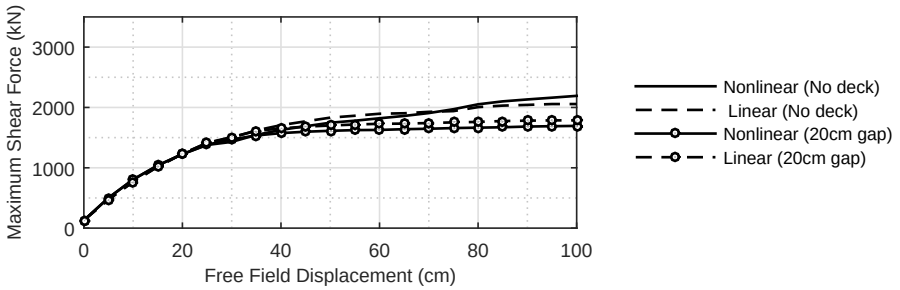

(a) Evolution of maximum shear force.

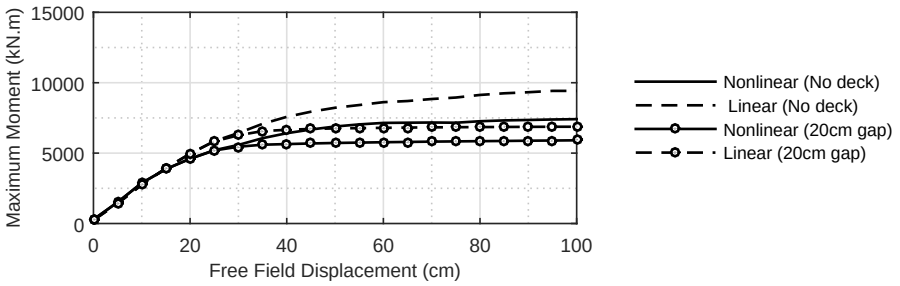

(b) Evolution of maximum bending moment.

Figure 9.27: Effect of linearity of structural elements on evolution of structural demands (Pile 9).

transverse direction are generally ignored in simplified methods because they are based on either 1-D analysis or 2-D plane strain simplifications, for both of which the strains in the transverse direction are assumed to be zero. However Figure 9.31 shows that depending on the geometry of the problem, if 3D structural effects are present, not only these are not conservative assumptions but also the demands in the transverse direction can in some cases be in the same order of magnitude as the main direction.

Figures 9.32 and 9.33 show the demand profiles for pile 1 at 25^{cm} free field displacement and 1^{m} free field displacement. The figures show that the response of the shafts in the transverse direction varies quite differently for each shaft. These demands remain relatively constant after the closure of the gap as is the case with the demands in the main direction as well.

The effect of gap size on structural demands are shown in Figures 9.34. The bending demands increase with gap size. This indicates that the resistance provided by the deck is an important component of the lateral resistance provided by the foundation system. For the no-deck case, the demands exceed the capacity of the pier column, and plastic hinges form at the connection between

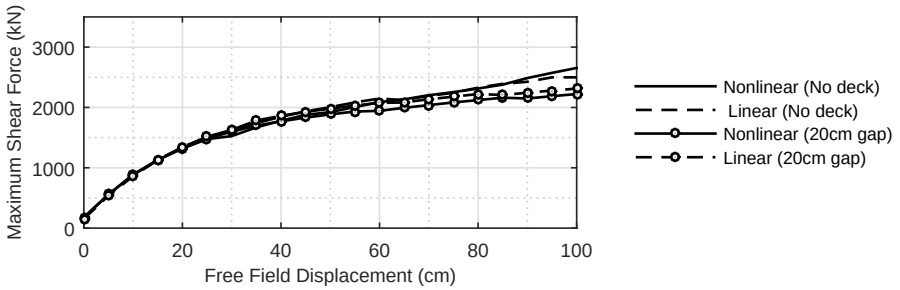

(a) Evolution of maximum shear force.

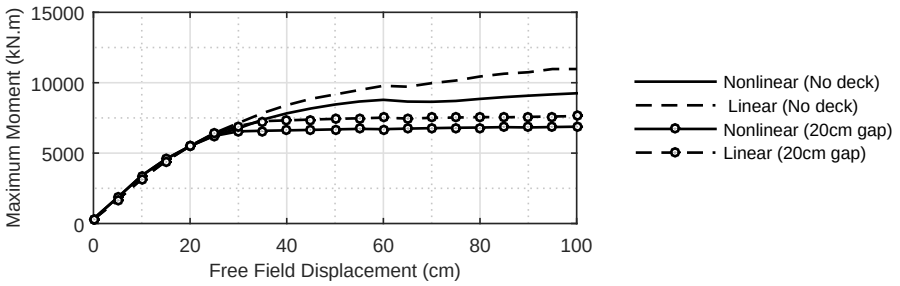

(b) Evolution of maximum bending moment.

Figure 9.28: Effect of linearity of structural elements on evolution of structural demands (Pile 11).

the column to the pile cap.

Figure 9.35 shows the effect of gap size over the course of kinematic loading. This figure shows that after the gap is closed, the demands remain essentially constant, emphasizing the influence of the gap size on shaft demand. Additionally it shows that given the resistance provided by the

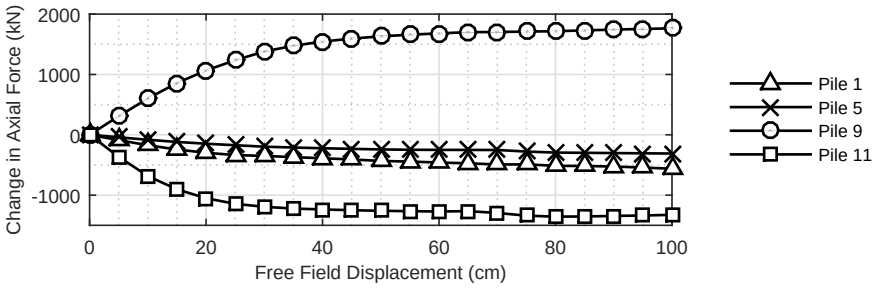

Figure 9.29: Evolution of change in axial force in structural elements for no deck case. Refer to Figure 9.9 for pile numbering.

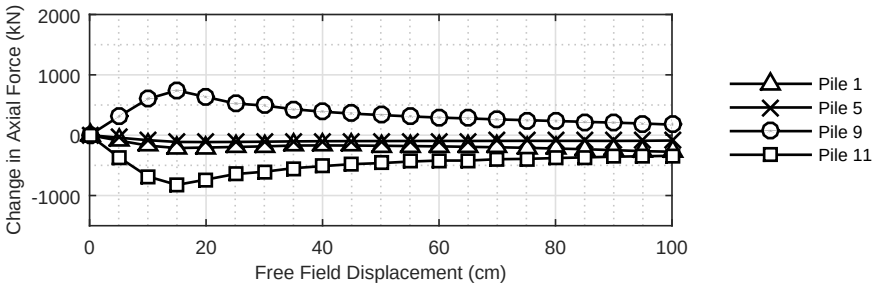

Figure 9.30: Evolution of change in axial force in structural elements for 10^{cm} case. Refer to Figure 9.9 for pile numbering.

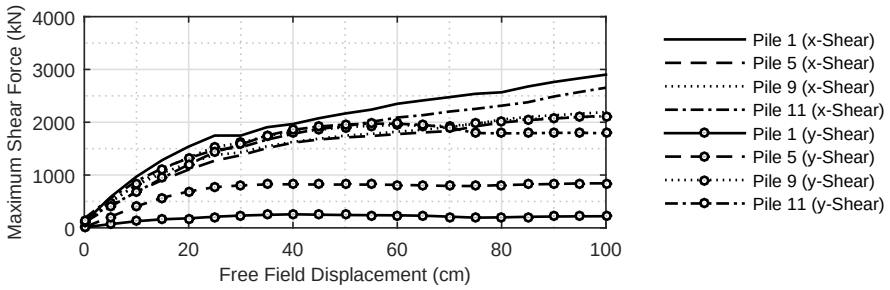

(a) Evolution of maximum shear force.

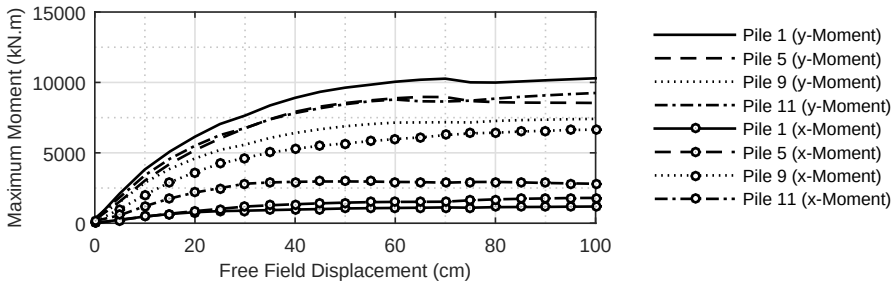

(b) Evolution of maximum bending moment.

Figure 9.31: Evolution of maximum shear force and maximum bending moment parallel (X) and perpendicular (Y) to the direction of loading for various piles for 10^{cm} gap case. Refer to Figure 9.9 for pile numbering.

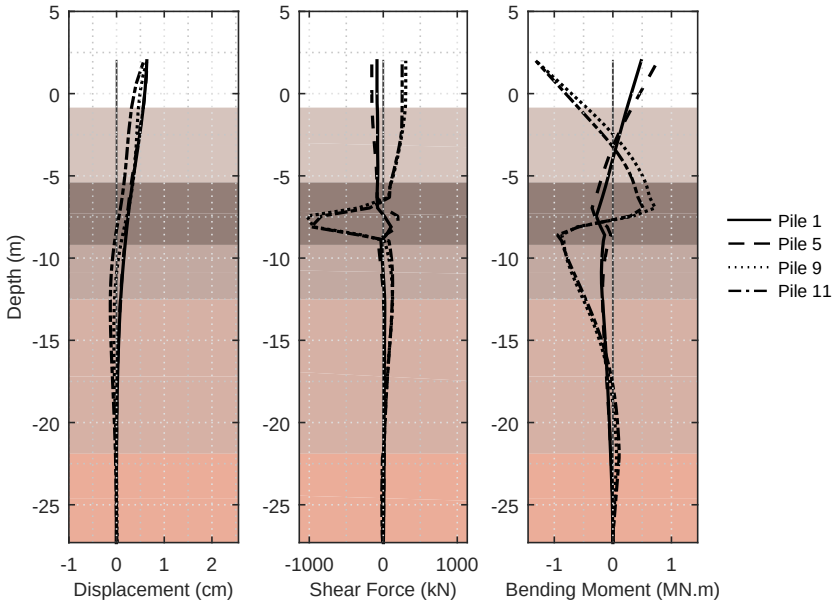

Figure 9.32: Transverse shaft bending demands at 25$^{\text{cm}}$ free field displacement for 10$^{\text{cm}}$ gap case. Refer to Figure 9.9 for pile numbering.

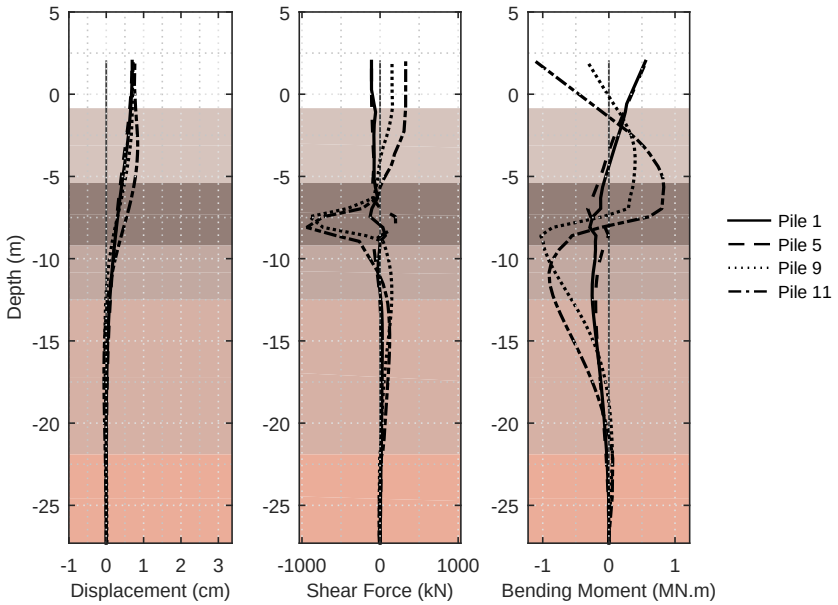

Figure 9.33: Transverse shaft bending demands at 100$^{\text{cm}}$ free field displacement for 10$^{\text{cm}}$ gap case. Refer to Figure 9.9 for pile numbering.

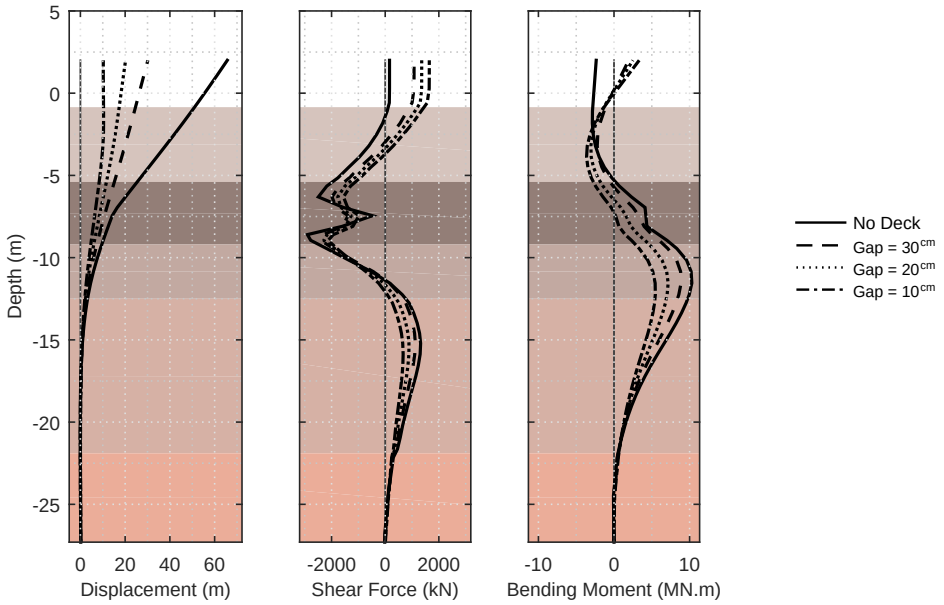

Figure 9.34: Effect of gap size on shaft bending demands at the end of analysis.

bridge deck is large, the structural demands are governed by the size of the gap to the point that the maximum demand observed when the gap size is 10^{cm} is about half the demand in a scenario where the gap is never closed and the deck resistance does not play a role.

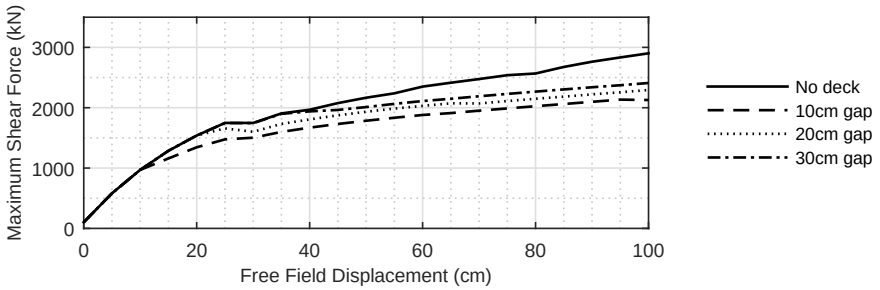

(a) Evolution of maximum shear force.

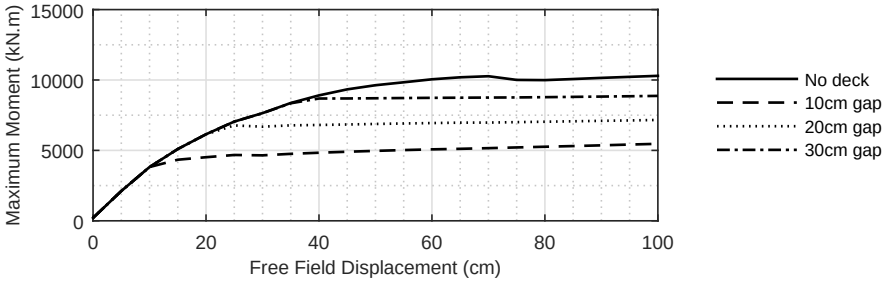

(b) Evolution of maximum bending moment.

Figure 9.35: Effect of gap size on evolution of structural demands.

9.3 Comparison of 3D FE and Pile Pinning Analysis

The pile-pinning model described in Section 9.1 represents a simplified model to be used for the design of deep foundations against loads due to liquefaction-induced lateral spreading. A second distinct numerical technique using a 3D finite element model of the bridge approach was explained in Section 9.2 to account for some of the three dimensionality which could not be captured in the first method. Results of these two models are compared to reveal their similarities and differences. Contrasting results of a simplified 1D model against a more complicated 3D model also demonstrates positive aspects and possible shortcomings of the simplified pile-pinning BNWF method.

Figures 9.36 and 9.37 show the evolution of maximum displacement, shear force and bending moment of the foundation elements over the course of the free field displacement application considering linear and nonlinear shaft behavior respectively. The shaded part of the plots represent the range of values obtained in the 3D model for all 11 shaft elements. The 3D geometry of the bridge bent causes piles at different locations to respond differently to the lateral spreading loads. As a result, a relatively wide range of values are obtained from the 3D models.

The difference in initial slopes observed in these curves is expected due to the nature of applied boundary conditions in each model. Free field displacements shown on the horizontal axis of these plots, are applied as a far-field displacement pattern to the boundaries of the 3D model. Due to pinning effects, the pile elements do not feel the same amount of displacement in the local vicinity of themselves resulting in less demands on these elements. On the other hand, free field displacements are applied directly to the end of the p-y springs connected to the foundation elements, representing a near-field displacement. Therefore, the equivalent shaft in the 1D model feels the same free field displacements sooner than the elements in the 3D models.

The bending demands obtained from the BNWF analyses at the end of the free field displacement application fall within the range of 3D results, demonstrating the effectiveness of this analysis procedure for such problems. However if the estimated ground displacement does not mobilize the full passive resistance of the soils, the pile-pinning analysis results in conservative structural demands and probable over-design of the bridge foundation.

For the linear elastic case (Figure 9.36), after mobilization of the full passive resistance of the soils, the foundation response reaches a plateau state where any further ground lateral displacement has no additional effect on the foundation. However for the inelastic case (Figure 9.37) a plastic hinge is formed, thus unbounded displacement of column head. The evolution of the maximum bending moment shows that around 25^{cm}, the moment demands redistribute and a mechanism is formed. This phenomenon happens at about 70^{cm} in the 3D model suggesting that the near-field

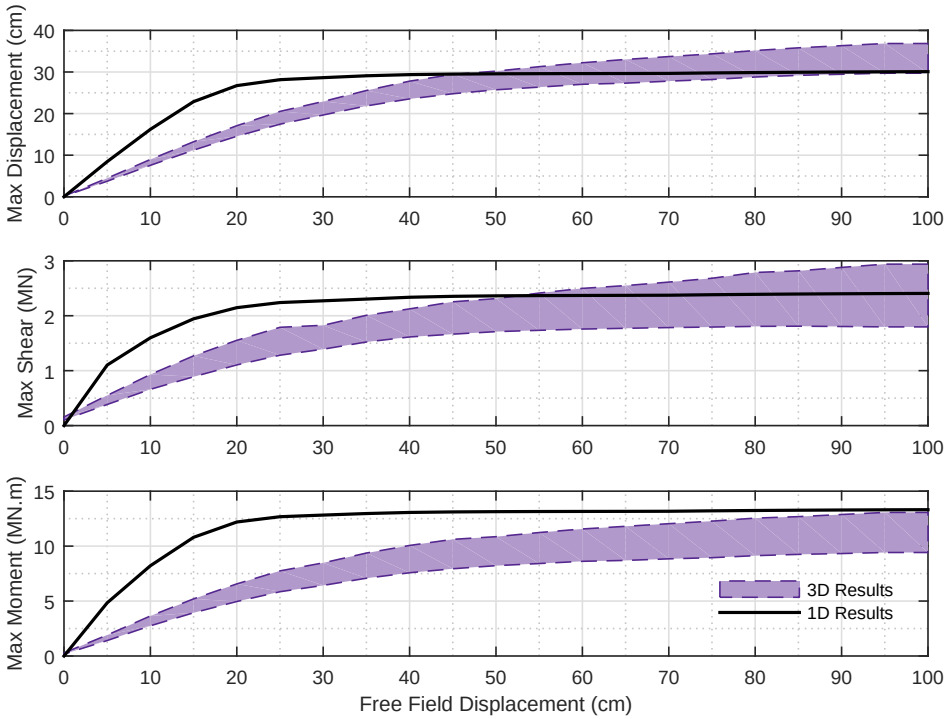

Figure 9.36: Evolution of maximum pier displacement, maximum shear force and maximum bending moment for no-deck case using linear structural elements. The shaded area demonstrates the range of various pile responses in 3D model.

displacement is about 25^{cm} when a far-field displacement of 70^{cm} is applied.

Figure 9.38 shows results for the range of foundation responses observed in the 3D model and the BNWF model at an applied free field of 25^{cm}. As shown in the previous plots, it is not appropriate to compare the results of the 3D models with the BNWF model at the same ground displacement. The discrepancy between the results observed in Figure 9.38 is partly a result of this issue, therefore profiles of results at a ground displacement of 10^{cm} – which seems to be the corresponding near-field displacement for a 25^{cm} far-field displacement in Figure 9.37 – is also plotted in this figure. Results fall in the same range emphasizing the importance of estimating equivalent lateral ground displacements for cases where flow failure is not likely to occur. When full passive forces are mobilized and flow failure happens, the results become insensitive to the ground displacement and as shown in Figure 9.39, a simplified BNWF analysis could be used for design purposes.

Results of cases considering a 10^{cm} gap deck spring are depicted in Figures 9.40 to 9.43. The results show that in the presence of a deck spring, if the deck provides enough resistance to the lateral

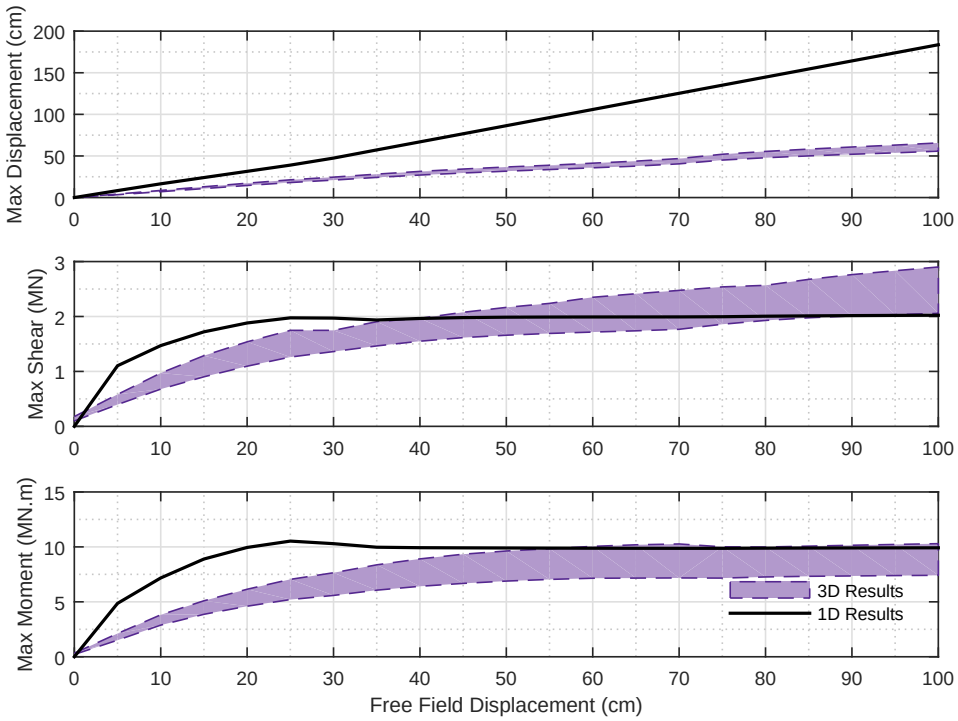

Figure 9.37: Evolution of maximum pier displacement, maximum shear force and maximum bending moment for no-deck case using nonlinear structural elements. The shaded area demonstrates the range of various pile responses in 3D model.

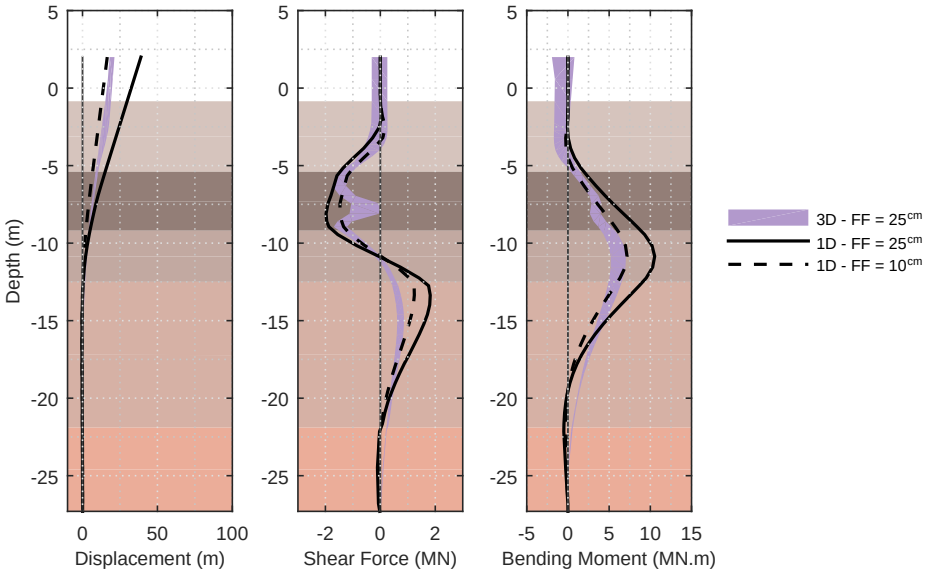

Figure 9.38: Shaft bending demands at 25$^{\text{cm}}$ free field displacement for no-deck case. The shaded area demonstrates the range of pile response in 3D models.

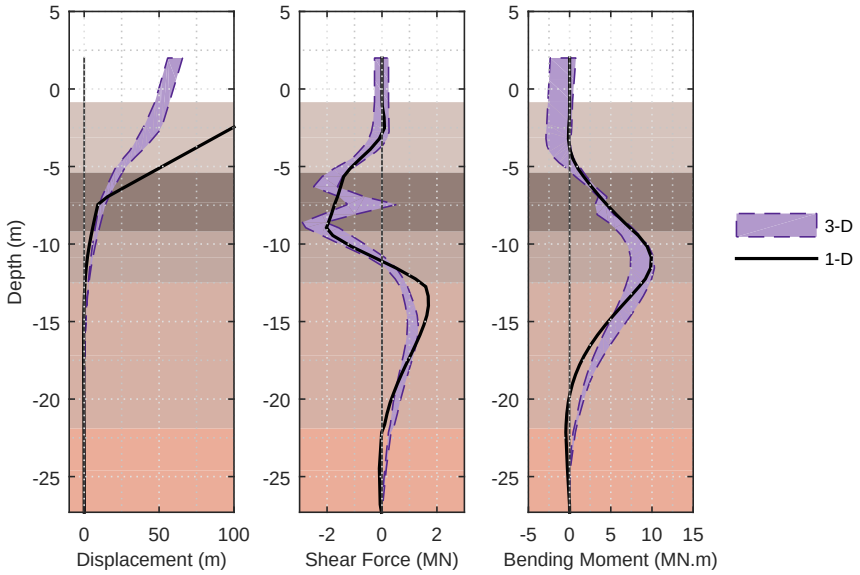

Figure 9.39: Shaft bending demands at 100$^{\text{cm}}$ free field displacement for no-deck case. The shaded area demonstrates the range of pile response in 3D models.

movement of the bridge bent, the impediment causes demands to reach a plateau before bending capacity of the elements are reached making the nonlinear behavior of these elements insignificant to some degree. Consideration of the bridge deck and expansion gap proves to be an important aspect to be considered in simplified design methods.

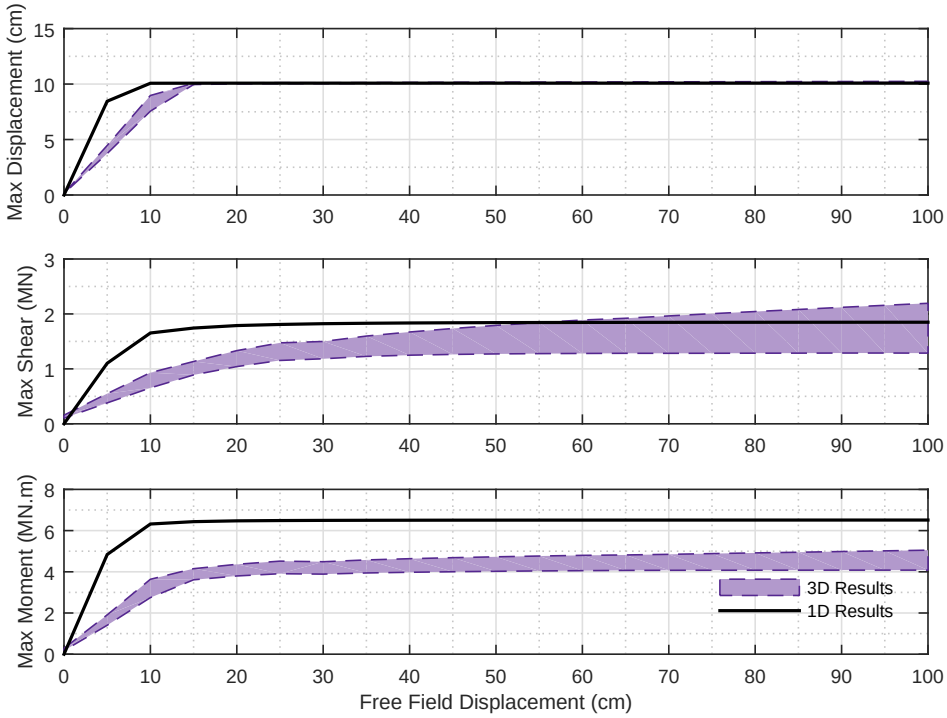

Figure 9.40: Evolution of maximum pier displacement, maximum shear force and maximum bending moment for 10^{cm} gap case using linear structural elements. The shaded area demonstrates the range of various pile responses in 3D model.

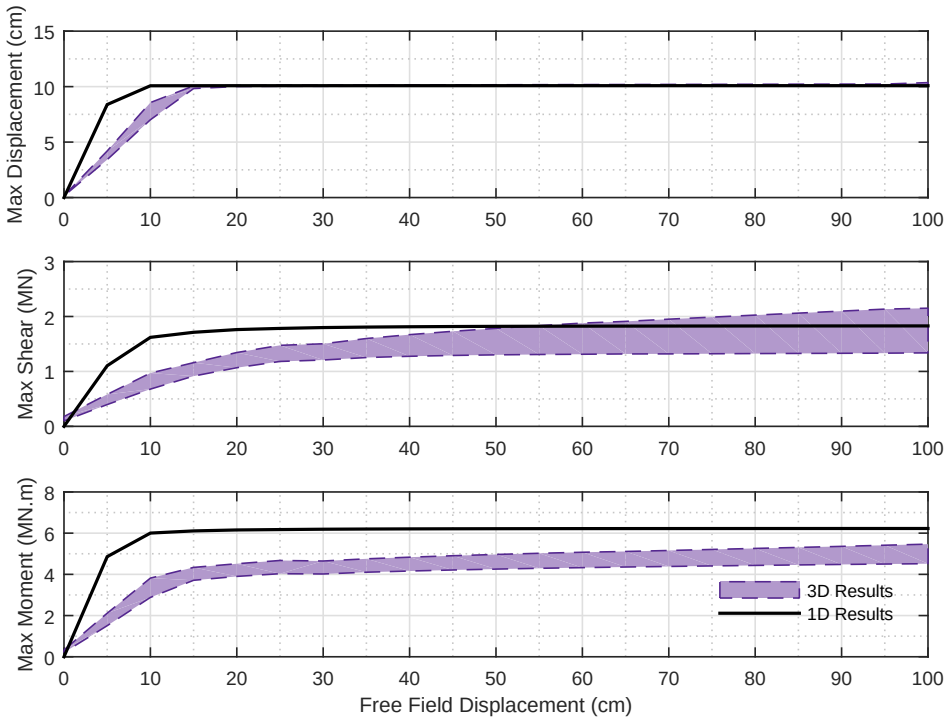

Figure 9.41: Evolution of maximum pier displacement, maximum shear force and maximum bending moment for 10^{cm} gap case using nonlinear structural elements. The shaded area demonstrates the range of various pile responses in 3D model.

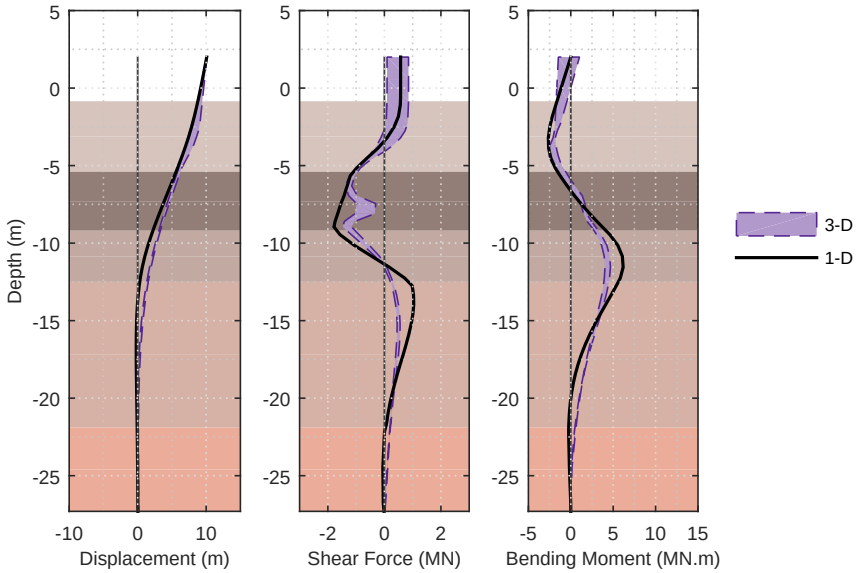

Figure 9.42: Shaft bending demands at 25^{cm} free field displacement for 10^{cm} gap case. The shaded area demonstrates the range of various pile responses in 3D model.

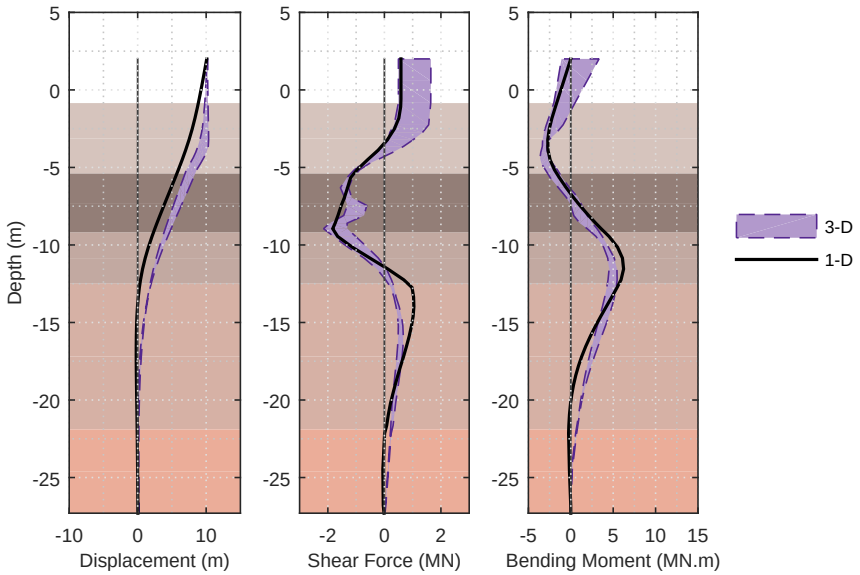

Figure 9.43: Shaft bending demands at 100^{cm} free field displacement for 10^{cm} gap case. The shaded area demonstrates the range of various pile responses in 3D model.

9.4 Summary

Two distinct analysis approaches were used to evaluate the response of the northeast approach of the Llacolén bridge to lateral spreading: simplified pile-pinning analysis method in which the foundation is modeled using a BNWF approach and a 3D finite element model considering the geometry of the bridge approach and the surrounding soil at the site. Comparison of results between these two methods is used to assess the viability of simplified design techniques for lateral spreading and gain insight into the 3D geometry effects that are particular for this bridge.

The 3D finite element analysis showed that even though the mass of the soil flowing into the foundation is very large compared to the resistance the foundation system can provide, deformation in the near-field of the foundation system is smaller specially in the case where the lateral resistance of the bridge deck is considered. This implies that even for this case pile pinning effects are relevant. The geometry of the bridge bent causes the soil to flow around the system reducing the amount of passive force exerted on the foundation assuming the soil would push directly into the foundation. Importance of considering the bridge deck resistance and the effects of the expansion gap size was also demonstrated in the 3D FE models. It was also shown that due to the three dimensional geometry of the bridge structure, transverse demands can be significant. These demands cannot be considered in simplified analysis.

Pile pinning analyses were also performed to evaluate their credibility to be used for design of such structures in practice. It was shown that if this method is applied carefully, with a careful estimation of ground displacement and correct definition of structural components in the problem, e.g. the expansion gap and bridge deck resistance, they are able to predict the bending demands in foundations subject to lateral spreading loading conditions.

Chapter 10

3D PARAMETER STUDY OF GEOMETRIC EFFECTS ON FOUNDATION RESPONSE TO LATERAL SPREADING

The 3D finite element models created and analyzed for Puente Mataquito and Llacolén have identified that the approach embankment geometry can influence the response of a bridge foundation to the kinematic demands of lateral spreading. Consideration for 3D embankment geometry was shown to produce structural foundation demands that are reduced in comparison to a two-dimensional description of the problem. The results obtained from the Mataquito and Llacolén case studies provide a useful evaluation of how and where these 3D effects are manifested at each particular site, however, a general description of the problem cannot be gained from a few combinations of bridge foundations and geometry, embankment sizes, and soil profiles. In order to further analyze how the site geometry affects foundation response, a parameter study is considered using a series of 3D finite element models with various combinations of shaft diameter and site geometry. These models are simplified in comparison to the Puente Mataquito and Llacolén models, however, the fundamental aspects of the approach embankment problem are captured.

10.1 Parameter Study Model Overview

The parameter study models consider a single pile or shaft foundation embedded in a layered soil profile with an embankment placed above the upper soil layer. This embankment is built with a 2H:1V side slope and extends across the length of the mesh as shown in Figure 10.1. Different combinations of embankment width, shaft diameter, liquefied layer depth, and liquefied layer thickness are considered to characterize the influence of site geometry on the response of the single shaft to lateral spreading.

10.1.1 Considered Site Geometries

Figure 10.2 shows a summary of the soil profiles and embankment geometries considered in the parameter study. The soil profile is varied with respect to the liquefied layer thickness, t, and the depth, z, to the top of the liquefied layer (dark blue layer in the plot). Three values of each parameter are selected: $t = 1.0,\ 2.0,\ 3.0$ m and $z = 1.0,\ 2.0,\ 3.0$ m. For each of these nine soil profiles, three

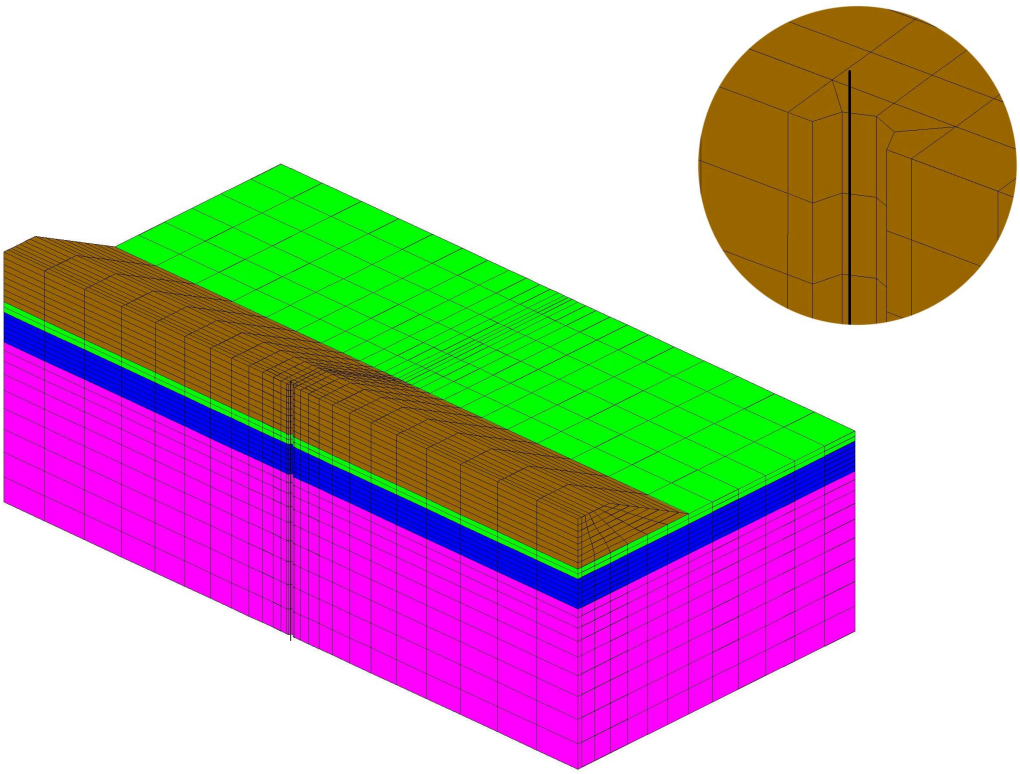

Figure 10.1: Example 3D finite element mesh used in the parameter study.

embankment crest widths, $w = 4.0,\ 8.0,\ 16.0$ m, are considered in addition to a fourth case in which the embankment extends across the full width of the model (35.0 m). These full width cases are used to simulate a two-dimensional description of the problem similar to the Llacolén bridge, and are compared to the other embankment configurations in order to assess the reduction in foundation bending demands relative to the plane strain case. Models are generated for each of the 36 site geometric configurations with consideration of two shaft foundation designs, leading to 72 distinct cases in the parameter study. Two shaft diameters are considered, $D = 0.6,\ 1.4$ m, to assess the effects of foundation size, and each shaft is based on a separate template cross-section design to assess the effects of foundation bending stiffness on the response of the system.

10.1.2 Boundary and Loading Conditions

The boundary and loading conditions for the parameter study models are similar to those used in the applied kinematic model for Puente Mataquito and Llacolén bridge. The nodes on the base of the mesh are fixed against vertical translation, and elemental body forces are used to consider the effects of gravity on the soil continuum. Symmetry is considered as shown in Figure 10.1, with the symmetry plane cutting through the center of the shaft foundation such that only one half of

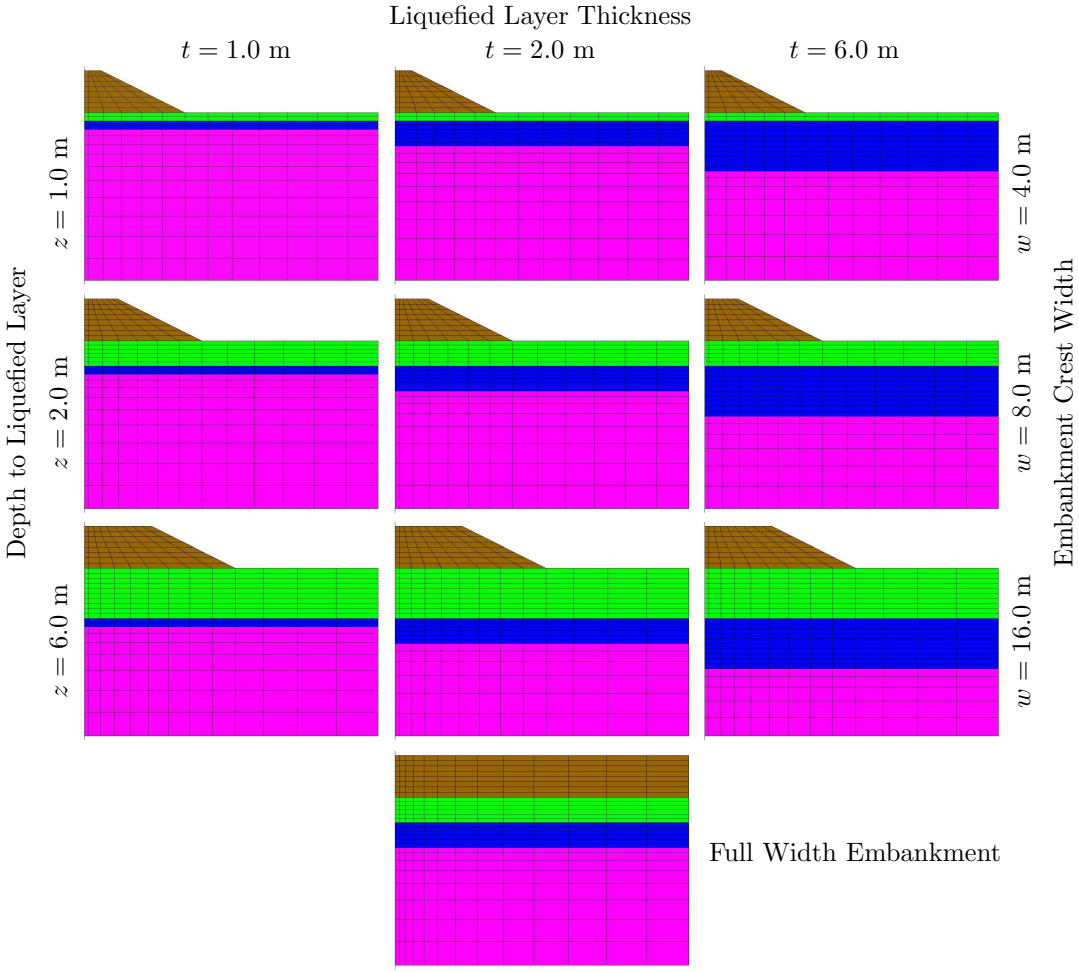

Figure 10.2: Summary of cases considered in the parameter study.

the shaft is considered in the model. The nodes on the vertical boundary opposite the symmetry plane are fixed against all horizontal translation, and the nodes on the remaining non-symmetry vertical boundaries are fixed against out-of-plane translations only. The effects of lateral spreading are simulated using the applied kinematic approach introduced in the discussion of the Puente Mataquito and Llacolén bridge modeling effort, in which a set displacement profile is gradually applied to the non-symmetry vertical boundaries of the mesh. This displacement profile is constant above the assumed liquefied layer, linearly-increasing across the liquefied layer, and zero below this point. The soil mesh boundaries are placed 35 m away from the shaft centerline in both horizontal directions, and the mesh is 20 m deep vertically with a 5 m tall embankment for all configurations.

The shaft foundation is modeled with a displacement-based beam-column element that interfaces with the surrounding solid elements via the beam-solid contact elements of Petek (2006). A detail of the mesh immediately surrounding the shaft centerline is provided in Figure 10.1. As shown, a semi-circular space is built-in to the solid element mesh to consider the physical size of the shafts

Table 10.1: Model properties for soil layers in parameter study.

Layer	ρ (Mg/m^3)	ϕ (°)	$G_{\max}$ (MPa)	$K_{\max}$ (MPa)	S_u (kPa)
dry loose sand	1.7	32	75	200	–
sat. loose sand	1.7	–	6.0	175	5.0
dense sand	2.0	38	100	300	–
embankment fill	1.9	48	130	390	–

Table 10.2: Model material and section properties in parameter study shaft foundations.

Shaft diameter	A (m^2)	E (GPa)	G (GPa)	I (m^4)
0.6 m	0.15	31.3	12.5	0.0038
1.4 m	0.74	28.7	11.5	0.0869

considered in the study. The nodes for the beam-column elements are fixed against translation normal to the symmetry plane, and rotations about the direction of loading and the axis of the shaft. The beam node at the base of the model is fixed against vertical translation, and the beam node at the top of the model is fixed against rotations in the plane of loading to represent a rigid connection to a hypothetical shaft cap or superstructure body.

10.1.3 Soil Properties

Generic soil properties are assumed for the various soil layers in the model. Four layers are defined: the embankment fill, a dry crustal sand layer, a liquefiable saturated loose sand layer, and an underlying denser sand layer. The constitutive models of Elgamal et al. (2003) discussed in Section 5.1 are used to model the material response of all considered soils. The embankment fill, crust, and dense sand layers are modeled with Drucker-Prager type failure surfaces with friction angle dependent strengths, while the liquefied loose sand layer is modeled as a pressure independent material with a residual undrained shear strength defining the bounds of the failure surface. As with the applied kinematic model for Puente Mataquito and Llacolén bridge, the liquefied layer is assigned residual shear strength and stiffness properties at the beginning of the analysis, as it is assumed that liquefaction has already occurred.

10.1.4 Shaft Foundation Models

Two template shaft models are used in the parameter study, a 0.6 m diameter shaft and a 1.4 m diameter shaft. These shaft models are based on actual deep foundation designs, and consider linear elastic bending stiffness values determined from the initial tangent of the nonlinear moment

curvature responses of the template cross-sections. The material and section properties used to define the shaft models are provided in Table 10.2. For each shaft, the cross-sectional area, A, and second moment of the area, I, are determined based on half of the shaft cross-section for consistency with the symmetry conditions assumed in the model. The shaft elastic modulus values are chosen such that the linear elastic bending stiffness, EI, corresponds to the initial bending stiffness of the template cross-sections, and the elastic shear modulus, G, for each shaft is based on an assumed Poisson's ratio of 0.25. Further details on the template cross-section designs used to define these shaft models are discussed in McGann et al. (2012).

10.2 General Effects of Site Geometry on Foundation Response

The effects of approach embankment and soil profile geometry on the flexural response of the shaft foundations are assessed through comparisons of the results obtained from the various cases considered in the parameter study. These comparisons are made both qualitatively and quantitatively, and the discussion of the observed effects is organized into several sections in order to isolate the individual effects of each considered geometric aspect.

10.2.1 Summary of Global Model Response

In general, the results of the parameter study demonstrate that the presence of the shaft foundation alters the soil deformation field such that only the material near the boundaries experiences the full free-field displacement applied to the model. This resistance varies depending on the geometric configuration of the site, as certain combinations lead to greater and more widespread resistance, while others indicate a less significant effect. To demonstrate the range of responses obtained, Figures 10.3 and 10.4 show the deformed mesh for two models in which the only difference is the embankment width. The soil profiles shown in these plots consider a 0.6 m diameter shaft with a 3 m thick liquefied layer located 1 m below the base of the embankment fill.

The mesh shown in Figure 10.3 considers an embankment defined with $w = 8$ m. In this case, the shaft provides substantial resistance to the lateral deformation of the soil, as the deformations near the shaft are approximately one-quarter of the free-field displacement, and this effect is manifested over a fairly large portion of the soil domain. In contrast, Figure 10.4, which shows the same results for the full width embankment, demonstrates that with the 2D geometry, the shaft offers only minimal lateral resistance as nearly the entire soil domain experiences the free-field deformation profile. This general trend of increased embankment width leading to a more homogeneous soil deformation field corresponds to observations made using the Puente Mataquito and Llacolén bridge

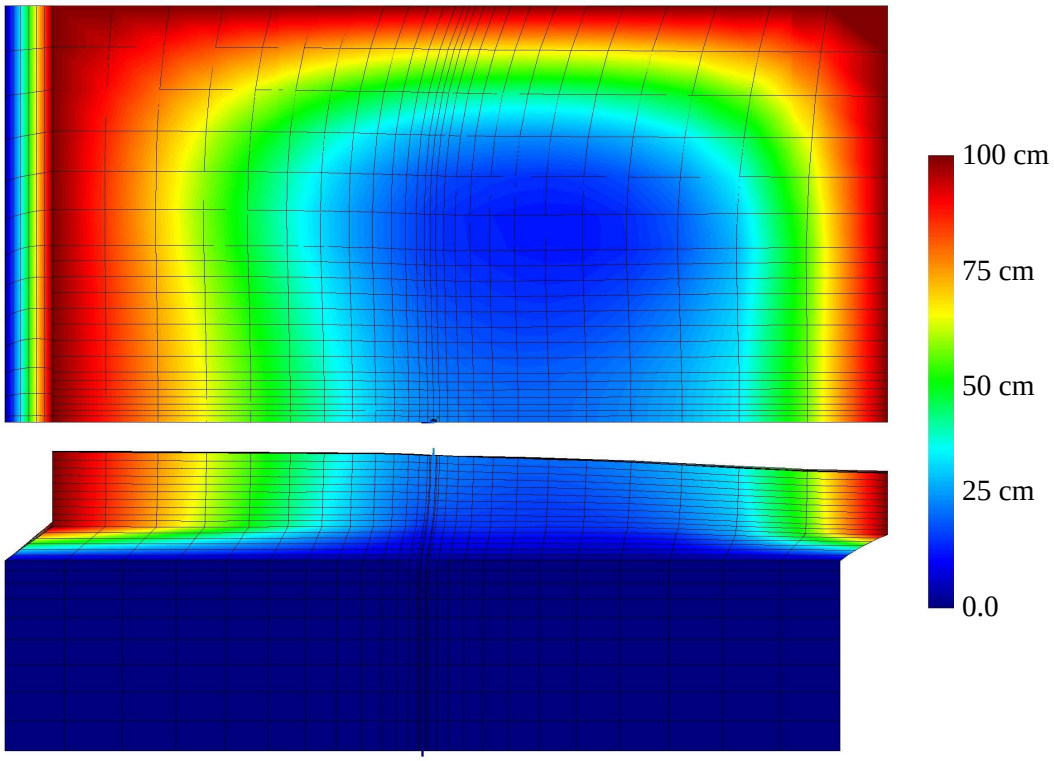

Figure 10.3: Deformed mesh (magnified 4 times) with contours of horizontal deformation for $w = 8$ m case with $D = 0.6$ m, $z = 1$ m, and $t = 3$ m.

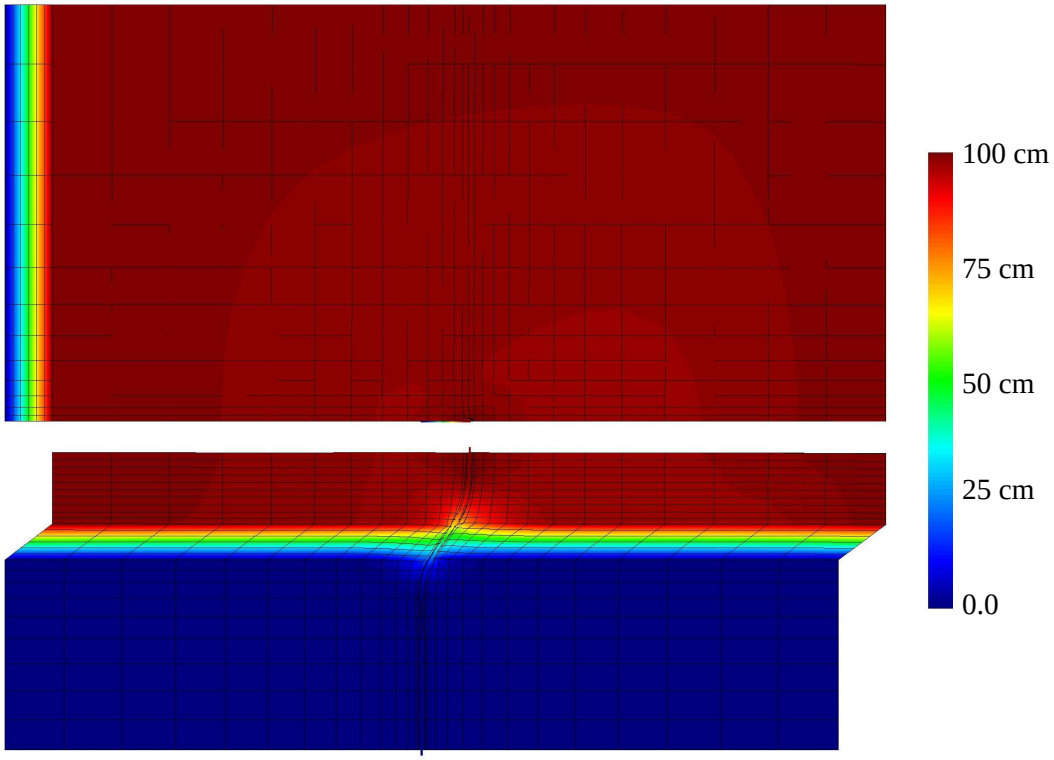

Figure 10.4: Deformed mesh (magnified 4 times) with contours of horizontal deformation for full width case with $D = 0.6$ m, $z = 1$ m, and $t = 3$ m.

models; in particular at the end of the free field displacement.

10.2.2 Effects of Embankment Crest Width

The general effects of increasing embankment width are demonstrated through a comparison of Figures 10.3 and 10.4, however, it is also of interest to assess the differences in how the three considered embankment crest widths affect the embedded shaft foundations. The effects of the different embankment sizes on the foundation demands are demonstrated in Figures 10.5 through 10.10, which show the shaft bending demand profiles (displacement, shear force, and bending moment) for the indicated parameter combinations. In these plots, *w1* through *w4* correspond to the four embankment crest widths ordered from low to high (4, 8, 16, and 35 m, respectively), and the liquefied layer thickness is indicated by the extents of the gray shaded zones. Each individual figure considers the combination of liquefied layer depth, z, and shaft diameter, D, noted in its caption, and the portion of the soil profile corresponding to the approach embankment is shaded in brown for reference.

As expected based on the Puente Mataquito and Llacolén bridge results and the soil deformation fields of Figures 10.3 and 10.4, increased embankment width leads to increased shaft bending demands. This is most clearly seen in Figures 10.5 and 10.6, which consider the shallowest liquefied layer depth, though it can been seen to some extent in all of the bending demand summary plots. The general forms of the displacement, shear force, and bending moment profiles remain similar for the four widths, however, the magnitudes become larger, and, in general, for constant D, z, and t, the locations of the shear and moment inflection points move further apart as the embankment becomes wider.

Figures 10.11 through 10.16 support some of these observations by showing how the maximum displacement, shear force, and bending moment demands change with increasing free-field displacement for each considered combination of shaft design and soil configuration. As shown, perhaps with the exception of the first few analysis steps, for all levels of free-field displacement, larger embankment widths lead to larger maximum bending demands. The maximum displacement, shear, and moment demands are affected similarly by changes in w, and it appears that for constant values of D, z, and t, the relative difference between the results for each embankment width remains nearly constant over the course of the free-field displacement application. In all cases, the bending demands obtained from the wide embankment geometry are greater than or equal to the bending demands for the 3D embankment geometries.

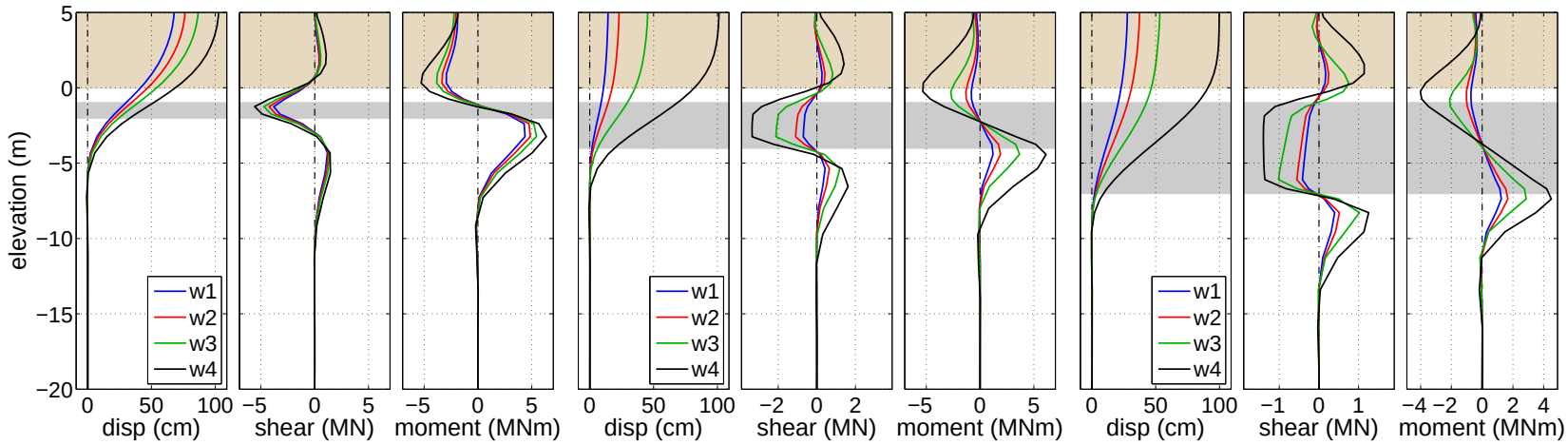

Figure 10.5: 0.6 m dia. shaft bending demands for three liquefied layer thicknesses and four embankment widths with $z = 1$ m.

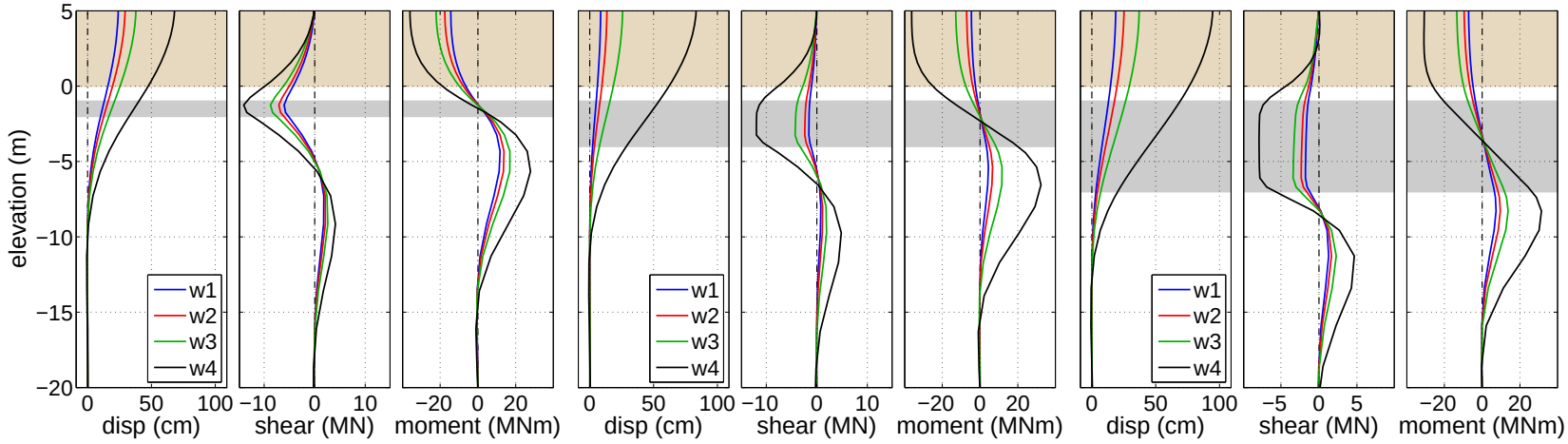

Figure 10.6: 1.4 m dia. shaft bending demands for three liquefied layer thicknesses and four embankment widths with $z = 1$ m.

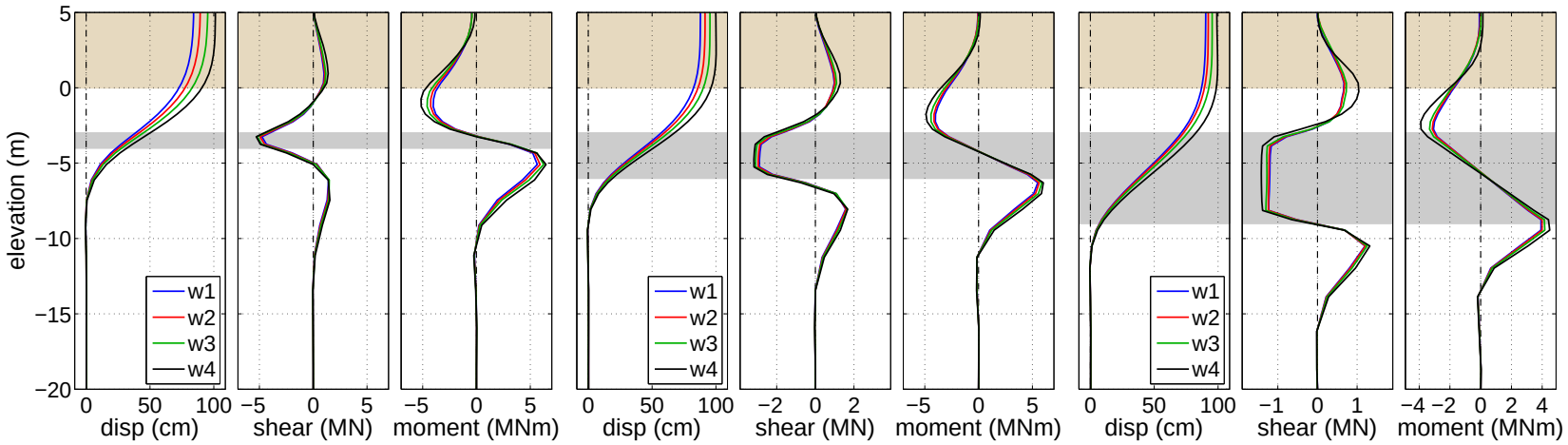

Figure 10.7: 0.6 m dia. shaft bending demands for three liquefied layer thicknesses and four embankment widths with $z = 3$ m.

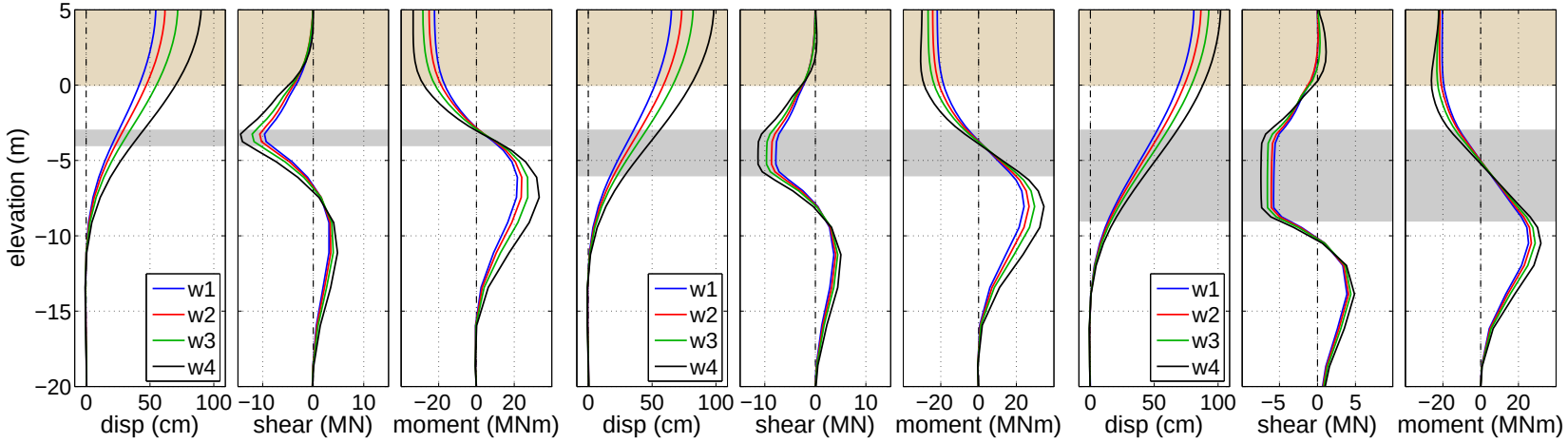

Figure 10.8: 1.4 m dia. shaft bending demands for three liquefied layer thicknesses and four embankment widths with $z = 3$ m.

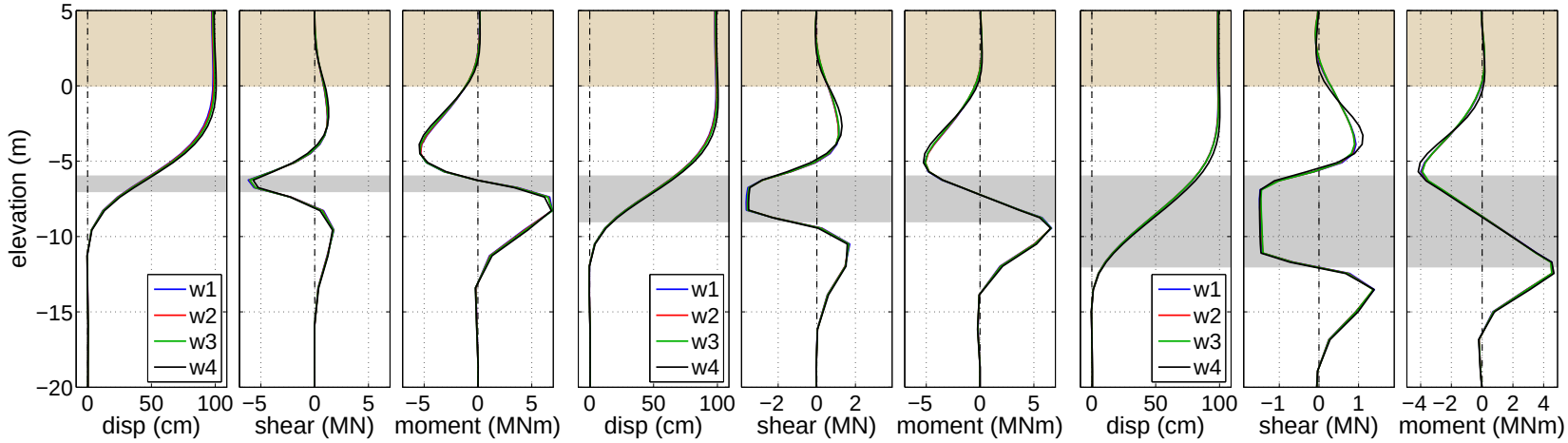

Figure 10.9: 0.6 m dia. shaft bending demands for three liquefied layer thicknesses and four embankment widths with $z = 6$ m.

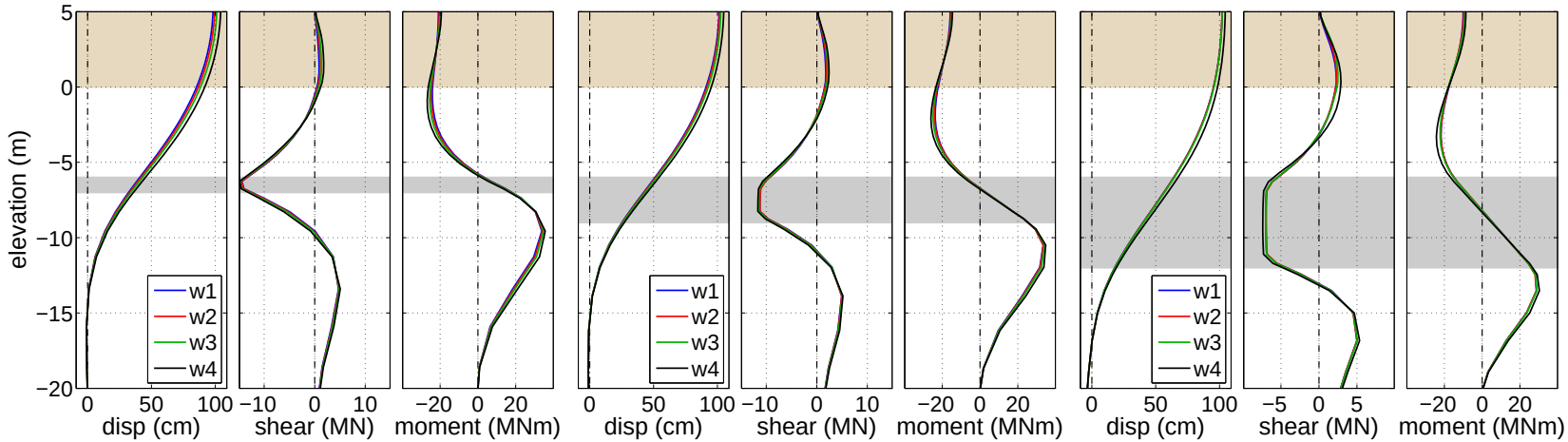

Figure 10.10: 1.4 m dia. shaft bending demands for three liquefied layer thicknesses and four embankment widths with $z = 6$ m.

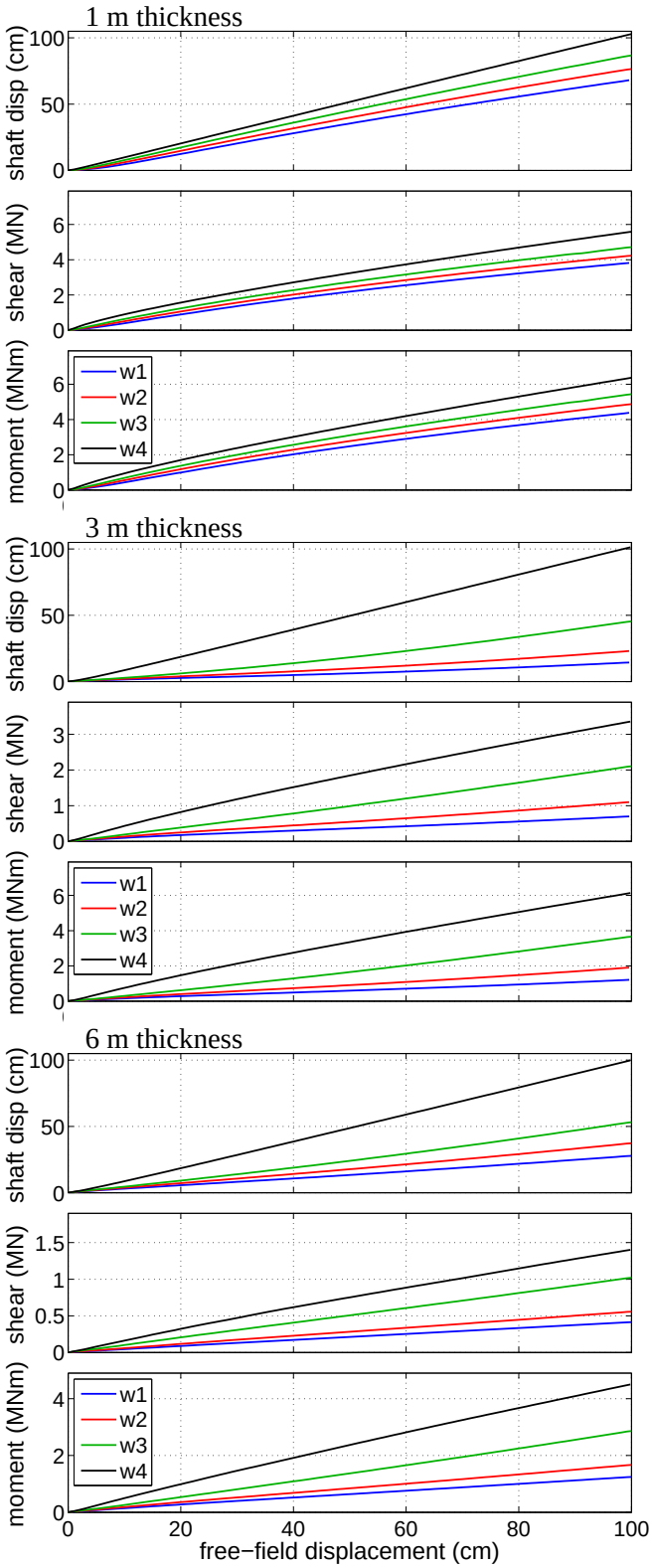

Figure 10.11: Maximum shaft bending demands for three liquefied layer thicknesses and four embankment widths with $D = 0.6$ m and $z = 1$ m.

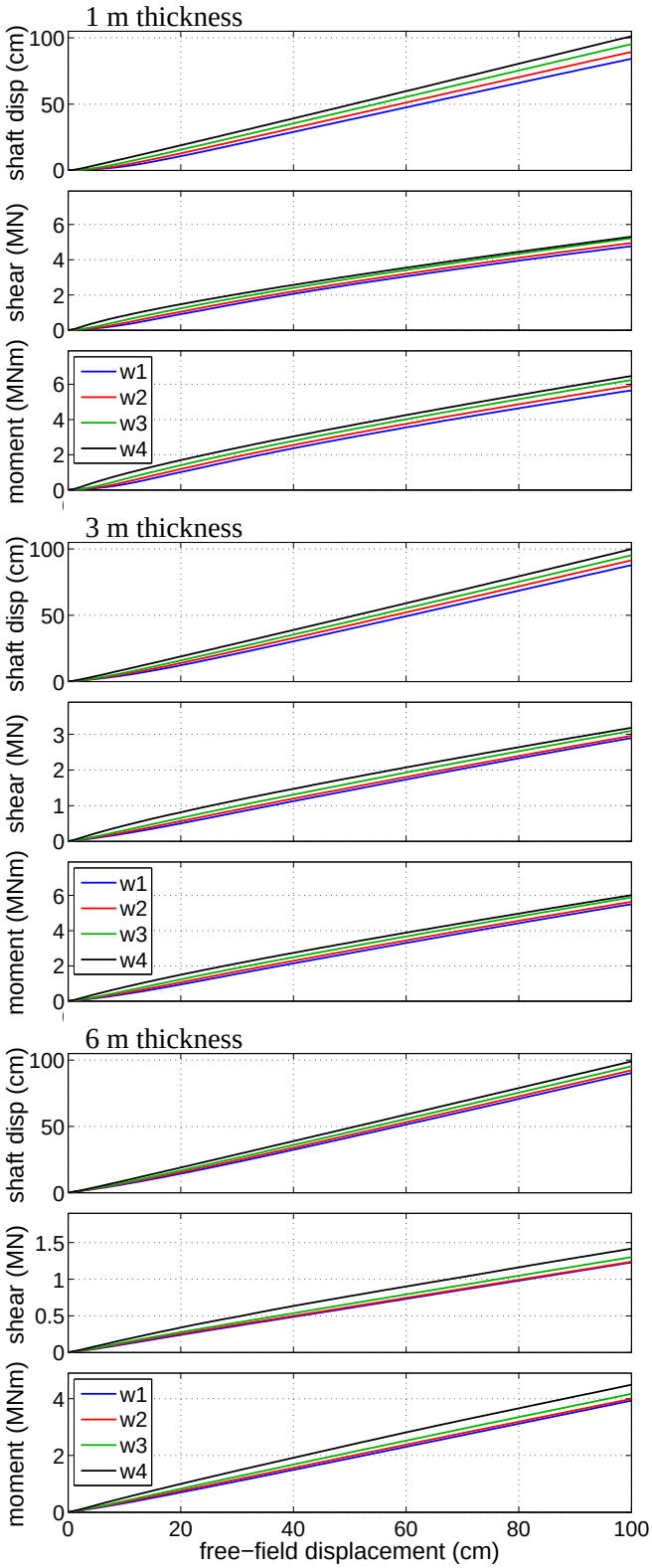

Figure 10.12: Maximum shaft bending demands for three liquefied layer thicknesses and four embankment widths with $D = 0.6$ m and $z = 3$ m.

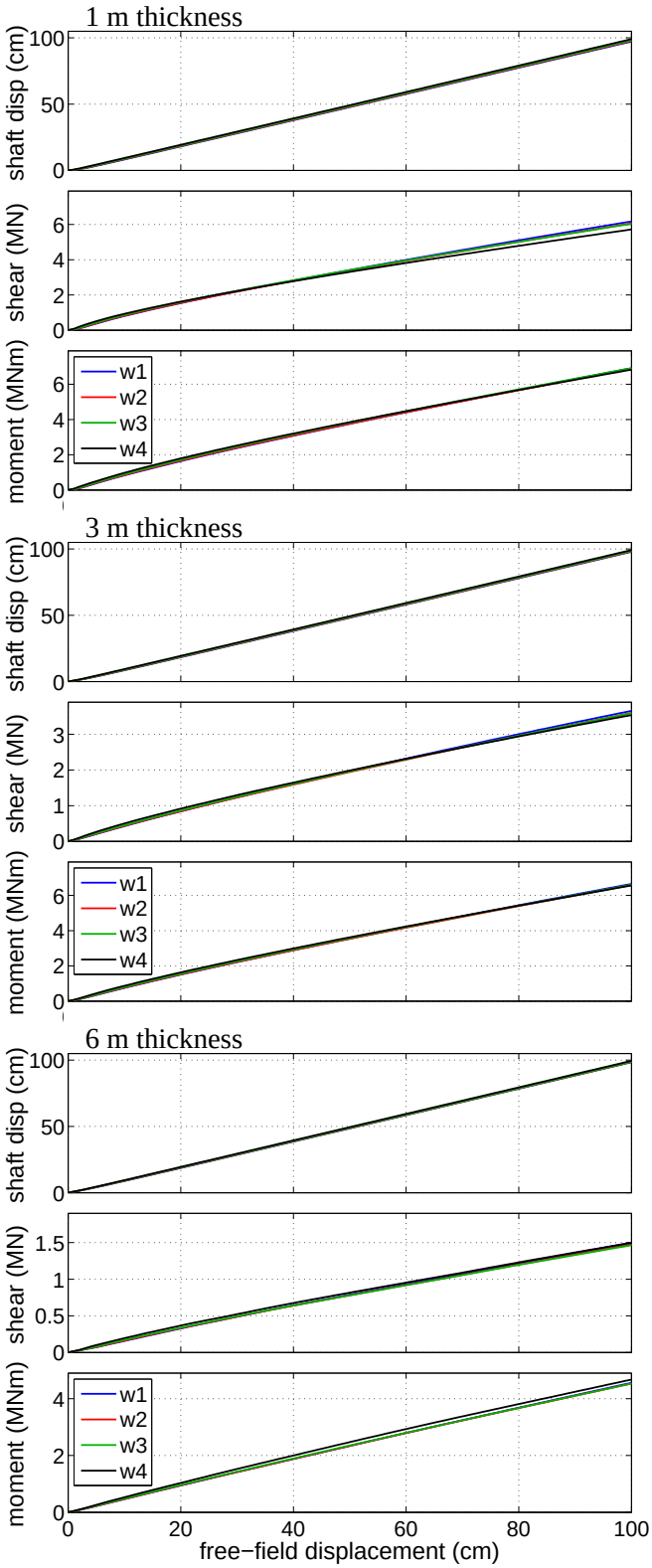

Figure 10.13: Maximum shaft bending demands for three liquefied layer thicknesses and four embankment widths with $D = 0.6$ m and $z = 6$ m.

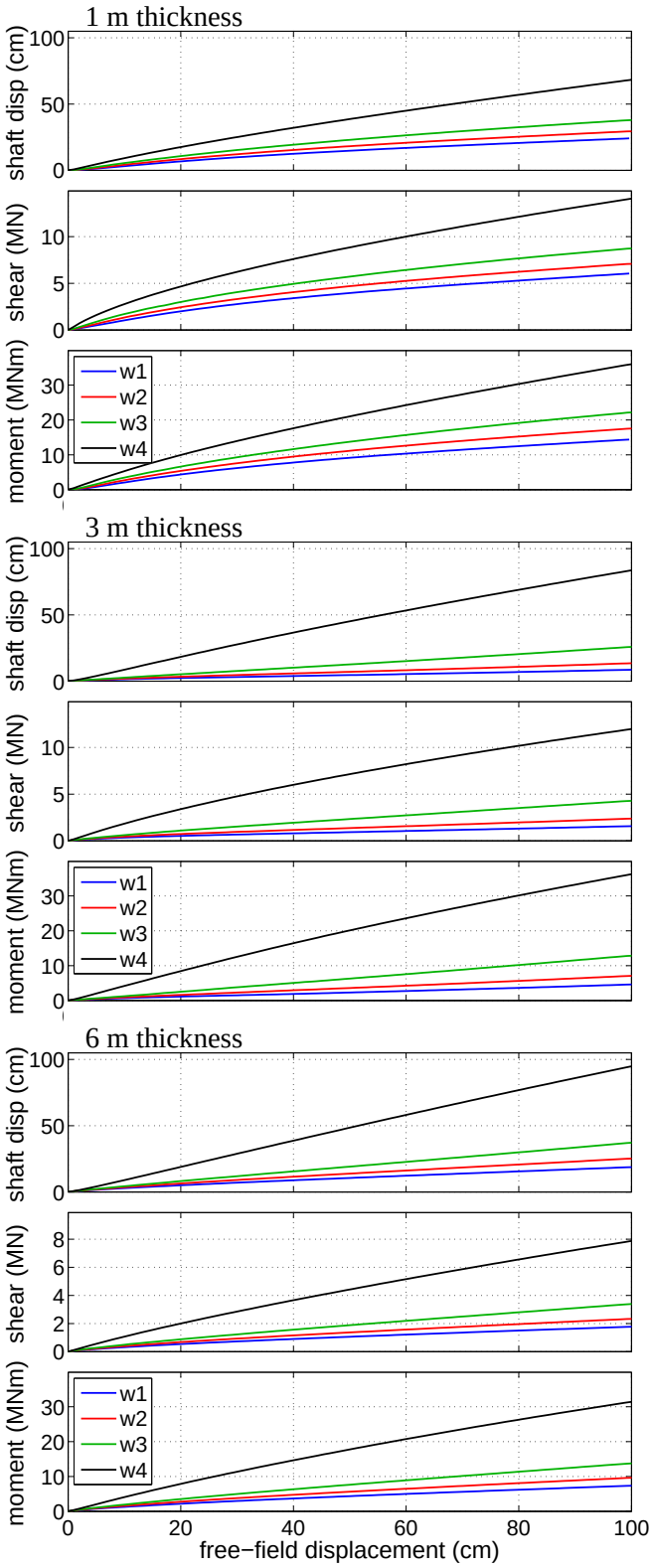

Figure 10.14: Maximum shaft bending demands for three liquefied layer thicknesses and four embankment widths with $D = 1.4$ m and $z = 1$ m.

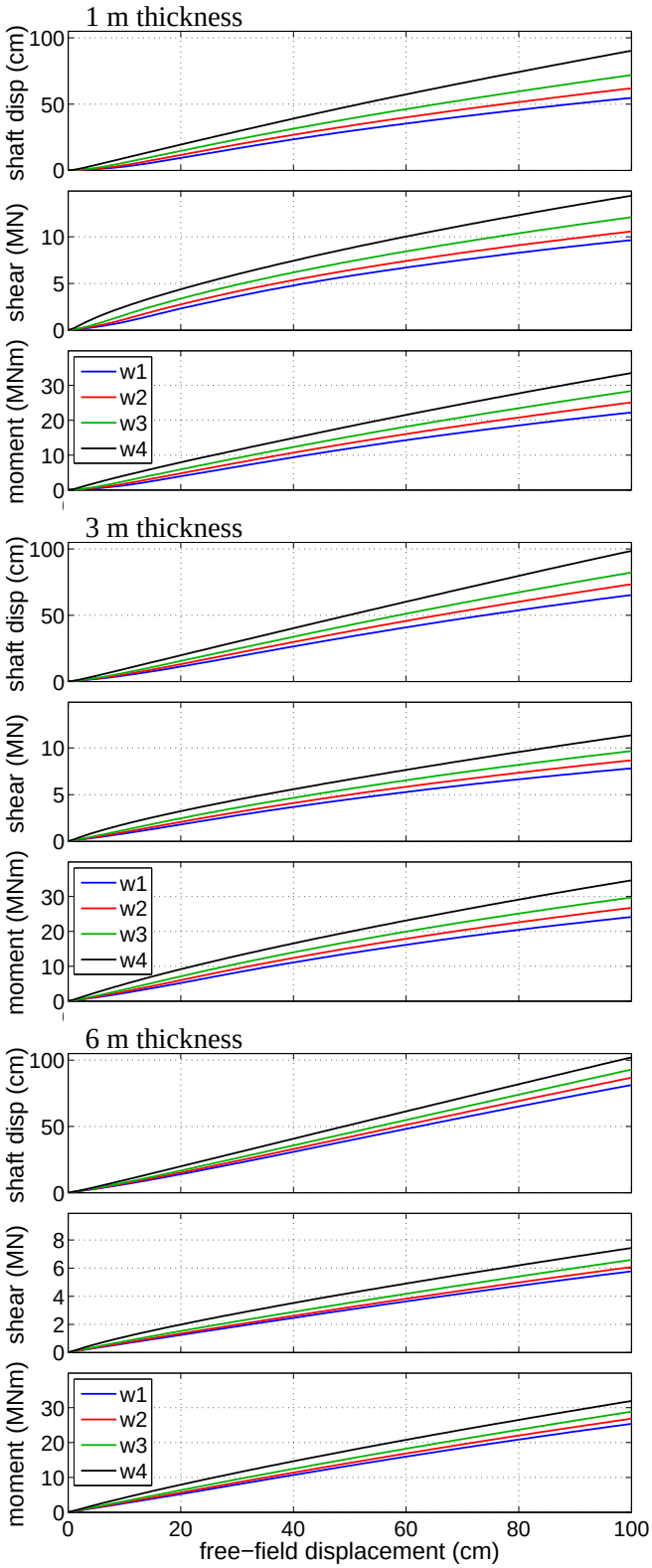

Figure 10.15: Maximum shaft bending demands for three liquefied layer thicknesses and four embankment widths with $D = 1.4$ m and $z = 3$ m.

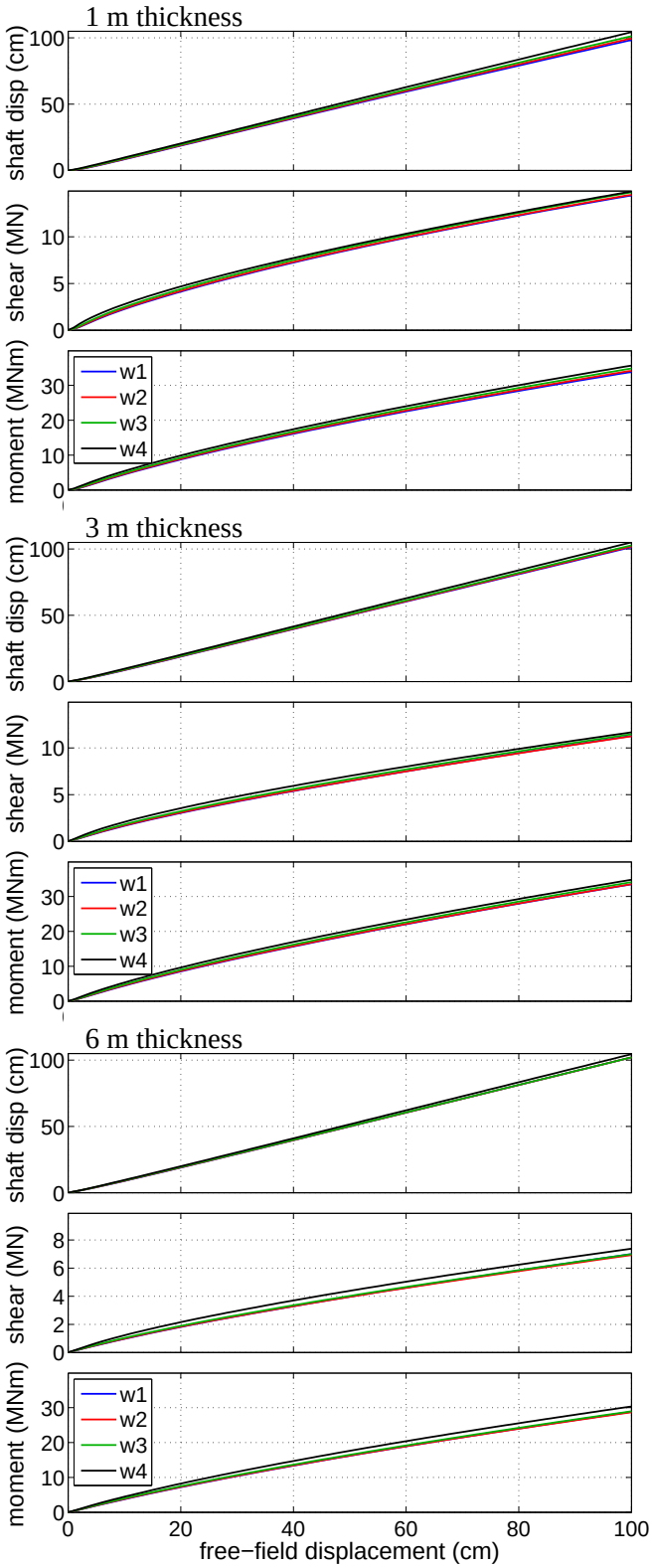

Figure 10.16: Maximum shaft bending demands for three liquefied layer thicknesses and four embankment widths with $D = 1.4$ m and $z = 6$ m.

10.2.3 Effects of Liquefied Layer Depth

The depth of the liquefied layer plays an important role in defining how changes in embankment crest width affect the embedded foundation during lateral spreading. For the cases with shallow liquefied layers, the width of the embankment is very influential to the shaft response. As shown in Figures 10.5 and 10.11 for the 0.6 m shaft, and Figures 10.6 and 10.14 for the 1.4 m shaft, there are significant differences in the shaft bending demand profiles and in the maximum bending demands for the four considered crest widths. As the depth to the liquefied layer is increased, the differences between the shaft bending demands resulting from the four widths become less significant. With $z = 3$ m (e.g., Figures 10.7 and 10.12), there is less variation in the shaft demands for increasing values of w than for the corresponding cases with $z = 1$. With $z = 6$ m (e.g., Figures 10.9 and 10.13), there is almost no difference in the demands manifested by the four crest widths.

These observations suggest that for these single shaft cases, there is a limiting liquefied layer depth at which the 3D embankment effects are no longer a significant factor in defining the structural demands in the foundation. When the liquefied layer is relatively shallow, the approach embankment is the primary source of kinematic demands on the shaft foundation during lateral spreading, and thus, differences in the geometry of the embankment are very influential on the foundation response. As the amount of crustal soil is increased, a greater amount of soil below the embankment is mobilized during the simulated lateral spreading event, and the kinematic demands placed on the foundation by the lateral movement of this crustal layer begins to control the overall shaft response.

10.2.4 Effects of Liquefied Layer Thickness

The effects of liquefied layer thickness are more subtle than those observed for the embankment crest width and liquefied layer depth. Based on the results shown in Figures 10.5 through 10.16, it does not appear that there is a clear trend that holds for all cases demonstrated by changes in t, however, there are differences in how the foundation is affected for the considered liquefied layer thickness values. One effect of the liquefied layer thickness is manifested in the foundation shear force diagrams. As shown in Figures 10.5 and 10.6, for the same values of D, w, and z, thinner liquefied layers lead to larger shear force demands. This is primarily due to how the applied displacement profile changes for thinner layers. As the thickness of the liquefied layer decreases, the shear demands on the shaft should approach the maximum possible value that would result in the absence of the linearly-distributed portion of the displacement profile. In contrast, the bending moment demands are much less affected by changes in t, though the distance between the maximum moment demands naturally increases with liquefied layer thickness.

The thickness of the liquefied layer also appears to affect how the embankment width influences the foundation response, and these effects show a depth dependence. As shown in Figures 10.11 and 10.14, the relative differences between the maximum bending demands for the four crest widths are not uniform for the three thicknesses considered. With $t = 1$ m, there is less variation with width than for the 3 and 6 m layer thicknesses. For deeper layer configurations, e.g., Figures 10.12 and 10.15, this effect is not as apparent and there is more consistency in the relative demands for the four widths at each thickness value.

10.2.5 Effects of Shaft Bending Stiffness

Some of the differences observed for the two shaft designs are expected effects of the two bending stiffness values represented by the shafts. The smaller shaft has a lower bending stiffness in comparison to the soil stiffness ($EI_{0.6} = 119$ MN·m^2 compared to $EI_{1.4} = 2494$ MN·m^2), therefore, for corresponding soil profiles the displacements of the 0.6 m shaft are larger and more closely resemble the applied displacement profile, while the larger shaft design offers more resistance to the lateral soil deformation. Since the larger shaft has a larger stiffness, for similar levels of shaft displacement, the shear and moment demands in the 1.4 m shaft are much larger than those in the 0.6 m shaft.

The liquefied layer depth effects discussed in the preceding sections appear to change based on the shaft bending stiffness. A comparison of Figures 10.12 and 10.15 demonstrates this effect; with $z = 3$ m, there is more variation with width in the maximum bending demands for the 1.4 m shaft than for the 0.6 m shaft. This observation also holds for the $z = 6$ m cases of Figures 10.13 and 10.16, as there is almost no variation with w for the 0.6 m shaft design, while the larger shaft still shows some visible differences for the considered crest widths. The implications of these observations make sense in the context of the problem, as it seems natural that the amount of crustal soil necessary to negate the three-dimensional effects of the embankment on the foundation response depends on the stiffness of the foundation itself.

10.3 Characterization of Geometric Site Effects

The basic observations made in the previous discussion demonstrate that geometric site effects during lateral spreading are not exclusive to the approach embankment. The amount of lateral pinning resistance that can be expected from a given foundation is not only dependent on the width of the embankment, but on the arrangement of the soil profile and stiffness of the foundation as well. The simplified pile pinning analysis approach discussed throughout this work likely captures the depth and thickness effects in the slope stability/deformation phase. A deeper liquefied layer

results in a larger failure mass and correspondingly larger resisting forces required to contain the failure. This shifts the compatible design displacement to the right, indicating that there is less available foundation resistance for the system. The foundation stiffness effects should be captured by altering the pushover curve obtained from the foundation model. Therefore, while it is likely that the geometric effects observed in the parameter study are captured in the pile pinning analysis approach, an independent prediction of the expected amount of lateral pinning resistance for a given foundation and site geometry represents a useful supplementary design tool.

In order to characterize the expected amount of lateral resistance for a particular case, the problem is framed in terms of a reduction in foundation bending demands from those returned by the pseudo plane strain geometry of the full width embankment cases. These reductions are characterized in terms of a reduction ratio computed by dividing the displacement, shear force, and bending moment demands at each analysis step by the corresponding demands for the wide embankment case with matching soil profile and shaft design. Figures 10.17 through 10.22 show these computed ratios plotted against the free-field displacement in the model. In these plots, a reduction ratio of 1.0 implies no reduction from the plane strain case, while a reduction ratio less than 1.0 indicates that the bending demands are less than those in the plane strain case. For example, a reduction ratio of 0.2 indicates bending demands that are 20% of those predicted using a two-dimensional description of the site geometry.

The reduction ratio plots of Figures 10.17 through 10.22 support the observations made in the previous sections, while providing a better representation of how the bending demands relate to each other over the full span of the free-field displacement, and thus illuminating aspects of the geometric site effects that are obscured in previous plots. Most of the site configurations display a similar trend in how the reduction ratios develop; the ratios are lower over the initial portion of the free-field displacement, and then gradually increase before reaching an essentially steady final value. There are some exceptions to this general trend, particularly for the $z = 1$ m configurations with $t > 1$ m, which, as shown in Figures 10.17 and 10.20, display the opposite ratio development pattern, with initially higher ratios becoming smaller with increasing free-field displacement and, for the 0.6 m diameter shaft cases, the reduction ratios do not all reach a steady value prior to the end of the analysis. The other exceptions to the general trend of reduction ratio evolution are displayed for the $z = 3$ m cases shown in Figures 10.18 and 10.21. Here, the ratios initially become smaller before they begin to gradually increase to their steady-state values. It is not yet clear whether this is a relevant effect due to these geometric conditions or a numerical effect due to differences in the model between the initial state and the loading state.

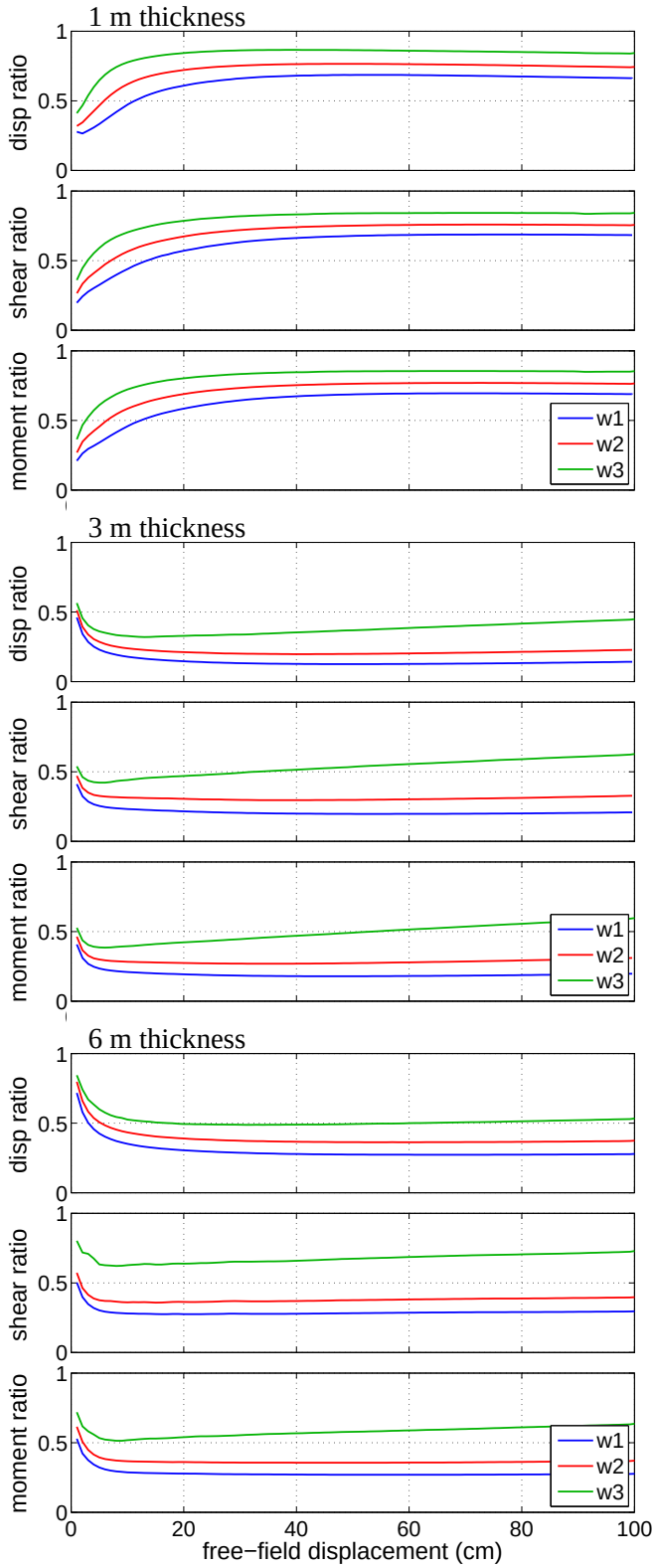

Figure 10.17: Bending demand ratios for three liquefied layer thicknesses and three embankment widths with $D = 0.6$ m and $z = 1$ m.

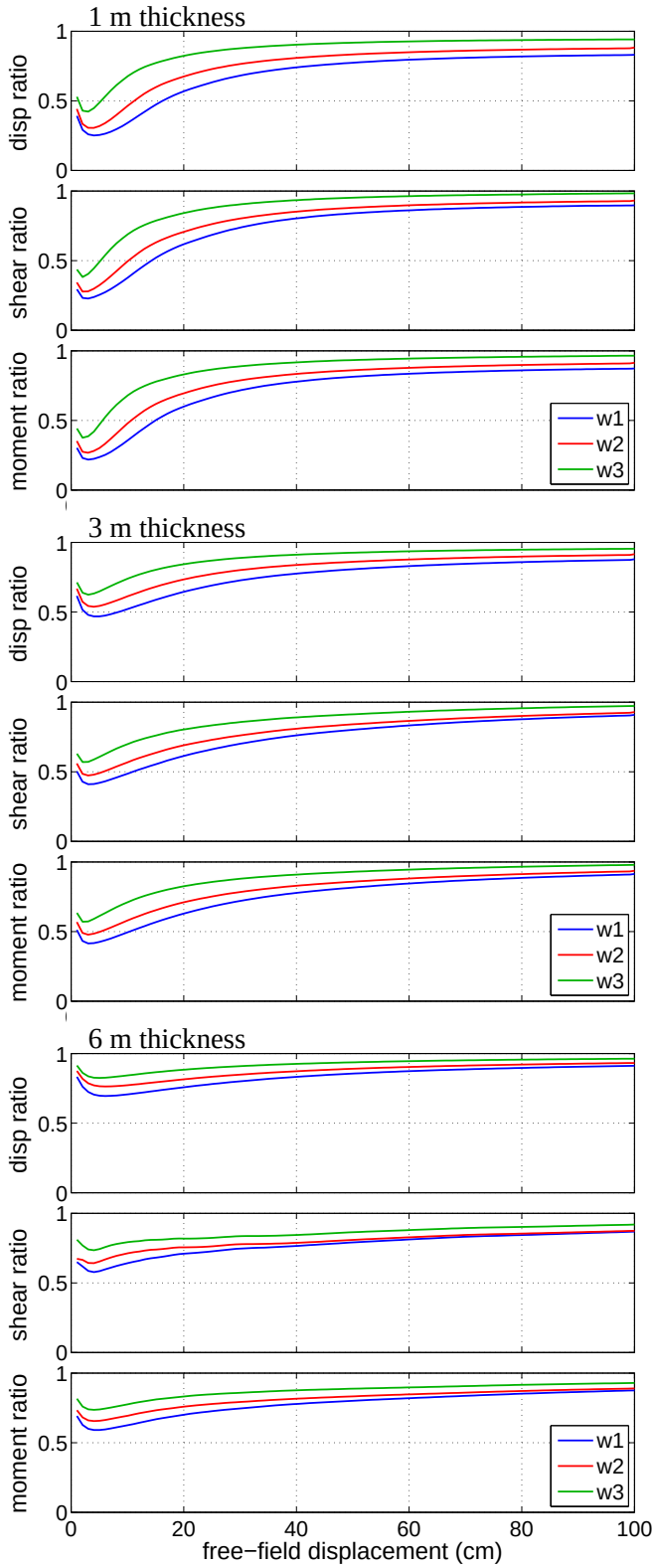

Figure 10.18: Bending demand ratios for three liquefied layer thicknesses and three embankment widths with $D = 0.6$ m and $z = 3$ m.

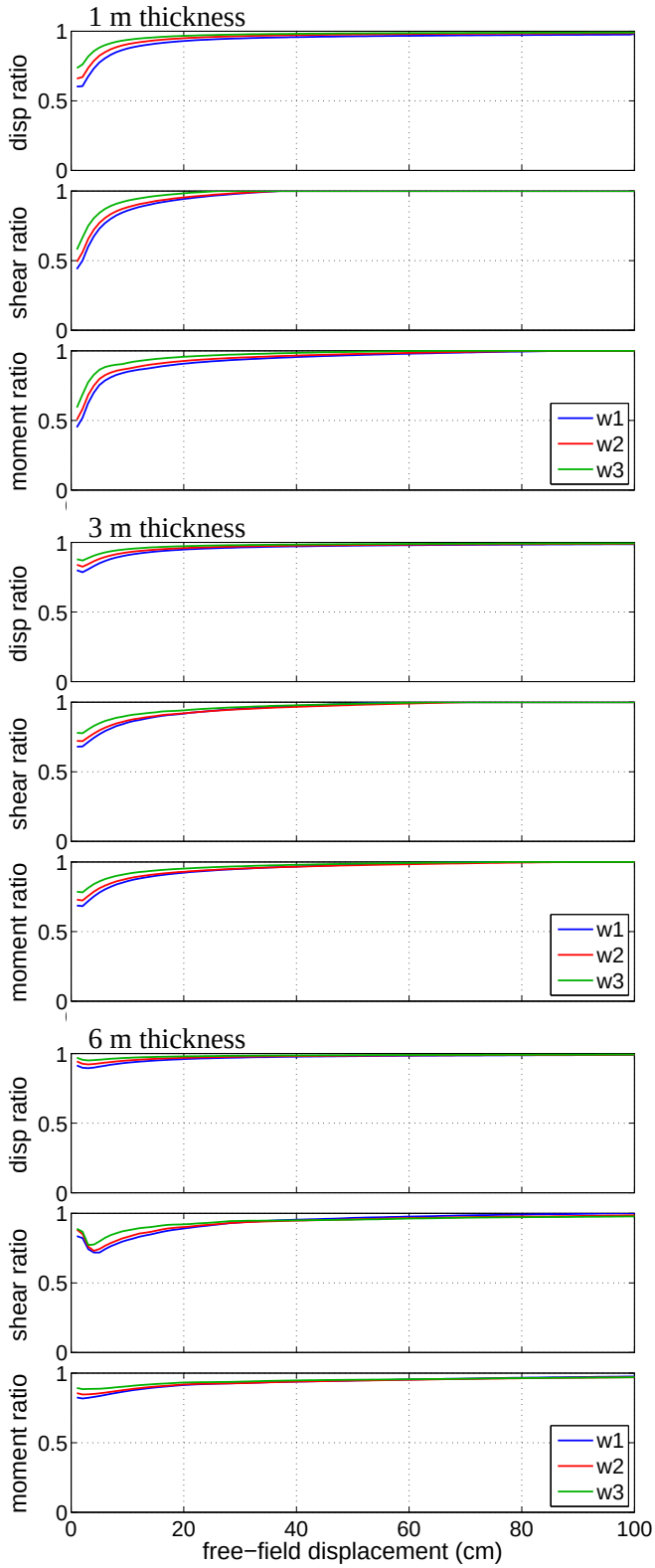

Figure 10.19: Bending demand ratios for three liquefied layer thicknesses and three embankment widths with $D = 0.6$ m and $z = 6$ m.

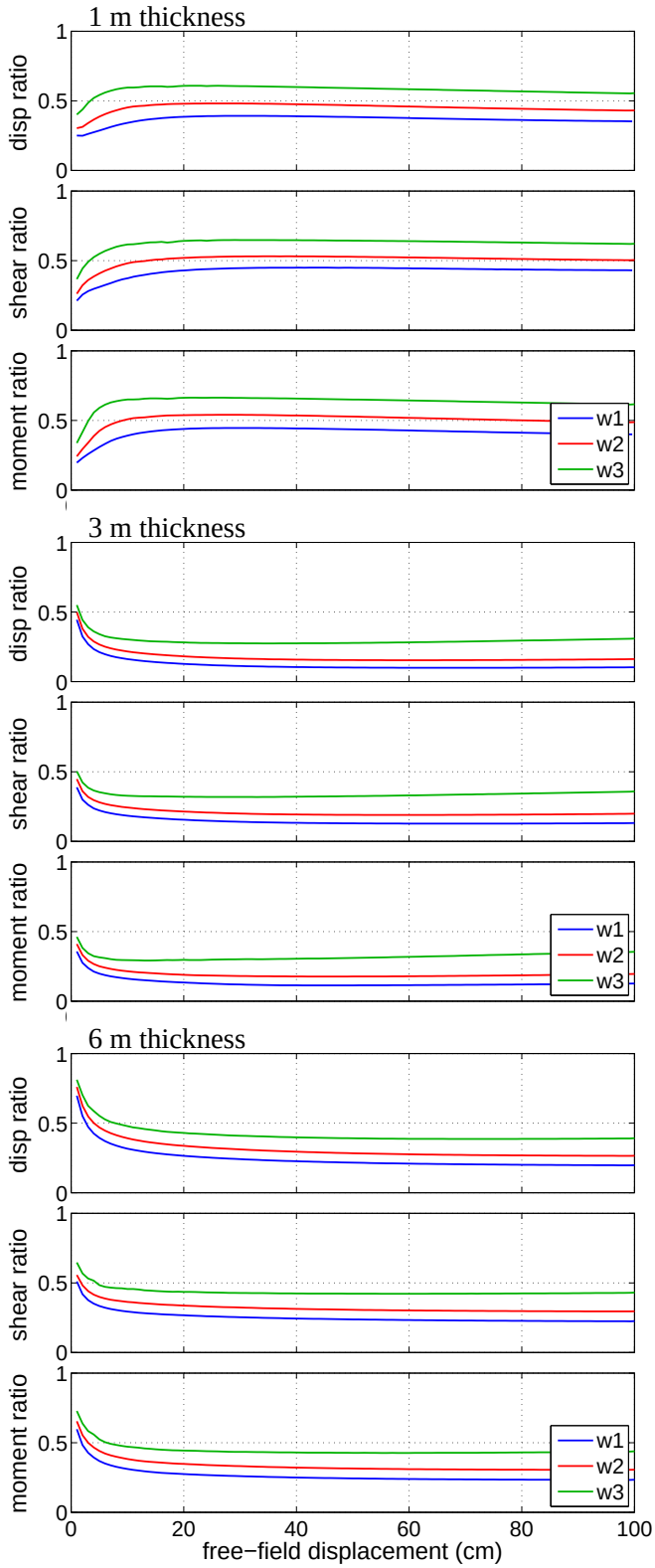

Figure 10.20: Bending demand ratios for three liquefied layer thicknesses and three embankment widths with $D = 1.4$ m and $z = 1$ m.

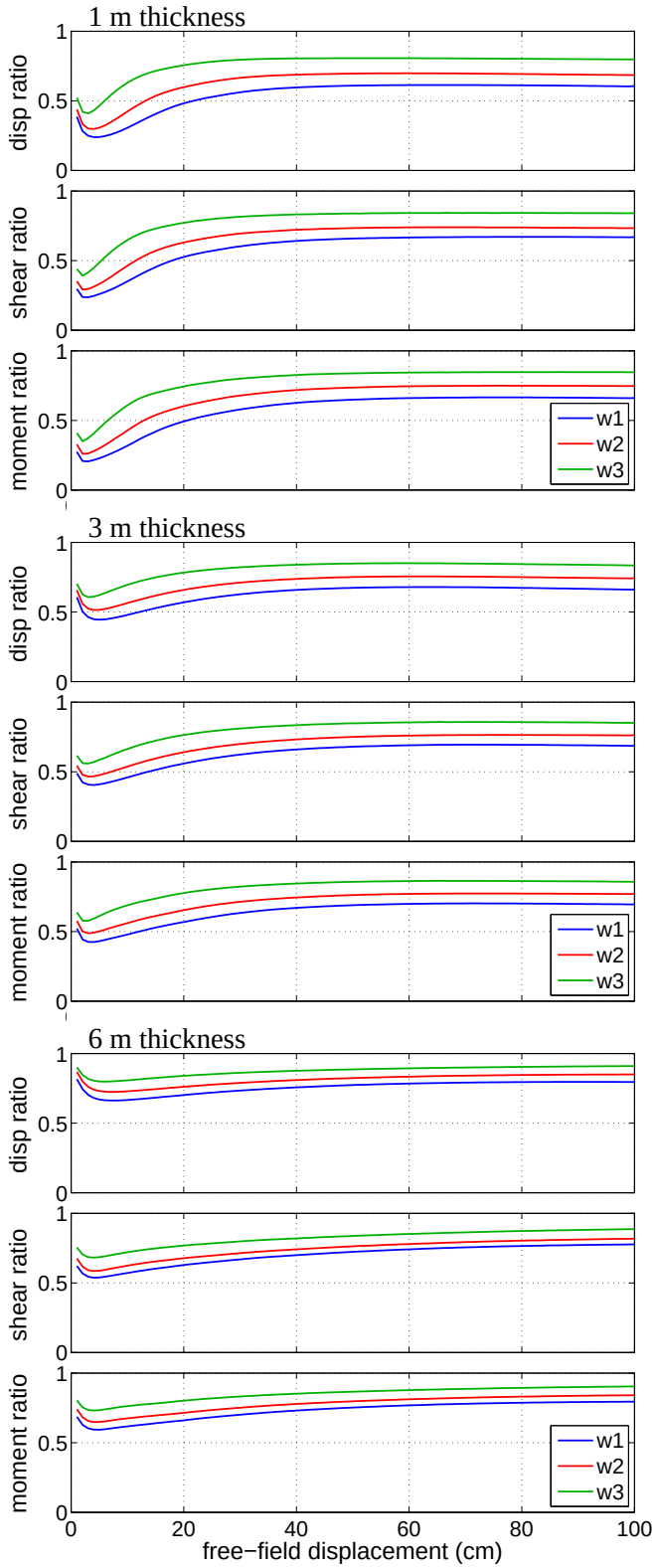

Figure 10.21: Bending demand ratios for three liquefied layer thicknesses and three embankment widths with $D = 1.4$ m and $z = 3$ m.

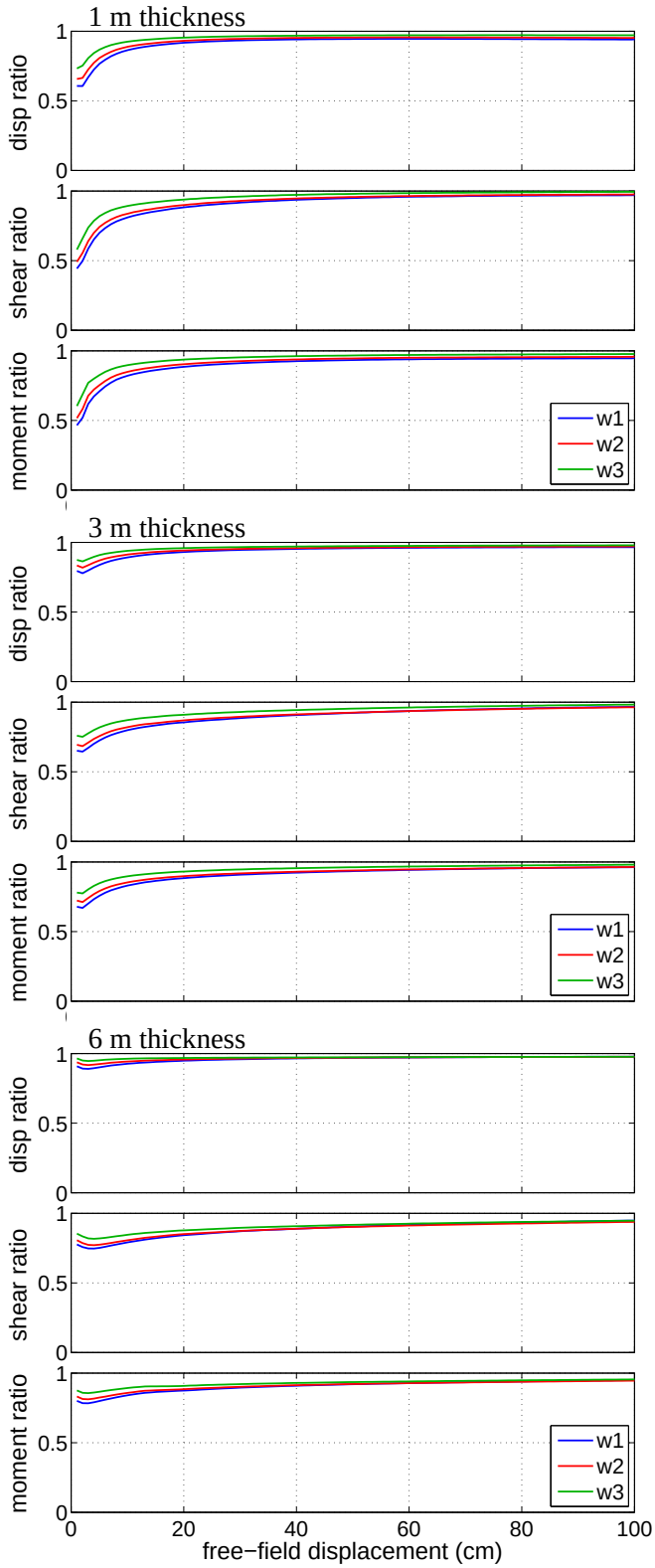

Figure 10.22: Bending demand ratios for three liquefied layer thicknesses and three embankment widths with $D = 1.4$ m and $z = 6$ m.

10.3.1 Reduction Model

The residual reduction ratio values (i.e., those at the end of the free-field displacement), are used to establish a means to predict expected reductions in shaft displacement, shear force, and bending moment demands for a given site geometry. By plotting the residual reduction ratios, R, against various combinations of liquefied layer depth, z, liquefied layer thickness, t, embankment width, w, and foundation bending stiffness, EI, in a natural-log plot, dimensionless relations are established that relate the reduction ratio to the site parameters. For this purpose, the tributary width introduced by Boulanger et al. (2006)

$$w = w_c + \frac{2}{m}h \tag{10.1}$$

where w_c is the crest width, m is the embankment side slope, and h is the embankment height, is used to describe the width of the embankment. The parameter study models all consider a 2H:1V side slope and a 5 m height, thus, the tributary widths are simply the sum of the crest widths and the height. This consideration results in a modified set of widths, $w = 9,\ 13,\ 21$ m.

Other than the unit weight of the crustal soil layer, γ, considered to provide a set of force units to offset those in EI, soil properties are not considered when constructing the relations between the reduction ratio and site parameters. All of the parameter study models consider the same set of soil properties, and since the problem has been framed in terms of reduction ratios for shaft bending demands, any effects related to the strength and stiffness of the soil should cancel out when the ratios between the various cases are computed.

The relations for which the data displayed the best correlation in the natural-log plots define two dimensionless parameters: the dimensionless reduction ratio,

$$\eta = \frac{\gamma^2 z^6 t^7}{(EI)^2 w^3} R \tag{10.2}$$

and the dimensionless site parameter,

$$\beta = \frac{\gamma z^3 t^3}{EIw} \tag{10.3}$$

These dimensionless parameters are computed for the 54 sets of residual reduction ratios for the maximum shaft displacement, maximum shaft shear force, and maximum shaft bending moment demands shown in Figures 10.17 through 10.22, as well as an additional 72 residual reduction ratios computed as the ratio of the shaft head displacement in each case to the applied free-field displacement.

Figures 10.23 through 10.26 show the relations between the dimensionless reduction ratio and

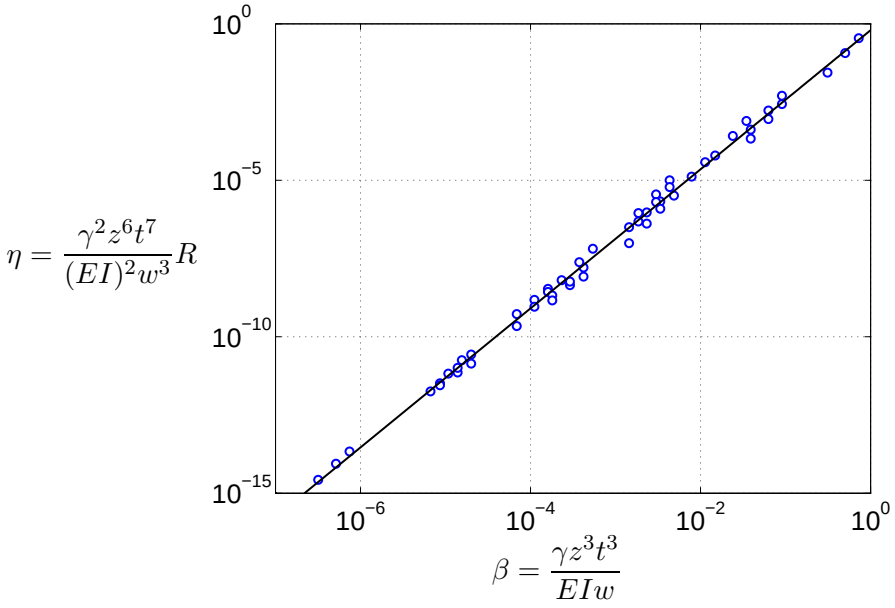

Figure 10.23: Dimensionless relationship between reduction ratio, R, and maximum shaft displacement.

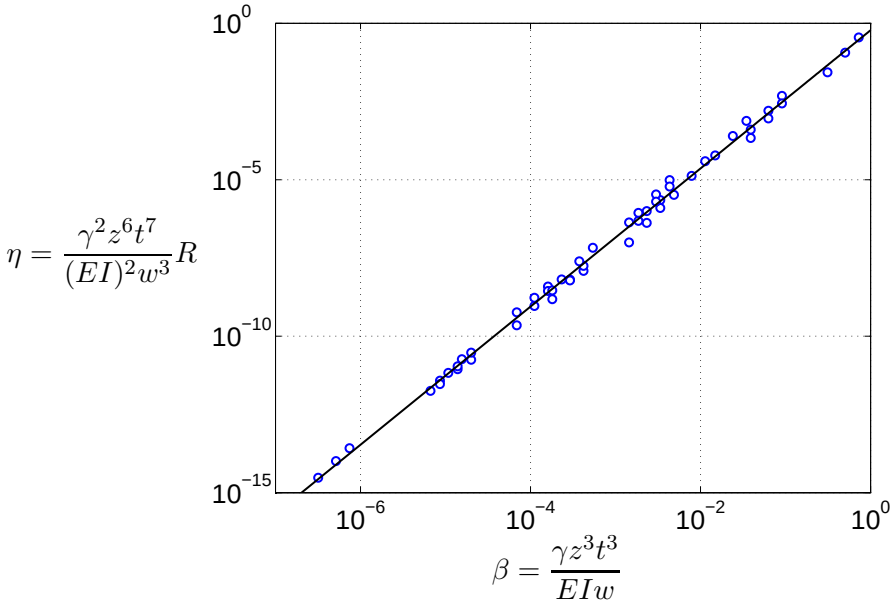

Figure 10.24: Dimensionless relationship between reduction ratio, R, and maximum shaft shear force.

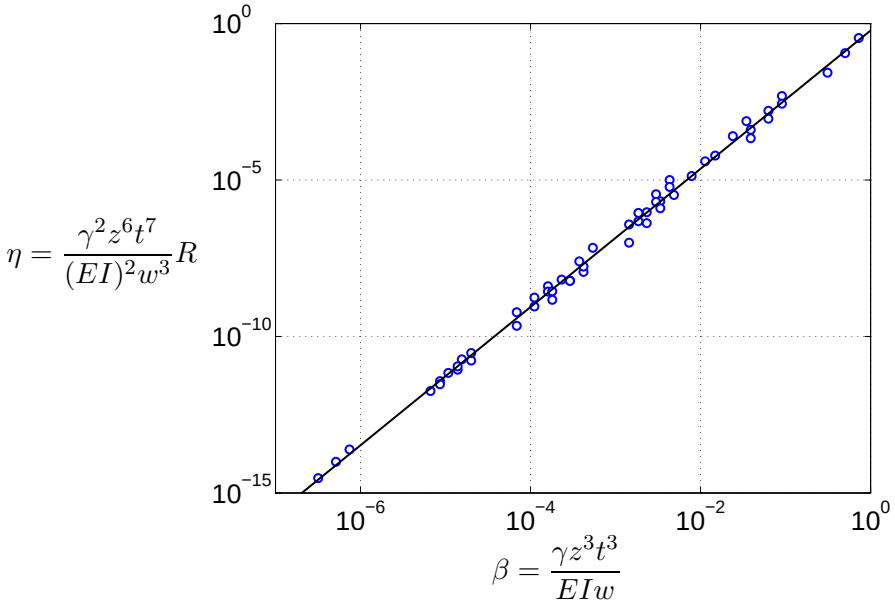

Figure 10.25: Dimensionless relationship between reduction ratio, R, and maximum shaft bending moment.

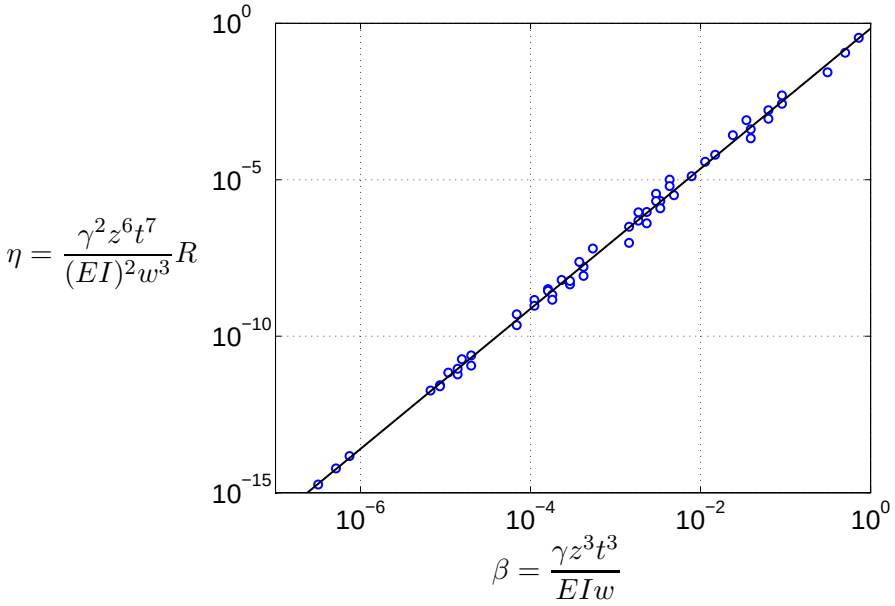

Figure 10.26: Dimensionless relationship between reduction ratio, R, and free-field displacement.

site parameters for each of these four cases. As shown, the data points for each reduction ratio type display a strong linear trend when plotted using the dimensionless parameters, β and η. Lines are fit to the data using least squares in order to establish expressions for the observed trends. A straight line in natural-log space represents

$$\ln \eta = b \ln \beta + \ln a \tag{10.4}$$

where the coefficients a and b are determined from the linear least squares procedure for the reduction ratios. Solving this expression for η gives

$$\eta = a\beta^b \tag{10.5}$$

which, when combined with (10.2) and (10.3) defines the following expression for the reduction ratio in terms of the site parameters and the least squares coefficients

$$R = aw^{3-b}\gamma^{b-2}z^{3b-6}t^{3b-7}(EI)^{2-b} \quad \leq \quad 1.0 \tag{10.6}$$

A reduction ratio greater than 1.0 implies an increase in the shaft bending demands as compared to 2D conditions, therefore, the expression is defined such that $R \leq 1.0$ to ensure that such values are not considered.

As shown in Figures 10.23 through 10.26, the dimensionless reduction ratio relationships for each of the four considered cases display nearly identical trends. This appears reasonable based on the reduction ratios plotted in Figures 10.17 through 10.22, which display little difference in the residual values for each maximum bending demand. As expected based on the observed similarity between the four reduction ratio types, the least squares coefficients computed for each case and shown in Table 10.3 are all nearly the same. Due to this similarity between the reduction ratio types, it is proposed that a single reduction ratio model that uses average least squares coefficients can be applied to determine reductions in any of the considered quantities without resulting in significant error. The a- and b-coefficients computed for the maximum shaft displacement reduction ratio are used to define this master model, which can now be expressed as

$$R = 0.63\frac{w^{0.8}\gamma^{0.2}z^{0.6}}{(EI)^{0.2}\,t^{0.4}} \quad \leq \quad 1.0 \tag{10.7}$$

By multiplying the value of R computed from Equation (10.7) with the maximum bending demands obtained from a simplified analysis of a bridge foundation, e.g., the initial BNWF pushover phase of the pile pinning analysis procedure, a designer can obtain a first-order approximation of the foundation bending demands with consideration for the 3D geometry of a given site. Alternatively,

Table 10.3: Least squares coefficients for each reduction ratio type.

Reduction ratio type	a	b
max shaft displacement	0.63	2.22
max shear force	0.60	2.21
max bending moment	0.60	2.21
free-field displacement	0.68	2.22

given a particular set of site parameters, the reduction ratio can be applied to the free-field lateral spreading displacement value estimated using a predictive method (e.g., Baska, 2002; Youd et al., 2002; Idriss and Boulanger, 2008) in order to estimate the expected shaft cap displacement at the site. The scope of the current data set used to establish this reduction model is not sufficiently large and diverse as to suggest that the reductions predicted by its application are definitive results, however, this reduction model can be an effective tool if used in support of an independent analysis, with the reductions computed from (10.7) serving as an estimate of the amount of lateral resistance a foundation may provide during lateral spreading.

10.3.2 Effects of Site Parameters on Reduction Model

It is of interest to evaluate the effects of each of the four primary site parameters on the reduction ratio estimated from (10.7). These observations overlap somewhat with those made previously, but evaluating the effects of these parameters in the context of the reduction ratio allows for them to be isolated further. In order to make these evaluations, a generic site profile is assumed where $EI = 10$ MN·m, $t = 4$ m, $z = 2$ m, $\gamma = 17$ kN/m^2, and $w = 10$ m. In the discussion that follows, unless otherwise stated, these parameters apply to the results shown.

Figure 10.27 shows how the reduction ratio varies with foundation bending stiffness, and also demonstrates how the relationship between R and EI is affected by changes in the other site parameters. These plots generally show the expected effects of foundation bending stiffness on the reduction ratio. As EI is increased, R becomes smaller, implying a greater reduction from the plane strain case. As the depth to the liquefied layer or the embankment width are increased, larger values of EI are required to affect a similar reduction in the system. The inverse relation holds for changes in liquefied layer thickness, as larger values of t decrease the amount of foundation stiffness required to achieve a particular reduction. Additionally, these plots show that for the assumed generic site parameters, the thickness of the liquefied layer is less influential on the R-EI relationship than the other parameters.

To assess the effects of liquefied layer thickness on the computed reduction ratio, the relations

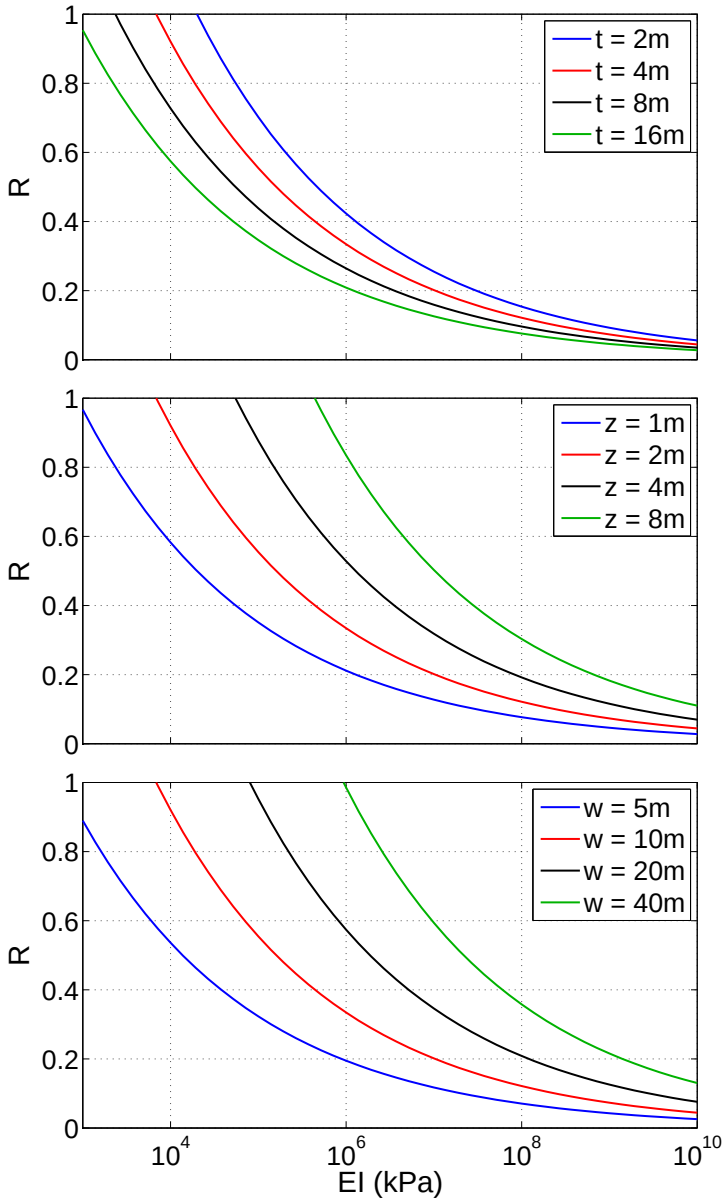

Figure 10.27: Variation of reduction ratio, R, with shaft bending stiffness, EI, and effects of changing t, z, and w on this relationship.

between t and R are similarly plotted in Figure 10.27. Because t and EI are both located in the denominator of (10.7), they share a similar overall trend in relation to R, and in how the other parameters influence this relation. Increases in embankment width and liquefied layer depth necessitate a larger liquefied layer thickness to maintain a steady reduction ratio, while increasing the foundation bending stiffness decreases the thickness necessary to maintain a certain level of reduction. The amount of influence of the non-thickness site parameters on the R-t relation appears to be similar based on the spread between the individual curves in the plots of Figure 10.27.

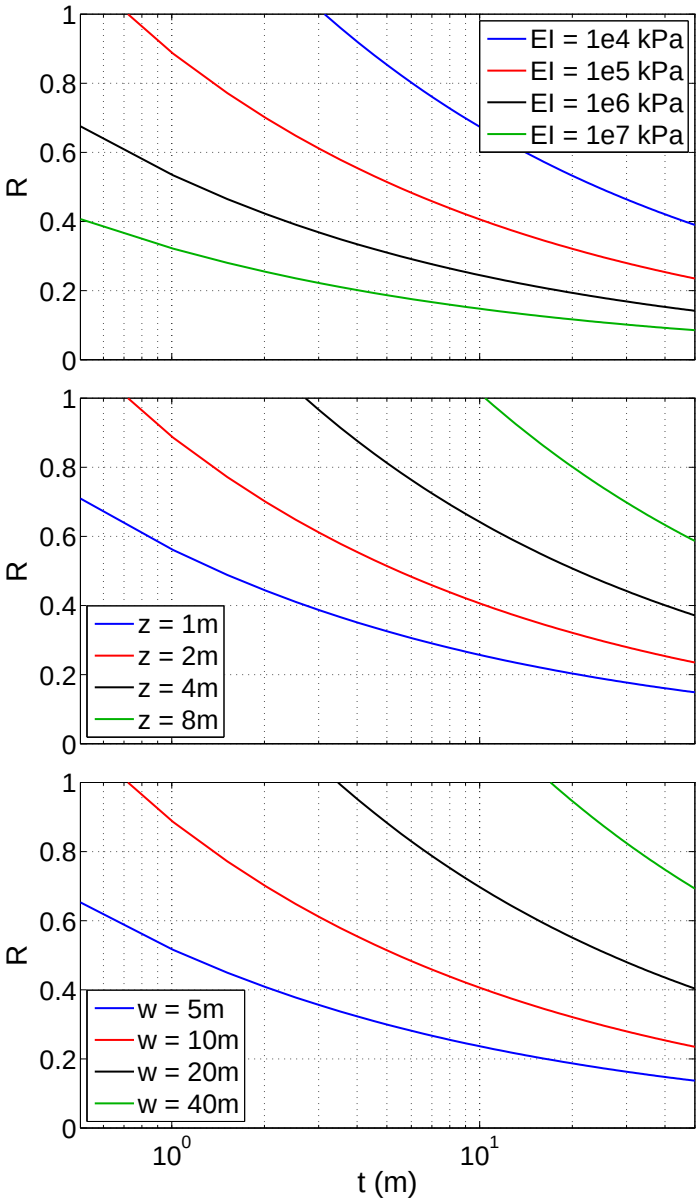

Figure 10.28: Variation of reduction ratio, R, with liquefied layer thickness, t, and effects of changing EI, z, and w on this relationship.

The relations between the reduction ratio and the liquefied layer depth and embankment width shown in Figures 10.29 and 10.30 confirm the previously observed effects of these parameters on the amount of lateral foundation resistance available for a given site configuration. Decreasing either of these parameters leads to larger reductions in foundation demands as compared to the 2D site description, and this is manifested in the plots as smaller reduction ratios for smaller values of z and w. Increasing either the liquefied layer thickness or foundation stiffness increases the amount of crustal soil which can be present in the soil profile before the reduction becomes negligible, with EI

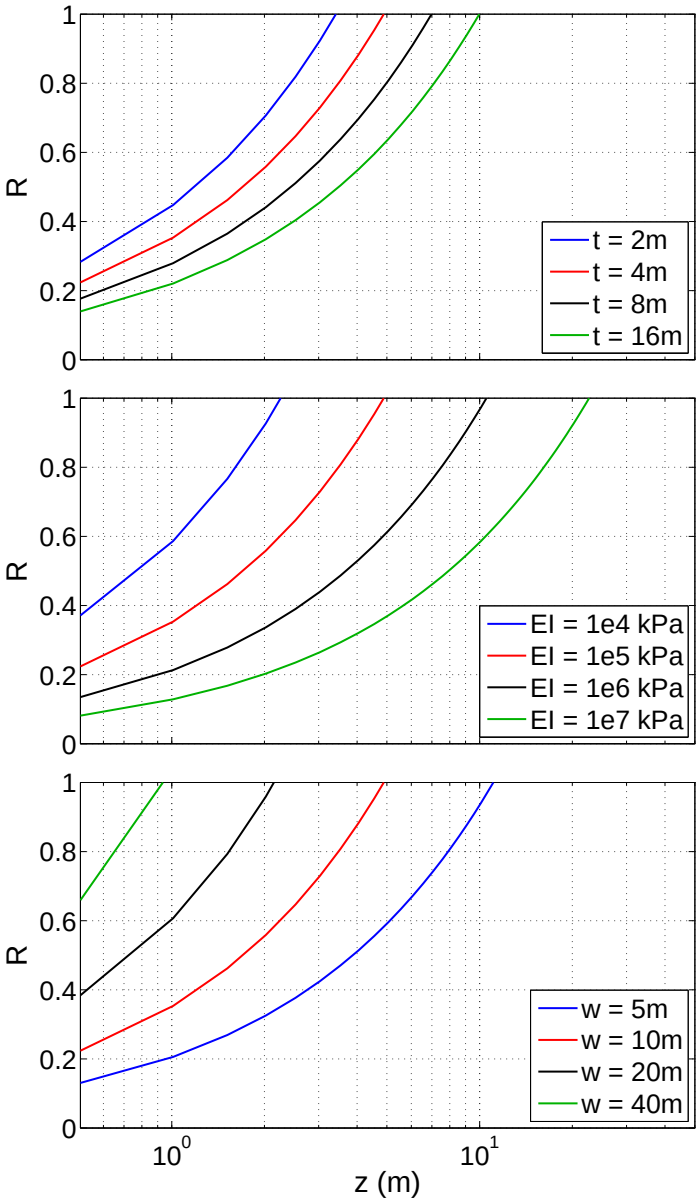

Figure 10.29: Variation of reduction ratio, R, with liquefied layer depth, z, and effects of changing t, EI, and w on this relationship.

demonstrating the greater amount of influence on this effect. Increases in t and EI affect the embankment width similarly, demonstrating that as these parameters become larger, the embankment width at which 3D effects become insignificant also becomes larger. The influence of w on the depth effect and z on the width effect are also evident in these results, with Figures 10.29 and 10.30 demonstrating that larger embankment widths require shallower liquefied layers to affect a similar level of reduction in the foundation demands. These observations correspond with those made qualitatively from previous plots, lending confidence to the final form of the reduction ratio model.

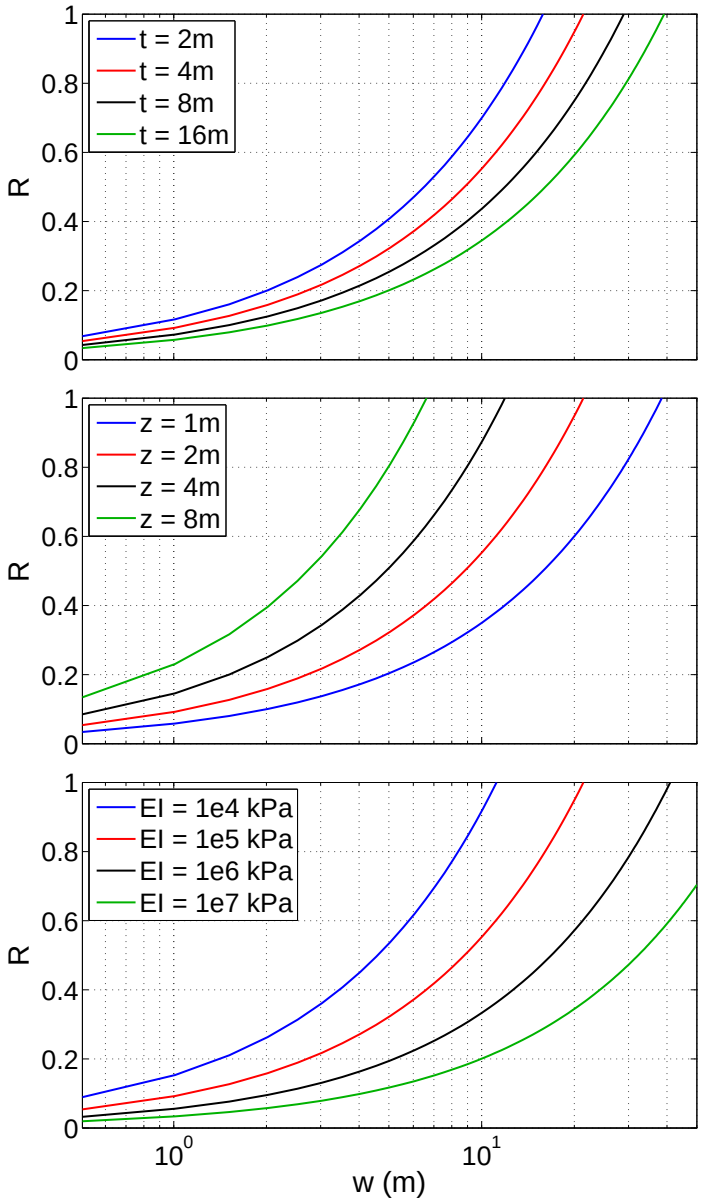

Figure 10.30: Variation of reduction ratio, R, with embankment tributary width, w, and effects of changing t, z, and EI on this relationship.

10.4 Summary

A series of 3D finite element models was used to examine the influence of various site parameters on the response of a single deep foundation to the kinematic demands of lateral spreading. These models focused on assessing the effects of changes in the embankment width, the depth to the liquefied layer, the thickness of the liquefied layer, and the bending stiffness of the foundation. The observed effects were framed within the context of a reduction in foundation bending demands as compared to a

plane strain description of the site. Based on this parameter study, it was determined that the interaction of the geometric site parameters defines the overall lateral response of the system.

Reductions ratios were computed by comparing the foundation demands from the cases with 3D geometries to corresponding results obtained from wide geometry configurations that mimic plane strain conditions. The residual reduction ratios were compared to various combinations of the site parameters in order to establish dimensionless parameters, which, when plotted in natural-log space, demonstrated a strong correlation for the data set. A mathematical model that describes the residual reduction ratio in terms of the site parameters was obtained from this plotted data using least squares. Using this proposed reduction model, a first-order approximation can be obtained for the expected amount of pinning resistance available for a particular site configuration. Properly validated this reduction model will represent a valuable tool to the designer, especially when used in concert with other simplified analysis procedures, as it provides an independent assessment of the general foundation response to lateral spreading.

Chapter 11

RESEARCH OUTCOMES

This report presents a research program performed in the pursuit of identifying and quantifying mechanisms that lead to reductions in bridge foundation demands during lateral spreading with consideration for three-dimensional site geometry effects. This research encompasses the review of current design procedures, the identification of appropriate case history bridges, and the development and analysis of numerical models to study the response of two case history bridge foundations to the kinematic demands of lateral spreading. The research also includes a parameter study and development of a simplified procedure to estimate reduction factors for shafts subjected to lateral spreading.

11.1 Summary and Conclusions

A summary of the completed work and a discussion of the related research findings are presented for each of the primary topics considered in the work. The following sections reiterate the fundamental aspects of each topic and identify any conclusions drawn from that portion of the research. Finally a description of the recommended design guidelines for lateral spreading as well as a simplified demand reduction equation for lateral spreading are presented in Appendix A.

11.1.1 Review of Current Simplified Design Procedures

The design procedures used by the California Department of Transportation and Washington State Department of Transportation for bridge foundations subject to liquefaction-induced lateral ground deformation were reviewed to assess the state of current design practice for this load case. These two approaches are based off of the same underlying documents, and consider similar analysis components such as beam on nonlinear Winkler foundation and slope stability models, however, due to key differences in assumptions, they lead to different outcomes for certain site configurations.

The Caltrans procedure makes a distinction between cases for which it is expected that the foundation will provide lateral pinning resistance, and cases for which no resistance is assumed. For the cases where assuming foundational restraint appears to be reasonable, the pile pinning analysis procedure (Martin et al., 2002; Boulanger et al., 2006; Ashford et al., 2011), which is based on

the assumption of compatibility between the foundation resistance and embankment deformation during lateral spreading, is adopted by Caltrans. The WSDOT design procedure makes no explicit distinction between these two types of cases, and instead assumes that the bridge foundation shall be designed to withstand the soil deformation and attendant lateral forces that would occur due to liquefaction-induced flow failure or lateral spreading in the absence of a foundation.

11.1.2 Case History Evaluation

A series of Chilean bridge sites affected by lateral spreading due to the 2010 offshore Maule earthquake were examined for potential use as a case study to support this research. These bridge sites were evaluated in terms of the evidence of three-dimensional soil deformation effects, the sufficiency of the available structural and geotechnical data, and the applicability of the bridge design details to newly designed structures. Based on this evaluation, Puente Mataquito and Llacolén bridge were selected for use as the primary case study sites for this research, while several other bridges were identified as candidates for future consideration.

11.1.3 Numerical Analysis of Case Study Sites

Three numerical modeling techniques were used to examine the effects of lateral spreading on the selected case study bridges. These models vary in complexity and in their intended use. A summary of each technique and the associated findings follows.

11.1.3.1 Plane Strain Models

Dynamic plane strain effective stress models of the Puente Mataquito site were developed and analyzed to evaluate the response of the bridge and soils to seismic excitation. This model was used to demonstrate the effects of the soil domain thickness on the response of the bridge foundations, and to verify assumptions made during the development of the idealized soil profile used for the numerical models of the site. A version of the plane strain model was used to assess the performance of the bridge to a ground motion similar to what may have been experienced at Puente Mataquito. This analysis returned results that were reasonably similar to observations made following the Maule earthquake, and confirmed the susceptibility of the site to liquefaction. Lateral spreading deformations associated with liquefaction were observed in these models, and the abutment foundations were found to be affected more significantly by this soil deformation than most of the interior pier foundations. Based on the scope of liquefaction and lateral spreading in the soil near the two abutments,

and a comparison of the foundation demands imposed upon the bridge foundations due to these paired phenomena, the southwest abutment was identified for further study.

Plane strain models were not developed for Llacolén bridge. This bridge has 56 spans and it is 2,160^{m} long. A complete 2D analysis of this bridge would be too expensive numerically and would not provide further information than what was learned from the Puente Mataquito case.

11.1.3.2 Three-Dimensional Models

Three-dimensional finite element models of the southwestern abutment of Puente Mataquito and the northeastern approach of the Llacolén bridge were developed and analyzed in an effort to identify the mechanisms leading to the reductions, if any, in foundation demands implied by the combination of large free-field lateral spreading deformation and minimal structural damage observed at the site. Overall, the results obtained from the 3D modeling effort compared favorably to the site observations.

In the case of Puente Mataquito the general soil deformation patterns were the same, with the approach embankment tending to slump vertically and spread outwards instead of moving only in the direction of lateral spreading. The magnitudes of these deformations did not directly correspond with the reported site response, however, the similarity in the trends captured by the model to those observed increases confidence in the results obtained from the model.

In the case of Llacolén bridge the 3D finite element analysis showed that even though the mass of the soil flowing into the foundation is very large compared to the resistance the foundation system can provide, deformation in the near-field of the foundation system is smaller specially in the case where the lateral resistance of the bridge deck is considered. This implies that even for this case pile pinning effects are relevant. It was also shown that due to the three dimensional geometry of the bridge structure transverse demands can be significant. These demands cannot be considered in simplified analysis.

The primary goal of these models is to assess the response of the foundation to a set of demands similar to those that would occur during an actual lateral spreading event. All of the 3D analysis presented in this work was conducted pseudo statically, working from the assumptions that liquefaction has already developed and inertial effects can be ignored. In the case of the Puente Mataquito the validity of these assumptions was addressed through the consideration of two distinct approaches to simulating the kinematic demands of lateral spreading. The foundation bending demands resulting from each approach were found to be similar, further increasing confidence in the results from the 3D modeling effort. Based of these results, for the Llacolén bridge only one approach to simulating the kinematic demands was used.

Models that simulated lateral spreading using an applied kinematic approach demonstrated a reduction in the soil and foundation demands when 3D site geometry was considered. These models identified the importance of the lateral resistance provided by the bridge superstructure in defining the response of the foundation, and demonstrated the differences in foundation response before and after the deck expansion gap was closed due to lateral foundation movement. The models that simulated lateral spreading through gradual reductions in the shear strength and stiffness of the liquefiable soil layer identified how the presence of the approach embankment creates instability in the liquefied soil system. Further evidence of the foundation pinning effect was obtained through the comparison of models both with and without the bridge foundation.

11.1.3.3 Simplified Models

The pile pinning analysis procedure (Martin et al., 2002; Boulanger et al., 2006; Ashford et al., 2011) was assessed through an application of the Caltrans (2011) version of the procedure to the southwest abutment of Puente Mataquito and the northeast approach of Llacolén bridge. In the case of Puente Mataquito the compatible displacements obtained from the pile pinning analysis were shown to possess great variability with respect to the particular assumptions and modeling choices made in the individual analysis phases that comprise the pile pinning approach. It was proposed that the compatible displacement used in the final foundation design phase be selected as an average of the compatible displacements resulting from a series of different modeling configurations and assumptions. In this manner, the design solution that is most representative of the site conditions can be obtained.

The pile pinning analysis procedure was shown to produce foundation demands that were consistent with the results obtained from certain 3D model configurations. When a smaller deck expansion gap was considered in the 3D model, the two approaches produced reasonably similar foundation bending demands. When the 3D models considered a larger expansion gap, comparisons of the two sets of foundation demands were not as favorable. A potential solution to this problem was proposed and demonstrated in which the design displacement is defined as the sum of the gap magnitude and the compatible displacement obtained from the pile pinning approach. With this modification, the pile pinning results were much more similar to those obtained from the large expansion gap 3D models.

Pile pinning analyses were also performed for the Llacolén bridge to evaluate their credibility to be used for design in practice for a case where soil embankment three dimensional effects are not present. It was shown that if this method is applied carefully, with a careful estimation of ground

displacement and correct definition of structural components in the problem, e.g. the expansion gap and bridge deck resistance, they are able to predict the bending demands in foundations subject to lateral spreading loading conditions.

11.1.4 Parameter Study of Geometric Site Effects

A series of 3D finite element models was developed and analyzed to investigate the effects of various site parameters on the response of a single deep foundation to the kinematic demands of lateral spreading. This modeling effort provided further evidence that consideration for the 3D geometry of the site is an important factor in this type of analysis. It was determined that the lateral response of the foundation for a particular site is governed by the interaction of multiple site parameters, including the location and size of the liquefied layer, the width of the approach embankment, and the size and stiffness of the foundation.

A predictive model was developed from the parameter study data set that can be used to estimate the reductions in foundation demands as compared to a two-dimensional description of the site. The reductions returned by this model can be applied to the foundation shear force and bending moment demands obtained from a simplified analysis in order to get a first-order approximation of the expected demands with consideration for 3D site effects. The reduction model can also be used to inform a simplified analysis approach by providing an estimate of how much lateral pinning resistance can be expected for a particular case. Due to the limited size of this parameter study data set the proposed reduction equation should be used with care and only to inform a simplified analysis approach.

11.2 Directions for Future Research

The research discussed in this document has identified several avenues for further study into the effects of lateral spreading on bridge foundations. This future research is divided into two broad groups: (1) the further numerical evaluation of case history bridges with consideration for 3D effects, and (2) the expansion and refinement of the parameter study data set for the evaluation of geometric site effects.

11.2.1 Case Study Evaluation

The 3D finite element simulations related to Puente Mataquito and Llacolén bridge have demonstrated the effectiveness of this approach for learning about the behavior of bridge foundations during lateral spreading, however, the results obtained from these models need further verification

and validation that can only be gained through the consideration of one or more different bridges. Several potential bridge sites have been identified for this purpose, both in Chile (see Chapter 4), and elsewhere in the world (see Chapter 1), and there are undoubtedly other bridges not identified in this work that would be suitable for the purpose.

The selection of any future case study bridges for use in a numerical evaluation of this problem should focus on site configurations and modeling aspects that were not considered in the Puente Mataquito and Llacolén bride cases. The parameter study presented in Chapter 10 has identified the importance of consideration for the full geometry of the site in determining the response of the foundation to lateral spreading. A bridge that is constructed in a different manner than Puente Mataquito or Llacolén would be useful for furthering the understanding of this problem. The current work has identified the influence of the bridge deck as a major factor in defining the lateral response of the foundation, therefore, it could be useful to incorporate a more rigorous description of the bridge deck, the expansion gap, and the deck to abutment connection in future models.

A dynamic analysis is another modeling refinement that holds potential for a three-dimensional assessment of the effects of lateral spreading on bridge foundations. The current work has focused simulating the kinematic demands of lateral spreading through simplified techniques. While this has shown to be an effective method with which to study foundation response to lateral soil deformation, the pseudo static approach employed in the models ignores certain aspects of the problem such as inertial forces and pore pressure generation effects. A dynamic effective stress model could allow for a more natural consideration of the problem, though such a model would present several challenges for the hypothetical future researcher.

In addition to the potential for modeling refinements or alternative configurations in advancing the understanding of the mechanisms governing the lateral spreading problem, future case study models could be used to support the further validation of the pile pinning analysis approach. This work has shown that this approach compared favorably with certain 3D models for Puente Mataquito and Llacolén bridge, but it is of interest to expand the scope of this validation effort to different bridge configurations and soil profiles. The pile pinning approach holds great potential for use as the primary simplified design technique for bridge foundation subject to lateral spreading, and any improvements or refinements that can be achieved through comparison to 3D models will greatly benefit the profession.

11.2.2 Parameter Study Expansion/Refinement

Another direction for future work lies in furthering the ideas obtained from the parameter study presented in Chapter 10. Specifically, it is of interest to determine whether a new series of models that considers a new set of site parameters produces bending demands that correspond to those obtained in this work. This future parameter study effort could focus on parameters that were not explicitly considered here, such as the height of the approach embankment, or on further variations in the parameters that were considered, such as more liquefied layer arrangements and different shaft designs. The consideration of more liquefied layer depths closer to the ground surface would be particularly useful, as this would expand the number of cases with smaller reduction ratios.

Other potential effects that may be beneficial to include in future studies of this nature are the effect of shaft groups or deck resistance on the influence of the geometric site parameters. The current data set includes only a single deep foundation, and it is not clear whether the addition of shaft foundations will affect the reduction in a manner similar to increases in foundation bending stiffness, or whether it will manifest as some other effect entirely. It is likely conservative to generate the reduction ratio data set in the absence of the additional lateral resistance provided by the bridge deck, however, it may be useful to include this aspect of the problem in order to be able to predict how this resistance affects the overall behavior of the system.

Appendix A

CONVERSION TABLE

Quantity	**From Metric Units**	**To English Units**	**Multiply by**
Length			
	km	mile	0.6214
	m	foot	3.2808
	m	inch	39.3701
Area			
	m^2	square foot	10.7639
	m^2	square inch	1550.0
Mass			
	kg	lb	2.2046
Mass density			
	kg/m^3	pcf	0.0624
Force			
	N	lb	0.2248
	kN	kip	0.2248
Pressure, stress, modules of elasticity			
	kPa	ksf	0.0209
	MPa	ksi	0.1450
Bending moment, torque, moment of force			
	kN·m	ft-kip	0.7376
Second moment of area			
	m^4	in^4	2402509.61
Velocity, speed			
	m/s	ft/s	3.2808
Acceleration			
	m/s^2	ft/s^2	3.2808

BIBLIOGRAPHY

Abdoun, T. and Dobry, R. (2002). "Evaluation of pile foundation response to lateral spreading." *Soil Dynamics and Earthquake Engineering*, 22, 1051–1058.

American Association of State Highway and Transportation Officials (AASHTO) (2010a). *Guide Specifications for LRFD Seismic Bridge Design*. Washington, D.C., 1st edition.

American Association of State Highway and Transportation Officials (AASHTO) (2010b). *LRFD Bridge Design Specifications*. Washington, D.C., 5th edition.

American Concrete Institute (ACI) Committee 318 (2011). *Building Code Requirements for Structural Concrete (ACI 318-11) and Commentary (ACI 318R-11)*. Farmington Hills, MI.

American Petroleum Institute (API) (1987). *Recommended Practice for Planning, Designing and Constructing Fixed Offshore Platforms*. API Recommended Practice 2A(RP-2A), Washington, D.C., 17th edition.

American Petroleum Institute (API) (2007). *Recommended Practice for Planning, Designing and Constructing Fixed Offshore Platforms–Working Stress Design*. API Recommended Practice 2A-WSD (RP 2A-WSD), 21st edition. Errata and Supplement 3, October 2007.

ARCADIS (2010). *Geostudies for infrastructure, mining & energy*. Trifold Brochure, ARCADIS Chile S.A., Providencia, Santiago, Chile.

Arduino, P., Kramer, S. L., Li, P., and Horne, J. C. (2006). "Stiffness of piles in liquefiable soils." *Seismic Performance and Simulation of Pile Foundations in Liquefied and Laterally Spreading Ground*, R. W. Boulanger and K. Tokimatsu, eds., GSP 145, ASCE. 134–148.

Armstrong, R. J. (2010). *Evaluation of the Performance of Piled Bridge Abutments Affected by Liquefaction-Induced Ground Deformations Through Centrifuge Tests and Numerical Analysis Tools*. Ph.D. Dissertation, University of California at Davis.

Armstrong, R. J., Boulanger, R. W., Galerce, U., Kutter, B. L., and Wilson, D. W. (2008). "Centrifuge modeling of pile pinning effects." *Geotechnical Earthquake Engineering and Soil Dynamics IV*, D. Zeng, M. T. Manzari, and D. R. Hiltunen, eds., GSP 181, ASCE.

Ashford, S. A., Boulanger, R. W., and Brandenberg, S. J. (2011). "Recommended design practice for pile foundations in laterally spreading ground." *PEER Report No. 2011/04*, Pacific Earthquake Engineering Research Center, University of California, Berkeley.

Ashford, S. A. and Juirnarongrit, T. (2006). "Push-over analyses of piles in laterally spreading soil." *Seismic Performance and Simulation of Pile Foundations in Liquefied and Laterally Spreading Ground*, R. W. Boulanger and K. Tokimatsu, eds., GSP 145, ASCE. 109–120.

Ashour, M. and Ardalan, H. (2011). "Piles in fully liquefied soils with lateral spread." *Computers and Geotechnics*, In Press, Corrected Proof.

Ashour, M., Norris, G., and Pilling, P. (1998). "Lateral loading of a pile in layered soil using the strain wedge model." *Journal of Geotechnical and Geoenvironmental Engineering, ASCE*, 124(4), 303–315.

Ashour, M., Norris, G., and Pilling, P. (2002). "Strain wedge model capabiity of analyzing behavior of laterally loaded isolated piles, drilled shafts, and pile groups." *Journal of Bridge Engineering, ASCE*, 7(4), 245–254.

Ates, S. and Constantinou, M. C. (2011). "Example of application of response history analysis for seismically isolated curved bridges on drilled shaft with springs representing soil." *Soil Dynamics and Earthquake Engineering*, 31, 334–350.

Aviram, A., Mackie, K. R., and Stojadinovic, B. (2008a). "Effect of abutment modeling on the seismic response of bridge structures." *Earthquake Engineering and Engineering Vibration*, 7(4), 395–402.

Aviram, A., Mackie, K. R., and Stojadinovic, B. (2008b). "Guidelines for nonlinear analysis of bridge structures." *PEER Report No. 2008/03*, Pacific Earthquake Engineering Research Center, University of California, Berkeley.

Basha, B. M. and Babu, G. L. S. (2009). "Computation of sliding displacements of bridge abutments by pseudo-dynamic method." *Soil Dynamics and Earthquake Engineering*, 29, 103–120.

Baska, D. A. (2002). *An analytical/emirical model for prediction of lateral spreading displacements.* Ph.D. Dissertation, University of Washington.

Berrill, J. and Yasuda, S. (2002). "Liquefaction and piled foundations: Some issues." *Journal of Earthquake Engineering*, 6(Special Issue 1), 1–41.

Berrill, J. B., Christensen, S. A., Keenan, R. P., Okada, W., and Pettinga, J. R. (2001). "Case study of lateral spreading forces on a piled foundation." *Géotechnique*, 51(6), 501–517.

Bhattacharya, S., Bolton, M. D., and Madabhushi, S. P. G. (2005). "A reconsideration of the safety of piled bridge foundations in liquefiable soils." *Soils and Foundations*, 45(4), 13–25.

Bielak, J., Loukakis, K., Hisada, Y., and Yoshimura, C. (2003). "Domain reduction method for three-dimensional earthquake modeling in localized regions, Part I: Theory." *Bulletin of the Seismological Society of America*, 93(2), 817–824.

Biot, M. A. (1941). "General theory of three dimensional consolidation." *Journal of Applied Physics*, 12, 155–164.

Biot, M. A. (1956). "Theory of propagation of elastic waves in a fluid saturated porous solid." *Journal of the Acoustical Society of America*, 28, 168–191.

Biot, M. A. (1962). "Mechanics of deformation and acoustic propagation in porous media." *Journal of Applied Physics*, 33, 1482–1498.

Bishop, A. W. (1955). "The use of the slip circle in the stability analysis of slopes." *Géotechnique*, 5(1), 7–17.

Boroschek, R., Soto, P., and León, R. (2010). *Registros del Terremoto del Maule, Mw=8.8, 27 de Febrero de 2010*. RENADIC Report 10/05.

Boulanger, R. W., Chang, D., Gulerce, U., Brandenberg, S. J., and Kutter, B. L. (2006). "Evaluating pile pinning effects on abutments over liquefied ground." *Seismic Performance and Simulation of Pile Foundations in Liquefied and Laterally Spreading Ground*, R. W. Boulanger and K. Tokimatsu, eds., GSP 145, ASCE. 306–318.

Boulanger, R. W., Kutter, B. L., Brandenberg, S. J., Singh, P., and Chang, D. (2003). *Pile Foundations in liquefied and laterally spreading ground during earthquakes: Centrifuge experiments and analyses*. Center for Geotechnical Modeling, University of California at Davis, Davis, CA. Rep. UCD/CGM-03/01.

Bozorgzadeh, A., Ashford, S. A., and Restrepo, J. I. (2008). "Effect of backfill soil type on stiffness and ultimate capacity of bridge abutments." *Geotechnical Earthquake Engineering and Soil Dynamics IV*, D. Zeng, M. T. Manzari, and D. R. Hiltunen, eds., GSP 181, ASCE.

Bradley, B. A., Cubrinovski, M., Dhakal, R. P., and MacRae, G. A. (2009). "Intensity measures for the seismic response of pile foundations." *Soil Dynamics and Earthquake Engineering*, 29, 1046–1058.

Bradley, B. A., Cubrinovski, M., Dhakal, R. P., and MacRae, G. A. (2010). "Probabilistic seismic performance and loss assessment of a bridge-foundation-soil system." *Soil Dynamics and Earthquake Engineering*, 30, 395–411.

Bradley, B. A., Cubrinovski, M., and Haskell, J. J. M. (2011). "Probabilistic pseudo-static analysis of pile foundations in liquefiable soils." *Soil Dynamics and Earthquake Engineering*, 31, 1414–1425.

Brandenberg, S. J., Boulanger, R. W., Kutter, B. L., and Chang, D. (2005). "Behavior of pile foundations in laterally spreading ground during centrifuge tests." *Journal of Geotechnical and Geoenvironmental Engineering, ASCE*, 131(11).

Brandenberg, S. J., Boulanger, R. W., Kutter, B. L., and Chang, D. (2007a). "Liqufaction induced softening of load transfer between pile groups and laterally spreading crusts." *Journal of Geotechnical and Geoenvironmental Engineering, ASCE*, 133(1), 91–103.

Brandenberg, S. J., Boulanger, R. W., Kutter, B. L., and Chang, D. (2007b). "Static pushover analyses of pile groups in liquefied and laterally spreading ground in centrifuge tests." *Journal of Geotechnical and Geoenvironmental Engineering, ASCE*, 133(9), 1055–1066.

Brandenberg, S. J., Zhang, J., Kashighandi, P., Huo, Y., and Zhao, M. (2011). "Demand fragility surfaces for bridges in liquefied and laterally spreading ground." *PEER Report No. 2011/01*, Pacific Earthquake Engineering Research Center, University of California, Berkeley.

Bray, J. D. and Travasarou, T. (2007). "Simplified procedure for estimating earthquake-induced deviatoric slope displacements." *Journal of Geotechnical and Geoenvironmental Engineering, ASCE*, 133(4), 381–392.

Brinch Hansen, J. (1961). "The ultimate resistance of rigid piles against transversal forces." *Bulletin No. 12*, Geoteknisk Institute, Copenhagen, 5–9.

Broms, B. B. (1964). "Lateral resistance of piles in cohesionless soils." *Journal of the Soil Mechanics and Foundations Division, ASCE*, 90(SM3), 123–156.

Brown, D. A. and Shie, C. F. (1990). "Three-dimensional finite element model of laterally loaded piles." *Computers and Geotechnics*, 10(1), 59–79.

Brown, D. A. and Shie, C. F. (1991). "Some numerical experiments with a three-dimensional finite element model of a laterally loaded pile." *Computers and Geotechnics*, 12, 149–162.

Brown, D. A., Shie, C. F., and Kumar, M. (1989). "*p-y* curves for laterally loaded piles derived from three-dimensional finite element model." *Proceedings of the III International Symposium, Numerical Models in Geomechanics (NUMOG III)*. Elsevier Applied Sciences, 683–690.

California Department of Transportation (Caltrans) (2011). *Guidelines on Foundation Loading and Deformation Due to Liquefaction Induced Lateral Spreading*. Internal Policy Proposal, February 2011.

Cetin, K. O., Seed, R. B., Der Kiureghian, A., Tokimatsu, K., Harder, L. F., Kayen, R. E., and Moss, R. E. S. (2004). "Standard penetration test-based probabilistic and deterministic assessment of seismic soil liquefaction potential." *Journal of Geotechnical and Geoenvironmental Engineering, ASCE*, 130(12), 1314–1340.

Chang, D., Boulanger, R. W., Brandenberg, S. J., and Boulanger, R. W. (2006). "Dynamic analyses of soil-pile-structure interaction in laterally spreading ground during earthquake shaking." *Seismic Performance and Simulation of Pile Foundations in Liquefied and Laterally Spreading Ground*, R. W. Boulanger and K. Tokimatsu, eds., GSP 145, ASCE. 218–229.

Chang, D. W., Lin, B. S., Yeh, C. H., and Cheng, S. H. (2008). "FD solutions for static and dynamic winkler models with lateral spread induced earth pressures on piles." *Geotechnical Earthquake Engineering and Soil Dynamics IV*, D. Zeng, M. T. Manzari, and D. R. Hiltunen, eds., GSP 181, ASCE.

Cheng, Z. and Jeremic, B. (2009). "Numerical modeling and simulation of pile in liquefiable soil." *Soil Dynamics and Earthquake Engineering*, 29(11-12), 1405–1416.

Cowan, M. (2011). *R101 South Brighton – Bridge Status Summary Report*. Opus International Consultants, Wellington, New Zealand.

Cubrinovski, M. and Ishihara, K. (1998a). "Modeling of sand behavior based on state concept." *Soils and Foundations*, 38(3), 115–127.

Cubrinovski, M. and Ishihara, K. (1998b). "State concept and modified elastoplasticity for sand modeling." *Soils and Foundations*, 38(4), 213–225.

Cubrinovski, M. and Ishihara, K. (2004). "Simplified method for analysis of piles undergoing lateral spreading in liquefied soils." *Soils and Foundations*, 44(5), 119–133.

Cubrinovski, M. and Ishihara, K. (2006). "Assessment of pile group response to lateral spreading by single pile analysis." *Seismic Performance and Simulation of Pile Foundations in Liquefied and Laterally Spreading Ground*, R. W. Boulanger and K. Tokimatsu, eds., GSP 145, ASCE. 242–254.

Cubrinovski, M. and Ishihara, K. (2007). "Simplified analysis of piles subjected to lateral spreading: Parameters and uncertainties." *Proceedings of the 4th International Conference on Earthquake Geotechnical Engineering*, Thessaloniki, Greece, June 25-28, Paper No. 1385.

Cubrinovski, M., Kokusho, T., and Ishihara, K. (2006). "Interpretation from large-scale shake table tests on piles undergoing lateral spreading in liquefied soils." *Soil Dynamics and Earthquake Engineering*, 26, 275–286.

Cubrinovski, M., Uzuoka, R., Sugita, H., Tokimatsu, K., Sato, M., Ishihara, K., Tsukamoto, Y., and Kamata, T. (2008). "Prediction of pile response to lateral spreading by 3-D soil-water coupled dynamic analysis: Shaking in the direction of ground flow." *Soil Dynamics and Earthquake Engineering*, 28, 421–435.

Dafalias, Y. F. and Manzari, M. T. (2004). "Simple plasticity sand model accounting for fabric change effects." *Journal of Engineering Mechanics*, 130(6), 622–634.

Dash, S. R., Bhattacharya, S., and Blakeborough, A. (2010). "Bending-buckling interaction as a failure mechanism of piles in liquefiable soils." *Soil Dynamics and Earthquake Engineering*, 30, 32–39.

Desai, C. S. and Appel, G. C. (1976). "3D analysis of laterally loaded structures." *Proceedings of the 2nd International Conference on Numerical Methods in Geomechanics*, Blacksburg, VA.

DFSAP (2006). *Deep Foundation System Analysis Program.* JP Singh & Associates *in association with* M. Ashour and G. Norris, *Prepared for* Washington State Department of Transporation (WSDOT).

Dicleli, M. (2005). "Integral abutment-backfill behavior on sand soil-pushover analysis approach." *Journal of Bridge Engineering, ASCE*, 10(3), 354–364.

Dicleli, M. and Erhan, S. (2005). "Effect of soil and substructure properties on live-load distribution in integral abutment bridges." *Journal of Bridge Engineering, ASCE*, 13(5), 527–539.

Duncan, J. M. and Chang, C. Y. (1970). "Nonlinear analysis oof stress and strain in soil." *Journal of the Soil Mechanics and Foundations Division, ASCE*, 96, 1629–1653.

Dungca, J. R., Kuwano, J., Takahashi, A., Saruwatari, T., Izawa, J., Suzuki, H., and Tokimatsu, K. (2006). "Shaking table tests on the lateral response of a pile buried in liquefied sand." *Soil Dynamics and Earthquake Engineering*, 26, 287–295.

Elgamal, A., He, L., Lu, J., Abe, A., Abdoun, T., Dobry, R., Sato, M., Takimatsu, K., and Shantz, T. (2006). "Liquefaction-induced lateral loads on piles." *Proceedings of the 4th International Conference of Earthquake Engineering*, Taipei, Taiwan, October 12-13, Paper No. 42.

Elgamal, A., Yan, L., Yang, Z., and Conte, J. P. (2008). "Three-dimensional seismic response of Humbolt Bay bridge-foundation-ground system." *Journal of Structural Engineering, ASCE*, 134(7), 1165–1176.

Elgamal, A., Yang, Z., Parra, E., and Ragheb, A. (2003). "Modeling of cyclic mobility in saturated cohesionless soils." *International Journal of Plasticity*, 19, 883–905.

Faraji, S., Ting, J. M., Crovo, D. S., and Ernst, H. (2001). "Nonlinear analysis of integral bridges: Finite element model." *Journal of Geotechnical and Geoenvironmental Engineering, ASCE*, 127(5), 454–461.

Faris, A. T., Seed, R. B., Kayen, R. E., and Wu, J. (2006). "A semi-empirical model for the estimation of maximum horizontal displacement due to liquefaction-induced lateral spreading." *Proceedings, 8th U.S. National Conference on Earthquake Engineering*, San Franciso, CA, April 18-22, Paper No. 1323.

Faruque, M. O. and Desai, C. S. (1982). "3D material and geometric nonlinear analysis of piles." *Proceedings of the 2nd International Conference on Numerical Methods in Offshore Piling*, University of Texas at Austin. 553–576.

Federal Highway Administration (FHWA) (1978). *Guidelines for Cone Penetration Test Performance and Design.* J. H. Schmertmann, Report FHWA-TS-78-209, U.S. Department of Transportation, Washington.

Federal Highway Administration (FHWA) (2011). *Post-Earthquake Reconnaissance Report on Transportation Infrastructure: Impact of the February 27, 2010, Offshore Maule Earthquake in Chile.* W.-H. P. Yen, G. Chen, I. Buckle, T. Allen, D. Alzamora, J. Ger, and J. G. Arias, Publication No. FHWA-HRT-11-030, U.S. Department of Transportation, McLean, VA.

Finn, W. D. L. (2005). "A study of piles during earthquakes: Issues of design and analysis." *Bulletin of Earthquake Engineering*, 3(2), 141–234.

Fleming, W. G. K., Weltman, A. J., Randolph, M. F., and Elson, W. K. (1985). *Piling Engineering*. Surrey University Press, London.

Franke, K. W. (2011). *A Performance-Based Model for the Computation of Kinematic Pile Response Due to Lateral Spread and its Application on Select Bridges Damaged During the M7.6 Earthquake in the Limon Province, Costa Rica*. Ph.D. Dissertation, Brigham Young University.

Geo-Engineering Extreme Events Reconnaissance (GEER) Association (2010a). *Geo-engineering Reconnaissance of the 2010 Maule, Chile Earthquake*. J. Bray and D. Frost, eds., Report No. GEER-022.

Geo-Engineering Extreme Events Reconnaissance (GEER) Association (2010b). *Geotechnical Reconnaissance of the 2010 Darfield (New Zealand) Earthquake*. R. A. Green and M. Cubrinovski, eds., Report No. GEER-024.

Geo-Engineering Extreme Events Reconnaissance (GEER) Association (2011). *Geotechnical Reconnaissance of the 2011 Christchurch, New Zealand Earthquake*. M. Cubrinovski, R. A. Green, and L. Wotherspoon, eds., Report No. GEER-027.

Gonzalez Lagos, L. L., Abdoun, T., and Dobry, R. (2007). "Centrifuge modeling of permeability and pinning reinforcement effects on pile response to lateral spreading." *Technical Report MCEER-07-0020*, Multidisciplinary Center for Earthquake Engineering Research, University at Buffalo, The State University of New York.

M. Hamada and T. O'Rourke, eds. (1992). *Case Studies of Liquefaction and Lifeline Performance During Past Earthquakes, Volume 1, Japanese Case Studies*. Technical Report NCEER-92-0001, National Center for Earthquake Engineering Research, Buffalo, NY.

Hara, T., Yu, Y., and Ugai, K. (2004). "Behavior of piled bridge abutments on soft ground: A design method proposal based on 2D elasto-plastic-consolidation coupled FEM." *Computers and Geotechnics*, 31, 339–355.

Hashiguchi, K. and Chen, Z.-P. (1998). "Elastoplastic constitutive equation of soils with the subloading surface and the rotational hardening." *International Journal for Numerical and Analytical Methods in Geomechanics*, 22(3), 197–227.

Idriss, I. M. and Boulanger, R. W. (2007). "Residual shear strength of liquefied soils." *Proceedings of the 27th USSD Annual Meeting and Conference, Modernization and Optimization of Existing Dams and Reservoirs*.

Idriss, I. M. and Boulanger, R. W. (2008). *Soil Liquefaction During Earthquakes*. Earthquake Engineering Research Institute (EERI), MNO-12.

Ingeniería Cuatro Ltda. (2006). *Ruta Costera, Proyecto de Modificación de Estribo Sur del Puente Mataquito, Proyecto de Construcción*. Documento No. 286-Mataquito MOD-ES-010, 06 de Octubre.

International Center for Numerical Methods in Engineering (CIMNE) (2008). *GiD The Personal Pre and Post Processor*. `http://gid.cimne.upc.es/`.

Janbu, N. (1973). "Slope stability computations." *Embankment Dam Engineering – Casagrande Volume*, R. C. Hirschfeld and S. J. Poulos, eds., John Wiley & Sons, New York. 47–86.

Jeremic, B., Guanzhou, J., Preisig, M., and Tafazzoli, N. (2009). "Time domain simulation of soil-foundation-structure interaction in non-uniform soils." *Earthquake Engineering and Structural Dynamics*, 38(5), 699–718.

Joyner, W. B. and Chen, A. T. F. (1975). "Calculation of nonlinear ground response in earthquakes." *Bulletin of the Seismological Society of America*, 65(5), 1315–1336.

Katayama, S., Fujii, T., and Takahashi, Y. (1966). "Damage caused by the Niigata Earthquake and the geological features of national highway in the suburbs of Niigata City." *Soil and Foundation*, VI(1), 54–70.

Kent, D. C. and Park, R. (1971). "Flexural members with confined concrete." *Journal of the Structural Mechanics Division, ASCE*, 97(ST7), 1969–1990.

Khalili-Tehrani, P., Ahlberg, E., Rha, C., Lemnitzer, A., Salamanca, A., Nigbor, R., Stewart, J. P., Wallace, J., and Taciroglu, E. (2007). "Field-testing and modeling of soil-structure interaction for highway support structures." *Proceedings of the 2007 Structures Congress*, R. Lyons, J. W. Wallace, and E. Stovner, eds., Long Beach, CA. ASCE.

Knappett, J. A. and Madabhushi, S. P. G. (2006). "Modelling of liquefaction-induced instability in pile groups." *Seismic Performance and Simulation of Pile Foundations in Liquefied and Laterally Spreading Ground*, R. W. Boulanger and K. Tokimatsu, eds., GSP 145, ASCE. 255–267.

Knappett, J. A., Mohammadi, S., and Griffin, C. (2010). "Lateral spreading forces on bridge piers and pile caps in laterally spreading soil: Effect of angle of incidence." *Journal of Geotechnical and Geoenvironmental Engineering, ASCE*, 136(12), 1589–1599.

Kondoh, M. and Tamura, K. (2003). "Experimental study on liquefaction-induced earth pressure on bridge abutment." *Proceedings of the 19th U.S.-Japan Bridge Engineering Workshop*, Tsukuba, Japan, October 27-30.

Kotsoglou, A. N. and Pantazopoulou, S. J. (2009). "Assessment and modeling of embankment participation in the seismic response of integral abutment bridges." *Bulletin of Earthquake Engineering*, 7(2), 343–361.

Kraft, L. M., Ray, R. P., and Kagawa, T. (1981). "Theoretical *t-z* curves." *Journal of the Geotechnical Engineering Division, ASCE*, 107(11), 1543–1561.

Kramer, S. L. (2008). *Evaluation of Liquefaction Hazards in Washington State.* Washington State Department of Transportation (WSDOT), WA-RD 668.1.

Kramer, S. L. and Mayfield, R. T. (2007). "Return period of soil liquefaction." *Journal of Geotechnical and Geoenvironmental Engineering, ASCE*, 133(7), 802–813.

Kulhawy, F. H. (1991). "Drilled shaft foundations." *Foundation Engineering Handbook, 2nd Ed.*, H.-Y. Fang, ed., New York. Van Nostrand Reinhold.

Kulhawy, F. H. and Mayne, P. W. (1990). "Manual on estimating soil properties for foundation design." *Report no.*, Electric Power Research Inst., Palo Alto, CA (USA); Cornell Univ., Ithaca, NY (USA). Geotechnical Engineering Group. EPRI EL-6800, Project 1493-6 Final Report.

Land Information New Zealand (LINZ) (2011). *Christchurch Post-Earthquake Aerial Photos (24 February 2011).* 10cm colour orthophotography of the area affected by the 22 February 2011 Christchurch earthquake. `http://http://koordinates.com/layer/3185-christchurch-post-earthquake-aerial-photos-24-feb-2011/#`. Accessed 17 February 2012.

Ledezma, C. (2012). "Case study of three pile-supported bridges affected by liquefaction-induced lateral spreading after the M8.8 2010 Maule Chile earthquake." *Second International Conference on Performance-Based Design in Earthquake Geotechnical Engineering*, Taormina, Italy, May 28-30, Paper No. 6.13.

Ledezma, C. and Bray, J. D. (2008). "Factors that affect the performance of bridge foundations undergoing liquefaction-induced lateral spreading." *Geotechnical Earthquake Engineering and Soil Dynamics IV*, D. Zeng, M. T. Manzari, and D. R. Hiltunen, eds., GSP 181, ASCE.

Ledezma, C. and Bray, J. D. (2010). "Probabilistic performance-based procedure to evaluate pile foundations at sites with liquefaction-induced lateral displacement." *Journal of Geotechnical and Geoenvironmental Engineering, ASCE*, 136(3), 464–476.

Lemitzer, A., Ahlberg, E. R., Nigbor, R. L., Wallace, A. S. J. W., and Stewart, J. P. (2009). "Lateral performance of full-scale bridge abutment wall with granular backfill." *Journal of Geotechnical and Geoenvironmental Engineering*, 135(4), 506–514.

Lemitzer, A., Khalili-Tehrani, P., Ahlberg, E. R., Rha, C., Taciroglu, E., Wallace, J. W., and Stewart, J. P. (2010). "Nonlinear efficiency of bored pile group under lateral loading." *Journal of Geotechnical and Geoenvironmental Engineering*, 136(12), 1673–1685.

LPILE (2010). *A Program for the Analysis & Design of Piles and Drilled Shafts Under Lateral Loads*. `http://www.ensoftinc.com`. Ensoft, Inc. Engineering Software, Austin, Texas.

Lysmer, J. and Kuhlemeyer, A. M. (1969). "Finite dynamic model for infinite media." *Journal of the Engineering Mechanics Division, ASCE*, 95, 859–877.

Manzari, M. T. and Dafalias, Y. F. (1997). "A critical state two-surface plasticity model for sands." *Géotechnique*, 47(2), 255–272.

Martin, G. R. (2004). "The seismic design of bridges - Geotechnical and foundation design issues." *Geotechnical Engineering for Transportation Projects*, M. K. Yegian and E. Kavazanjian, eds., GSP 126, ASCE. 137–166.

Martin, G. R., March, M. L., Anderson, D. G., Mayes, R. L., and Power, M. S. (2002). "Recommended design approach for liquefaction induced lateral spreads." *Proc., 3rd Natl. Seismic Conf. and Workshop on Bridges and Highways*, MCEER-02-SP04, Buffalo, NY.

Matlock, H. (1970). "Correlations for design of laterally loaded piles in soft clay." *Proceedings of the 2nd Offshore Technology Conference*, Houston, TX. (OTC 1204), 577–594.

McGann, C. R. (2009). "Analysis and evaluation of single piles in laterally spreading soil. Master's thesis, University of Washington.

McGann, C. R., Arduino, P., and Mackenzie-Helnwein, P. (2010). "Lateral resistance reduction for static analysis of lateral spreading." *Joint Conference Proceedings, 7th International Conference on Urban Earthquake Engineering (7CUEE) & 5th International Conference on Earthquake Engineering (5ICEE)*, Tokyo Institute of Technology, Tokyo, Japan. 593–600.

McGann, C. R., Arduino, P., and Mackenzie-Helnwein, P. (2011). "Applicability of conventional p-y relations to the analysis of piles in laterally spreading soil." *Journal of Geotechnical and Geoenvironmental Engineering, ASCE*, 137(6), 557–567.

McGann, C. R., Arduino, P., and Mackenzie-Helnwein, P. (2012). "Development of simplified analysis procedure for piles in laterally spreading layered soils." *PEER Report No. 2012/05*, Pacific Earthquake Engineering Research Center, University of California, Berkeley.

McGann, C. R., Arduino, P., and Mackenzie-Helnwein, P. (2015). "A stabilized single-point finite element formulation for three-dimensional dynamic analysis of saturated soils." *Computers and Geotechnics*, 66(0), 126–141.

McKenna, F., Scott, M. H., and Fenves, G. L. (2010). "Nonlinear finite element analysis software architecture using object composition." *Journal of Computing in Civil Engineering*, 24(1), 95–107.

McKenna, F. T. (1997). *Object-Oriented Finite Element Programming: Frameworks for Analysis, Algorithms and Parallel Computing*. Berkeley, California.

Meera, R. S., Shanker, K., and Basudhar, P. K. (2007). "Flexural response of piles under liquefied soil conditions." *Geotechnical and Geological Engineering*, 25(4), 409–422.

Meyerhof, G. G. (1956). "Penetration tests and bearing capacity of cohesionless soils." *Journal of the Soil Mechanics and Foundations Division, ASCE*, 82(SM1), 1–19.

Meyerhof, G. G. (1976). "Bearing capacity and settlement of pile foundations." *Journal of the Soil Mechanics and Foundations Division, ASCE*, 102, 197–228.

Mid-America Earthquake (MAE) Center (2010). *The Maule (Chile) Earthquake of February 27, 2010 Consequence Assessment and Case Studies*. A. S. Elnashai, B. Gencturk, O.-S. Kwon, I. L. Al-Qadi, Y. Hashash, J. R. Roesler, S.-J. Kim, S.-H. Jeong, J. Dukes, and A. Valdivia, Report No. 10-04.

Ministerio de Obras Públicas (MOP) (2002). *Manual de Carreteras, Vol. 3, Instrucciones y Criterios de Diseño*. Santiago, Chile.

Miwa, S., Ikeda, T., and Sato, T. (2006). "Damage process of pile foundation in liquefied ground during strong motion." *Soil Dynamics and Earthquake Engineering*, 26, 325–336.

Mokwa, R. L. and Duncan, J. M. (2000). *Investigation of the Resistance of Pile Caps and Intregral Abutments to Lateral Loading*. Publication No. FHWA/VTRC 00-CR4, Virginia Transportation Research Council, Charlottesville, VA.

Mokwa, R. L. and Duncan, J. M. (2001). "Laterally loaded pile groups and *p-y* multipliers." *Foundations and Ground Improvement: Proceedings of a specialty conference: June 9-13, Blacksburg, VA*, T. L. Brandon, ed., Geotechnical Special Publication No. 113. ASCE, 728–742.

Mokwa, R. L. and Duncan, J. M. (2003). "Rotational restraint of pile caps during lateral loading." *Journal of Geotechnical and Geoenvironmental Engineering, ASCE*, 129(9), 829–837.

Mosher, R. L. (1984). *Load transfer criteria for numerical analysis of axial loaded piles in sand*. Army Engineer Waterways Experiment Station, Vickburg, MS.

Moss, R. E. S., Seed, R. B., Kayen, R. E., Stewart, J. P., Der Kiureghian, A., and Cetin, K. O. (2006). "CPT-based probabilistic and deterministic assessment of in situ seismic soil liquefaction potential." *Journal of Geotechnical and Geoenvironmental Engineering, ASCE*, 132(8), 1032–1051.

Muqtadir, A. and Desai, C. S. (1986). "Three-dimensional analysis of a pile-group foundation." *International Journal for Numerical and Analytical Methods in Geomechanics*, 10, 41–58.

National Cooperative Highway Research Program (NCHRP) (2002). *Comprehensive Specification for the Seismic Design of Bridges*. NCHRP Report 472, National Academy Press, Washington, D.C.

Olson, S. M. and Stark, T. D. (2002). "Liquefied strength ratio from liquefaction flow failure case histories." *Canadian Geotechnical Journal*, 39, 629–647.

Ooi, P. S. K., Lin, X., and Hamada, H. S. (2010). "Numerical study of an integral abutment bridge supported on drilled shafts." *Journal of Bridge Engineering, ASCE*, 15(1), 19–31.

OpenSees (2007). *Open System for Earthquake Engineering Simulation*. `http://opensees.berkeley.edu`. Pacific Earthquake Engineering Research Center (PEER), University of California, Berkeley.

Park, R. and Paulay, T. (1975). *Reinforced Concrete Structures*. Wiley & Sons, New York.

Peck, R. B., Hanson, W. E., and Thornburn, T. H. (1974). *Foundation Engineering*. John Wiley & Sons, New York. 2nd Edition.

PEER (2010). *PEER Ground Motion Database for Shallow Crustal Earthquakes in Active Tectonic Regimes*. `http://peer.berkeley.edu/peer_ground_motion_database`. Pacific Earthquake Engineering Research Center, University of California, Berkeley.

Pender, M. J. and Robertson, T. W. (1987). "Edgecumbe earthquake: Reconnaissance report." *Bulletin of the New Zealand National Society for Earthquake Engineering*, 20(3), 201–249.

Petek, K. A. (2006). *Development and Application of Mixed Beam-Solid Models for Analysis of Soil-Pile Interaction Problems*. Ph.D. Dissertation, University of Washington.

Petrus Consultores Geotecnicos (2006). *Informe Complementario de Mecánica de Suelos, Puente Mataquito (Ruta Costera), Camino Quivolgo-Iloca (Cruce J-60).* Informe No. 2619-ING-SGC-150/2006 (Rev 1).

Prevost, J. H. (1977). "Mathematical modeling of monotonic and cyclic undrained clay behavior." *International Journal for Numerical and Analytical Methods in Geomechanics*, 1, 195–216.

Prevost, J. H. (1985). "A simple plasticity theory for frictional cohesionless soils." *Soil Dynamics and Earthquake Engineering*, 4, 9–17.

Priestley, M. J. N., Singh, J. P., Youd, T. L., and Rollins, K. M. (1991). "Costa Rica Earthquake Reconnaissance Report: Bridges (EERI)." *Earthquake Spectra*, 7(S2), 59–91.

Reese, L. C., Cox, W. R., and Koop, F. D. (1974). "Analysis of laterally loaded piles in sand." *Proceedings of the 6th Offshore Technology Conference*, Vol. 2, Houston, TX. 473–483.

Reese, L. C., Isenhower, W. M., and Wang, S.-T. (2006). *Analysis and Design of Shallow and Deep Foundations*. John Wiley & Sons, Inc., Hoboken, New Jersey.

Reese, L. C. and Van Impe, W. F. (2001). *Single Piles and Pile Groups Under Lateral Loading*. A.A. Balkema, Rotterdam, Netherlands.

Reese, L. C. and Van Impe, W. F. (2010). *Single piles and pile groups under lateral loading*. CRC Press.

Reese, L. C. and Welch, R. C. (1975). "Lateral loading of deep foundations in stiff clay." *Journal of the Geotechnical Engineering Division, ASCE*, 101(GT7), 633–649.

Rocscience (2010). *Slide 6.0 Slope Stability and Groundwater Software*. `http://www.rocscience.com`. Rocscience, Inc., Toronto, Ontario.

Rollins, K. M., Gerber, T. M., Lane, J. D., and Ashford, S. A. (2005). "Lateral resistance of a full-scale pile group in liquefied sand." *Journal of Geotechnical and Geoenvironmental Engineering, ASCE*, 131(1), 115–125.

Romstad, K., Kutter, B., Maroney, B., Vanderbilt, E., Griggs, M., and Chai, Y. H. (1995). "Experimental measurements of bridge abutment behavior." *Report No. UCD-STR-95-1*, Dept. of Civil and Environmental Engineering, University of California, Davis, CA.

Seed, H. B. and Reese, L. C. (1957). "The action of soft clay along friction piles." *Transactions, ASCE*, 122, 731–754.

Seed, R. B. and Harder, L. F. (1990). "Spt-based analysis of cyclic pore pressure generation and undrained residual strength." *Proceedings of the H. Bolton Seed Memorial Symposium, Vol. 2*, Vancouver, BC, Canada. BiTech Pub, Ltd., 351–376.

Sextos, A. G. and Taskari, O. (2008). "Comparative assessment of advanced computational tools for embankment-abutment-bridge superstructure interaction." *Proceedings of the 14th World Conference on Earthquake Engineering*, Beijing, China, October 12-17.

Shamsabadi, A., Ashour, M., and Norris, G. (2005). "Bridge abutment nonlinear force-displacement-capacity prediction for seismic design." *Journal of Geotechnical and Geoenvironmental Engineering*, 131(2), 151–161.

Shamsabadi, A., Khalili-Tehrani, P., Stewart, J. P., and Taciroglu, E. (2010). "Validated simulation models for lateral response of bridge abutments with typical backfills." *Journal of Bridge Engineering, ASCE*, 15(3), 302–311.

Shamsabadi, A., Rollins, K. M., and Kapuskar, M. (2007). "Nonlinear soil-abutment-bridge structure interaction for seismic performance-based design." *Journal of Geotechnical and Geoenvironmental Engineering, ASCE*, 133(6), 707–720.

Shin, H. (2007). *Numerical Modeling of a Bridge System & Its Application for Performance-Based Earthquake Engineering*. Ph.D. Dissertation, University of Washington.

Shin, H., Arduino, P., Kramer, S. L., and Mackie, K. (2008). "Seismic response of a typical highway bridge in liquefiable soil." *Geotechnical Earthquake Engineering and Soil Dynamics IV*, D. Zeng, M. T. Manzari, and D. R. Hiltunen, eds., GSP 181, ASCE.

Silva, P. F. and Manzari, M. T. (2008). "Soil-structure interaction analysis of bridge columns supported on CISS piles." *Geotechnical Earthquake Engineering and Soil Dynamics IV*, D. Zeng, M. T. Manzari, and D. R. Hiltunen, eds., GSP 181, ASCE.

Stewart, J. P., Taciroglu, E., Wallace, J. W., Ahlberg, E. R., Lemnitzer, A., Rha, C., and Khalili-Tehrani, P. (2007). "Full scale cyclic large deflection testing of foundation support systems for highway bridges. Part I: Drilled shaft foundations." *UCLA - SGEL Report 2007/01*, Department of Civil and Environmental Engineering, University of California, Los Angeles.

Suzuki, H., Tokimatsu, K., Sato, M., and Abe, A. (2006). "Factor affecting horizontal subgrade reaction of piles during soil liquefaction and lateral spreading." *Seismic Performance and Simulation of Pile Foundations in Liquefied and Laterally Spreading Ground*, R. W. Boulanger and K. Tokimatsu, eds., GSP 145, ASCE. 1–10.

Takahashi, A., Sugita, H., and Tanimoto, S. (2006a). "Beam on Winkler foundation methods for piles in laterally spreading soils." *Seismic Performance and Simulation of Pile Foundations in Liquefied and Laterally Spreading Ground*, R. W. Boulanger and K. Tokimatsu, eds., GSP 145, ASCE. 230–241.

Takahashi, A., Sugita, H., and Tanimoto, S. (2006b). "Permanent deformation of bridge abutment on liquefiable soils." *Technical Memorandum of Public Works Research Institute*, 4009, 411–424.

Takahashi, A., Sugita, H., and Tanimoto, S. (2010). "Forces acting on bridge abutments over liquefied ground." *Soil Dynamics and Earthquake Engineering*, 30, 146–156.

Tobita, T., Iai, S., Sugaya, M., and Kaneko, H. (2006). "Analysis of group pile behavior under lateral spreading." *Seismic Performance and Simulation of Pile Foundations in Liquefied and Laterally Spreading Ground*, R. W. Boulanger and K. Tokimatsu, eds., GSP 145, ASCE. 294–305.

Tokimatsu, K., Suzuki, H., and Sato, M. (2005). "Effects of inertial and kinematic interaction on seismic behavior of pile with embedded foundation." *Soil Dynamics and Earthquake Engineering*, 25, 753–762.

Uzuoka, R., Cubrinovski, M., Sugita, H., Sato, M., Tokimatsu, K., Sento, N., Kazama, M., Zhang, F., Yashima, A., and Oka, F. (2008). "Prediction of pile response to lateral spreading by 3-D

soil-water coupled dynamic analysis: Shaking in the direction perpendicular to ground flow." *Soil Dynamics and Earthquake Engineering*, 28, 436–452.

Valsamis, A., Bouckovalas, G., and Chaloulos, Y. (2011). "Simplified design of single piles under liquefaction induced lateral spreading." *Proceedings of the 5th International Conference on Earthquake Geotechnical Engineering*, Santiago, Chile, January 10-13, Paper No. SDOVA.

Vijayvergiya, V. N. (1977). "Load movement characteristics of piles." *Proceedings of the Ports '77 Conference, ASCE, Vol II.* 269–284.

Wallace, J. W., Fox, P. J., Stewart, J. P., Janoyan, K., Qiu, T., and Lermitte, S. (2001). "Cyclic large deflection testing of shaft bridges Part I: Background and field test results." *Report to California Department of Transportation.*

Wang, C.-H. (2003). *Prediction of the Residual Strength of Liquefied Soils.* Ph.D. Dissertation, University of Washington.

Washington State Department of Transportation (WSDOT) (2011a). *Bridge Design Manual (LRFD).* Technical Manual M 23-50.05, May 2011.

Washington State Department of Transportation (WSDOT) (2011b). *Geotechnical Design Manual (LRFD).* Technical Manual M 46-03.04, April 2011.

Wotherspoon, L., Bradshaw, A., Green, R., Wood, C., Palermo, A., Cubrinovski, M., and Bradley, B. (2011). "Performance of bridges during the 2010 Darfield and 2011 Christchurch earthquakes." *Seismological Research Letters*, 82(6), 950–964.

Wu, J. (2002). *Liquefaction Triggering and Post-Liquefaction Deformation of Monterey 0/30 Sand Under Uni-Directional Cyclic Simple Shear Loading*, Vol. 1. University of California, Berkeley.

Yang, Z. and Jeremic, B. (2002). "Numerical analysis of pile behavior under lateral loads in layered elastic-plastic soils." *International Journal for Numerical and Analytical Methods in Geomechanics*, 26(14), 1385–1406.

Yang, Z. and Jeremic, B. (2003). "Numerical study of the effective stiffness of pile groups." *International Journal for Numerical and Analytical Methods in Geomechanics*, 27(15), 1255–1276.

Yang, Z. and Jeremic, B. (2005). "Study of soil layering effects on lateral loading behavior of piles." *Journal of Geotechnical and Geoenvironmental Engineering, ASCE*, 131(6), 762–770.

Yoshimura, C., Bielak, J., Hisada, Y., and Fernández, A. (2003). "Domain reduction method for three-dimensional earthquake modeling in localized regions, Part II: Verification and applications." *Bulletin of the Seismological Society of America*, 93(2), 825–840.

Youd, T. L. (1993). "Liquefaction-induced damage to bridges." *Transportation Research Record No. 1411*, 35–41.

Youd, T. L., Hansen, C. M., and Bartlett, S. F. (2002). "Revised multilinear regression equations for prediction of lateral spread displacement." *Journal of Geotechnical and Geoenvironmental Engineering, ASCE*, 128(12), 1007–1017.

Youd, T. L., Idriss, I. M., Andrus, R. D., Arango, I., Castro, G., Christian, J. T., Dobry, R., Finn, W. D., Harder, L., Haynes, M. E., Ishihara, K., Koester, J. P., Liao, S. S. C., Marcuson, W. F., Martin, G. R., Mitchell, J. K., Moriwaki, Y., Power, M. S., Robertson, P. K., Seed, R. B., and Stokoe, K. H. (2001). "Liquefaction resistance of soils: Summary report from the 1996 NCEER and 1998 NCEER/NSF workshops on evaluation of liquefaction resistance of soils." *Journal of Geotechnical and Geoenvironmental Engineering, ASCE*, 127(10), 817–833.

Zha, J. (2004). "Lateral spreading forces on bridge abutment walls/piles." *Geotechnical Engineering for Transportation Projects*, M. K. Yegian and E. Kavazanjian, eds., GSP 126, ASCE. 1711–1720.

Zha, J. (2006). "Lateral spreading forces on bridge piles." *Seismic Performance and Simulation of Pile Foundations in Liquefied and Laterally Spreading Ground*, R. W. Boulanger and K. Tokimatsu, eds., GSP 145, ASCE. 71–82.

Zhang, G., Robertson, P. K., and Brachman, R. W. I. (2004). "Estimating liquefaction-induced lateral displacements using the standard penetration test or cone penetration test." *Journal of Geotechnical and Geoenvironmental Engineering, ASCE*, 130(8), 861–871.

Zienkiewicz, O. C. and Shiomi, T. (1984). "Dynamic behavior of saturated porous media; the generalized Biot formulation and its numerical solution." *International Journal for Numerical Methods in Geomechanics*, 8, 71–96.

Americans with Disabilities Act (ADA) Information:
This material can be made available in an alternate format by emailing the Office of Equal Opportunity at wsdotada@wsdot.wa.gov or by calling toll free, 855-362-4ADA(4232). Persons who are deaf or hard of hearing may make a request by calling the Washington State Relay at 711.

Title VI Statement to Public:
It is the Washington State Department of Transportation's (WSDOT) policy to assure that no person shall, on the grounds of race, color, national origin or sex, as provided by Title VI of the Civil Rights Act of 1964, be excluded from participation in, be denied the benefits of, or be otherwise discriminated against under any of its federally funded programs and activities. Any person who believes his/her Title VI protection has been violated, may file a complaint with WSDOT's Office of Equal Opportunity (OEO). For additional information regarding Title VI complaint procedures and/or information regarding our non-discrimination obligations, please contact OEO's Title VI Coordinator at (360) 705-7082.